UNIVERSITY of CALIFORNIA
Santa Barbara

Optical detection of quantum dynamics in GaAs neutral donors

A dissertation submitted in partial satisfaction of the
requirements for the degree of

Doctor of Philosophy

in

Physics

by

Dan G. Allen

Committee in charge:

Professor Mark Sherwin, Chair
Professor David D. Awschalom
Professor Elliott R. Brown
Professor Leon Balents

April 2008

The dissertation of Dan G. Allen is approved:

Professor David D. Awschalom

Professor Elliott R. Brown

Professor Leon Balents

Professor Mark Sherwin, Chair

June 2008

Optical detection of quantum dynamics in GaAs neutral donors

by

Dan G. Allen

Acknowledgements

I wish to thank Prof. Sherwin foremost for being at all times an example of professionalism and most especially his understanding, encouraging, supportive and considerate nature under every circumstance. These frequent examples will have the greatest long term impact on my life and future success. To those who lead the way before me in the Sherwin group: Sam Carter, Matt Doty, Kohl Gill, Brendan Serapiglia, and Nathan Jukam I am grateful for patient explanations and frequent help. Each of them persisted in the face of disappoints and plot twists to ultimate success and this was inspirational and encouraging to me, as I tended to give up too easily. To Sangwoo Kim, a good friend and partner in as many successes as failures I am much indebted. A good portion of the measurements presented here are the result of our time-intensive, and productive collaboration. To the current Sherwin group graduate students and post docs I am also grateful for continuous encouragement, listening ears and helpful suggestions: Chris Morris, Cristo Yee, Ben Zaks, Susumu Takahashi, and Dominik Stehr. I'm also grateful to Physics Dept's Mike Deal and Mike Wrocklege and Jeff Dutter at the machine shop for never actually banning me, frequently salvaging my poor designs, and kindly laughing at my many bad jokes–thanks. To my fellow classmates who helped me with my homework, and to my coursework instructors I am most grateful. Classroom instruction here, as a rule, topped that of any previous institution I have attended. I thank Profs. Joe Incandela, Gary Horowitz, Leon Balents, Matthew Fischer, Elliott Brown, Robert Sugar, Stephen Long, and Tony Zee. To Dave Enyeart and Gerry Ramian for keeping the Free Electron Laser working and many good times–thank you and best wishes. To my thesis committee and their busy students I am also grateful. I freely admit having been the beneficiary of sometimes one-sided collaborations with knowledgeable and expert graduate student researchers in the Awschalom and Brown groups: Vanessa Sih, Felix Mendoza, Zach Taylor, Adam Young and Jon Bjarnason. To CNSI and Holly Woo for the CNID fellowship and genuine help, to IQCD's Marlene Rifkin and her cheerful staff a big thanks as well. To the UCSB Physics department and the generous support of the Broida Fellowship ,which kept food in my children's mouths and shoes on their feet I extended heartfelt gratitude.

To the bright star of my life, Amanda Allen and my beautiful children whose pure and shining faces make a Santa Barbara sunset pale by comparison–I extend my thanks for patience and never-failing hope and my eternal love.

Curriculum Vitæ

Dan G. Allen

Education

1998–2004	Ph.D. Experimental Physics University of California, Santa Barbara Santa Barbara, California
1996–1997,1999-2001	B.S. Physics Brigham Young University Provo, Utah
1991–1996	Box Elder High School Brigham City, Utah

Employment

9/01-4/08	Graduate Student Researcher, University of California, Santa Barbara. Advisor: Prof. Mark S. Sherwin
6/07-2/08	Consultant: optomechanics and new products, New Focus Corporation, San Jose, CA
11/98-12/00	Teaching Assistant, Brigham Young University, Provo, UT
5/01-8/01	Graduate researcher, Los Alamos National Laboratory, Supervisors: Jennifer Hollingsworth, Victor Klimov

1/97-5/01	Undergraduate Researcher, Brigham Young University. Supervisor: Prof. Robert Davis

Publications

2008	D. G. Allen, Sangwoo Kim, C. R. Stanley, and M. S. Sherwin Rydberg atom physics in the solid state: resonance fluorescence detection of interactions in terahertz-excited hydrogenic impurity ensembles (Manuscript in preparation).
2008	D. G. Allen, Sangwoo Kim, C. R. Stanley, M. S. Sherwin Lifetime measurements of excited neutral donor states with optical readout (Manuscript to be submitted).
2007	J. He, H. J. Krenner, C. Pryor, J. P. Zhang, Y. Wu, D. G. Allen, C. M. Morris, M. S. Sherwin, and P. M. Petroff Growth, Structural, and Optical Properties of Self-Assembled (In,Ga)As Quantum Posts on GaAs Nano Letters **7** 802-806 (2007).
2007	D. G. Allen, L. Persechini, S. Takahashi, G. Ramian, M. S. Sherwin A diffraction-compensating 025 ns free space terahertz delay line for coherent quantum control. Rev. Sci. Instrum. **78** 113103 (2007)
2005	D. G. Allen, C. R. Stanley, M.S. Sherwin Optically detected measurement of the ground-state population of an ensemble of neutral donors in GaAs Phys. Rev. B. **72** 035302, (2005).

Conference Presentations

2007	Fundamental Optical Properties of Semiconductors (FOPS), Big Sky, MT Probing excited state lifetimes of electrons bound to donors with THz excitation and optical readout (poster)
2007	March APS meeting, Denver CO Optically detected quantum dynamics of neutral donor qubits (talk)
2006	CLEO/QELS, Long Beach, CA Lifetime measurements of excited neutral donor states in GaAs detected by resonant elastic light scattering (talk)

2005	March APS meeting, Long Angeles, CA Detection of quantum state of electrons bound to shallow donors via resonance fluorescence: ensemble measurements (talk)
2005	Gordon Research Conference on Quantum Information, Ventura, CA Detection of Quantum State of Electrons Bound to Shallow Donors via Resonance Fluorescence (poster)

Patents

2008	Dan G. Allen, Dongho Choi Open frame cage assembly (U.S Patent application pending)

Abstract

Optical detection of quantum dynamics in GaAs neutral donors

by

Dan G. Allen

Hydrogenic neutral donors in semiconductors are attractive candidates for the study of quantum dynamics of weakly interacting ensembles in the solid state. States of interest are the hydrogenic orbitals of the single electron that is weakly bound to a positively charged donor. Transitions between hydrogen-like bound electron orbitals fall in the terahertz region of the spectrum. For these atom-like, solid state-embedded quantum systems, photo-excitation to a short lived donor bound exciton D^0X state is dependent on the orbital state of the neutral donor.

State-dependent optical light scattering has previously enabled sensitive readout of quantum dynamics of localized quantum systems such as quantum dots, and quantum nondemolition readout of trapped ions via cycling transitions, especially for spin states. In previous research investigating dynamics of charge states, however, transport measurements based on photoconductivity, selective ionization, or field effect transistor devices have been emphasized.

As an alternative *optical* readout scheme, it is demonstrated that ground state (1S) neutral donors exhibit strong light scattering at the D^0X resonance, which fluorescence is quenched when donors are excited out of the ground state with terahertz radiation. The recovery of D^0X resonance fluorescence indicates the return of donors to the emitting ground state. Fluorescence recovery is expected to be limited by the long lifetime of the low-lying bound states, where a phonon-bottleneck is expected. Measured lifetimes are observed to depend sensitively on parameters affecting free carrier density, including sample temperature and dopant density, as well as excitation fraction and readout laser intensity. Recovery of fluorescence after pulsed resonant terahertz excitation to the $2P^-$ state exhibits strongly nonexponential decay. Two regimes of donor relaxation are observed: an initial fast decay in a tens of ns-scale decay limited, where inelastic scattering with unintentionally-excited free carriers reduces the bound state lifetimes, and a slow hundreds of ns-scale from phonon-limited decay of excited electrons out of the $2P^-$ state.

Optical readout of ground state neutral donors demonstrated here is complimentary to photoconductivity, which detects the ionized population. The demonstrated resonance fluorescence-based scheme enables sensitive detection of the internal quantum dynamics of neutral donors. Changes in the spectrum of both the free and donor bound exciton observed as a lineshift and broadening at higher excitation fractions are evidence of terahertz-activated interactions of ground state donors and/or excitons with excited or ionized neighbor donors.

Contents

List of Figures

Chapter 1

Introduction

1.1 Optical studies of quantum dynamics of impurity centers

There is increasing scientific and engineering interest in atomic defects for various applications including optoelectronics, spin physics, single photon sources, quantum bits and quantum repeaters for quantum information processing and quantum cryptography, as well as fundamental understanding of physics at nanoscale.

While the spectroscopic energy levels of impurity states in semiconductors are often easily measured, the dynamics associated with internal degrees of freedom are typically more difficult to measure, especially via means of detection which, of necessity, cause the transition of the charge or spin being interrogated into a continuum of states. Examples of such methods are photoconductivity, electron energy loss spectroscopy, photoemission spectroscopy, selective field ionization in atomic gases, deep level transient spectroscopy, temperature dependent mobility measurements, etc..

The dynamics of localized, few state quantum systems are more easily addressed when localized optical excitations are strong. Examples of such include Nitrogen-vacancy centers in diamond, epitaxial and colloidal quantum dots, carbon nanotubes, and ZnO nanowires, and various optically active impurities in semiconductors and insulators. Rapid developments in optical sources and detectors, especially ultrafast lasers and narrowband tunable lasers, has continually enhanced the capabilities of spectroscopists for studying these systems in recent years.

The work of this thesis focuses on optically detecting quantum state dynamics in a ubiquitous and well-studied type of defect: shallow donors in GaAs.

Shallow or hydrogenic donors consist of a single substitutional atom with one more proton than the atom expected at that position in the crystal. The positive charge of the impurity has a 1/r Coulomb potential which binds a single electron, with a Hamiltonian identical to that of hydrogen atom, with proper scaling for the electron conduction band effective mass and reduction of the fine structure constant by the bulk static dielectric permittivity (Fig. [**?**]). This results in an energy spectrum for a single electron with levels given by the familiar Rydberg formula and wavefunctions as given by Schrödinger, and found in every college quantum mechanics and chemistry textbook. The original theory of explaining the neutral donor bound state spectrum in terms of the band effective mass was proposed by W. Kohn, in 1957. In the intervening period, a mass of literature has been produced relevant to donors in nearly all technologically relevant semiconductors, especially in III-V and II-VI semiconductors, which occupy a fundamental place in the the solid state laser, LED and fiber optics/optoelectronic industry.

1.1.1 Quantum mechanical properties

Other interest in atomic defect centers focuses on their quantum mechanical properties, with relevancy to quantum information transmission and computation. The reasons for this are several. Optical activity makes them remotely addressable. Additionally, impurities in dilute concentrations can have very narrow ensemble linewidths (inhomogeneous broadening). Lastly, localized electronic and

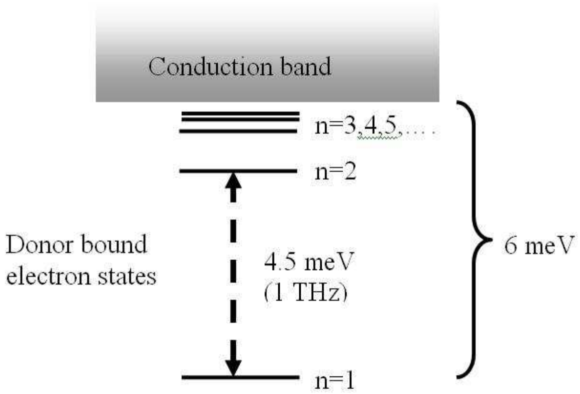

Figure 1.1: Energy level diagram of neutral donors. For clarity, only levels corresponding to principle quantum number n less than 5 are shown. Bound electron states have a hydrogenic spectrum with an ionization potential of approximately 5.7 meV, yielding bound state transitions in the THz.

spin states can have relaxation and decoherence times which are appreciably long compared to the time scale over which the states can be controlled and measured (see Appendix B).

For over a decade scientists have been searching for a suitable qubit: a few level quantum system marrying such desirable qualities as robust coherence, ensemble homogeneity, unique addressability and readout, energy tunability, conditional coupling to other qubits and a scalable geometry.[5, 6, 7] The goal of storing and manipulating quantum information has led to increased investigations of both atomic gas and solid state quantum systems, but has not yet turned up a suitable qubit for implementation of a logical (error-corrected) qubit.

A somewhat general engineering tradeoff has become appreciated since the search for a suitable quantum computing architecture commenced in earnest. For the study and manipulation of quantum states—in other words, for the study and manipulation of quantum information—atomic (gas) systems and solid state systems offer complimentary benefits and challenges. These qualities are summarized in Table 1.1.

In general, atomic systems, such as trapped ions and atoms exhibit very little inhomogeneous broadening. One atom is pretty much the same as another (ignoring Doppler effects), and the environment counts for little. In addition, isolated atoms have extremely small spatial extent, small dipole moments, are not intimately exposed to fluctuations and excitations in a thermal bath, such as a crystal lattice, and when dilute enough, can be confidently treated as well-isolated, independent systems (provided they are not laser-cooled to nanokelvin temperatures). In trapped ion systems, long-lived nuclear hyperfine states are typically used as quantum states for information storage and atomic optical (cycling) transitions are used for and readout and optionally state manipulations via stimulated raman transitions.[8, 9]

Solid state quantum systems such as donor/acceptor/vacany type defects, epitaxially self-assembled or lithographically defined quantum dots, or superconducting circuit devices are respectively inserted into a random crystal environment with other nearby defects, assembled stochastically, or fabricated onto their host crystal with limited precision. These systems exhibit well-defined quantum variables such as electronic spin state, orbital or exciton basis state, and superconducting current. However, such systems typically exhibit much more ensemble broadening

Property	Atomic	Solid State
Dephasing	slow (homogeneous)	rapid (inhomogeneous)
Coherence time	long (slow decoherence)	short (rapid decoherence)
Tunability	limited	broad
Coupling	difficult/weak	easy/strong

Table 1.1: Generalized advantages and challenges of studying quantum information in atomic (gas) and solid state systems. *Dephasing* is an ensemble property related to spread in transition energies; decoherence is a measure of sensitivity on an individual quantum system to environmental fluctuations. *Tunability* relates to a fractional change in transition energy due to an applied field. *Coupling* refers to the straightforwardness of addressing individual quantum systems and/or bringing two separate systems into interaction in a controllable way.

or time variance than atomic systems.

For solid state systems, crystal vibrations, strain, stray electric fields, nuclear spin bath fluctuations, etc. can be troublesome sources of decoherence. However, those same mechanisms open up possibilities for manipulation and selective coupling of the quantum states. Such interactions can even strongly modify the character of those states, as in the case of exciton-polaritons in photonic microcavities.

Because many of these systems are either man-made or self-assembled, the conditions of growth and fabrication pattern can be altered to *engineer* (I reserve the term "tune" for something that can be dynamically altered) energy spacings, which is useful in practice when other variables, such as a laser or cavity frequency, remain fixed due to financial, lab space, or technological limits. This engineerability and/or tunability makes these systems quite ideal for proof of concept quantum measurements.

However, increased accessibility and the attendant engineering handles have their price, and that is usually increased rates of dephasing and decoherence.

In many ways, atomic impurities accomplish a compromise which marries the high coherence and homogeneity of isolated atoms with the tunability and addressability of solid state systems.[10] An example are shallow neutral donors in GaAs. Based on the few available measurements and theoretical prediction in the published literature we expect long excited state lifetimes (∼100's of nanoseconds), reasonably high homogeneity (∼0.3%), and good energy tunability (∼10%).

1.2 Scientific merit

The study of neutral donors in GaAs invites progress in at least three areas of physics for which expertise in experiment and theory, let alone agreement are particularly difficult and/or rare. These are a few of the frontiers of science which neutral donors allow us to explore:

1. The ways and means of relaxation and decoherence in solid state systems
2. Many particle dynamics in the weakly interacting regime
3. Practical engineering of useful qubits

It should be said at the beginning that our investigations of quantum dynamics of neutral donors are contingent on our ability to interrogate the internal state of neutral donors, meaning we want to know which orbital the electron is in. The following motivates our choice of optical readout for detecting neutral donor quantum dynamics.

1.3 Why Optical Readout?

In previous investigations of neutral donor bound state dynamics, photoconductivity has been the workhorse, with the more challenging Thz pump-probe spectroscopy as runner-up.

The conductivity of high purity n-GaAs relates to the conduction population band (CB) in a known (though not necessarily linear) way. [11] The free electron population in the CB increases when neutral donors are excited to more weakly bound hydrogenic states, where the electron can be more easily thermally ionized. Based on this mechanism of readout, photoconductivity can be used to infer an excited state population with ∼20 ns time sensitivity.

For measurement of quantum *dynamics*, or when the application of an electrical bias is not desired, Terahertz pump-probe measurements can be used to deduce bound state population differences in time-resolved experiments.[12, 13]

Measuring terahertz photon absorbtion directly with low noise is challenging, since sensitive detectors are comparatively slow and must cryogenically cooled, and also because the high power free electron laser (FEL) source at UCSB does not run at high enough repetition rates to use lock-in detection.

For time-resolved measurements it is desirable to monitor a quality of the sample which can be detected instantaneously (∼ns) and is also particularly sensitive and directly dependent on the state of neutral donors.

Methods of optical detection of atomic dynamics were pioneered in the atomic physics community. The method of “quantum jumps” improved the sensitivity of readout to the single atom level.[9, 14, 15, 16] In trapped atoms and ions the presence of strict selection rules enables quantum nondemolition measurements of the nuclear hyperfine state of single atoms via resonant light scattering (resonance fluorescence and/or resonant Rayleigh scattering). Admittedly, much atomic physics research still relies on selective field ionization–the AMO experimental equivalent of photoconductivity.[17]

In the solid state community optical detection of THz dynamics is a well-used technique, owing to the availability of excellent sources and detectors in the optical and near infrared (NIR) spectral range and optical activity in many electronic materials of interest.[18, 19, 20, 21] The sensitivity of donor-bound exciton fluorescence to the state of neutral donors opens the possibility of optical detection of neutral donor bound state dynamics or bound exciton dynamics as proposed by Strauf et al.[22] Sensitive optical readout schemes exist for other solid state systems as well, which utilized both nonresonant (photoluminescence) and resonant (resonance fluorescence/resonance Rayleigh scattering) excitation scheme. For states based on localized electron spins, both optical readout and optical manipulation have been demonstrated. Notably, photoluminescence-based readout of another type of impurity, nitrogen vacancy centers in diamond, has been demonstrated.[23, 24, 25]. In epitaxial quantum dots, resonance fluorescence has also been used recently to study and manipulate single electron spins.[26, 27, 28] For colloidal quantum dots, photoluminescence optical readout and off-resonant polarization modulation readout have been demonstrated.[29]

In this thesis a new, sensitive optical detection technique is introduced for the study of the quantum dynamics of electrons bound to shallow atomic impurities in semiconductors. This technique is used to make a detailed study of factors affecting the lifetime of transitions between the bound states of electrons localized at shallow donor defects in GaAs (neutral donors).

The optical detection scheme is based on measuring resonantly scattered laser light from a localized interband transition—the donor-bound exciton. Absorption and re-emission of photons at the bound exciton resonance occurs only at shallow donors in the lowest Rydberg state. Whereas, resonant light scattering from donors in excited states is not observed. In ensemble measurements, the intensity of the resonant elastic light scattering (RELS) is proportional to the fraction of donor-bound electrons in the ground state. Changes in light scattering intensity/resonance fluorescence enable sensitive detection of the internal dynamics of these hydrogen-like atomic defects. The narrowband RELS readout technique is also sensitive to changes in the bound electron state energies via the a change in the bound electron or exciton binding energy relative to the band edge. This allows for detection of line shifts caused by donor-donor interactions. This state-dependent optical scattering demonstrated here-in, coupled with a reliable return from the bound exciton state to the neutral donor ground state, form the basis of a nondestructive readout technique, similar to the cycling transition based readout used ion trap quantum computing schemes.

The studied donor impurities are at a sufficiently low concentration that adjacent ground state donors are largely noninteracting. Using the optical readout technique terahertz-induced changes in the ground state population are observed in an ensembles of the atom-like neutral donors dispersed randomly in the host crystal lattice. The sensitivity of optical emission to changes in donor binding energy reveals donor-donor interactions as bound electrons are excited to more larger excited states with resonant terahertz excitation.

Chapter 2

Swept frequency terahertz spectroscopy

In this chapter I briefly explain terahertz photoconductivity and optical emission spectra of neutral donors in GaAs relevant to optical readout of donors via resonance fluorescence. I will refer the reader to Matt Doty's thesis *Coherent Manipulations of Ensemble of Hydrogenic Donors in GaAs*,[1], which gives a thorough and detailed review of donors states in a magnetic field which I will not attempt to improve upon or replace. Rather, by including here an abbreviated introduction, I wish to highlight salient features of the neutral donor properties for the purpose of motivating my studies of neutral donor dynamics.

2.1 Terahertz spectrum

The hydrogenic spectrum of neutral donors was known since the late 1950's.[30, 31] At cryogenic temperatures an electron can be bound to a shallow donor impurity by a $1/r$ coulomb potential from the extra proton in the donor impurity nucleus relative to the native lattice species. In the GaAs lattice, shallow donors form when Si, Ge, or Sn incorporate at a Ga site, or S, Se, or Te at an As site. The electron bound states are a hydrogenic series with a Rydberg energy

$$E_{ryd}[eV] = \frac{m^* e^4}{8\epsilon^2 h^2} = 13.6 * \frac{m^*/m_e}{\epsilon_r^2} = 0.0057. \tag{2.1}$$

The dramatic rescaling of energy is due to the small electron effective mass ($m^* = 0.0665 m_e$) and large static dielectric constant ($\epsilon_r = 12.56$). Note, the donor mass is effectively infinite so change of variables to a reduced mass (e.g. $\mu = m_e * m_p/(m_e + m_p)$) is not needed in the solid state system.

A small shift in the binding energy due to a donor-specific potential within the unit cell containing the donor atom can be seen in FTIR terahertz absorption photoconductivity spectra. This "central cell correction" in GaAs has been measured most accurately from optical spectra (ref. [32, 33]). The central cell correction is small and all the 1S–2P donor transitions for all of the common GaAs shallow donors falls within about a 1 cm^{-1} ($\sim$30 GHz) span.[34, 35]

Donor levels can be strongly altered by the application of a magnetic field. For purposes of scale, I can set the cyclotron energy equal to the Rydberg to obtain the crossover field B_c at which magnetic confinement in the plane perpendicular to the field begins to dominate the energy of Coulomb confinement.

$$\begin{aligned}\frac{\hbar e B_c}{m^*} &= E_{ryd} \qquad (2.2)\\ B_c &= \frac{E_{ryd} e m^*}{\hbar} = 3.29T \qquad (2.3)\end{aligned}$$

(In atomic physics literature the magnetic energy is estimated as the ground state cyclotron energy ($\hbar eB/2m$), rather than the Landau level splitting ($\hbar eB/m$) I used, so they come out with a value for the unit of atomic field strength larger by a factor of two.) For a neutral donor 3.3 T is equivalent to a magnetic field of ($\sim 10^5$ T) for atomic hydrogen.

Calculations of hydrogen orbitals in strong magnetic fields have been performed by various methods,[36, 37, 38, 39] and can be scaled directly by the electron effective mass ratio and two factors of the dielectric constant, then offset by the central cell correction E_{cc} for use with shallow donors in GaAs.[40, 41]

$$Ry_{donor} = \frac{m^*}{\epsilon^2} Ry_{hydrogen} + E_{cc} \qquad (2.4)$$

Theory for the 2P levels only from the work of Makado and McGill[40] is shown in a figure reproduced from the Thesis of Matt Doty (Fig. 2.1).

In the regime of magnetic fields 0–6 T, neutral donor wave functions are intermediate between the Landau orbitals and the zero field hydrogenic wavefunctions.

In the presence of a magnetic field the degenerate 2P states are Zeeman split into a triplet, labelled in the common notation (in increasing energy) $2P^-$, $2P^0$, and $2P^+$. One may assume two sets of equivalent energy level spectra identical to

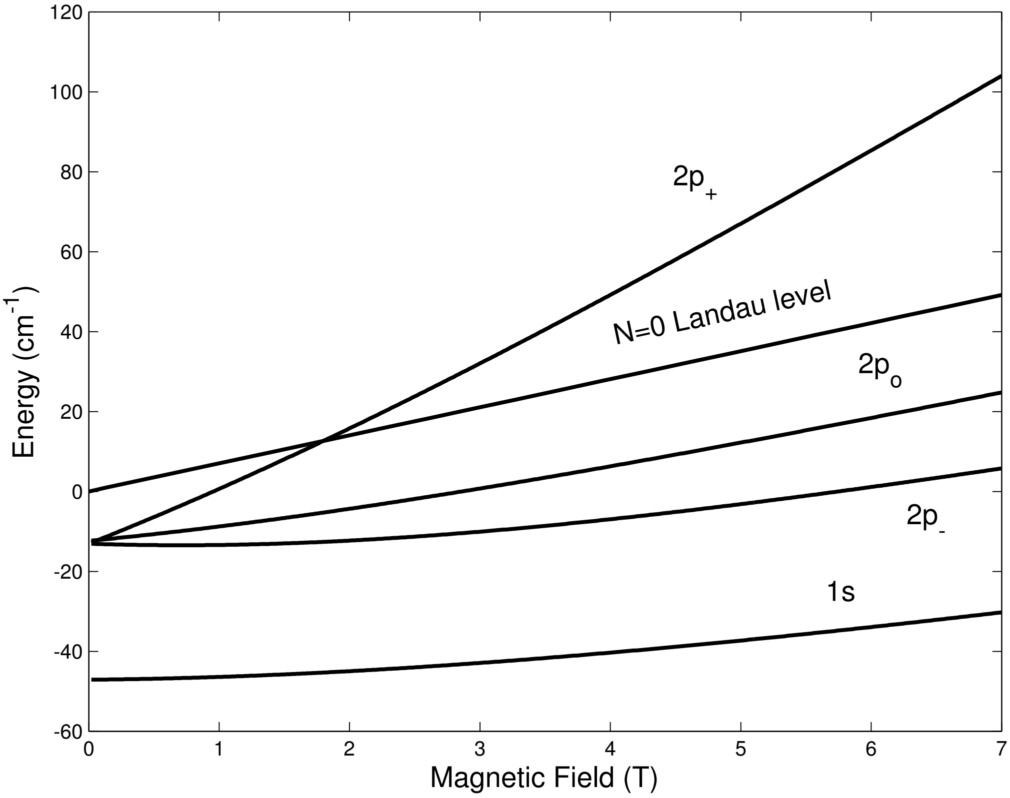

Figure 2.1: The energy levels of the 1s and 2p states as a function of magnetic field. Lines are drawn through points from the Makado and McGill calculation. The lowest two Landau levels are included, and the central cell shift is included in the 1s state energy. The energy of the lowest Landau level at zero field is taken to be zero. Figure from thesis of M. Doty.[1]

figure 2.1, for each of the two electronic spin states (up or down).[42] Spin-orbit coupling due to band nonparabolicity begin to make the 2P levels for up and down spin electrons inequivalent at higher magnetic fields.[43] However, in our samples inhomogeneous broadening at measured terahertz intensities apparently drowns spin-orbit effects in magnetic fields below 5 T, as no spin orbit splitting is observed in our high resolution spectroscopy.

I now consider the lowest energy bound-to-bound state transition (1S–2P$^-$).

2.2 1S–2P$^-$ photoconductivity spectroscopy

To measure the inhomogeneous broadening present in samples of high purity GaAs I performed high resolution, scanned frequency measurements of GaAs photoconductivity. These measurements reveal the inhomogeneous broadening at each magnetic field, which is due to stochastic placements of a majority of donors at concentration n_d, in the presence of compensating acceptors at relative concentration $n_a/n_d \sim 0.1$.[44]

Samples (see Appendix A) were grown by molecular beam epitaxy at the facility of Collin Stanley in the late 1980's as he was attempting to purify his MBE machine for growth of very high mobility material.[45] The epitaxial layers were grown on either undoped or semi-insulating substrates (substrates cut from crystals grown with free carrier-gettering deep impurities such as Fe). Epilayer thicknesses are 10–20 μm. Some samples have a capping layer of 10–20 nm thickness doped with 10^{18}cm^{-2} Si. This capping layer is ionized by surface impurities which pin the Fermi level in the middle of the band gap at the surface. The total dose of Si dopants is less than the equivalent surface charge of the impurities, so the dopants in the surface layer are all ionized. This capping layer greatly reduces the depletion region within the sample, which enables better homogeneity due to confinement of the depletion field to a small region near the surface. It also allows for ohmic contacts to be made to the high purity epilayer. Uncapped material with depletion lengths of 1–5 μm is increasingly difficult to contact for low impurity concentrations

The sample is prepared for photoconductivity measurements using the processing method described in the Matt Doty's thesis, Appendix A.[1] A 50x50 μm mesa of epilayer is contacted on two sides by annealed Ti/Pt/Au electrodes with a comb of narrow fingers so as to reduce absorption to THz polarization in the polarization perpendicular to the gap between the leads.

Resistance at low temperature (<4 K) is in the MΩ range, highly nonlinear[11] and very sensitive to both donor-ionizing radiation and radiation which promotes donor-bound electrons to higher lying, thermally ionizable levels.

The sample (B434, $n_d - n_a = 2.8 \times 10^{14}$cm^{-3} at 77 K, see Table A.1) is mounted inside the bore of a superconducting solenoid immersed in liquid He. The liquid He is cooled to below the superfluid transition for optical clarity (no bubbles). The experimental arrangement is depicted schematically in Fig. 2.2.

The sample is biased at 50 mV with a Stanford Research Instruments cur-

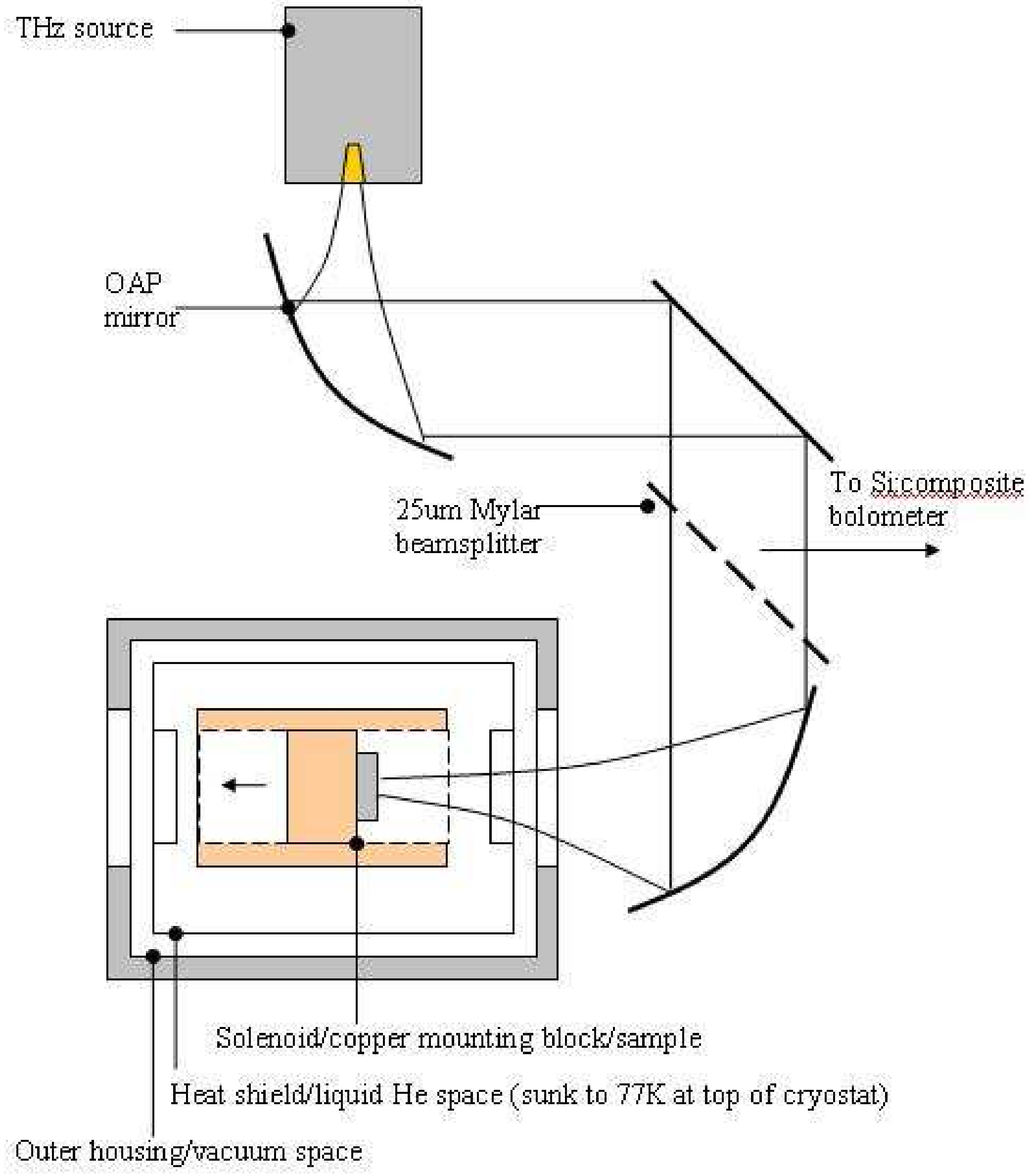

Figure 2.2: Experimental arrangement for photoconductivity experiments. Terahertz from a solid state source is coupled to a free space Gaussian mode by a feedhorn, collimated and the focused onto the sample by a pair of off-axis parabolic mirrors. A thin film mylar beamsplitter sends a few percent of the beam to a bolometer to record the output power at each frequency. The sample is enclosed in a 0–6.5 T superconducting solenoid, immersed in liquid He at 2 K mounted in the Faraday configuration. Z-cut quartz windows shield thermal radiation while transmitting the FIR excitation.

rent sensitive (transimpedance) amplifier. Excitation is provided by a tunable solid state frequency source. The source (Virginia Diodes, Inc.) uses a 13 GHz microwave synthesizer, a doubler amplifier, and a chain of two tunable doubly input-output resonant doubler/tripler Schottky diode multipliers to multiply the the AC microwave signal by a factor of 72 to 1 THz. The synthesizer is tunable in steps of 1 kHz, so the the THz source output tunes in 72 kHz steps. The solid state source provides about 5 μ W continuous wave (CW) power and an extremely narrow linewidth in a 10% tunable bandwidth (960–1080 GHz) for high resolution terahertz excitation spectroscopy. The source is coupled to free space via a feedhorn with a 1 mm output aperture in the horizontal polarization (Fig. 2.2). The emergent Gaussian beam is collimated with a 3.5" focal length 90° off-axis parabolic (OAP) mirror, and directed onto a second 5" focal length OAP which focuses the terahertz onto the photoconductive gap. The focal spot size is estimated to be approximately 2 mm. A mylar beamsplitter directs a small portion of the beam to a Si:composite bolometer which monitors the source output intensity in order to normalize out changes in output intensity with frequency. The beam is modulated below 200 Hz with an optical chopper or PIN switch that chops the microwave synthesizer output. The amplified photoconductivity signal is detected with a lock-in amplifier using a time constant of 0.3-1 s and a three pole low pass filter.

Figure 2.3 shows measured photoconductive response versus frequency at several magnetic fields.

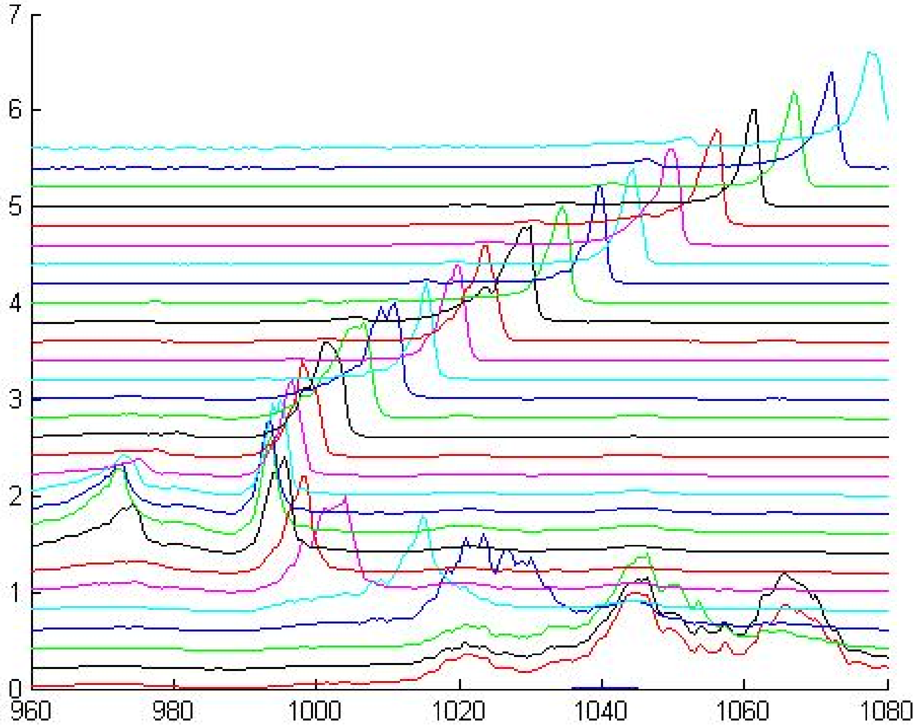

Figure 2.3: Neutral donor photoconductivity (vertical axis) at several magnetic fields are plotted versus frequency [GHz] (horizontal axis). Traces are shown normalized in linear arbitrary scale. Traces offset by the magnetic field (T) at which they were taken, which is the scale on the vertical axis. Resonances changing with magnetic are due to 1S–2P$^-$ absorption from at least two donor species. Static resonances are attributed to Fabry-Perot effects.

In the data periodic resonances in frequency are observed which are not magnetic field dependent. These resonances are attributed to Fabry-Perot effects in the sample and antenna effects in the leads and sample mount geometry. When a donor line shifts into one of these resonances, its apparent magnitude increase. A water absorption line is also apparent in the data near 990 GHz.

Peaks in the photoconductivity spectrum indicate the transition energies of donor species at each magnetic field. Two donor species are present in the spectrum of this sample; one donor species is dominant. The relative peak spacing for the two species is more than 20 GHz at fields of 4 T and higher. The separation of the lines and the spectral locations are consistent with the assignment of Ge as the majority donor species and Si as the minor donor. This contradicts the assumption made by Cole and Doty[46, 1] based on reported impurities in wafers from other growths in the same MBE chamber given by Stanley.[45] Other donor species except for S, which appears between the two donors species are not expected to be present in significant amounts in these samples. High resolution photoconductivity spectra were not taken for every sample investigated in this thesis, however magnetic fields scans at a fixed (though uncalibrated) FEL laser frequencies show either one or two peaks consistent with the presence of Ge and/or Si donors.

A minimum linewidth of 3 GHz is seen at 5T, corresponding to a T_2^* of 100 ps. The asymmetric lineshape is understood to be a result of the random placement of donors and compensating impurities in the lattice.[44]

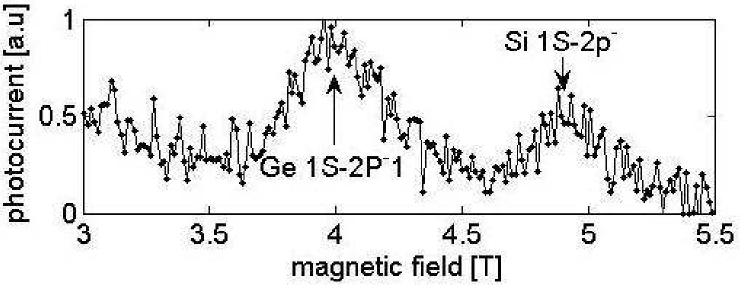

Figure 2.4: Fixed frequency (FEL terminal voltage at 2.48 mV, approximately 34.5 cm^{-1}), swept magnetic field photoconductivity spectrum of sample B763, $1 \times 10^{14}\text{cm}^{-3}$. Peaks have approximately similar amplitude, even without taking into account the decrease in efficiency of photoconductive readout with magnetic field. The low magnetic field peak is attributed to Ge and the higher peak with Si.

Resonances at identical magnetic fields for the highest donor species were observed for another sample (B671, $3 \times 10^{14}\text{cm}^{-3}$) on which electrodes with larger 3 μm fingers were fabricated with a smaller 30x30 μm gap. The Fabry-Perot or antenna resonances were much stronger in this sample, and applied biases were two to three times higher. This photoconductivity data is used to calibrate the free electron laser (Jan 10, 2008) terminal voltage relative to the donor resonances. Transient photoconductivity due to an FEL pulse was recorded by varying the magnetic field, and data was obtained similar to that obtained by Doty.[1] Once the magnetic field at which a donor 1S–2P$^-$ resonance occurs is known for a given FEL terminal voltage, the frequency of the FEL can be referenced to the position of the resonance measured by the frequency-calibrated VDI source at the same magnetic field. (This was done since the FEL calibration changes whenever hardware or software changes are made to the generating volt meter that senses the terminal voltage or its readout software. Also, a NIR sideband generation

FEL voltage (MV)	B field resonance (T)	Freq. resonance(GHz)
2.46	3.82	—
2.48	4.2	1037 ± 3
2.49	4.5	1044 ± 2
2.50	4.75	1052 ± 2
2.51	4.95	—
—	5.0	1068 ± 5
2.52	5.1	—
—	5.25	1072 ± 2
2.53	5.35	—

Figure 2.5: FEL calibration based on 1S–2p$^-$ photoconductivity resonance. Values for the 1S–2P$^-$ resonance are recorded at fixed FEL frequency and varied magnetic field, and at fixed magnetic field and varied solid state source frequency. Note that the calibration of the FEL is based on coincidence of Ge resonances, and is not dependent on the accuracy of the magnetic field reading, only its repeatability. It is also dependent on the settings for converting the voltage read by the generating volt meter embedded in the wall of the accelerator into an estimate of the terminal voltage (which can be changed via software).

experiment[47] has not been available to measure the FEL frequency directly, as was done for calibration in Matt's experiments.) Table 2.5 summarizes the magnetic field at which 1S–2P$^-$ resonances were found at fixed FEL frequencies, together with the frequency of peaks measured by the VDI source on the sample B671.

This high-resolution, swept frequency spectroscopy is the first of its kind to the author's knowledge for neutral donors in GaAs. Typically narrowband emission from a molecular gas laser is used at a single frequency and energy resonances are tuned through the laser by magnetic field tuning. Alternatively FTIR spectroscopy can be done with a broadband light source. However, Swept frequency spectroscopy can be useful alternative to FTIR spectroscopy, for instance, in order to avoid certain transitions excited by broadband light. It also allows for determination of lineshapes without tuning a magnetic field, which is useful when a fixed magnetic field is required or when lineshape properties. For instance, we are able to determine that the minimum linewidth occurs at 5 T.

Chapter 3

Neutral donor resonance fluorescence

3.1 Photoluminescence spectroscopy

In GaAs, donors (and acceptors) act as recombination centers for bound electro-hole pairs. In high purity direct band gap semiconductors such as GaAs in which there is a predominance of donors, donors are responsible for most of the band edge emission. Direct recombination of excitons only begins to show up at densities in the low 10^{13}cm^{-3}, with donor and acceptor densities of comparable order.

Due to the coulomb attraction, optically excited electrons are bound to their vacant valence orbital. This electron-hole pair, termed *exciton*, is a hydrogenic system with a lifetime in n-GaAs of approximately 1 ns,[48] but can be even shorter in a quantum well.[49] Excitons are attracted to both neutral and ionized donors and acceptors and emission from such are identifiable in photoluminescence (PL) spectra.

Karasyuk and coworkers performed a detailed high resolution spectroscopic study of donor-bound exciton emission in GaAs over a wide range of magnetic fields in both the Faraday and Voigt geometries,[35]. In the prevalent notation used by Karasyuk et al., ionized donors are denoted by the symbol D^+, likewise ionized acceptors as A^-. Neutral donors and acceptors are symbolized by D^0 and A^0, respectively.

Excitons bind to ionized and neutral impurities, forming a transient molecular species. The donor bound exciton, written D^0X, is like a neutral hydrogen molecule, complete with a rotational spectrum. The difference is that one atom is fixed and after 1 ns, the exciton decays, usually via emission of a photon in the absence of mid-gap impurity states.

The spectrum of impurity-bound exciton emission is recorded by optically exciting a cooled (5K) GaAs sample with a laser exciting above the band gap at 1.52 eV (816 nm) (see Fig. 3.1). Excitation is from a tunable external cavity diode laser incident at Brewster's angle. 0.01–1 mW average optical power is incident on a region of 2x2 mm size, for typical intensities in the range 1–100 $\mathrm{mWcm^{-2}}$. Surface emission is collimated and measured by a 0.75 m imaging spectrometer with a CCD detector. Spectrometer resolution is 0.01 nm (20 μeV).

The PL features in figure 3.1 are identified by the labelled arrows and discussed in turn.

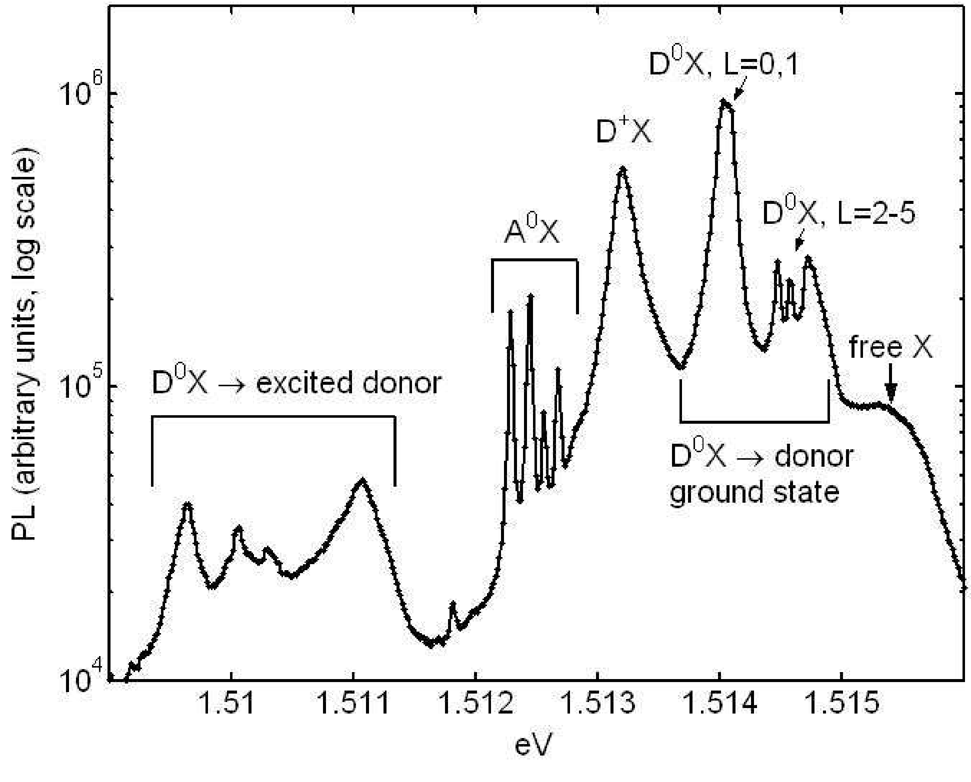

Figure 3.1: Donor- and acceptor-bound exiton photoluminescence (PL) in from n-GaAs (sample B48) excited above the band gap plotted versus energy on a logarithmic scale. Relevant spectral features are labelled: direct exciton (X), direct neutral donor bound exciton (D^0X), ionized donor bound exciton (D^+X), neutral acceptor bound exciton (A^0X), and indirect (Auger or two-electron satellite) neutral donor bound exciton transitions ($D^0X \rightarrow$ excited donor).

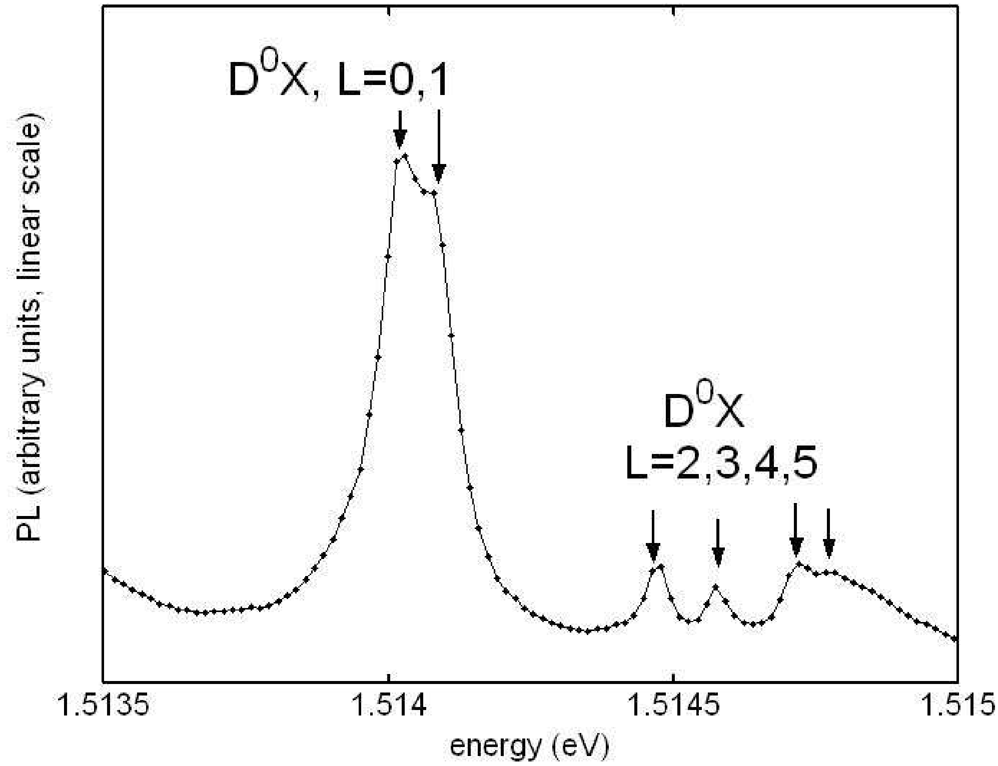

Figure 3.2: D^0X photoluminescence showing rotational transitions. 4 K, 0 T photoluminescence from n-GaAs doped below $10^14 cm^{-3}$ includes transitions from initial states from within a manifold of rotational hydrogen molecule-like transitions. Spectral resolution is 20 μeV.

- The free exciton emission (X) is seen above 1.515 eV.

- Below the band gap, the neutral donor bound exciton (D^0X) emission is observed. D^0X transitions occur from a variety of initial rotational states; the final state is a ground state neutral donor (D^01S). I term these *direct* recombination transitions; these transitions are depicted schematically in figure 3.3. The rotational/vibrational spectrum is shown in detail in figure 3.2.

- The ground state binding energy of the exciton to the neutral donor can be seen to be ∼1 meV, for an effective ionization activation temperature of $E/k_B = 11.6$ K. A zoomed view shows lowest two rotational transitions are barely resolved (Fig. 3.2). Transitions originating from different donor species are not resolved in direct transitions, but can be resolvable with a higher resolution spectrometer in the two-electron satellite transitions.[35]

- Emission from excitons bound to ionized donors D^+X–D^+ is seen at 1.5325 eV. The significant inhomogeneous broadening of this peak suggests the ionized donor emission occurs in an area distinct from neutral donor emission. This is consistent with the most ionized donor emission coming from the densely doped capping layer/surface depletion region. However, due to a finite acceptor compensation ($n_a/n_d \sim 0.2$, where n_a is the concentration of acceptor impurities and n_d is the donor concentration) ionized donors are present throughout the sample and are primarily responsible for inhomogeneous broadening of donors transition line widths.

- The weak neutral acceptor-bound exciton A^0X peaks near 1.5125 eV suggest a low amount of background acceptor compensation. Private communications by Stanley estimate the background acceptor concentration at about 0.2 for samples in which the hall mobility and peak mobility were both measured.

- The weakest emission occurs in the region 1.509–1.5115 eV. The lines are known as two-electron satellite or TES transitions. TES emission originates from donor bound excitons in various rotational states, but the final state is *not* the neutral donor ground state. The final state is, rather, a neutral donor with its bound electron in an excited hydrogenic (2S, 2P, 3S, 3P, 3D, etc.) bound state orbital (Fig. 3.3). This transition occurs via the Auger process in which the bound exciton decays, but simultaneously gives part of its energy to the donor, and emitting a photon with correspondingly reduced energy. The difference between the energy of the direct transition and Auger transition is the difference between the ground and final state of the neutral donor (4–6 meV). These lines are weaker than direct transitions because the semiconductor has a direct band gap, so that the comparatively slow Auger process does not compete strongly. However, in Si, an indirect band gap semiconductor, a nonradiative Auger auto-ionization process dominates over phonon-assisted exciton recombination resulting in weak impurity-bound

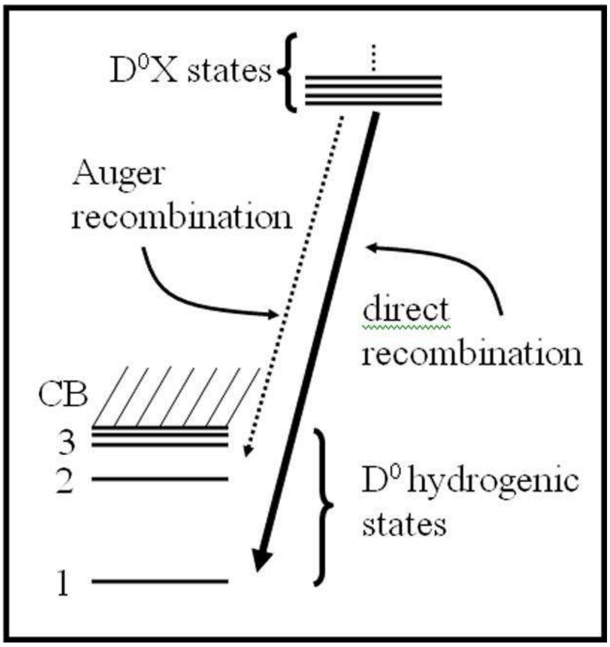

Figure 3.3: A schematic energy level diagram (not to scale) in the exciton basis contrasting the final states of direct bound exciton recombination and Auger recombination.

luminescence.

3.2 Resonant excitation spectroscopy

Electrons bound to donors are a zero dimensional system, meaning the electron momentum is quantized in all three directions. Because of this, the density of states for each donor comprises a series of delta functions in energy. Bound exciton states share this same dimensionality constraint and exhibit a discrete energy level spectrum. As described in the previous section, bound excitons can be created by exciting free excitons, which then relax to the band edge and bind to donors, releasing the difference of the excitonic band edge E_g and binding energy E_b as a phonon or series of phonons. But the bound exciton state can also be created resonantly with excitation at energy E_g-E_b, just below the free exciton peak.

3.2.1 Excitation fraction

The fraction of excited donor-bound excitons can be estimated. The frequency integrated cross section for bound exciton absorption is $\sigma = 3.9 \pm 0.9 \times 10^{-11}\text{cm}^{-2}$ from Ref. [48], and the lifetime is estimated to be $\tau = 1 \pm 0.1$ ns. Piling all the transition strength into a single effective transition, I can estimate an upper bound on the number of donors bound excitons created on average. For a sample with dopant density $n_d - n_a = 10^{14}\text{cm}^{-3}$ the absorption length is $1/(n_d - n_a)\sigma = 5\mu\text{m}$. Thus, nearly all photons in a 10 μm epilayer are absorbed, as long as the excitation is well below saturation. This criterion is met when average excitation fraction is small compared to unity. The following are needed: the photon flux $\phi[photons/scm^2]$, the neutral donor concentration $n_d - n_a$, and the bound exciton lifetime τ.

The photon flux $\phi[mWcm^2s]^{-1}$ at photon energy E=1.5 eV, with X mWcm^{-2} excitation and electron charge e is

$$\phi = \frac{0.001X}{Ee} = \frac{4X \cdot 10^{15}[photons]}{[scm^2]}. \tag{3.5}$$

Assuming all photons are absorbed, and no photons are reabsorbed, the total number of excitation events is just $\phi\sigma$, and the average excited fraction is $\phi\sigma\tau$

$$\phi\sigma\tau = 4X \cdot 10^{-5} \tag{3.6}$$

The highest NIR intensity used is ∼100 $\mathrm{mWcm^{-2}}$, for an average excitation fraction of 0.4%.

The assumption that no emitted photons are reabsorbed is certainly not justified, but not all donors are excited by the narrow linewidth laser, so we are confident this is an upper bound and that excitation is not sufficient to saturate the transition. Spectroscopists prefer to work below 1 $\mathrm{mWcm^{-2}}$[48], but I find 10–20 $\mathrm{mWcm^{-2}}$ is sufficiently low intensity to constitute a "weak continuous probe". At 10 $\mathrm{mWcm^{-}2}$ each donor is probed on average only once every 2.5 μs, which is much longer than the neutral donor lifetime.

3.2.2 Excitation processes

At least five processes occur under resonant excitation of donor the bound exciton.

1. Free exciton creation

   Free exciton absorption occurs due to the tail of band edge absorption decaying into the gap. This process is weak, since excitation is more than $k_B T$ below the band gap. However, GaAs wafers are not fully transparent at this wavelength. From measurements of samples put in backwards, we can estimate semi-insulating substrates are at least 10% transmissive, if not more.

2. Resonance fluorescence

   This is simply resonant creation of a bound exciton, followed by emission of an incoherent (randomly polarized) photon of the same energy.

3. Rayleigh scattering

   In resonance Rayleigh scattering (RRS), a photon is coherently scattered from the bound exciton resonance. RRS is copolarized with the excitation. I was unable to measure any preferential polarization in the emission from the sample on resonance, however, other authors claim that up to 80 % of resonant elastic light scattering from neutral donors occurs via resonant rayleigh scattering.[50, 2] In either event, resonant elastic light scattering from either fluorescence or Rayleigh scattering dominates over inelastic processes.

4. Inelastic scattering/photoluminescence

   Inelastic scattering or photoluminescence occurs via a virtual or real creation of an exciton at the bound exciton resonance. The scattered or emitted photon energy differs by the energy of a bound exciton rotational transition. It may also differ by the energy of a phonon (Raman scattering) or the energy of a donor bound electron Lyman transition (via the Auger process). In the last case the decay of the exciton leaves the neutral donor in an excited bound state. Inelastic scattering is comparatively weak in GaAs, owing to fast direct band gap recombination. However, at significant pump

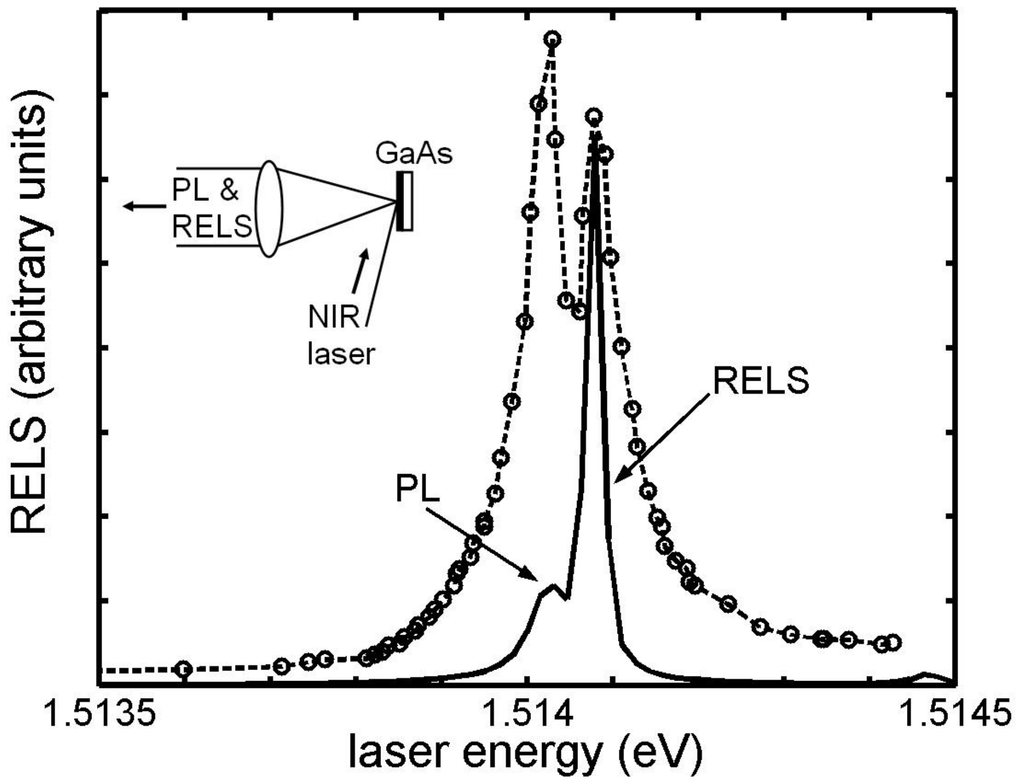

Figure 3.4: Resonant elastic light scattering and PL from high purity n-GaAs at 5 K. Inset shows experimental geometry. The solid curve shows the spectrum of emission including elastic (resonance fluorescence) and inelastic (photoluminescence) components with excitation at 1.5141 eV. The dotted line is comprised of data points indicating the magnitude of the resonant elastic light scattering with excitation at that frequency. Data published previously in ref. [2].

intensities, a finite population is transferred to long-lived excited neutral donors states, thereby reducing the ground state population. This effect is known as *shelving*, and is a mechanism for reducing fidelity in a quantum nondemolition measurement.

Elastic light scattering in the region of the direct donor bound exciton transitions from a sample of high purity n-GaAs at 4 K is presented in figure 3.4.

Data is taken by exciting high purity n-GaAs at Brewster's angle with a single frequency, grating-tuned external cavity diode laser <10 mWcm^{-2} intensity. Surface emission is collected and sent to a 0.75 m focal length imaging spectrometer with a liquid nitrogen cooled CCD detector (0.01 nm effective resolution). The RELS spectrum shows the elastic light scattering cross section, which rises rapidly on resonance. The two lowest rotation states of the donor bound exciton are more well resolved by RELS than in PL (fig. 3.2). The RELS emission may be spread over several CCD pixels, but a Gaussian fit yields the effective amplitude of RELS and the excitation wavelength with much higher precision than the resolution of the spectrometer (Max. Res[nm]$\sim$0.25 $\times$pixel width [mm]$\times$linear dispersion [nm/mm]). This is responsible for the effective increase in resolution of RELS relative to PL. For RELS the minimum step size in the tuning of the laser or certainty in the Gaussian fit will limit the resolution rather than diffraction.

3.2.3 State dependent scattering

Notably, bound exciton Auger transitions are out of resonance with light exciting direct D^01S–D^0X transitions. Light of 1.514 eV energy excites excitons at ground state donors. The Lyman-α transition ($\sim$4 meV) is much larger than the binding energy of the exciton (1 meV). This means that all transitions from the excited donor states to excited bound exciton states are out of resonance with D^01S–D^0X excitation by at least 3.5 meV (Fig. 3.5). Further, these transitions

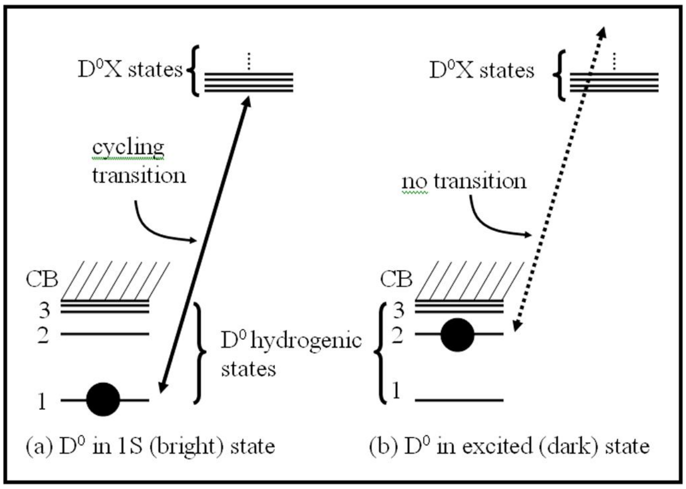

Figure 3.5: Resonant D01S–D^{0}X excitation does not promote excited donors to bound exciton states.

are weak, even under resonant excitation.

RELS measured from the direct D^{0}X transition should be dependent on the internal state of a neutral donor. Ground state donors should scatter the incident light and return to the ground state with high probability, whereas excited donors should not interact with the off-resonant excitation.

Under this hypothesis a reduction in D^{0}X RELS should occur when donors are excited out of the ground state.

This state-dependent emission is reminiscent of the *cycling transition* used in atomic physics for quantum nondemolition readout of ions in vacuum electromagnetic traps.[14, 15, 16]

3.2.4 Intensity dependence

At low intensities in samples with dopant densities less than 10^{14}cm^{-3} or with insufficient doping in the capping layer, the D^0X direct emission is superlinear with excitation intensity, contrary to the usual effect of reduction in fluorescence emission efficiency with increasing power (Fig. 3.6-upper).

The initial superlinear rise in some samples is attributed to the creation of free charge (donor ionization) in the depletion region (e.g from exciton scattering). This effect is depicted schematically in Fig. 3.7. This free charge separates to screen the depletion length near the surface, creating more neutral donors where NIR intensity is high and light collection is efficient. The change in slope efficiency to sublinear behavior is associated with a decrease in PL efficiency from exciton-exciton scattering, and also a potential shelving of donors into long-lived Rydberg bound states (e.g. 2S) via Auger transitions. In other samples, no superlinear rise due to surface charging is seen, but rather a slow saturation behavior attributable to shelving or reduced fluorescence efficiency from exciton-exciton or exciton-carrier scattering (Fig. 3.6-lower).

Surface charging can be observed directly in dynamical and spectrally resolved power dependent experiments. For time resolved measurements the NIR excitation laser is left off and then switched on with a Pockels cell with a 20 ns rise time (see Appendix F). Figure 3.8-upper) shows a sharp turn-on when the Pockels cell fires, followed by a a slow intensity dependent rise in the resonant elastic light

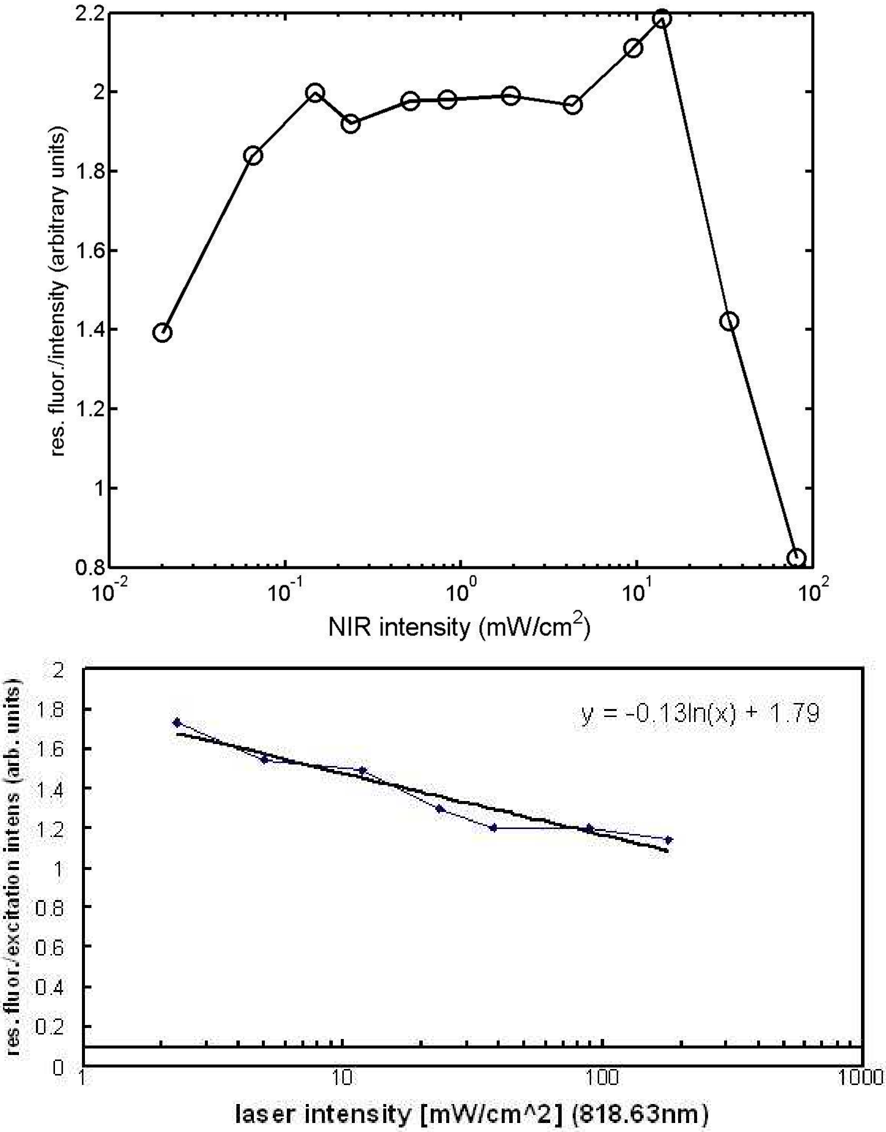

Figure 3.6: (Upper) Integrated GaAs D^0X photoluminescence versus excitation intensity in the range for sample B48. Excitation intensity is on a normalized scale with maximum intensity less than 1000 $mWcm^{-2}$. (Lower) Power dependence of D^0X fluorescence for sample B763 ($1 \times 10^{14}cm^{-3}$). Normalized data is plotted linearly versus the logarithm of the incident intensity, and shown with a logarithimic fit for comparison, revealing a continuous slow saturation behavior over the relevant experimental range.

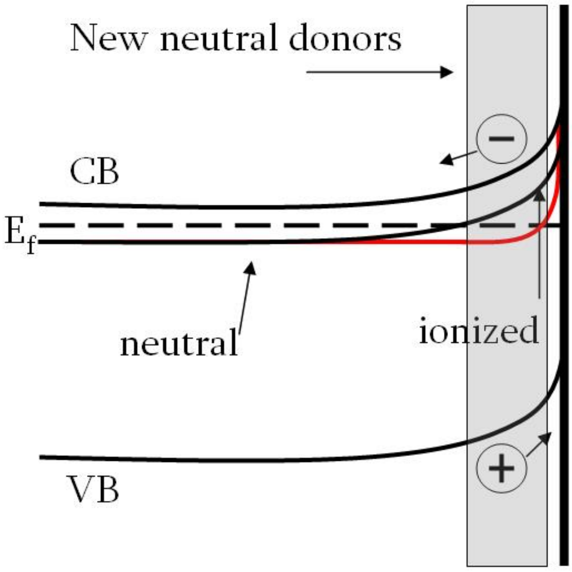

Figure 3.7: Enhancement of RELS intensity due to NIR excitation: surface charging effect. Diagram (not to scale) showing bending of the valence and conduction bands near the surface. Broken bonds and defects act as charge traps which pin the Fermi level (dashed line) mid gap at the surface. The surface charge repels electrons and attracts holes with a field which decays over a region whose length is determined by the ratio of surface change density to dopant density. Donors in the this depletion region are ionized and do not contribute to RELS. When excitons (e^-, h^+) are created in the depletion region, they may separate to screen the surface depletion field, resulting in a shorter depletion length (solid red curve). Emission from donors in the shaded region is thus "activated" in the presence of band gap excitation.

scattering to the maximum value for a sample with insufficient surface doping. Figure 3.8-lower) shows linear response in resonance fluorescence emission for a sample with sufficient surface doping.

The relative power dependence of peaks in the PL spectra are shown in (Fig. 3.9) for a sample (B763) with sufficient surface doping. By scaling each spectrum by the incident power it is apparent that the exciton peak increases relative to the ionized donor peak, while the ionized donor peak increases linearly. The D^0X peak does not increase at the expense of the D^+X peak, indicating the increase in exciton fluorescence is due to a combination of mechanisms such as passivation of nonradiative relaxation pathways associated with defects and deep impurities by free carriers generated at higher excitation powers, partial saturation of nonradiative recombination channels and/or decreased coupling of acoustic phonons to bound excitons via increased charge screening. Some broadening of the bound exciton transition occurs at higher pump intensities. This effect was not investigated in detail.

These data suggest that to limit the free charge density and associated charging effects it is important to work in an excitation intensity regime below 100 $\mathrm{mWcm^{-2}}$ for PL measurements of neutral donors.

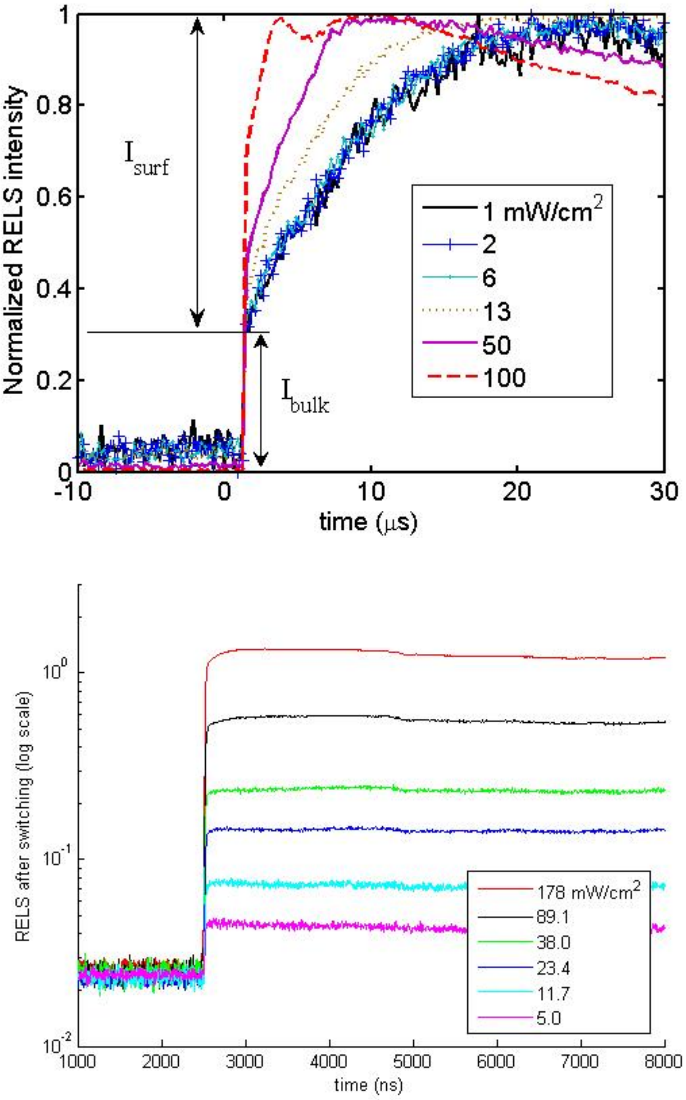

Figure 3.8: (Upper) Change in fluorescence intensity after switching on interband excitation. Sample is A422, 6×10^{13}cm^{-3}. After switching, a slow, intensity dependent rise in D^0X resonance fluorescence to the saturated value is observed. Traces are normalized by to the maximum emission. (Lower) Similar traces for sample B763, 1×10^{14}cm^{-3} shown on a logarithmic scale. (Oscillation in the signal is seen beyond 2 μs due to a slow electrical oscillation resulting from due to competition of the DC Pockels effect and ringing in the electrical driver circuit.)

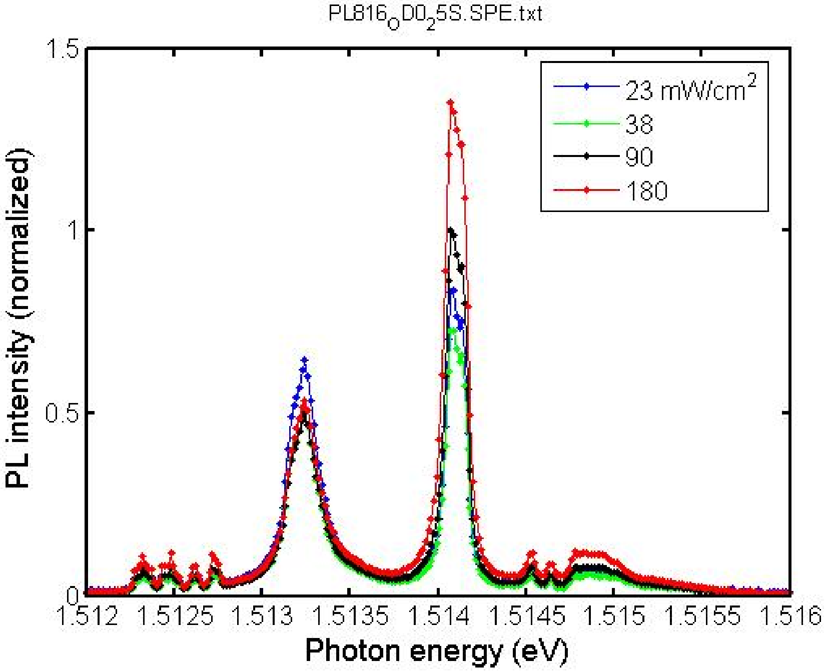

Figure 3.9: Pump power dependence of the T=2 K photoluminescence spectrum of sample B763 ($1 \times 10^{14}\mathrm{cm}^{-3}$), excitation at 1.52 eV, with traces normalized by incident intensity. Other than the small relative shift of the red trace which is due to a static offset in the dark current on the CCD, the intensity of the ionized peak is approximately linear, whereas the exciton peak increases superlinearly.

3.3 RELS in a magnetic field

For measurements of donor spectra in a magnetic field a sample is place in a liquid He immersion optical magnet cryostat with Z-cut crystal quartz windows and pumped to below the superfluid transition for optical clarity. The sample arrangement is shown in Fig. 3.10. The optical sample is held with in a free fitting copper box with apertures for admitting light on both the front and back faces. NIR excitation is incident on the epilayer surface, while terahertz focused by an off-axis parabolic mirror is incident through the undoped or semi-insulating substrate. A second sample with leads for measuring photoconductivity is placed off axis within the bore on the backside of the sample mount. A lens is placed within the bore of the magnet to maximize the solid angle of light collected from the sample. A portion of the lens is removed by a diamond grinding tool to allow the excitation laser to pass. A mirror mounted on the sample holder directs the p-polarized excitation light onto the sample at an angle of 60° incidence from normal, which is as close to Brewster's angle as this arrangement will admit. Prior to entering the cryostat, the NIR laser is expanded and then brought to an elliptical focus by a pair of orthogonally oriented cylindrical lenses of different focal length, so as to produce a nearly circular spot on the sample at high angles of incidence. To reduce scatter light, dense black paper is used to trap the surface reflection. Additionally, a piece of terahertz-transmissive black polyethylene can be mounted behind the sample inside the box to reduce laser light transmitting through the substrate and scattering off the copper mount. This is especially important for semi-insulating substrates.

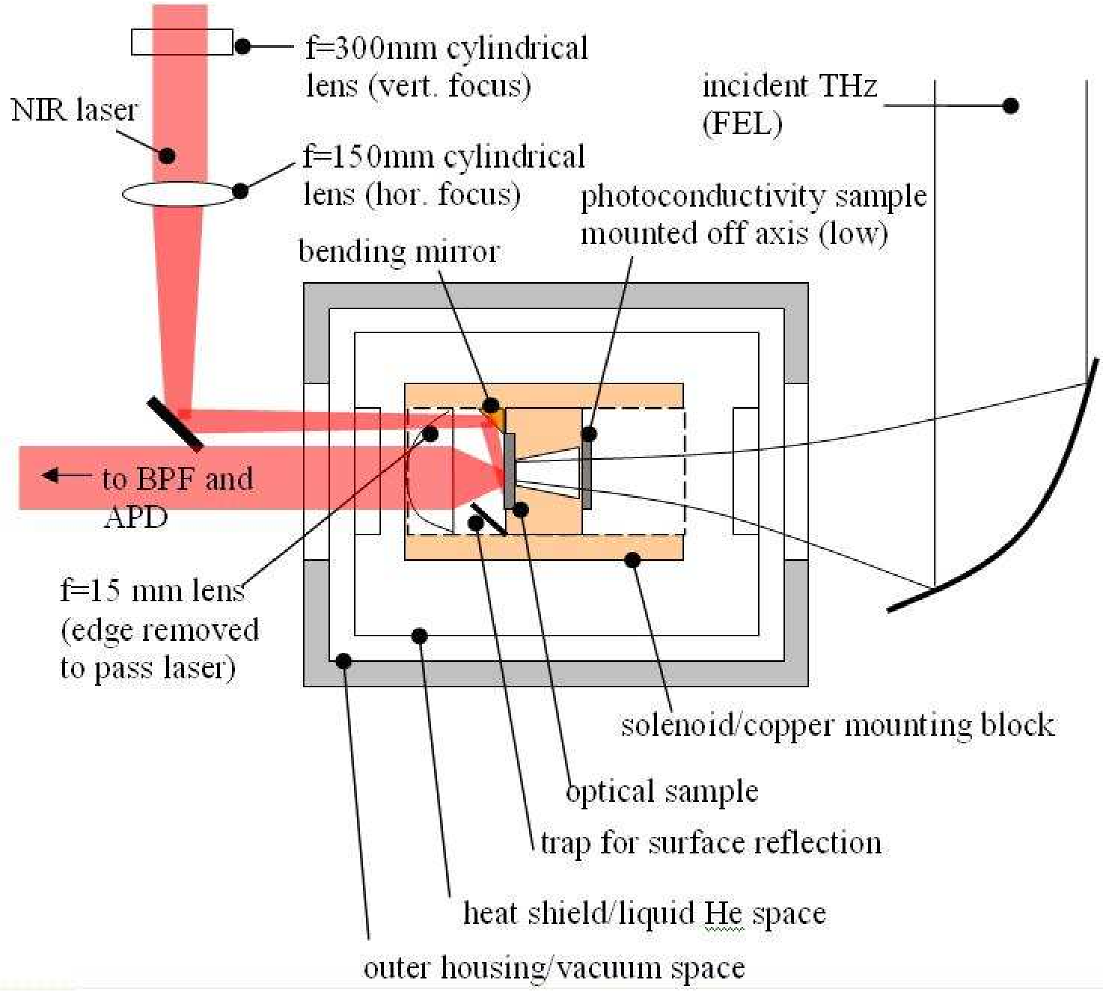

Figure 3.10: Sample arrangement for optical and photoconductivity measurements in a magnetic field. Important parts are label or described in the text.

In a magnetic field, each of the donor bound exciton rotational states becomes Zeeman split. The electronic spin in the bonding orbital shared by the spin-paired electrons is zero, so the total spin of bound exciton spin is simply the 3/2 spin of the hole. The final states corresponding to ground state neutral donors are also spin split. Neglecting minor nuclear spin effects the neutral donor spin is

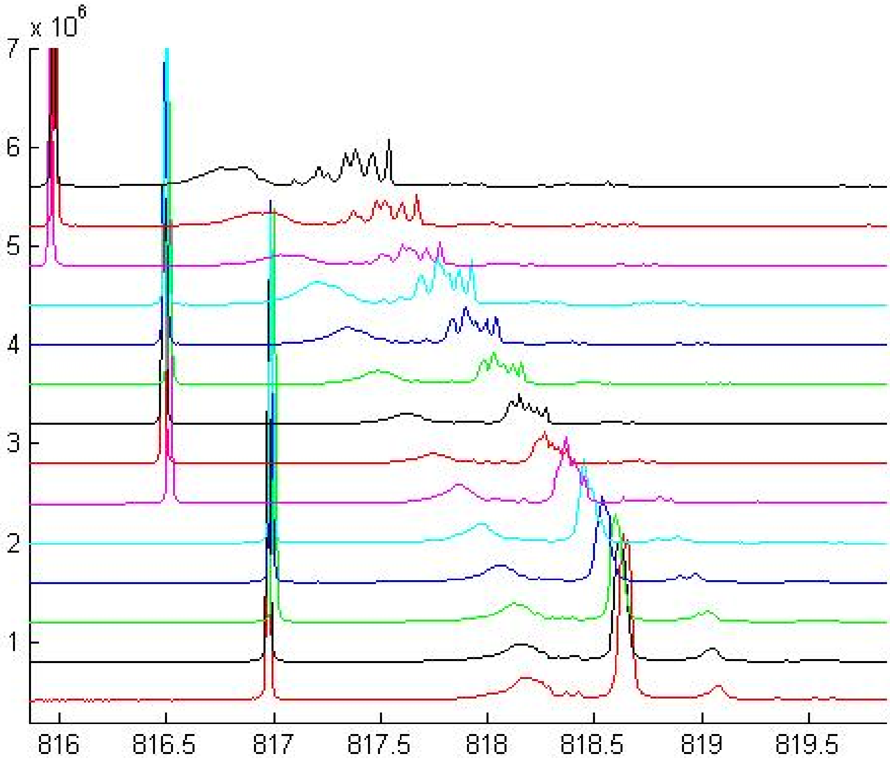

Figure 3.11: n-GaAs photoluminescence (PL) spectra vs. magnetic field. The horizontal axis is wavelength in nm. The vertical axis is intensity. Spectrometer resolution is 0.01 nm. For reference, the spectral range showing the positions of the excitation laser line is included in each spectrum.)

due to the spin 1/2 bound electron. This produces a rich and varied spectrum of bound exciton transitions originating from various spin states of various rotational levels to either ground state spin. (The Auger transition spectra are even more complicated.[35]) At magnetic fields near and above 5 T, sharp lines in the direct transition spectral region are resolved (Fig. 3.11).

In principle, any of these lines can be used to observed light scattering from a ground state neutral donor state. In practice, the laser can be tuned through these lines to optimize the elastic light scattering signal. The brightest resonance fluorescence transition is not necessarily the brightest line in the PL, because in the case of PL, off resonant excitation produces a thermal distribution in the bound exciton states which convolved with the oscillator strength to produce the emission spectrum.

As the laser is tuned into resonance with a particular D^0X transition, emission from two electron satellite (TES) transitions arising from that bound exciton initial state are enhanced.[35] Fig. 3.12 shows two graphs from series of spectra taken each magnetic in half Tesla steps from 1–6 T (the remaining graphs are given in Appendix C). D0X direct emission (PL) is recorded by a single 10 sec CCD exposure with excitation just above the band gap (see Fig. 3.12 caption). Resonant excitation spectra are recorded as a series of CCD exposures between which the external cavity diode laser emission wavelength is adjusted by a small amount with piezoelectric cavity tuning. The peak position and peak height are extracted from a Gaussian fit to the spectral maximum. The TES photoluminescence excitation (PLE) is recorded by integrating the emission in the entire TES region for each exposure and plotting the integrated emission at the location of the excitation laser peak. Each photon collected from the TES region reports that one donor had its state changed by interaction with the laser. For nondemolition detection of the donor bound state, an important figure of merit related to measurement fidelity is the ratio of the amount of light emitted from direct D^0X to D^01S transitions to the amount of light collected from state-altering Auger transitions. This figure can be estimated from the ratio of the RELS emission to TES emission in Fig. 3.12.

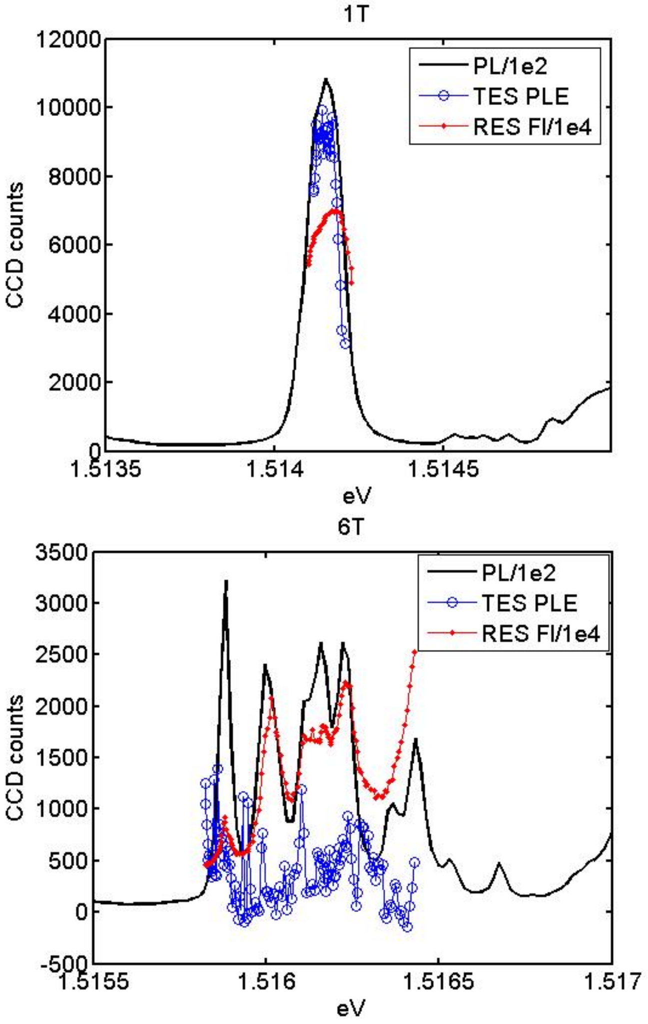

Figure 3.12: Excitation spectroscopy in the region of the donor bound exciton for 1 and 6 T. Graphs show 1 and 6 T neutral donor bound exciton (D^0X) emission due to above gap excitation at 1.517 and 1.519 eV, respectively recorded at 20μeV resolution by a grating spectrograph and liquid nitrogen cooled CCD. (See Appendix G for description of apparatus.) Elastic light scattering near bound exciton resonances (RELS) is plotted using procedure described in the text. Photoluminescence excitation (PLE) spectra are recorded at each excitation position for the two electron satellite (TES/Auger) region (Fig. 3.1) and shown scaled for comparison as noted in the figure inset.

At zero magnetic field, exciting at 1.5142 eV (above the two lowest direct D^0X transitions), the amount of light collected in the direct transition region

(1.5138-1.515 eV) is 133 times larger than light collected in the TES region (1.509-1.5117 eV). Exciting on resonance with the D^0X, L=0 transition at 1.5140 eV, the ratio increases to a maximum of 1250. Simultaneously the total signal–the integrated emission in the direct transition region–*also* increases by a factor of 60. This indicates resonant excitation provides both superior signal and measurement fidelity compared to PL and/or off resonant excitation.

Moving to magnetic fields as high as 6T, RELS emission decreases by one order of magnitude due to the spreading of oscillator strength from Zeeman splitting. However, TES emission is suppressed by almost two orders of magnitude. At 6T the fidelity is more than 10^4 throughout the D^0X direct transition region.

Chapter 4

Terahertz modulation of light scattering

4.1 Optically detected terahertz resonance

Researchers have frequently resorted to visible or near infrared light as a probe of terahertz-induced dynamics. The main reason is that optical detectors and sources abound, and are extremely sensitive. Cerne, Kono, Su and Sherwin observed changes in quantum well exciton photoluminescence (PL) due to terahertz excitation,[20] work which is discussed in greater detail on John Cerne's thesis.[51] An improvement in sensitivity of detection of terahertz-induced dynamics was demonstrated by Kioseoglou and coworkers who measured changes in reflection, rather than PL.[18] In that work, terahertz transitions were associated with neutral donor excitons (D^0X) and negative donor exciton complexes D^-X in quantum wells. The present work differs from previous observation schemes in that resonant excitation is used (unlike PL measurements which use above gap excitation), and scattered light is measured (rather than reflectivity), which affords an opportunity for lower background levels and probing of deeper structures without a buried reflector. All of these techniques allow more detection of *specific* terahertz-induced effects which would otherwise be difficult to identify from terahertz absorption alone. The cause of terahertz absorption in a sample is not always known, but optical signatures can be very specific to layers within a heterostructure or from impurity centers.

4.2 Continuous readout

With excitation at the transition $D^0$1S –D^0X (direct bound exciton transition), donors originating in the ground state rapidly cycle between the ground (1S) state and the short-lived excited (D^0X) state, scattering the light. Thus, donors measured to be in the ground state appear bright. Donors in excited bound states or ionized donors appear dark or transparent under continuous readout at the $D^0$1S–D^0X transition. This scattering is intense and dramatic enough to seen with a handheld IR viewer. A sample of GaAs with an epilayer containing an ensemble of resonantly excited donors thermally initialized to the ground state, appears similar to frosted glass, but becomes almost transparent when the laser is tuned below that energy.

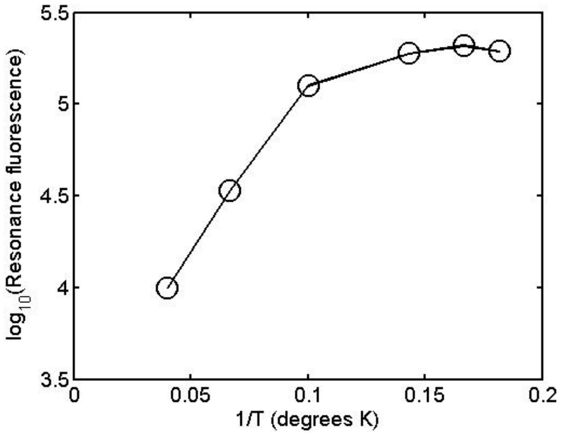

Figure 4.1: Arrhenius plot of temperature dependence of D^0X resonant elastic light scattering (resonance fluorescence). The ionization energy for bound excitons is 11 K, however the presence of free excitons and many intermediate rotational states complicates the temperature dependence, so that at least two slopes are seen.

4.3 Terahertz modulation of RELS

The assumption that the NIR light scattered from donors at the bound exciton resonance come from ground state donors may be tested by promoting donors out of the 1S state and observing the change in RELS intensity. When exciting donors out of the ground state, it is important to be sure that the excitation source does not create other changes in the sample which affect RELS efficiency, such as heating (Fig. 4.1). CW excitation of sufficiently low intensity will avoid heating effects.

For RELS measurements in the presence of terahertz excitation a sample of high purity n-GaAs with a 15 μm thick epilayer of high purity n-GaAs ($n_d - n_a = 3 \times 10^{14}/\text{cm}^3$) is mounted in a strain-free manner on the cold finger of a sample-in-vacuum flow cryostat. The sample is cooled to 5 K, and excited with NIR light of intensity 1 mW/cm^2 resonant with the lowest energy D^{0}X transition. The NIR light is incident at Brewster's angle. Scattered light in the direction of the surface normal is collected and sent to a spectrometer, which admits D^0 PL and RELS to a photomultiplier tube (PMT) detector with an integral high gain transimpedance amplifier, 0–20 kHz bandwidth.

Terhertz excitation is provided by a molecular gas laser, lasing on the methanol rotational transition at 1.6 THz, which is pumped at a vibrational transition by a CO$_2$ laser. The 1.6 THz radiation ionizes donors, moving electrons from the localized 1S state directly to the conduction band. The terahertz beam is focused onto the epilayer through the semi-insulating substrate. Terahertz intensity at the sample is estimated to be <20 mW/cm^2. The terahertz excitation is mechanically chopped at several hundred Hz and the change in RELS due to the terahertz excitation is measured by a lockin amplifier.

A decrease in RELS is observed when terhertz is present, however, the decrease in RELS is observed only when the NIR laser is in resonance with a D^{0}X transition (Fig. 4.2). This ensures the change in RELS is not due to non-donor-related effects. The percent change in RELS, or RELS modulation, is calculated as $100(A-B)/[(A+B)/2]$, where B and A are the respective RELS signals with and without THz excitation. The curve in Fig. 4.2 indicates the modulation is greatest when the NIR is resonant with a D^{0}X transition. The experimentally observed modulation depends on the relative sizes and overlap of the NIR and FIR laser spots, the NIR laser frequency and intensity, THz intensity and sample temperature. The maximum experimentally observed value of the modulation with excitation at 1.6 THz was 30%. Modulation of the RELS due to excitation at both 1.4 THz (5.78 meV, below the electron ionization energy) and 1.04 THz (4.31 meV, slightly detuned from the 1S–2P bound transition) is similar in magnitude.

Due to the weak binding energy of excitons to shallow donors, RELS efficiency is strongly sensitive to changes in sample temperature (1 meV $= k_B T$ at 11.6 K). RELS efficiency drops (approximately linearly) to 1/7 of the 5 K value by 15 K, and then more slowly to 0.1 of the 5 K value by 20 K. In order to be useful for qubit readout, the measured change in RELS would have to be due to a change in the population of donors in the ground state, and not merely a reduction in RELS intensity due to lattice heating.

Fig. 4.3 shows the dependence of the RELS modulation on incident THz intensity. The modulation saturates at 30%, a value much lower than is achievable by thermal effects ($B = 1/7$ or 90%). The fact that the change in RELS is constant to within 1% for modulation frequencies ≤ 400 Hz, implies the thermal time constant (τ) of the sample is $< 1/10$ kHz. The corresponding temperature rise (ΔT) in terms of the absorbed power (P_{abs}), mass (m) and specific heat (c_p) is approximately given by $\Delta T \leq P_{abs}\tau/(mc_p) = 0.2$ K. Also, the linear response at low THz intensities, where thermal effects are smallest, is consistent with absorption modulation due to changes in the ground state population. This is consistent with the conclusion that modulation is dominated by changes in the population of donors in their ground states, not heating.

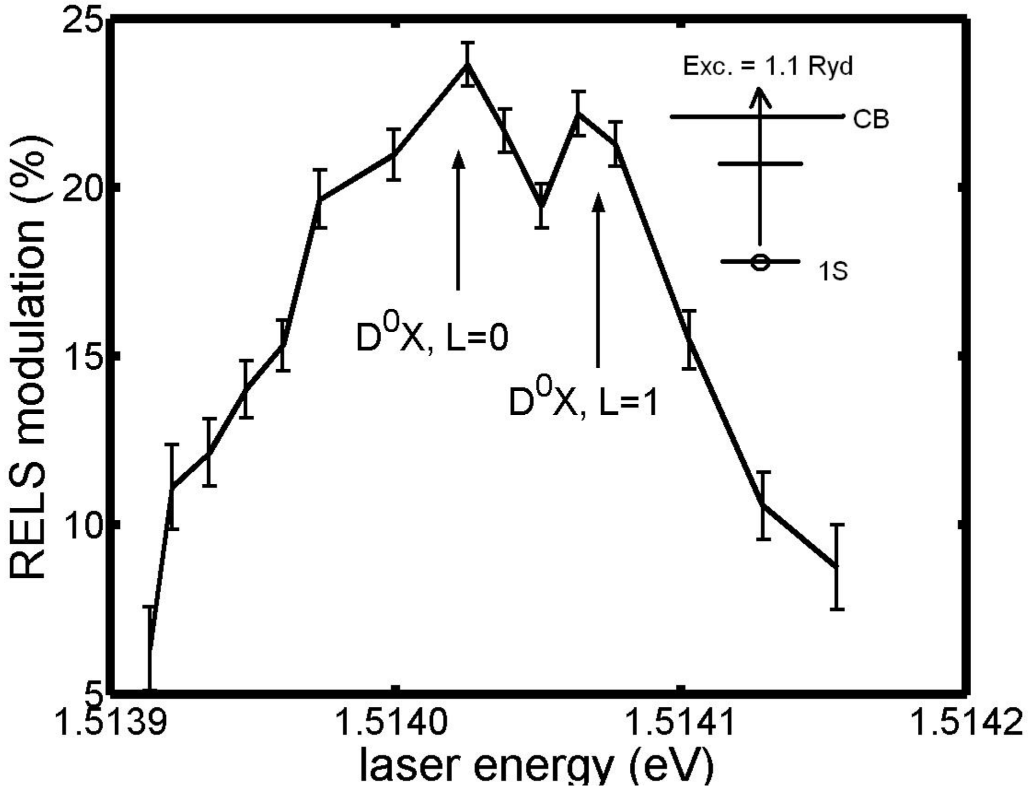

Figure 4.2: THz modulation of RELS. The plotted points are change in RELS normalized to RELS intensity. Enhanced modulation is seen when the NIR excitation is in resonance with a neutral donor bound exciton transition. This may be due to the presence of a static background of scattered light coming from other than donors, e.g. surface roughness or the copper sample mount. Strongest RELS modulation is observed at the positions of transitions to the two lowest neutral donor bound exciton (D^{0}X) rotational levels. Note that on resonance the exciton density is highest and the sample has a larger population of thermally ionized excitons and potentially terahertz absorbing free carriers. However, the magnitude of the modulation suggests a direct sensitivity to population, rather than a heating effect, which is expected to be minor at intensities used in this experiment as explained in Ref. [2].

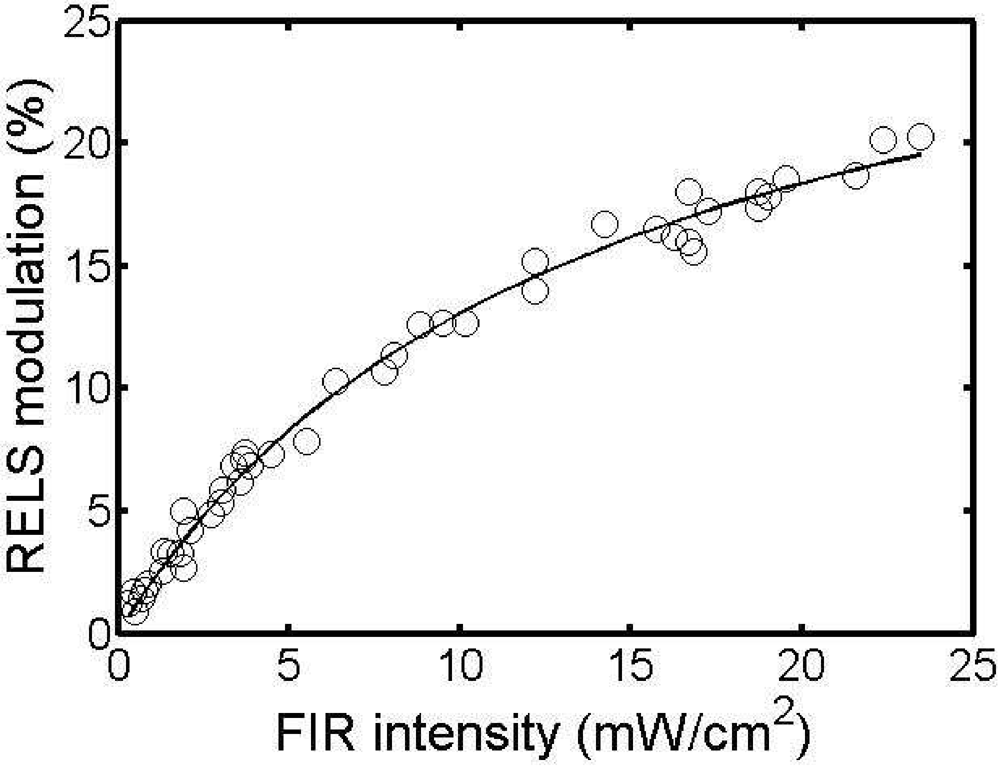

Figure 4.3: RELS modulation versus incident THz intensity. Open circles are data points. A fit to a two-level absorption saturation curve of the form $A[1 - (1 + I/I_0)^{-1}]$ is included as a guide to illustrate the asymptotic behavior (solid line). The fit parameters are $I_0 = 13.7$ and $A = 31$.

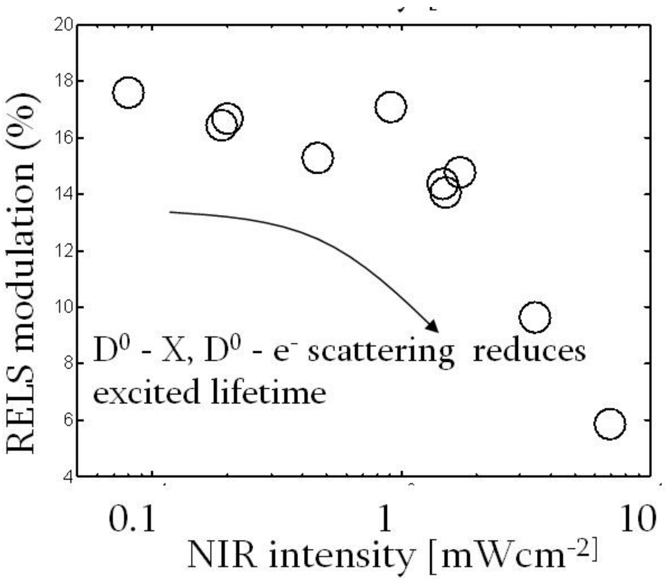

Figure 4.4: Dependence of the terahertz-induced modulation of D^0X resonant elastic light scattering (RELS) on NIR laser intensity showing a decreasing trend at higher intensity.

The dependence of the modulation depth on NIR intensity is revealing. The efficiency of D^0X RELS iteself does not begin to decrease until 10 $mWcm^{-2}$ (Fig. 3.6). Interestingly, the depth of terahertz modulation of RELS due to ionizing terahertz radiation has already dropped appreciably by $10mWcm^{-2}$ (Fig. 4.4). At high NIR intensities, donor excited state lifetimes are reduced by the presence of higher free carrier concentration, which means that a donor which is excited, will return more quickly to the emitting ground state. This is responsible for the reduction in the terahertz-induced RELS modulation amplitude. (This threshold for modulation efficiency roll-off is later seen to be somewhat higher when terahertz radiation is used to excite neutral donor bound states instead of ionizing neutral donors.)

Naively, measurement of donor ground state occupation via D^0X RELS may provide a solution for single donor readout, provided adjacent donors can be optically resolved, and Auger transitions can be reduced to a manageable level via, for instance, choice of magnetic field, crystal orientation and NIR polarization. With a D^0X lifetime of 1ns, a single donor may scatter up to 10^9 photons per second, if excited near saturation, and no Auger transitions to excited states occur. For a collection efficiency of 0.1, 10 photons could be collected in 100 ns (10 photons per 23 ns in a quantum well). In practice, the collected RELS is limited by the NIR excitation intensity. Higher NIR intensities result in decreased RELS modulation (-3dB at 4± 1 mW/cm^2 for 1.6 THz excitation). The reason for the decrease in RELS modulation with increasing NIR intensity is investigated via time resolved measurements in Ch. 5.

Significantly, D^0X RELS provides an alternative means of detection for studying properties of bound electron quantum states, in addition to absorption saturation spectroscopy and photoconductivity. The technique does not require a magnetic field, external electric bias, and does not require strong THz excitation. Further, it utilizes compact and commercially available semiconductor lasers and can be detected by silicon-based optoelectronics, which typically have their peak responsivity near 1.5 eV.

Chapter 5

Optical readout of the $2P^-$ lifetime

5.1 Resonant terahertz excitation of 1S–2P transition

The UCSB free electron lasers provide a source of high power tunable narrowband radiation in the sub-mm (300-3000 μm), terahertz (100-1000 μm), and FIR (30–300 μm) regions of the spectrum. (The three spectral regions are overlapping and generally ill-defined and fungible, but authors tend to use *terahertz* whenever possible in keeping with the current vogue.) The free electron laser (FEL) used in this thesis during my time here was able to provided multimode lasing (1 GHz linewidth, 20 MHz mode spacing) at $\leq$1 kW power, for $\leq$8 μs, at $\leq$1.5 Hz repetition rate. The FEL beam is delivered to the user laboratory in an evacuated pipe, emerging as a 4” diameter beam. The FEL power is monitored during each pulse by a fast pyroelectric detector.

The FEL pulse can be temporally shaped via photo-activated semiconductor window/mirror switches, which utilize an intense near infrared (NIR) or visible laser pulse to generate a dense, reflective electron-hole plasma in an otherwise transparent Si wafer. The plasma cut offs further terahertz transmission and reflects incident terahertz for times as long as several microseconds, due to the long carrier lifetime in Si. A single transmission switch can be used to truncate an FEL pulse. With a pair of these semiconductor switches, by taking the reflection from the first wafer and the transmission through the second wafer, one may obtain a sliced pulse of variable 5 ps–3 ns duration.[52].

For experiments involving optical pulses for slicing the FEL pulse, the FEL beam pulse is slaved to the timing of the amplified Ti:Saph femtosecond laser (Regen) or the Q-switched YAG via an advance trigger signal. In order to minimize timing jitter when averaging oscilloscope traces for sliced experiments, the scope is triggered by a fast photodiode which detects the optical laser pulse used for slicing.

To attenuate the FEL signal a cross polarizer can be used, however the contrast ratio of the wire grid polarizers is not excellent ($\sim 10^2$), so multiple sheets of 250 μm thick mylar are inserted in the beam near the sample to attenuate the beam as necessary. Two mylar beam splitters reduce the transmission at 34 cm^{-1} to approximately half, for an average optical density (OD) of 0.15 per sheet. Note, absorption in the mylar at 84 cm$^-$1 is four times as strong as it is at 34 cm^{-1}.

Frequencies in the range 32.6-36.5 cm^{-1} ($\sim$1 THz, 4 meV, 300 μm) are used to resonantly excite the 1S–2P bound-to-bound transition in GaAs neutral donors. The 1S–2P$^-$ transition energy tunes through this range with magnetic fields of 0–6 T (Fig. 5.1). This transition energy fortuitously corresponds to a window in the water vapor tranmission spectrum. There may be some third harmonic content in the FEL emission at this wavelength ($< 10^{-4}$). I have not measured this, although I did not see difference between data taken with and without a FIR long pass filter with 0.25 transmission at 1THz.

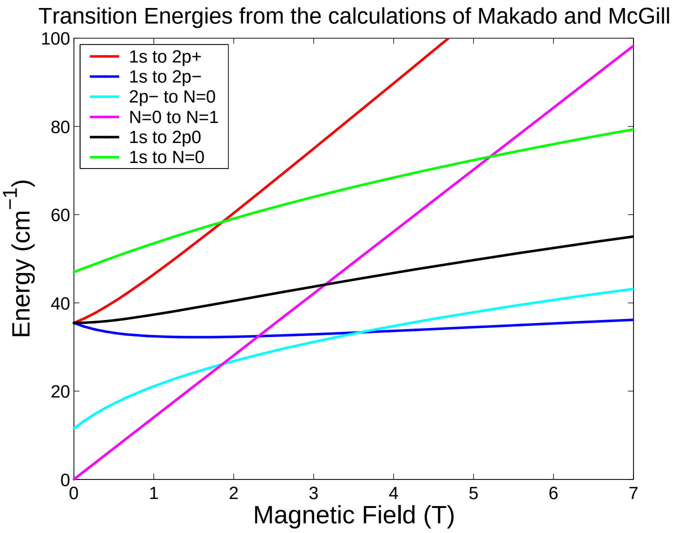

Figure 5.1: Energies of several terahertz transitions versus magnetic field, with hydrogenic levels taken from the calculations of Makado and McGill. Figure reproduced from Ref. [1]. The Landau levels comprising the conduction band are labelled by the index N.

5.2 RELS recovery after truncated terahertz pulses

In order to measure the neutral donor 2P$^-$ lifetime, I chose samples of n-GaAs samples with 15um thick epilayers, grown on semi-insulating or undoped GaAs substrates with dopant densities $3 \times 10^{13} - 5 \times 10^{14}\mathrm{cm}^{-3}$. Lower density samples in the $10^{12}\mathrm{cm}^{-3}$ have been grown by both MBE and liquid phase epitaxy, but tend to be either P-type or fluctuate locally between N- and P- type.

Samples (Table A.1 in Appendix A) were cooled to 5K in a flow cryostat for zero field experiments. THz excitation from the UCSB FEL was used to resonantly excite the three-fold degenerate 1S–2P transition. Photo-activation of an electron-hole plasma in a silicon wafer was used to truncate the THz pulse. The recovery of electrons to the ground state after the THz pulse was measured optically, by observing changes in the resonant elastic light scattering (RELS) from the D^0X transition (1.514 eV at 0 T) with continuous NIR illumination (<1 mWcm^{-2}). The RELS recovery is collimated and focused onto an avalanche photodiode detector (4 kHz–100MHz 3dB response). A narrowband 10 nm bandpass filter centered at 820 nm is used to filter the collected radiation and block stray light. During the terahertz pulse, RELS decreases as donors are excited to the 2P state by the terahertz radiation, depicted schematically in Fig. 5.2). When the pulse is truncated, donors decay to the ground state with a characteristic lifetime, causing a recovery of the RELS signal. The detected change in RELS intensity is amplified and recorded on an oscilloscope. Fig. 5.3(left) shows a typical scope trace showing

RELS response before, during and after resonant 1S–2P excitation.

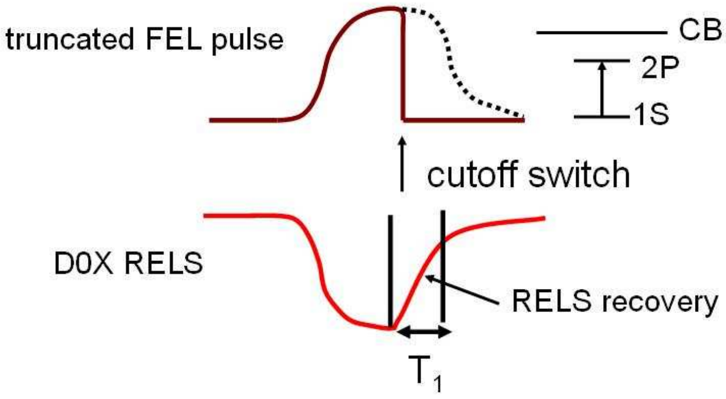

Figure 5.2: Schematic depicting a truncated terahertz pulse which resonantly excites the neutral donor bound transition 1S–2P^{-}. Upper curve is terahertz intensity. Lower curve is the observed resonant elastic light scattering (RELS). The recovery time constant T_1 is given by the time to return to $1 - 1/e$ of the original intensity.

An interesting affect can be seen by tuning the NIR laser into resonance with the ionized donor bound exciton transition ($D^0$1S–D^+X). Terahertz radiation causes a *rise* in emission, meaning the number of ionized donors increases (Fig. 5.3-right) during the FEL pulse. This is like a lead-less, zero-bias, photoconductivity measurement, indicating that some conduction band population is present when the terahertz is incident. This is expected at low magnetic fields, where a second terahertz photon has sufficient energy to ionize an excited donor (see Fig. 5.1). The recovery indicates the time scale for capture of free electrons by donors. The time scales on the two traces are remarkably similar, suggesting a strong correlation between the conduction band depopulation rate and the recovery of bound electrons to the ground state.

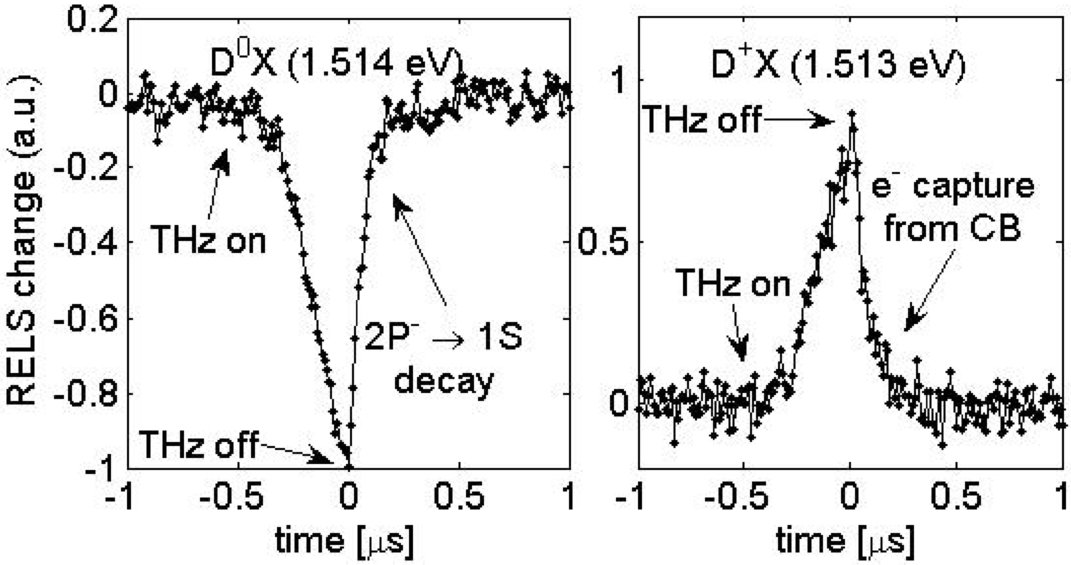

Figure 5.3: (Left)An oscilloscope trace showing RELS response to a THz pulse resonant with the $D^0$1S–2P transition and NIR excitation resonant with the lowest direct neutral donor bound exciton ($D^0$1S–D^0X,L-0) transition. An arrow indicates the point at which the terahertz pulse is truncated by an optical switch, with terahertz intensity going to zero in less than 5 ns.(Right) An oscilloscope trace showing RELS response to a THz pulse resonant with the D01S–2P transition, with NIR excitation resonant with the ionized donor bound exciton (D^+X). An arrow indicates the point at which the terahertz pulse is truncated by an optical switch, with terahertz intensity going to zero in less than 5 ns.

Surprisingly, after *resonant* terahertz excitation to the 2P state, a *non*exponential recovery is generally observed with a fast initial decay and slower decay at long times after a pulse.

The short lifetime component is on the order tens of nanoseconds, while the long lifetime component can be 100 ns or more.

By comparison, the terahertz pump-probe measurement presented in ref. [13] presents a single exponential lifetime of $250 \pm 50 ns$, measured in a magnetic field of B=5.1 T using 25 mWcm^{-2} terahertz intensity and 1 ns pulses. The intensity used was based on the 1S–2P$^-$ saturation intensity of 1 mWcm^{-2}.[53] Unfortunately, the pump-probe data does not include any data points at times less than 80 ns, so it neither confirms nor precludes the presence of a bi-exponential decay in a measurement sensitive to the difference in 1S and 2P$^-$ populations. However, the authors note the presence of a finite conduction band population detected via a photoconductive signal, even in the regime of a few percent excitation fraction.

Based on the length of pulse and intensities used in our FEL-based experiments we should also expect a population of conduction band electrons, which may be responsible for the nonexponential decay.

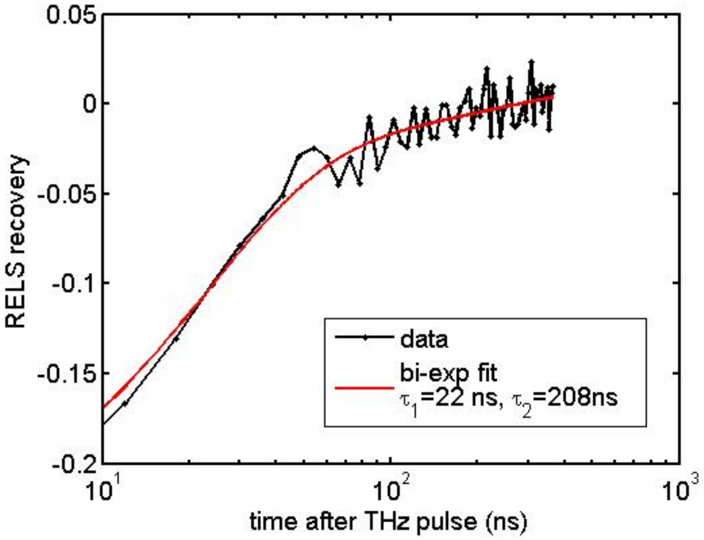

Figure 5.4: Log-log plot of a typical D^{0}X RELS recovery trace after a terahertz pulse with fit comprised of the sum of two exponential contributions. Distinct slopes are apparent at short and long times, respectively.

In the following section I discuss parameterization of this nonexponential relaxation in terms of models which include contributions from the exponentially relaxing 2P$^-$ population and the bimolecular recombination of excited, delocalized electrons by ionized donors.

5.2.1 Parameterization of RELS recovery

For the purpose of quantitative comparisons, a sum of two exponentials can be fit to the RELS recovery.

$$N_0 = 1 - A_1 e^{-t/\tau_1} + A_2 e^{-t/\tau_2} \tag{5.7}$$

The average time for recovery of RELS can be estimated from the fit parameters.

$$\tau_{avg} = (A_1\tau_1 + A_2\tau_2)/(A_1 + A_2) \tag{5.8}$$

This form of fit to the behavior is suitable if RELS probes two distinct types of emitters, such as donors in distinct highly and weakly doped regions. Based on the similarity of optical spectra between capped and uncapped samples I may assume the surface capping layer is ionized and does not contribute to the fast decay component. The near universality of this behavior in all samples under a variety of conditions and in different measured regions preclude the possibility that two different local areas within the laser spot are responsible for the two recovery times constants.

Alternative explanations for the nonexponential decay could be lasing or superradiance. The first requires population inversion, the second occurs on time scales less than T_2^* (100 ps). The presence of nonexponential decay after quasi CW excitation for 1 μs at small ≤ 0.1 excitation fractions precludes both.

Isolated donors

The observed nonexponential recovery is not expected for an ensemble of *isolated* neutral donors. In the case of an isolated donor, or ensemble of noninteracting donors, we have a two level system in which relaxation out of the excited state is due to a combination of radiative decay $\gamma_r = 10$ ms and a much faster nonradiative decay by phonon emission at a rate γ_{nr}.

$$\frac{dN_1}{dt} = -\frac{dN_2}{dt} \tag{5.9}$$

$$\frac{dN_2}{dt} = -\gamma_{nr}N_2 - \gamma_r N2 \tag{5.10}$$

The solution to Eq. 5.9 is a simple exponential

$$N_2(t) = N_2(0)e^{-t/T1_{eff}} \tag{5.11}$$

$$N_1(t) = 1 - N_2(t), \tag{5.12}$$

Since the scaled hydrogenic radiative lifetime is 10 ms, the effective relaxation time $T1_{eff}$ is approximately given by the acoustic phonon-limited lifetime, which is on the order of a few hundred nanoseconds.

$$T1_{eff} = (\gamma_{nr} + \gamma_r)^{-1} \approx 1/\gamma_{nr} \tag{5.13}$$

.

Strongly interacting donors

When electrons are excited to the 2P state, the Bohr radius increases by a factor of 4, meaning a 64 times larger effective volume. Near the Mott transition for an impurity band, when the ratio of Bohr radius to average donor spacing exceeds 0.25, excited electrons may become uncorrelated with donors via strong coulomb screening from neighbors, or electrons which were excited to a 2P state and subsequently ionized by absorption of a second terahertz photon, as explained in Fig. 5.9 caption. Whether orbital overlap with neighboring donors is large, or whether electrons are delocalized by excitation to the conduction band, in this "dissociated" regime, relaxation is expected to be proportional to both the number of excited electrons and number of ionized donors N_i.

$$\frac{dN_e}{dt} = \frac{-N_e N_i}{b} \tag{5.14}$$

$$\frac{dN_i}{dt} = \frac{-N_e N_i}{b} \tag{5.15}$$

Given the initial condition after a pulse $N_e(t=0) = N_0$, the solutions are

$$N_e(t) = \frac{b}{t + b/N_0} \tag{5.16}$$

$$N_i(t) = 1 - N_e(t). \tag{5.17}$$

RELS recovery in nearly every observed experiment can be fit to this type of $1/T$ power law recovery, where the equivalent nonlinear $1/e$ recovery time constant

T_{nl} is given by

$$T_{nl} = \frac{b(e-1)}{N_0}. \tag{5.18}$$

Note, the effective nonlinear lifetime T_{nl} increases with decreasing excitation fraction, whereas exponential yields a single $1/e$ decay time regardless of excitation fraction. An important feature of the bimolecular decay is that as the excitation population fraction goes down the observed recovery time is not bounded since the population of excited donors with which an excited electron may recombine uniformly vanishes.

$$T_{nl})(N_0 \to 0) = \infty \tag{5.19}$$

Donors affected only by free electrons

This $1/T$ power law type relaxation is expected as long as electrons are *not* correlated with donors, either due to orbital overlap with many ionized donors or ionization to the conduction band. Additionally, for electrons promoted to continuum states, there is the requirement that after capture by an ionized donor, relaxation to the ground state occur promptly, meaning less than or on the order of the time scale for electron capture.

Direct capture of free electrons to the 1S ground state is not expected to occur quickly, but rather the excited electron is expected to relax through the manifold of higher-lying closely spaced hydrogenic orbitals until it reaches a bottleneck state, where the jump to the next lower level requires the slow emission a high energy acoustic phonon. (Capture is most efficient to the S states with principle quantum number N=3 and N=4. Phonon emission is slow for the large jump to the 2S state and higher lying states have lower sticking coefficients.[54]) According to Burghoorn[55], the electron capture time is approximately 14ns at for large fractions of excited electrons, and surprisingly, in order to explain their data using a rate equation model, they must assume the net lifetime of the bound electron states is much less than the electron capture time. Burghoorn observes, “Apparently, the cascading time is negligible is the relaxation process.” This is in direct contrast to the measurements of Ref. [13] in which a pump probe measurement with resonant 1S–2P excitation at high magnetic fields (5.5T) reveals a bound state lifetime of at least 250 ns.

In the presence of a finite conduction band population, relaxation out of excited bound states may not be limited by phonon emission, but by inelastic scattering with free carriers, in which donor relaxation occurs via heating of free carriers (the magnetoimpurity effect). In this case the relaxation rate should be proportional to the the product of the respective excited donor and free carrier concentrations. As the number of free carriers wanes, the 2P relaxation rate is expected to decrease towards the phonon-limited rate. Similarly, the capture of free carriers proceeds more slowly due a paucity of available ionized donors. Both mechanisms point to a slowing of RELS recovery at lower excitation fractions at long times after a pulse.

A detail model based on a free-carrier dependent 2P lifetime for electron with rate equations is introduced and compared to other models in Ch. 6.

5.2.2 Fits to data

Regardless of the mechanism responsible for the observed nonexponential decay, the average RELS recovery rate can be obtained from fits of the bi-exponential form given in Eq. 5.7 or similarly, a power law (Eq. 5.16). Both forms give acceptable fits which are robust to variations in the initial fit parameters and against random noise added to the data of amplitude equal to the measured noise, using, e.g., the usual Monte Carlo ("bootstrap") fit procedure.

From fits such as in Fig. 5.7, I extract the average time for recovery of RELS emission, which is limited at short times by what I presume to be recovery from the conduction band and at long times by the long tail of the power law bimolecular recombination and also by the finite lifetime of the 2P$^-$.

In order to verify the role of free electrons as the mechanism behind the non-exponential fluorescence recovery, RELS recovery dynamics were investigated at under varied conditions. This average RELS recovery lifetime is observed to depend on several parameters including temperature, dopant density, NIR readout laser intensity and FIR intensity.

5.2.3 Temperature dependence

The temperature dependence of the average $1/e$ RELS recovery time is shown in figure 5.5. A strong decrease in lifetime is observed with increasing temperature. The mechanism for this decrease appears to have an activation temperature less than 10 K. This dramatic effect is not attributable to increased phonon-stimulated relaxation, since the background density of 1 THz acoustic phonons at temperatures these should be very low. Rather, it is likely due to donor relaxation via elastic scattering with a thermally-ionized conduction band population. Excitation out of the 2P state into higher lying, easily ionizable donor states has a much (at least 5 times) lower activation temperature than direct ionization from the 1S state (∼50 K). The thermally-activated conduction band population in

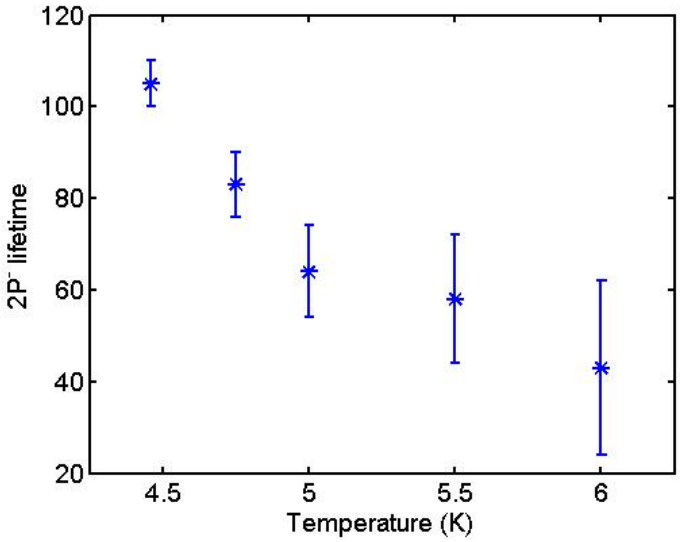

Figure 5.5: Average RELS recovery after resonant terahertz excitation of the 1S–2P transition vs. temperature. Dopant density is $n_d - n_a = 10^{14}\text{cm}^{-3}$ and NIR excitation intensity is <10 mWcm^{-2}.

the presence of a microsecond duration terahertz pulse should increase rapidly with temperature, providing a mechanism for donor relaxation through inelastic scattering. This inelastic scattering is observed in transport measurements by an increase in resistance due to heating of free carriers from inelastic scattering with excited donors, wherein an excited donor is demoted to the ground state (i.e. donor magnetoimpurity resonance, ref.[53]). This mechanism is efficient at zero magnetic field and in a magnetic field whenever the Landau level spacing corresponds to an excited donor transition and points to the free carrier population as an important cause contributing to a reduction of T_1.

5.2.4 Donor density dependence

The density dependence of the average RELS recovery time for neutral donors in GaAs is presented in Fig. 5.6. The decrease in lifetime with increasing dopant density may be due a number of effects. A simple explanation is that a larger density of excited donors contributes to a larger conduction band population. However this trend appears to hold even at very low excitation fractions, pointing to interactions with neighbors as a potential mechanism for enhance relaxation. I know of no theory which explains this effect satisfactorily. Kalkman and coworkers also expressed dismay that this phenomenon is apparently inexplicable in terms of isolated donors.[13] The effect may be attributable to a many-body phenomena, namely coulomb interactions facilitated by a noneligible overlap of neighboring

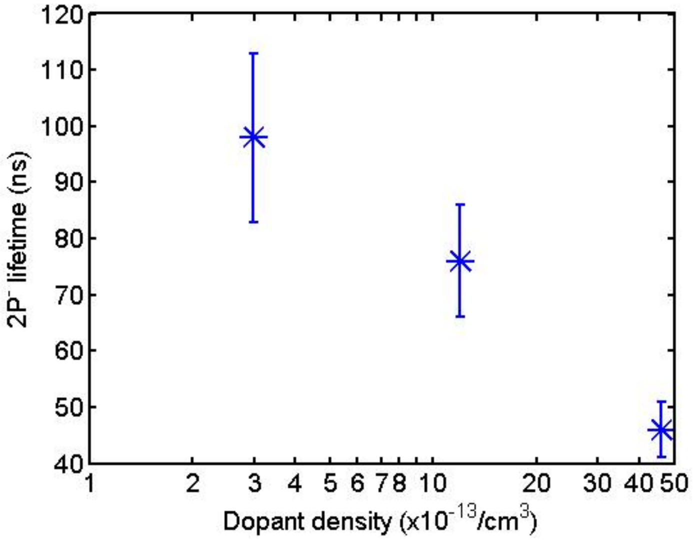

Figure 5.6: Average RELS recovery time for neutral donors in GaAs measured by RELS recovery after a truncated terahertz pulse which resonantly excites the 1S–2P transition. Sample temperature is 5 K. NIR excitation intensity is <10 mWcm^{-2}.

donor wavefunctions when one or both is promoted to a more spatially extended excited state. This is discussed further in Ch. 6.

5.2.5 Readout laser intensity

The dependence of the average lifetime on near infrared readout laser intensity is presented in Fig. 5.7. A reduction in the lifetime is seen a higher excitation intensities. This effect corroborates the reduced the RELS modulation amplitude seen at higher readout laser intensities in the molecular gas laser experiments and is attributed to creation of free excitons due to absorption in the tail of the band-edge exciton absorption feature. These free hydrogen atoms may cause relaxation by inelastic scattering with excited donors. Donor bound excitons are also very large and may have a large cross section for interactions with other bound or free carriers. Bound excitons are also known to mediate longer range interactions in solids.[56, 57] Additionally, free carriers can be generated when free excitons are heated and broken up by terahertz radiation.

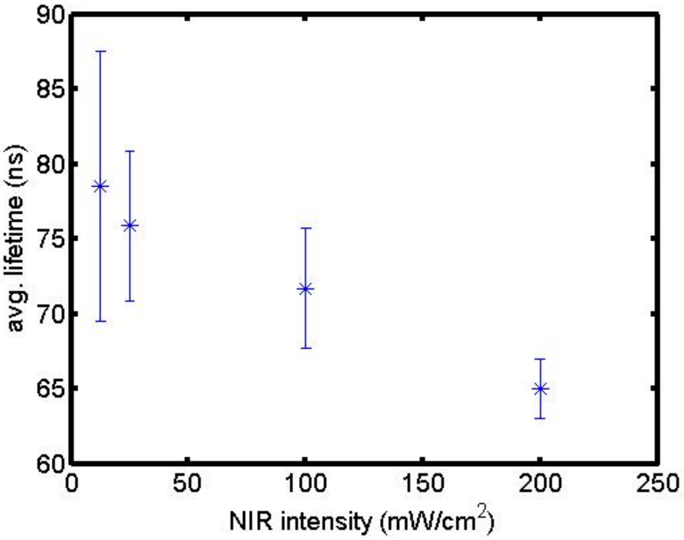

Figure 5.7: Dependence of the average RELS recovery time on NIR readout laser intensity. RELS intensity and the corresponding fit certainty decrease with incident intensity. Dopant density is 10^{14}cm^{-3}; temperature is 5 K.

The aggregate data are consistent with the assertion that the presence of free carriers speeds the relaxation from the 2P$^-$ state leading a more rapid recovery of electrons to the bright ground state and faster recovery of D^{0}X RELS. Regardless of the source of the carriers, be it increasing temperature, dopant density, or free exciton concentration, the result is faster relaxation of donors to the ground state. The presence of hot carriers are also expected to reduce RELS efficiency through inelastic collisions with donor bound excitons.

5.2.6 Terahertz intensity

Heating is seen to prevent RELS recovery after microsecond duration pulses at high intensity (Fig. 5.8). Cooling proceeds on the timescale of 1–2 μs. As terahertz intensity is lowered, the recovery rate increases to a maximum (inelastic scattering limited) and then decreases with terahertz intensity, as expected since fewer free carriers are ionized at low excitation fractions. Care is taken to operate in at terahertz intensities well below the level required to observe heating effects.

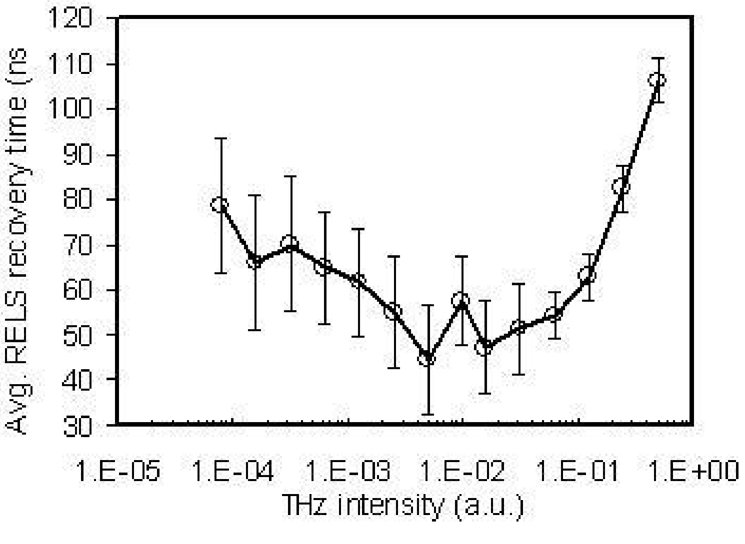

Figure 5.8: Average recovery time of RELS after truncated 1μs (Gaussian 1/e^2 half width), 1.03 THz, maximum 10 μJ incident pulse. Conditions are T=2 K, B=3.5 T, $n_d - n_a = 10^{14}$ cm^{-}3, focal spot $\sim$ 3mm diameter (estimated 180 V/cm peak electric field in sample, including surface losses). Recovery of RELS is limited at high intensities is by thermal heating which reduces resonance fluorescence efficiency. Increase in lifetime at lower intensities is attributed to a smaller conduction band population and reduced free carrier scattering.

.

5.3 Reducing carrier generation and inelastic scattering

In all samples a bi-exponential or power law decay is observed with a short lifetime component in the tens-of-ns time scale and a long lifetime component of order 100 ns. The reason for the fast initial recovery of fluorescence is not immediately apparent, although several theories are plausible, the most likely being the free carriers present at short times after the pulse.

In order to measure an unperturbed $2P^-$ lifetime it is desirable to reduce as much as possible the creation of free carriers. I use a combination of three tactics to attempt to eliminate scattering from free carriers.

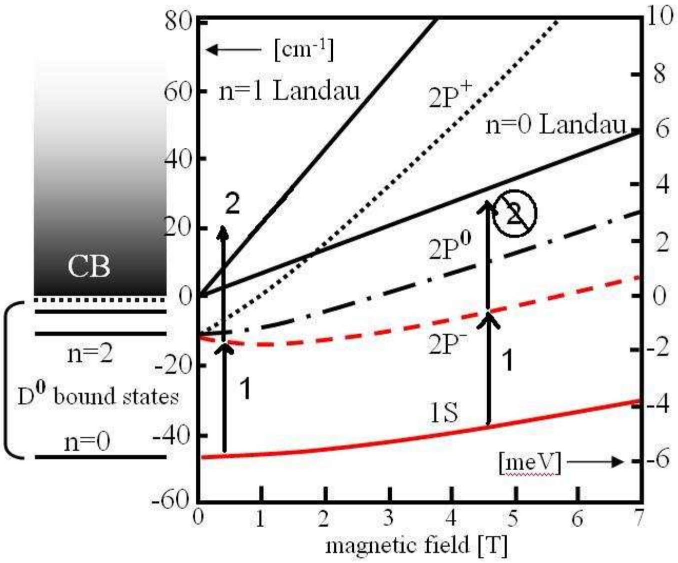

Figure 5.9: Prohibiting second photon ionization by going to higher magnetic fields. At low fields a second photon may cause and ionizing transition from an excited neutral donor to the CB/Landau levels. At fields exceeding B=3.5 T for Si (4.5 T for Ge), a terahertz photon resonant with the 1S–$2P^-$ transition has insufficient energy to ionize an excited donor.

1. I operate at *nonzero magnetic fields* (3.5–6.5 T). Inelastic scattering from free carriers is efficient at zero magnetic field and whenever the Landau level spacing is equal to a donor bound state transition. Thus, inelastic scattering from cold carriers can be suppressed somewhat by going to magnetic fields higher than 2.5T (the 1 THz cyclotron resonance). By going to higher magnetic fields I may also reduce the total concentration of of free carriers generated during a terahertz pulse. There are several mechanisms for free carrier generation during a strong terahertz pulse. The most obvious source of free carriers are the neutral donors which can become ionized during a terahertz pulse by absorption of a second photon in the excited state. At fields as high as 5.5T, however, this second photon ionization mechanism should be effectively suppressed for both donor species (Fig. 5.9 and Fig. 5.1).

The reduction in expected free carrier density at higher magnetic fields coupled with the extra confinement in the plane of the magnetic field give reason to expect longer bound state lifetimes. However, the additional confinement provided by the magnetic field also enhances coupling to acoustic phonons via the deformation potential. The smaller wavefunction results in a better form factor for emission of phonons with short wavelengths. Rikken, et al.[58] performed calculations for various phonon transitions for shallow donor states in InP in a magnetic field from an analytical solution based an approximate wavefunction which show enhanced phonon relaxation at higher magnetic fields. They obtain enhancements on the order of a factor 4 for bound-to-unbound transitions with magnetic fields in the range of 5 T.

In Ref. [58], phonon emission rates for transitions include a term of the form

$$q_0^n e^{-2a^2 q_0^2}, \tag{5.20}$$

Where $q_0 = \Delta E/\hbar\nu$ is the phonon wavevector in terms of the energy separation of the initial and final electron states and the speed of sound. a is given by

$$a^2 = \frac{a_\lambda^2}{(1 + a_\lambda^2/l^2)^2}, \tag{5.21}$$

where in terms of a_λ, the lengths scale for the cylindrical Landau-like electron orbit and $l_b = sqrt\hbar/eB$, the magnetic length. As l shrinks, a shrinks, and the phonon emission rate (Eq. 5.20) grows exponentially, dominating other factors. Thus, higher magnetic fields are bitter medicine, since they undo one of the advantages of the donor system which is the large Bohr radius and correspondingly weak coupling to acoustic phonons via the lattice-scale deformation potential.

2. The combination of the readout laser and incident terahertz act as an additional source of free charge, as evidenced by the more rapid RELS recovery

at higher NIR intensities (Fig. 5.7. The weakly bound excitons generated by the NIR laser can also be thermally ionized, transitioning through a dense manifold of rotational states to the continuum, then heated and broken apart by terahertz radiation. The other source of free excitons is due to the band edge free exciton absorption feature, which has a tail which extends to lower energies, overlapping with the D^0X transitions. Whenever the readout laser in on, creation of a population of free excitons, in addition to bound excitons, is unavoidable. Promotion of electrons to easily ionized, long-lived excited bound states (e.g. 2S) is also possible via Auger (two electron satellite) transitions from the bound exciton state. Electrons thus pre-shelved in excited donor states can be ionized and heated by incident terahertz. Shelving would cause a decrease in RELS emission after NIR excitation is switched on. In order to estimate the effect of shelving on RELS readout as well I implemented *fast optical switch* to turn the readout last on quickly and monitor for a reduction in the RELS intensity due to shelving. Also, the optical switch allows me to turn on the readout laser after the terahertz pulse in order to check the effect of continuous readout on the temporal dynamics of donor relaxation.

3. *Short terahertz pulses* (∼ 3 ns) are used to excite the ensemble in order to limit second photon ionization and associated heating. When excitation pulses are much shorter than the lifetime, and transitions to the continuum

are weaker than bound-to-bound state transitions transfer of a significant population to the conduction band is not expected.

The combination of these three methods is expected to largely reduce the short lifetime/power law recovery dynamics associated with free carriers.

In a magnetic field, the response of RELS to terahertz excitation can be recorded at various excitation energies, corresponding to different donor bound exciton transitions as shown in Fig. 5.10.

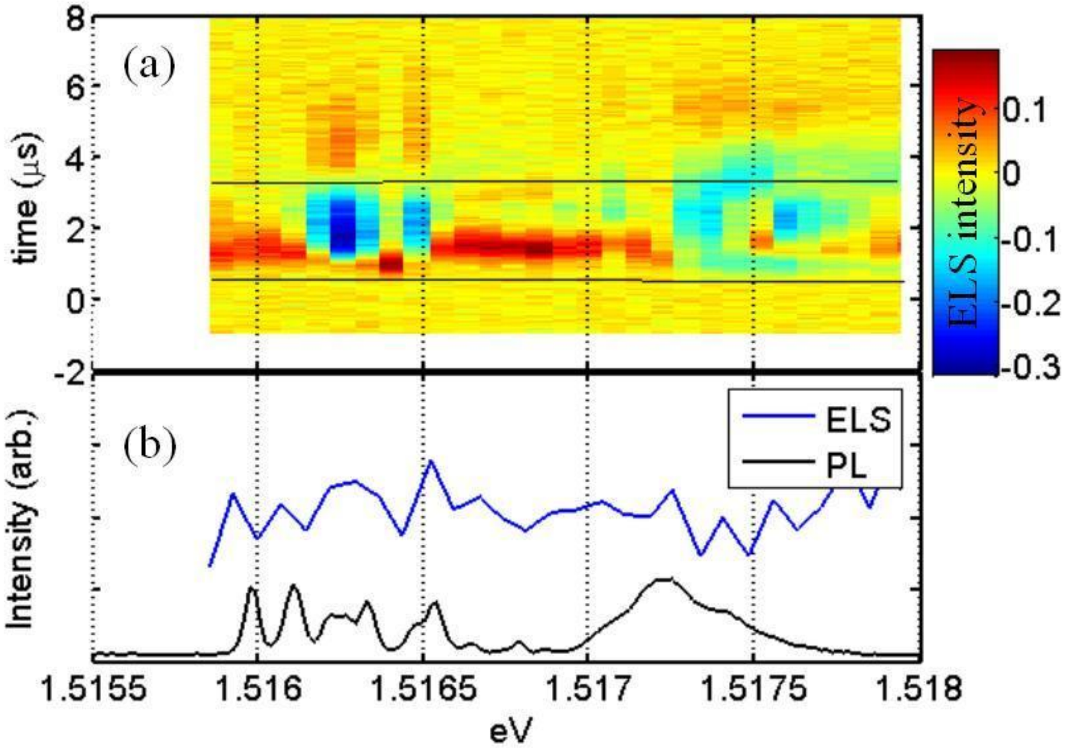

Figure 5.10: Spectrally resolved change in elastic light scattering (ELS) during a terahertz pulse resonantly exciting the 1S–2P$^-$ transition in a 6 T magnetic field. (a) 2D false color plot of ELS versus time, spanning the duration of a 1 μs FWHM terahertz pulse with an approximately Gaussian temporal profile. Emission at time t=0 is offset by the DC emission level since the detector is AC coupled, so that changes in emission are relative. (b) PL and RELS spectra aligned to the spectrum in (a), shown for reference.

Terahertz induced reduction of ELS is observed at points in the spectrum when elastic light scattering is resonant with Zeeman split direct bound exciton transitions (that is when ELS becomes RELS). Fewer data points are shown for the temporally resolved spectral scan and associated RELS spectrum compared to the PL spectrum, so high resolution is not achieved. A higher resolution scan shows terahertz modulation at three spectrally resolved D^{0}X lines. Reduction in ELS signal is also seen at the free exciton resonance near 1.5175 eV. Both regions show a small increase in ELS signal after the terahertz pulse, which remains for up to a microsecond. This is due to a surface charging effect explained in Fig. 3.7, and indicates that ionized carriers were generated during the FEL pulse. This may be due to second photon ionization of excited donors or similarly ionization of donors shelved into excited neutral donor states by the readout laser, Auger ionized donors (one donor decays to 1S, while the other donor is excited), or donors ionized by inelastic collisions with hot carriers. This "overshoot" is a marginal effect in dopant densities higher than 10^{14}cm^{-3}, but can be a significant perturbation in samples with very low dopant density and correspondingly long depletion regions or else insufficient doping in the surface capping layer, such as sample A421 (Table A.1 in Appendix A).

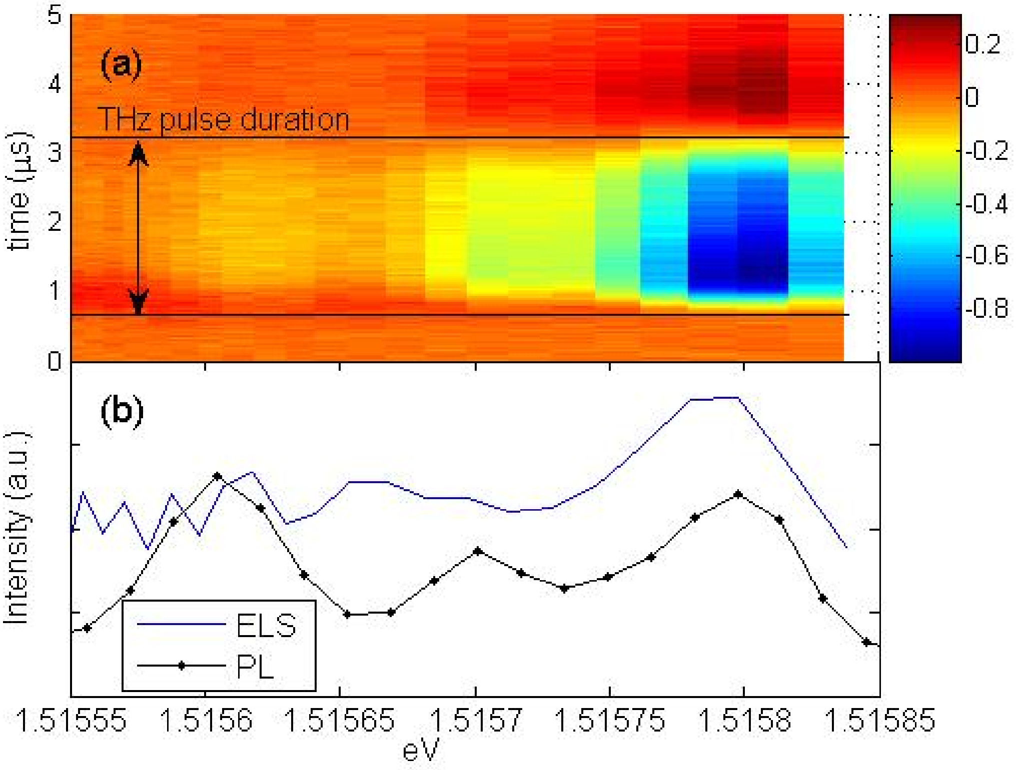

Figure 5.11: Same as Fig. 5.10, but taken with higher resolution steps in excitation energy.

5.3.1 Optical switch

Since an increase in the readout laser intensity results in a decrease in lifetime, lifetime measurements must be performed at very low NIR laser intensities, resulting in low signal to noise ratio (SNR). An alternative to implement an optical switch to so that the laser can be switched on at any point after the terahertz pulse during the recovery.

For pulsed readout measurements I implemented a fast optical switch using a Pockels cell between cross polarizers in a 2-pass geometry. The layout and alignment of the optical switch are described in Appendix F. The optical switch 10–90% rise time is measured to be 7.5 ns by a fast photodiode. The full NIR laser intensity is used in conjunction with pulsed readout so that instantaneous RELS is recorded with high confidence. The immediate presence of the full intensity of the NIR laser causes a more rapid decay of the excited neutral donor population. However the instantaneous RELS response can be recorded at various delays after the terahertz pulse. The locus of points marking the instantaneous RELS response maps out the envelope of the recovery in the absence of a NIR laser (Fig. 5.12-upper). If the lifetime measured with switched readout technique is the same as the lifetime measured with continuous readout, then confidence is high that the CW readout laser intensity is sufficiently low to not limit the 2P^{-} lifetime (Fig. 5.12-lower).

Linearity of the RELS modulation amplitude with respect to the NIR readout laser intensity indicates the laser intensity in is a regime where shelving is not modifying the ground state population. Data from a sample of dopant density 7.6×10^{13}cm^{-3} is linear to within the variation in optical density of the attenuating filters (Fig. 5.13).

For a two level system driven strongly, saturation at 50% population in the ground and excited state is expected. However, in donor ensembles driven to saturation by resonant terahertz excitation, quenching of the RELS greater than 50% is observed at zero magnetic field (Fig. 5.14-left). This is attributable to accumulation of electrons in the conduction band (i.e. not a two-level system) and heating. Complete or nearly complete quenching at zero magnetic field is observable in this sample because the background of scattered light is very low, otherwise the unquench background of scattered light remains as an offset. In this sample the substrate is undoped and is not as transparent near the D^{0}X resonance as the semi-insulating substrates which greatly reduces laser scatter coming from the copper surface behind the sample. At nonzero magnetic fields, all samples show incomplete quenching (Fig. 5.14-right). At high magnetic fields both an increase in substrate transparency and a reduction in total optical signal amplitude relative to the constant background scatter are generally observed so it is not known whether the RELS is indeed reduced to zero at higher fields.

The data in Fig. 5.14-left suggest either all the donors are excited or ionized or the relationship between RELS and donor population is nonlinear, meaning the efficiency of RELS is reduced at high excitation fractions. This is the case when heating occurs. The possibility of a nonlinear relationship between RELS and donor excitation fraction even in the absence of heating is discussed in Ch. 6. Potentially important is the fact that this sample has a predominance of a single donor species, Si, as shown by Stanley et al. in reference. If donors are present such as Si and Ge with 1S–2P transitions differing by 20 GHz or more, resonant excitation at one transition may not saturate the other, although with the FEL it is generally possible to saturate transitions with the excitation frequency more than 1 cm^{-}1 (30 GHz) off resonance.[45].

5.3.2 Nonresonant vs. resonant terahertz excitation

It is useful to compare measurements of RELS relaxation after pulsed terahertz excitation under two conditions:

1. Exciting off resonance at 2.5 THz. (In this case free carriers are created directly.)
2. Exciting on resonance with the 1S–2P$^-$ transition near 1 THz. (In this case excited donors are created directly, and free carriers are incidental.)

For these experiments the sample is B763 (Appendix A) with a dopant density $n_d - n_a = 1 \times 10^{14}\text{cm}^{-3}$. A sample from the same wafer is processed with leads for photoconductive measurements.

In the case of resonant excitation, the energy of the 1S–2P$^-$ transition is verified by scans in both terahertz frequency and magnetic field (Fig. 5.15). Significantly, both spectroscopies reveal two resonances attributed to Ge and Si donors, which provides additional evidence that RELS modulation is due to donor state changes and not effects which modify only fluorescence efficiency.

Nonresonant terahertz excitation

RELS recovery after pulsed 2.5 THz radiation is measured (Fig. 5.16) at zero magnetic field and at two excitation intensities. Fits to a single exponential and a power law (relaxation $\propto 1/t$) were both satisfactory. Fit parameters and uncertainty are determined by a Monte Carlo least squares (χ^2) technique, which is very robust and can be used even in situations where many interdependent fit parameters are used and assumptions on which to base initial fit parameters may not be justifiable, such as in fits to astronomical measurements of orbits. The only thing that must be known is the measurement uncertainty at each point and a range of physically allowable initial guesses for each fit parameter. In this "bootstrap" method random initial guesses are used to avoid potential local minima. Fits are made to data onto which has been added random Gaussian (white) noise equal in amplitude to the measured electrical noise prior to the FEL pulse from the same oscilloscope trace. The quoted fit parameters are calculated as the mean value for fit parameters obtained from 100 Monte Carlo fits and the uncertainty quoted as the standard deviation in the obtain series of fit parameters. 95% confidence intervals are shown corresponding to $\pm 2\sqrt{(R^2/(N-P))}$, where R is the sum of squares of residuals, N is the number of points, and $P = 4$ is the number of free parameters in the fits.

An important question is how the recovery dynamics depend on excitation fraction. Fig. 5.17 shows the extracted nonlinear recovery time b from fits to a series of RELS recovery curves taken at different terahertz intensities over more than two orders of magnitude.

If the recovery dynamics are independent of excitation fraction, recovery curves from lower excitations should fall onto the curve observed at higher excitation fractions. Curves with different initial amplitudes would be the same as curves taken at a different times during an exponential decay. In the case of exponential decay, curves at different times are self similar via a simple vertical scaling. In the case of a power law, traces with different initial amplitudes y_0 exhibit different effective $1/e$ lifetimes $T_{nl} = b(e-1)/y0$, but should show identical decay constants b. If behavior is limited by a single lifetime, a constant lifetime should be seen in recovery from various excitation fractions. If bimolecular only, a constant decay time constant b should be observed.

In the power dependence data presented in Fig. 5.17(left) the nonlinear decay time constant is seen to increase logarithmically with higher terahertz intensities but roughly linearly with the change in RELS (excitation fraction) (Fig. 5.17(right)). The approximately logarithmic dependence of change in RELS with respect to terahertz intensity is attributable to saturation of absorption.

The decrease in b at lower intensities is attributed to a limiting lifetime which emerges at lower excitation fractions.

In the case of both exponential and power law relaxation mechanisms I expect a reduced lifetime based on the parallel addition of the two relaxation times.

$$T_{eff} = \left(\frac{1}{T_1} + \frac{1}{T_{nl}}\right)^{-1} \tag{5.22}$$

Naively, I could choose a value for T_{nl} intermediate between the low (14 ns) and high excitation (50 ns) limits and fit only T_1. However, I must operate under the assumption that the 2P^{-} lifetime becomes very short whenever there is a significant CB population in order to explain presence of the the short lifetime in the first place. Since RELS measures the ground state and not the conduction band, it is incorrect to fix a single lifetime for carrier capture in a fit to nonlinear relaxation for a system in which the 2P$^-$ and other bound state lifetimes are evidently dependent free carrier concentration. The most meaningful measure of T_1 comes from the estimated recovery time in the low excitation limit.

To this end, RELS recovery was measured at B=4.5 T (Fig. 5.18) and found to be approximately 150 ns. This is the longest recovery time observed with nonresonant, 2.5 THz (85 cm$^-$1), excitation of donors directly to the conduction band.

Resonant terahertz excitation

Under resonant 1S–2P$^-$ excitation conditions (Fig. 5.15 considerably lower terahertz power can used to saturate the ensemble of neutral donors. The prepulse from an unattenuated 400 W terahertz pulse coming off two reflection switches oriented near Brewster's angle and transmitting through the Si transmission switch is sufficient to saturated the change in D^{0}X RELS emission even before the switches are illuminated. Contrast ratio is this experiment is only 10^2.

Fig. 5.18 shows RELS recovery after a 3 ns terahertz pulse. Some prepulse is visible before the reflection switches are activated by a uncompressed pulse from a regeneratively amplified Ti:Saph laser. The trace is well-fit by a power law recovery with a typical effective $1/e$ time constant $T_{nl} \sim 50$ ns.

At B=4 T, the recovery time constant is seen to be limited by both NIR and FIR intensity. Fig. 5.20 shows two traces taken in the respective limits of simultaneously high intensity NIR readout/terahertz excitation and low intensity NIR readout/THz excitation.

With NIR excitation ($\leq$10 mWcm^{-2}) and low excitation fractions (< 0.1 of saturation) recovery times as long as 200 ns are observed, which exceed those measured with nonresonant excitation (Fig. 5.18). This is presumably due to a majority of electrons being excited to a 2P state resulting in a smaller concentration of free electrons.

In sample B48, in which the primary donor is Si and no significant quantity of Ge donors is reported, even longer recovery times are observed (Fig. 5.21) in excess of 500 ns. Since Ge donors lie closer to the conduction band, second photon excitation to the continuum is allowed in samples containing Ge up to higher magnetic fields than in samples containing only lower lying donors Si and Ge. The presence of this less-suppressible second photon excitation of free carriers may be the reason the long lifetimes are not observed in other samples. It may also be due to the presence of some unsuppressed third harmonic content in the free electron laser spectrum, since the samples measured with a terahertz cutoff filter may have also had Ge donors. The presence of nearly ionized donors in the depletion region may also add to the free carrier concentration.

The lifetime in this series of measurements is observed to depend strongly on NIR intensity, so it is not attributable to leak through of terahertz from the pulse slicer creating apparent slow recovery tail after the truncation of the terahertz pulse.

It has been shown that optical readout, in conjunction with the previous established methods for study of neutral donor dynamics: photoconductivity and terahertz pump-probe can distinguish internal neutral donor dynamics from the dynamics associated with excitation and capture from the continuum.

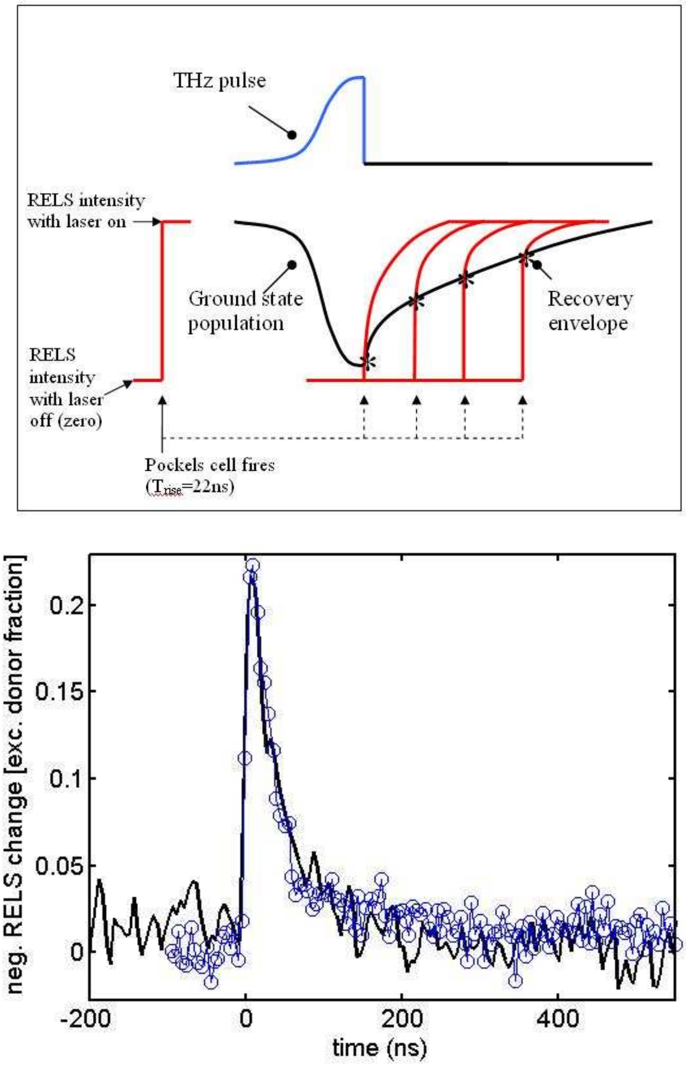

Figure 5.12: (Upper) Optical switch timing diagram. The blue trace shows the terahertz intensity from a truncated FEL pulse. The black curve plots the change in donor ground state population during a resonant excitation of the 1S–2P$^-$ transition, followed recovery in the absence of NIR illumination. The red lines depict observed RELS before and after the optical switch fires for five different delays. Asterisks mark points at which the instantaneous RELS values are recorded in order to record the envelope of RELS recovery in the absence of NIR. illumination. (Lower) Comparison of continuous (line) and pulsed NIR readout (circles) following a 3.5 ns, 1.03 THz pulse. Experimental conditions are T=2 K, B=4 T, $n_1 - n_a = 10^{14}\text{cm}^{-3}$ and estimated excitation fraction 0.21. Identical short lifetime components are observed, with comparable long lifetime behavior. Negative offset or "overshoot" of continuous readout trace (solid line) at long times is understood to be a decrease of the surface depletion length due to heating and charge separation of NIR-excited free excitons during an intense FEL pulse. Surface charging decays with a time constant of 1–3 microseconds.

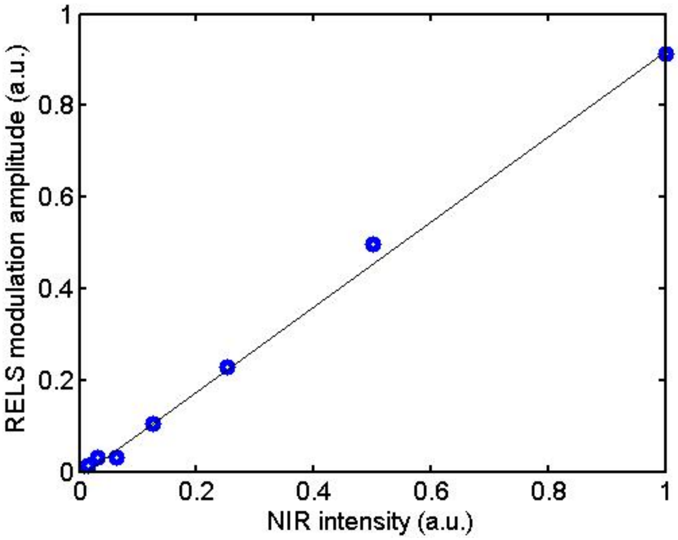

Figure 5.13: RELS reduction from a terahertz pulse resonant with the 1S–2P$^-$ transition at 4.25 T versus NIR readout laser intensity. Peak NIR intensity is estimated to be 100mWcm^{-2}: the actual spot size on the sample cannot be directly measured in situ because of the lens mounted within the bore of the magnet, but is estimated to be approximately 1x2 mm. A line is included as a guide to the eye.

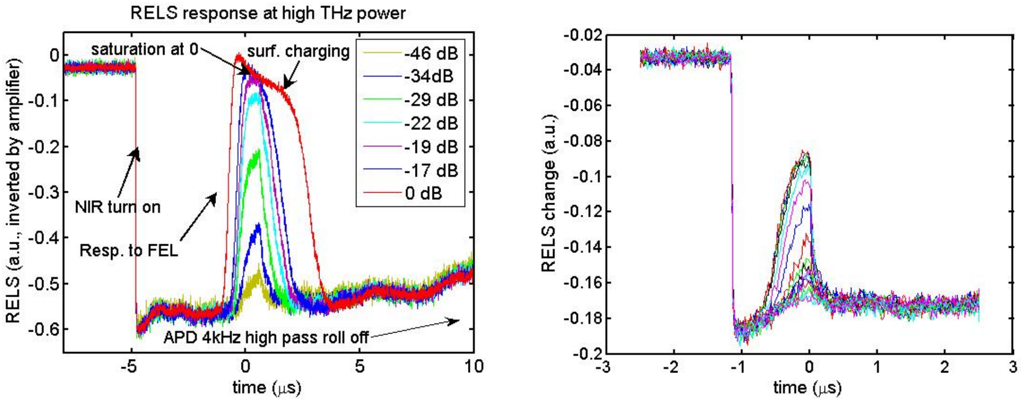

Figure 5.14: (Left) Complete quenching of D^0X RELS in response to strong terahertz excitation. Traces are AC inverted (up is less light). Sample is B48, $7.6 \times 10^{13}\text{cm}^{-3}$; sample conditions are T=2 K, B=0 T. Full ionization or quenching of RELS due to heating are possible explanations. Increase in the saturated fluorescence baseline is observed as a nonzero slope during the most intense terahertz pulse and is attributed to a surface charging effect. Apparently there is some amount of light leaking through the optical switched, evidenced by the negative pulse. The change of the RELS to a value lower than the steady state value is due to leak-through from the optical switch which was unfortunately not measured during the experiment, but is probably less than 10%. (Right) Similar traces for identical sample at B=4.9 T

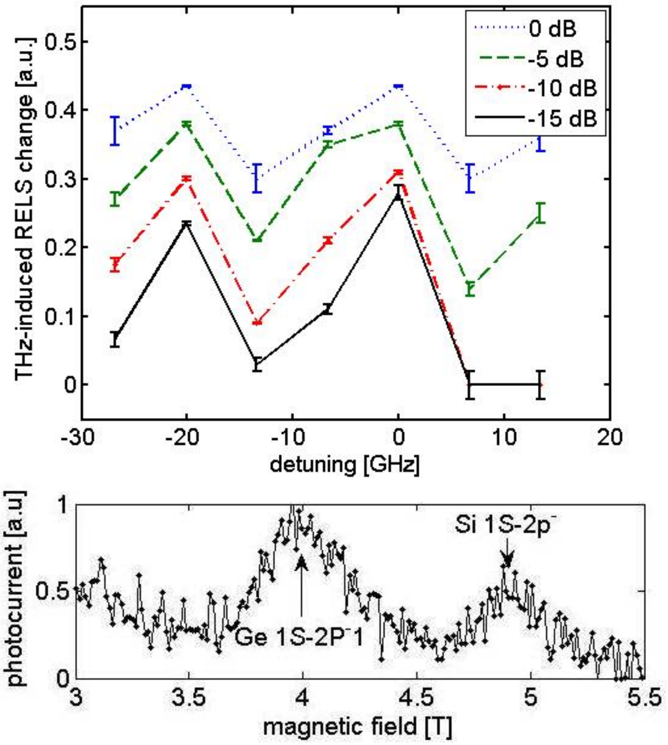

Figure 5.15: (a) Magnitude of normalized RELS change versus terahertz excitation wavelength for $n_d - n_a = 10^{14}\text{cm}^{-3}$ following a 3 ns THz pulse. Two resonances are observed at low intensity, which saturate at higher intensities. Error bars are due to fluctuations in terahertz intensity. (b) Integrated transient photoconductivity of a the same sample (30x30 μm) biased region during a 1μs free electron laser pulse near 1.04 THz. Two donor species are present (Ge and Si) with resonances at 4.0 and 5.0 T, respectively.

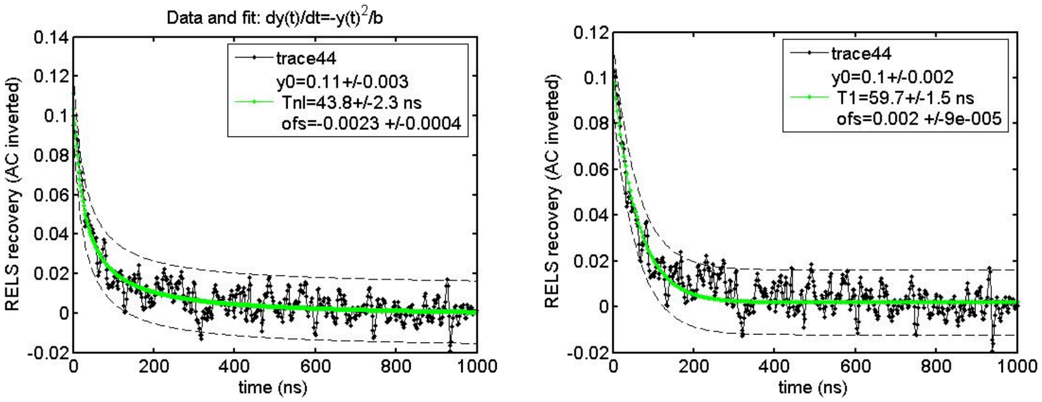

Figure 5.16: D^0X RELS recovery after pulsed terahertz excitation of sample B763 ($n_d - n_a = 10^{14}$cm^{-3}) at 2.5 THz, exciting the ionizing 1S–CB transition at T=2 K and B=0 T and NIR excitation at approximately 10 mWcm^{-2}. RELS change is negative in sign, but is shown inverted for clarity. Truncated FEL pulse was 5 μJ, 500 ns duration and estimated 2 mm spot size for an average power of ~60 Wcm^{-2}. (Left) Fit to power law of the form $b/(t + b/y0) + ofs$, with the nonlinear equivalent 1/e time T_{nl} calculated as $b(e-1)/y_0$ (see Ch. 6). Fit and uncertainty estimated based on average and standard deviation from a Monte Carlo method described in the text. (Right) Similar fit for the exponential model $y_0 exp(-t/T1) + ofs$.

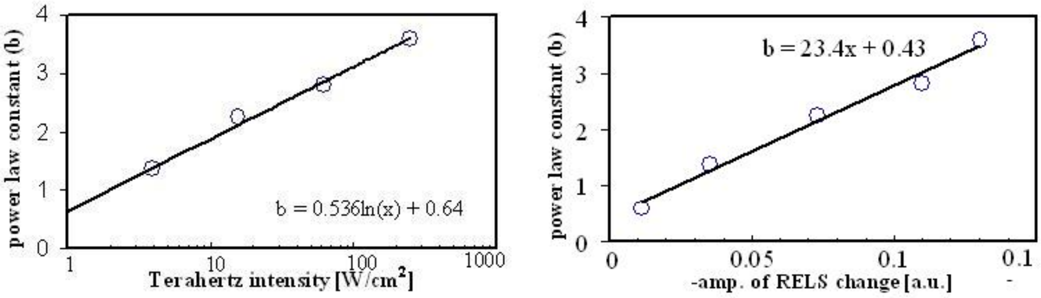

Figure 5.17: (Left) Terahertz intensity dependence of nonlinear relaxation time constant b from fits of the form $b/(t + y_0) + ofs$ under experimental conditions described in Fig. 5.17. (Right) Plot of b versus the amplitude of the negative change in RELS emission

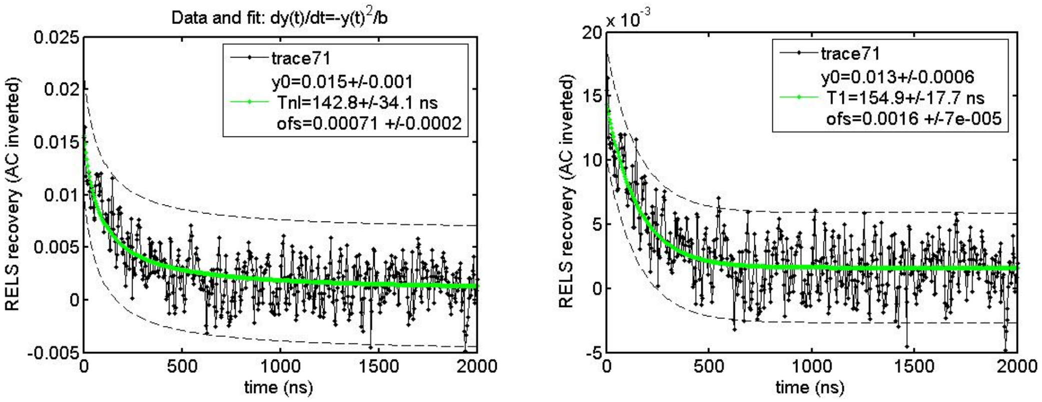

Figure 5.18: Recovery of RELS after 2.5THz pulse under conditions similar to Fig. 5.17, except at B=4.5 T and 15 Wcm^{-2} average intensity with fits to a power law (Left) and single exponential (Right).

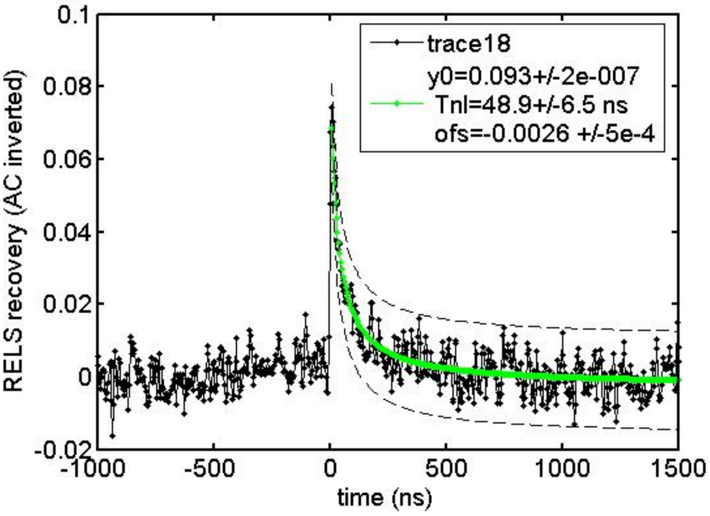

Figure 5.19: Recovery of RELS in sample B763 ($n_d - n_a = 10^{14}$cm^{-3}) after a 3ns, 1 THz pulse at B=0 T with 10 mWcm^{-2} continuous readout intensity. Fit is to a power law of the form given by Eq. 5.16 with the effective nonlinear $1/e$ decay time T_{nl} given by Eq. 5.18. The maximum decay time observed at low intensities is 100 ns.

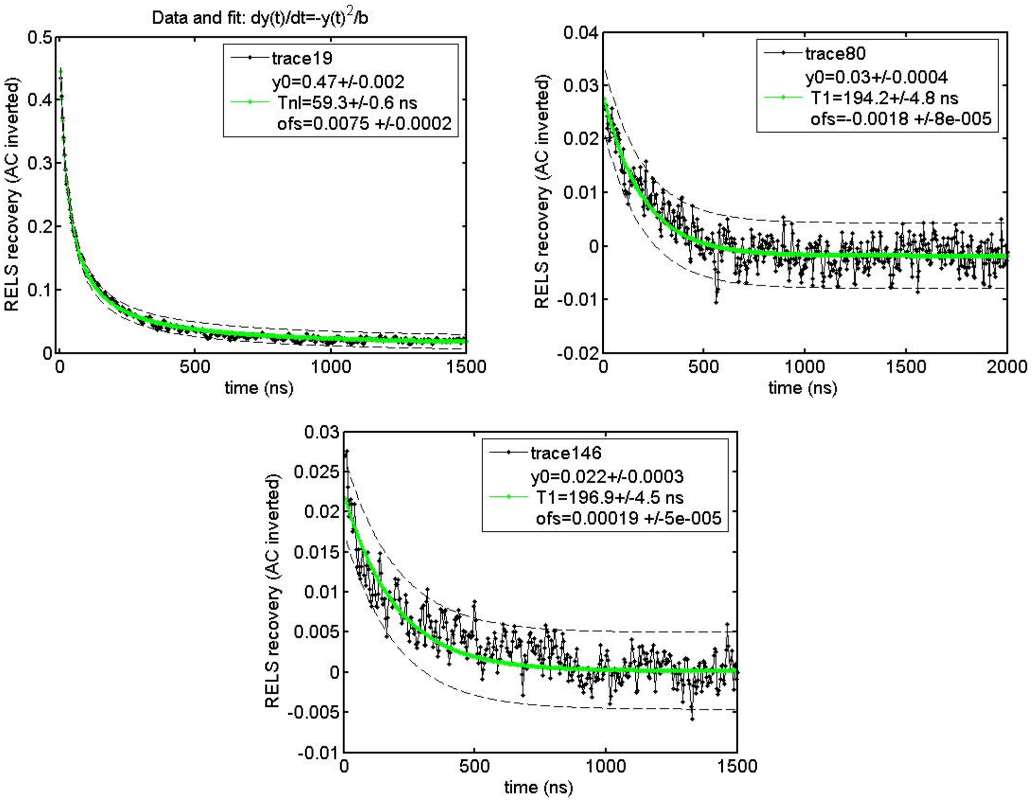

Figure 5.20: Change in RELS with excitation on resonance with the neutral donor 1S–2P$^-$ transition at B=4 T using 3 ns pulsed excitation near 1 THz. Traces are from an AC coupled detector and are shown inverted for clarity. (Left) Excitation near the Ge donor 1S–2P$^-$ resonance, with NIR power at 100 mWcm^{-2} and terahertz excitation sufficient to saturate the change in RELS. Data is well-fit by a power law. (Right) Excitation on resonance with Si donors and NIR readout laser power at 10 mWcm^{-2} with a minimum terahertz intensity. The trace is best fit by an exponential. (Bottom) Similar trace on resonance with Si donor 1S–2P$^-$ transition. The recovery time is observed to decrease uniformly with excitation intensity transitioning to a power law at intensities 2x the minimum detectable signal.

.

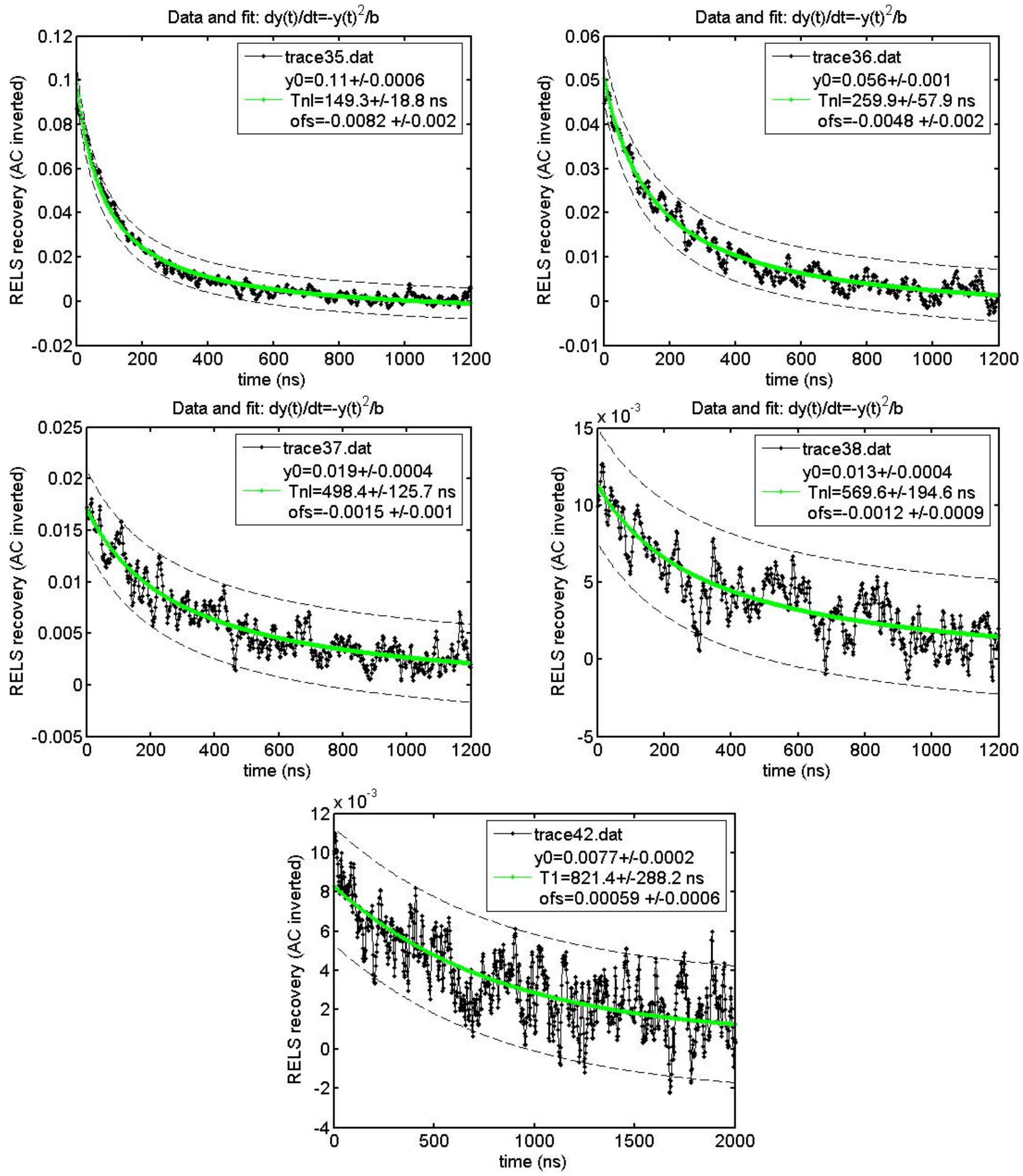

Figure 5.21: (Upper)A series of four RELS recovery traces for sample B48 ($n_d - n_a = 7.6 \times 10^{13}\text{cm}^{-3}$) with Si as the prevalent donor at B=4.5 T for NIR readout laser intensities decrease successively by factors of two. Traces are inverted for clarity. Fits are to a power law. In each case a power law fit is best at short times and an exponential at long times, with the exponential fraction increasing at lower NIR intensities. (Bottom) Near resonance at 4.9 T at the lowest NIR intensity an even longer lifetime was seen, in which the exponential part of the recovery is more than 0.75 of the total change in RELS. Note the exponential fit does not match at times less than 100 ns.

Chapter 6

Modelling of donor dynamics

6.1 Inelastic scattering model

In forming a realistic model for the fluorescence recovery, two previously observed properties about donor bound state lifetimes should be taken into account.

1. The lifetime of donor bound electron states is short $< 14ns$ in the presence of a substantial free carrier concentration.[53]

2. The lifetime of donor bound electron states is long T_1=250 ns, under conditions which produce a very small free carrier concentration.[13]

I will assume the reduction of the bound state lifetime is due to inelastic scattering with free carriers. Under this assumption, the relaxation rate γ_1 out of a bottleneck neutral donor state (e.g. 2S or 2P) is given (in the absence of carriers) by the phonon emission-limited lifetime $1/T_1$, plus a term proportional to the concentration of free carriers in the conduction band n_{cb}. b will represent the time constant of proportionality. Since the conduction band population decays quickly, the excited donor relaxation rate in this model is strongly time dependent. The time rate of change of the ground state population $n_g(t)'$ is proportional to the decay rate $\gamma_1(t)$ and excited bound state population $n_e(t)$ (Fig. 6.1).

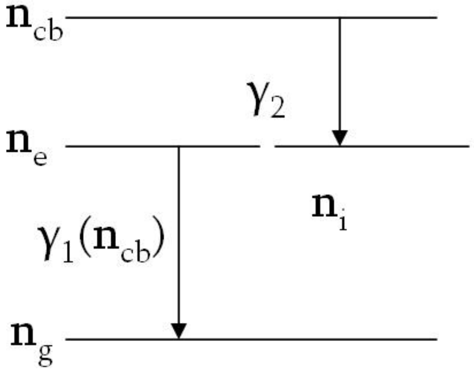

Figure 6.1: Three level relaxation scheme showing capture of a population of conduction band electrons n_{cb} by ionized donors n_i at a rate γ_2, with simultaneous relaxation of excited neutral donors n_e to the ground state n_g at a rate γ_1 which includes relaxation by phonon emission as well as contributions from inelastic scattering by free electrons.

$$n_g(t)' = \gamma_1(t) n_e(t), \tag{6.23}$$

$$\gamma_1(t) = 1/T_1 + n_{cb}(t)/b \tag{6.24}$$

The overall recovery of electrons to the ground state is determined by a set of rate equations which include rates γ_2 for free carrier capture and $\gamma_1(t)$ for relaxation of excited donors to the ground state. Capture of free electrons is proportional to the number of free electrons n_{cb} and ionized carriers n_i.

$$n_{cb}(t)' = -\gamma_2 n_i(t) n_{cb}(t), \tag{6.25}$$

$$n_i(t) \equiv n_{cb}(t) + n_a \tag{6.26}$$

I will model the excited donor states as a single level, with a depletion term for relaxation to the ground state and a refilling term due to capture of free electrons into excited bound states.

$$n_e(t)' = -\gamma_1(t) n_e(t) + \gamma_2 n_i(t) n_{cb}(t) \tag{6.27}$$

The resulting system of rate equations is explicitly given below.

$$n_g(t)' = \gamma_1[1 + n_{cb}(t)/b] n_e(t) \tag{6.28}$$

$$n_e(t)' = -\gamma_1[1 + n_{cb}(t)/b] n_e(t) + \gamma_2 \big[n_{cb}(t) + n_a\big] n_{cb}(t) \tag{6.29}$$

$$n_{cb}(t)' = -\gamma_2 \big[n_{cb}(t) + n_a\big] n_{cb}(t) \tag{6.30}$$

The parameters largely known from previous experiments: the carrier capture time $T_{cap} = (e-1)/\gamma_2 \sim 14$ ns, the phonon-limited donor relaxation rate $\gamma_1(b \rightarrow 0) = 1/T_1 = 1/250$ ns. b can be inferred from the requirement that for $n_{cb} \sim 1$, $1/\gamma_1 \ll 14$ns. It will suffice if $b = 1/(2\gamma_2)$;

The resulting system of equations can be numerically integrated, yielding behavior quite similar to the observed RELS recovery (Fig. 6.2).

In the limit of no conduction band population we return to the isolate donor case (Eq. 5.11). When the conduction band population is a large fraction, a significant number of donors will relax during the time scale for carrier capture. *These two behaviors describe qualitatively and quantitatively the observed behavior of donors during recovery of RELS after resonant terahertz excitation without parameters determined by independent measurements taken from the literature.*

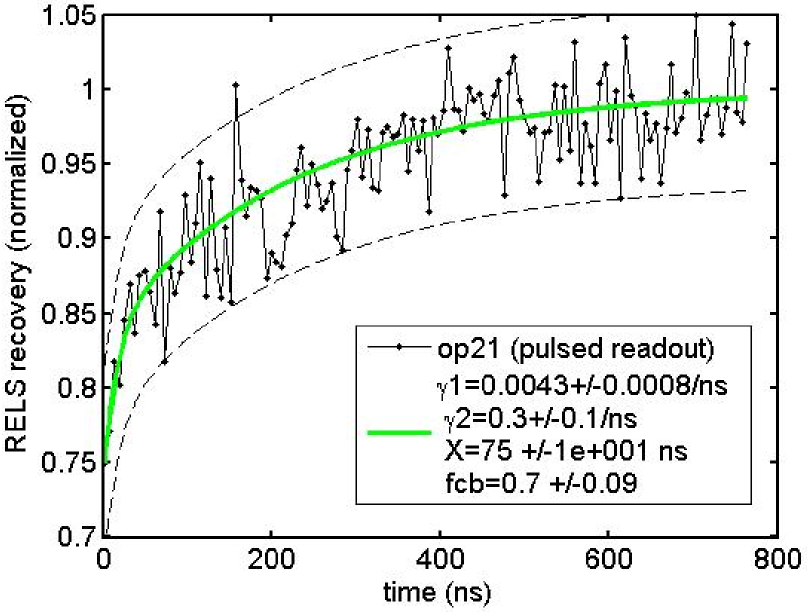

Figure 6.2: Plot of RELS recovery (normalized to saturated amplitude) and fit to rate equation model. Fit parameters are given in the inset. γ_1 is relaxation rate out of the $2P^-$ state, γ_2 is free carrier bimolecular capture rate (acceptor compensation ratio n_a/n_d is assumed to be 0.2). X corresponds to b in Eq. 6.28, the donor-free carrier inelastic scattering time constant, and $fcb = n_{cb}(0)/(1 - n_g(0))$ is the fraction of excited electrons in the conduction band. Sample is B48 ($n_d - n_a = 7.6 \times 10^{13}/\text{cm}^{-3}$; conditions are B=5.5T, with a 500ns right triangle-shaped terahertz pulse of rising intensity and pulsed optical readout (e.g. NIR intensity=0 during terahertz excitation). The trace shown is typical of terahertz intensity-limited recovery. The estimation of a large fraction of electrons in the conduction band is in agreement with photohall measurements in the literature which show the majority of electrons in the conduction band after a long pulse excitation.[3, 4]

To see the dynamics in a more analytically tractable, and only slightly less general way, consider conduction band fractions less than the acceptor compensation ratio (≤ 0.2), we may neglect $n_{cb}(t)$ in Eq. 6.26. The carrier capture rate then becomes a constant. If I further assume that the only relaxation is due to inelastic scattering I have an analytic solution for $n_e(t)$.

$$n_e(t, T_1 = \infty) = n_a\gamma_2 b + (-n_a\gamma_2 b + n_e(0))e^{n_i(0)/b\left[\exp(-\gamma_2 t)-1\right]} \tag{6.31}$$

Since I have assumed the conduction band population is smaller than n_a, if n_a is also small and $b < \gamma_2$, but the $n_e(0)$ is large, then I may keep only the term proportional to $n_e(0)$.

$$n_e(t) \sim n_e(0))e^{n_i(0)/b\left[\exp(-\gamma_2 t)-1\right]} \tag{6.32}$$

Which gives a conduction band population dependent decay (e.g. $\exp(-n_i(0)/bt)$), as expected for this limit. An excitation fraction dependent lifetime is observed experimentally, however this approximation breaks down when the exciation fraction is low enough that the excite donor lifetime becomes phonon-limited, rater than free carrier inelastic scattering-limited and is no longer negligible.

Note that this model is very sensitive to the conduction band population. This feature agrees well with the experimentally observed fact that in order to observe phonon-limited lifetimes I had to work with short pulses, high magnetic field, low NIR power and excite to very low (~ 0.01) excitation fractions. For example, with typical parameters γ_1=1/(250 ns), γ_2=1/(8 ns), b=60, the rate equation model predicts decay times of 60, 155, and 230 ns for ratios of n_{cb}/n_e of 0.5, 10, and 100, respectively. Even with just 1% of the excited electrons in the conduction band, the lifetime is reduced by nearly 10%.

6.1.1 Notes on fitting, acceptors, and the Mott transition

Via a simpler model, the recovery of fluorescence can be fit in almost every case to the solution of a differential equation with a linear decay term and bimolecular recombination term . At high excitation fractions only the bimolecular term is needed to fit the data.

This nonspecific model assumes an excited electron will either relax to the ground state in a time T_1, or recombine with an ionized donor in a time b, but it doesn't attempt to distinguish what energy level (2P or CB) the electron is in. This is applicable in the limit of strong excitation in highly doped and/or high compensated material (e.g.) near the Mott transition. Since the only source of electrons is ionized donors, the two populations are equal. This results in a single equation which can be solved for the relaxation behavior of the excited population $N_e(t)$ and the recovery of electrons to the ground state $(1 - N_e(t))$ for which we can also define an effective $1/e$ decay time T_{nl}.

$$N_e(t)' = -\frac{N_e(t)}{T_1} - \frac{N_e(t)^2}{b} \tag{6.33}$$

$$N_e(t) = \left(\frac{e^{-t/T1}(1 + N_0T_1/b)}{N_0} - \frac{T_1}{b}\right)^{-1} \tag{6.34}$$

$$T_{nl} = ln\left(\frac{N_0T_1 + be}{N_0T_1 + b}\right)T_1 \tag{6.35}$$

In the limit $b \to \infty$ we have the exponential case (Eq. 5.11); in the limit

$T_1 \rightarrow \infty$ we have a power law (Eq. 5.16). As dopant densities, excitation fractions and compensation ratios are lowered an excited donor will experience less overlap with adjacent donors and the bimolecular recombination time b is expected to go up. In the intermediate regime, both behaviors are expected. In the RELS recovery observed in this thesis, power law behavior associated with bimolecular recombination dominates for excitation fractions > 0.1, even at dopant densities as low as $3 \times 10^{13}/\text{cm}^3$.

The linear term in Eq. 6.33 also arises in pure bimolecular decay when there are compensating impurities. Stray acceptors (at concentration N_a) leave a fraction (~ 0.2 in our samples) of the donors ionized even in the absence of terahertz excitaion. The ionized donor population is not equal to the ionized electron concentration. We may substitute $N_i = N_e + N_a$ into Eq. 6.36 to obtain

$$N_e(t)' = \frac{-N_e(t)(N_e(t) + N_a)}{b} \tag{6.36}$$

$$= -\frac{N_e(t)}{b/N_a} - \frac{N_e(t)^2}{b}. \tag{6.37}$$

The solution is identical to Eq. 6.34 where we make the substitution $T_1 \rightarrow b/N_a$.

$$T_{nl} = ln\left(\frac{N_0 + Na * e}{N_0 + N_a}\right)\frac{b}{N_a} \tag{6.38}$$

At high excitation fractions, low temperature with CB electron and ionized donor fractions of approaching unity, the decay time τ of the photoconductivity is estimated to be 14 ns.[55] (Incidentally, the carrier capture cross section can be estimated from this relaxation time from the following relation, where N_d is the concentration of donors and $v_{th} = \sqrt{(}3kT/m^*)$ is the thermal velocity.

$$\tau_c = (N_d v_{th} \sigma)^{-1} \tag{6.39}$$

Alternatively, from the low temperature photoconductivity measurements we have an estimated electron temperature of 4 K for a thermal velocity 6×10^6cm/s, dopant density $5 \times 10^{14}/\text{cm}^3$, and a capture time of 14ns we obtain a carrier capture cross section $\sigma = 2.4 \times 10^{-14}/\text{cm}^2$. Low temperature time-resolved cathodoluminescence measurements[59] reveal a similar relaxation time $\tau = 22$ for an estimated capture cross section of $\sigma = 5 \times 10^{-15}/\text{cm}^2$. Noting the close correspondence of these two measurements, we may safely assume the shortest nonlinear recovery time ($N_e = 1$) of photoexcited carriers in our samples is $\sim$ 15 ns.)

In the weak excitation limit, where the lifetime of donor Rydberg transitions is negligibly short, the bimolecular lifetime goes to the limiting value b/N_a, where $N_a \sim 0.2$ is the fraction of compensating acceptors. In our case the lifetime which is limited by the capture of electrons by residual ionized donors is

$$T_{nl}(N_e \to 0) = b/N_a = 50ns \tag{6.40}$$

Since the excitation fraction is not exactly estimable due to the presence of a background of scattered light, the exact value of b for any given fit is not a calibrated measure. However, since we know $T_{nl}(N_e = 1) \sim 10$ ns and $T_{nl}(N_e \to 0) \sim 50$ns, we may simply state that *in the low-excitation limit, RELS recovery at* *times longer than 50 ns (or in the the high excitation limit longer than ∼10 ns) are attributable to the finite lifetime of donor bound electrons.*

I should also mention that at high donor and/or free carrier densities the capture cross section is reduced by screening.[60, 61] The Mott transition is attributable to this very effect, where electrons are delocalized because the screening length reaches the Bohr radius. The presence of more polarizable excited donors may reduce somewhat the carrier capture time at high densities. In the weakly interacting regime, where donors in excited states partially screen donors in the ground state, a solid with more donors in the excited states is likely to capture electrons to ionized donors more slowly. A simultaneous comparison of donor bound exciton fluorescence and photoconductivity may suffice to identify this effect, however such experiments have not yet been performed.

6.2 Excitation fraction dependent RELS efficiency model

It is the purpose of this section to investigate whether nonexponential decay can be explained by an excitation fraction dependent RELS intensity, namely excited donors shifting their neighbors out of resonance with the laser, thus creating a nonlinear relationship between D^0X RELS and and donor ground state population.

6.2.1 Distance to nearest neighbor

In order to quantify possible interference from neighbors I must calculate the typical distance between a donor and its nearest ground, excited or ionized neighbor.

If c is the concentration of donors per unit volume, we define an average donor spacing.

$$d_{avg} = 1/c^{1/3} \tag{6.41}$$

Where this definition becomes misleading is when the assumption is made that "there is a negligible probability of finding another donor within a distance d_{avg} from a given donor".

The probability of finding k donors in a volume V given the concentration $c = n_{tot}/V_{tot}$ (here I assume no acceptor compensation for simplicity) is given by the Poisson factor P(k,l),

$$P(k,\lambda) = \frac{\lambda^k e^{-\lambda}}{k!}, \tag{6.42}$$

λ is the average or expected outcome of the Poisson distribution and k is the number of occurrences. The probability of having a given number of occurrences drops exponentially with decreasing likelihood or rate of a single occurrence λ. In our case, the occurrence rate is a product of the measured volume V and the concentration c, where concentration is just a total number/volume ratio:

$$\lambda \equiv Vc \tag{6.43}$$

The probability of finding of a donor within a given distance r from another donor is given by the Poisson distribution for $k = 1$ and $V = 4/3\pi r^3$.

The total probability of finding at least one donor in a given volume is the sum of Poisson factors greater than zero.

$$P_{tot}(\lambda) = \sum_{k=1}^{\infty} \frac{\lambda^k \exp^{-\lambda}}{k!} = 1 - P(0, k) = 1 - e^{-\lambda} \tag{6.44}$$

Now I can ask what is the probability of having at least one donor within a distance $d_{avg}/2$ of a given donor. $r = c^{-1/3}/2$ and $V = 4/3\pi r^3$, so $\lambda = VC = \pi/6$.

$$P_{tot}(\pi/6) = 1 - e^{-\pi/6} = 0.4, \tag{6.45}$$

which is not a negligible fraction. In fact the probability exceeds half if I expand the allowable volume to just $0.55 d_{avg}$.

The maximum likelihood distance $< r_{nn} >$ for encountering a nearest neighbor is given by the following.[62]

$$< r_{nn} >= 0.9(4.15N_d)^{-1/3} \tag{6.46}$$

For donors in the range 3×10^{13}–$3 \times 10^{14}/\text{cm}^3$, $r_{nn} = 180$–83 nm, whereas $d_{avg} =$ 320–150 nm.

The Coulomb interaction deriving from the orbital overlap between two hydrogenic donors decreases exponentially with distance at long distances due to the exponentially decay of the wavefunctions. In a crude approximation, I may choose a threshold level of interaction required to perturb a donor and modify its emission properties, and the divide the population of donors into two categories:

Isolated donors, those with nearest neighbors greater than a critical distance r_c needed to reach the threshold and *perturbed donors*, those with nearest neighbors close enough for the interaction between them to exceed the threshold. (Note this criteria was also applied in Ref. [44].) The simplest question is how does the fraction of perturbed donors change with concentration.

The fraction of perturbed atoms n_p is

$$n_p(r_c) = P_{tot}[4/3\pi r_c^3 c] = 1 - e^{-4/3\pi r_c^3 c}, \tag{6.47}$$

while the fraction of isolated atoms n_i is

$$n_i(r_c) = 1 - P_{tot}[4/3\pi r_c^3 c] = e^{-4/3\pi r_c^3 c}. \tag{6.48}$$

The last result is the same as the Poisson factor $P(0, 4/3\pi r_c^3 c)$

6.2.2 Bound excitons perturbed by excited donors

I use Eq. 6.47 and 6.48 estimate the fraction of donors which become perturbed by one of the above effects. For comparison, I estimate first the number of perturbed 1S donors prior to excitation. I for an initial estimate of the 1S donor–1S donor perturbing radius $r_d = d_{mott} = 40$ nm, the average donor spacing at the critical density for a Mott transition $c = 1 \times 10^{16}$–$2 \times 10^{16}/\text{cm}^3$. Plots of the fraction of perturbed donors n_p versus donor concentration are shown in Fig. 6.3.

From Fig. 6.3 it can be seen that the number of perturbed (ground state) donors for samples with relevant donor concentrations is at most a few percent.

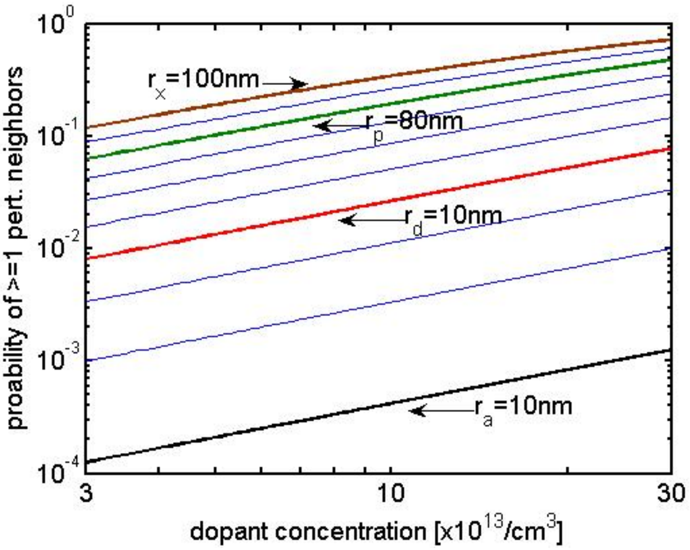

Figure 6.3: Log-log plot of number of donors with at least one neighbor near enough to perturb their wavefunction versus concentration for increasing values of the parameter r_c, a fictional radius at which donor-donor interactions exceed a critical value. The black trace represents $r_a = a_B$, the ground state donor bohr radius. The red trace is the value of $r_d = d_{mott} = 40$ nm, which is also the Bohr radius of a donor in an $n = 2$ orbital. The green trace is $r_p = 80$ nm, the estimated distance at which a 2P neutral donor will perturb a ground state neutral donor. The brown trace is $r_c = 100$ nm the estimated radius at which a 2P donor will perturb a donor bound exciton.

If we consider exciting a fraction of donors x to a 2P state, there will be two critical radii for perturbing a donor, one for ground state neighbors and one for excited state neighbors. Now I neglect the static and small population of perturbed ground state donors and consider only the dynamic effect of excitation fraction.

At low excitation fractions I may consider an equivalent problem, namely: how many donors will a particular donor perturb when it is excited to a 2P state? I choose a new critical radius r_p for which all inclusive ground state donors are perturbed. We may assume it can perturb donors within 80 nm. On average, at low excitation fractions we see the probability of perturbing a donor ground state is $0.03 \leq p_d[80nm] \leq 0.3$ over relevant concentrations.

If now I consider the probability of perturbing the weakly bound (and larger) donor bound exciton complex. I extend the range of 2P interaction by 20 nm to $r_x = 100$ nm, to account for the larger volume of the target species. The actual expectation value for the ground state radius of the hole is $1.4a_B = 14$ nm. Fig. 6.3 shows that for $r_c = 100$ nm at concentrations relevant to our experiment, $0.1 \leq p_x[100nm] \leq 0.7$ of the excited donors will perturb a donor bound exciton.

For a dynamical simulation of the effect of nearest neighbor perturbations on RELS recovery I consider bound exciton emission to come only from unperturbed ground state donors. I estimate from the Poisson distribution the fraction of ground state donors for which there are no excited 2P neutral donors within a critical volume $V_1 = 4/3\pi r_x^3$ at an initial concentration c and excitation fraction

x. Emission is proportional to the joint probability of being both in the ground state $(1-x)$ and unperturbed $P(0, V_1 xc)$.

$$n_i = n_{1s} * P(0, V_1 xc) = (1-x)e^{-V_1 xc} \tag{6.49}$$

If after excitation, 2P neutral donors relax according to the exponential law, the fraction of excited state donors x is given by substituting generally $x \rightarrow x \exp(-t/T_1)$. The number of emitting donors becomes

$$n_i(t) = (1 - xe^{-t/T1})e^{-4/3\pi r_x^3 xe^{-t/T_1}c} \tag{6.50}$$

In either the limit $r_x \rightarrow 0$ or $x \rightarrow 0$, we obtain the result expected for isolated donors. The simple theory predicts results in an increase the effective amplitude of RELS darkening relative to the isolated donor model (Fig. 6.4). It can also account for the complete quenching of fluorescence even in the presence of a nonzero ground state donor population, provided the excitation fraction is large enough to perturb all the ground state donors.

The key point to notice is that faster RELS recovery at shorter times is *not* predicted by Eq. 6.50, as seen in Fig. 6.4(lower right). I could do a similar plot for interactions with ionized donors, however the trends and overall behavior would not change. This model cannot explain the observed recovery behavior.

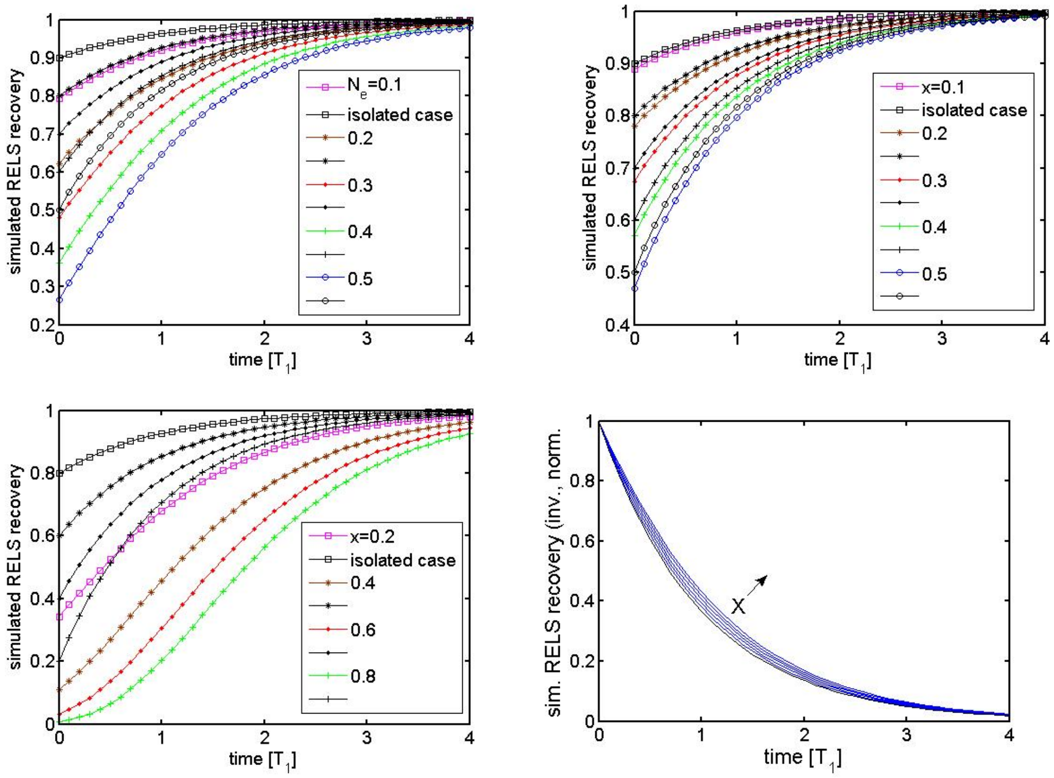

Figure 6.4: Simulated neutral donor ground state RELS emission according to Eq. 6.50 after resonant terahertz excitation in an ensemble of neutral donors for a series of excitation fractions. Donors bound excitons within a radius r_x of excited donors are presumed to be perturbed and unable to absorb/emitter at the energy of the excitation laser. (Left) RELS recovery for a donor density of $3 \times 10^{13}/\text{cm}^3$, with excitation fraction according to the inset. Black traces representing the ground state population in the noninteracting (isolated) case are included for comparison. (Right) Similar curves for donor density $3 \times 10^{13}/\text{cm}^3$ comparing isolated with interacting ensembles. (Lower left) RELS recovery for $3 \times 10^{13}/\text{cm}^3$ at higher excitation fractions and a larger critical radius of 120nm showing rollover at high excitation fractions. (Lower right) Simulated RELS recovery according to Eq. 6.50, inverted and normalized for comparison for a series of excitation fractions x=0.1, 0.2, 0.3, 0.4 and 0.5.

6.3 D^0X lineshifts and broadening

Since the mechanism suggested in the previous section does not explain the faster RELS recovery at short times after the pulse, it may be more useful to model by fitting the actual observed behavior in the D0X spectrum during the FEL, which is a line shift and/or broadening.

I consider the fraction of emitting donors to be the overlap of the probed ensemble D^0X transition and linewidth profile of the D^0X transition. I may assume the linewidth profile is Gaussian of initial full width at half maximum of $\Delta_0 = 120\mu\text{eV}$, which increases and potentially shifts with excitation fraction. I write the observed intensity of D^0X emission in the following way.

$$I(x) = \sqrt{\frac{\ln 2}{\Delta(x)\pi}} e^{-\left(\sqrt{\ln(2)}/\Delta(x)\left[E-E_0(x)\right]\right)^2} \tag{6.51}$$

First, I assume the decrease in emission is due to a linear change in linewidth with excitation fraction up to width $A\Delta_0$

$$\Delta(x) = \Delta_0(1 + (A-1)x) \tag{6.52}$$

This predicts less observed emission when a population of donors is excited and the exciton transition is broadened. The total ELS emission on resonance as a function of excitation with no excitation dependent line shift is

$$N_i \propto \frac{1-x}{\sqrt{\Delta(x)}} \tag{6.53}$$

Similarly, the emission in the presence of a line shift is

$$N_i \propto (1-x)e^{-\left(\sqrt{\ln(2)}/\Delta(x)\left[E-E_0(x)\right]\right)^2} \tag{6.54}$$

If the dependence of the line center and broadening are only polynomials of x, then behavior is observed which is very similar to Fig. 6.4, where the slope at t=0 is lower, not higher, than case isolated donors with exponential relaxation, and does not match the observed super-exponential behavior.

The only way to get a super-exponential slope from a line shift, broadening or excitation fraction dependent perturbation of donors is to have a singularity in r_x, $\Delta(x)$, or $E_0(x)$ such as would be expected if we approached a phase transition. I can't think of any physical reason for expecting this to happen in our samples.

However, line shifts do explain transient brightening behavior observed at early times in a terahertz pulse when the NIR laser is near off resonant with a donor bound exciton transition.

Neither a decreased RELS efficiency, nor a linewidth broadening or shift can satisfactorily explain the nonexponential decay, even qualitatively, making the assumed culprit: free carriers, the best explanation, as explained in Sec. 6.1.

However, the transient terahertz induced brightening observed off resonance from D^0X transitions (e.g. Fig. 7.1 may possibly be due to a line broadening/line shift effect. It remains to investigate this transient brightening and discuss the two possible explanations: strong field effects (AC Stark shift, Franz-Keldysh effect) and local field effects (screening and stochastic DC Stark broadening).

Chapter 7

Terahertz induced-brightening

7.1 Neighbor donor effects

The unexpected short recovery time for RELS associated with ground state neutral donors brings into question several of the initial assertions which motivated the studies of donor neutral donor quantum dynamics. Among these is the assumption that because the donor spacings are typically large compared to the ground state Bohr radius, the donors are “noninteracting”, especially when some are excited to the larger and more weakly bound 2P state.

In atomic physics, the effect of interactions of atoms due to excitation of a fraction of the atomic population can sometimes be observed by measuring the broadening of the transition versus excitation fraction, or by measuring the broadening of a cycling transition. In my case, I have no method for performing terahertz spectroscopy during an FEL pulse of the 1S–2P$^-$ transition at a fixed magnetic field. Swept field measurements with RELS are very hard to do because the dozen or so D^0X lines change with magnetic field in a very complex way. However the D^0X line serves as a cycling transition and changes in the donor ground state energy may affect the initial energy state from which the bound exciton recombines.

The hydrogen molecule-like D^0X itself is even more sensitive to neighboring donors because its spatial extent is greater than a 1S donor $\langle r_{d-h} \rangle = 1.4a_B$. The bound exciton may be utilized as sensitive probe of such interactions. The one caveat is that the more donors are excited, the smaller the signal (since there are less ground state donors to probe).

In the following section a nonlinear relationship between donor excitation fraction and elastic light scattering is observed for near off resonant excitation of the donor bound exciton transition. The data are not yet conclusive as to the cause of the effect. Several possible interactions between donors and excited donors, as well as ionized donors and free carriers as discussed in relation to the observed phenomena.

7.2 Transient brightening

The total collected intensity of RELS per incident NIR intensity is proportional to the emitting ground state population and relative strength of the RELS. RELS is maximized when the NIR laser is on resonance with a D^0X transition. And in the case of isolated donors, the total RELS signal is linearly reduced by exciting a fraction of the neutral donor population. But, when an ensemble of weakly interacting donors is observed at a single frequency by a narrowband laser, the elastic scattering amplitude near a D^0X transition can in principle either *increase or decrease*. For instance, with the laser set near a resonance peak, a shift in the peak towards the laser line will cause an increase in observed scattering. Likewise, broadening of a transition will cause an increase in emission away from the center resonance. Brightening can even be observed exactly on resonance with a line in the case that stronger nearby transition broadens.

Shifts and broadening in donor bound exciton transitions can be caused by either local field effects or strong field effects.

Such shifts and broadening in D0X lines are observed via time/terahertz intensity and frequency resolved elastic light scattering (ELS) measurements. For frequency resolved ELS measurements, the terahertz-induced change in D^0X emission is monitored at a specific energy via resonance fluorescence before, during and after a FEL pulse by an AC-coupled avalanched photodiode. The NIR laser energy is varied stepwise and the response to terahertz radiation is recorded in a series of FEL pulses. This technique yields good signal to noise ratio, since laser scatter itself is collected, rather than PL. Additionally the spectrum does not include a convolution with the thermal distribution of emission that is typical in PL measurements. Further, high resolution is possible without reducing light collection (resolution and light collection trade off with slit width in grating spectrometers),

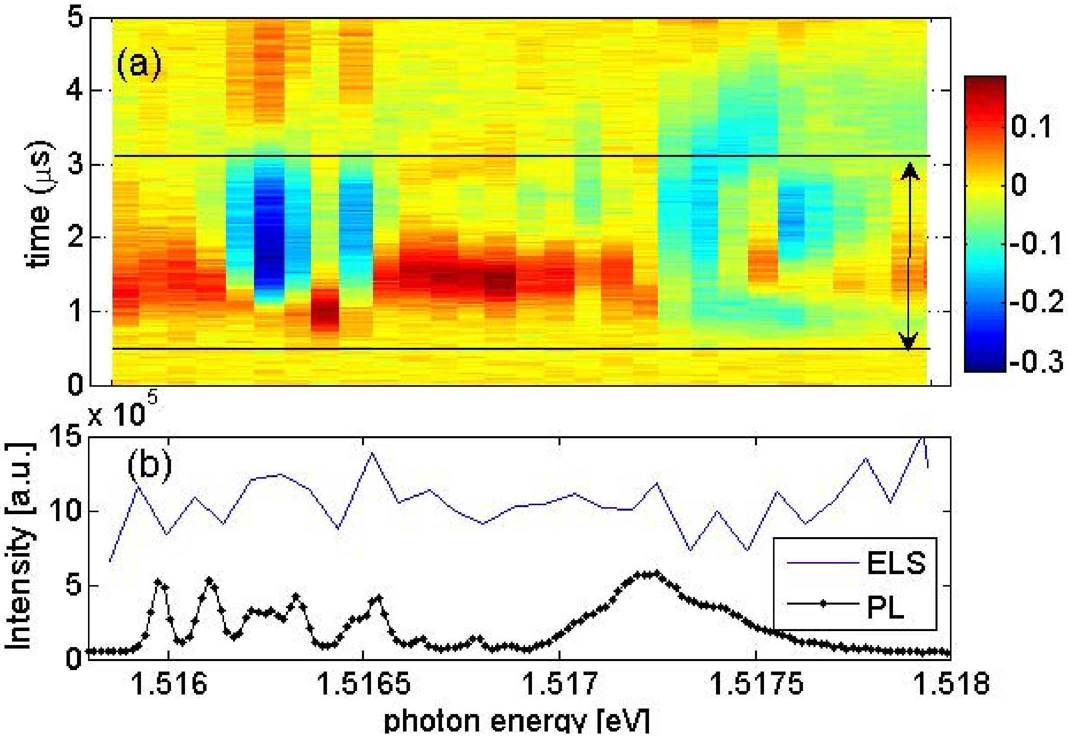

Figure 7.1: (a) Contour plot (arbitrary scale) of elastic light scattering change versus time before, during and after a 1.02 THz pulse. Quenching is observed on resonance with the strongest bound exciton transitions; transient brightening is also observed off-resonance. Terahertz excitation follows an approximately Gaussian temporal profile spanning the horizontal lines, with peak intensity $\sim 100W/cm^2$, sufficient to saturate the population during the pulse. Sample dopant density is $n_d - n_a = 3 \times 10^{13}/cm^3$ dopant density with extremely low compensation ratio (n_a/n_d) and excellent fluorescence efficiency. Experimental conditions are B=6 T, T=2 K, NIR excitation 50 mW/cm^2. (b) Elastic light scattering and photoluminescence (PL) spectra (excitation at 1.52 eV). Note, elastic light scattering includes a detected background of light scattered, also the brightest transition does not appear as the highest peak in PL due to convolution of the oscillator strength with thermal distribution of the excitons. The increase in emission after the pulse at locations of strong NIR response is due to reduction of the surface depletion length when free excitons are heated by the terahertz resulting in mobile charge carriers.

provided the laser scatter dominates the spectrum and laser line is finely tunable.

Although it is anticipated that local field effects will be important at high dopant densities, dynamical changes in the RELS spectrum were strongest in the samples with the lowest dopant densities, especially in sample A421 (Table A.1), which had excellent optical properties likely due to low compensation in the large 25μm epitaxial layer. Sample A421 ($n_d - n_a = 3 \times 10^{13}/\mathrm{cm}^3$) did show significant brightening after the NIR laser was turned on (Fig. 3.8), indicating a large depletion region at the substrate interface and potentially the front interface as well if the capping layer was insufficiently doped. Terahertz induced brightening was also observed in sample B48 ($n_d - n_a = 7.6 \times 10^{13}/\mathrm{cm}^3$), with a 15$\mu$m epilayer on an undoped substrate, with no capping layer although detailed spectral studies were not performed. In higher doped samples some brightening is observed, which is small in comparison to the observed fluorescence quenching, with a peak which varies in time randomly with fluctuations in the startup of the FEL, leading to an effective averaging out of the effect in traces with more than 60 averages. Although the effect is robust it is not immediately discernable, but can be more apparent to the "trained eye" (the squinting graduate student looking at the band pass filtered data).

A possibility which about which I spent a good deal of time worrying is the possibility that the transient brightening is due to a surface charging effect, rapid dynamics observed after the pulse make this an untenable hypothesis.

Figure 5.10 in Ch. 5, which is reproduced here as Fig. 7.1 shows terahertz-induced brightening at frequencies off resonance from the brightest D^0X transition. This brightening is observed to occur during the rising edge of Terahertz emission. During the most intense part of the pulse the "extra" fluorescence is quenched (blue), or rather quenchable–if the THz intensity is high enough. The brightening (red) is also observed during the falling edge of the FEL pulse. Asymmetry in the rising and falling edge is attributed to the finite lifetime of excited electrons in which emission follows intensity during the rising edge, but lags during the falling edge. The intensity dependence of the transient brightening is shown in figure 7.2

Notably, in the conjoining regions at the pileup of most loosely bound rotational states and the free exciton peak near 1.5175 eV several mechanism appear to present with competing brightening and quenching occurring simultaneously in different spectral regions. This is suggestive that the effect of quenching of the brightening is not, for instance, a thermal modulation of fluorescence efficiency, such as would have a monotonic effect on fluorescence.

Brightening occurs between two D^0X peaks near 1.5164 eV and afterward across the entire spectral region spanning the several bound transitions and the free exciton spectral feature. Uniform, comparatively weak brightening is seen in the region below the lowest bound exciton transition, which is probably due to the broad spectrum of the ionized donor emission which intensifies as bound electrons become ionized during the terahertz pulse.

On the high energy side of the D^0X spectral region, an abrupt change in behavior is from THz-induced brightening during the rise edge to darkening is observed at the peak of the photoluminescence emission near the presumed band edge for magnetoexcitons at 1.51725 eV. The band edge is identified by the continued quenching of ELS at microsecond timescales after the terahertz pulse occurring

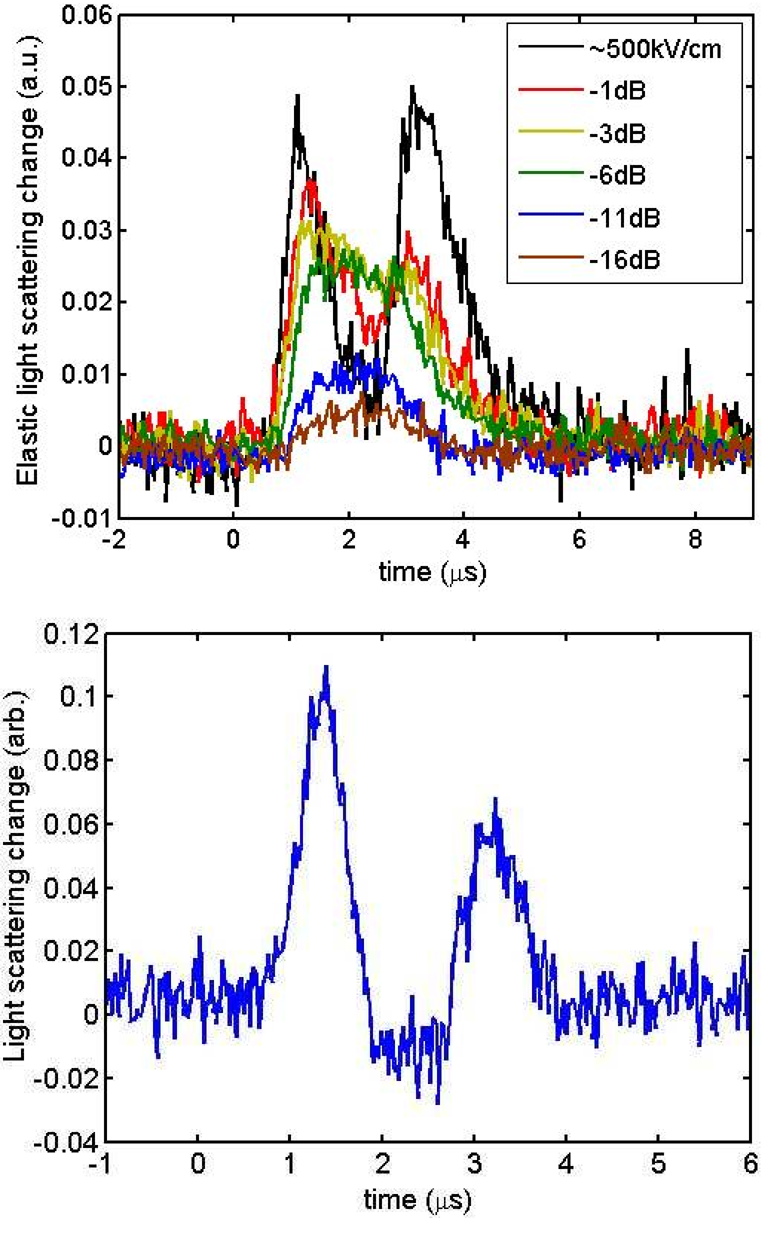

Figure 7.2: (Upper) Change in near resonant ELS during ~ 1.03 THz terahertz pulse of Gaussian temporal profile. Experimental conditions are T=2K, B=4.6 T, $n_d - n_a = 3 \times 10^{13}/\text{cm}^3$, NIR photon energy 1.5152 eV (near lowest energy, but not the brightest D^0X peak). Estimated peak electric field is shown for each trace in the legend. Brightening is observed at low intensities. At high intensities, quenching is observed associated with depletion of emitting ground state population. (Lower) Similar curve at 5T, with terahertz excitation at 1.02 THz showing hard line saturation.

with NIR excitation above 1.51725 eV. This is the effect of terahertz heating of free excitons generated by the NIR laser, which causes a rise in lattice temperature and thermal inhibition of RELS. When excitation is reduced below 1.51725 eV. no heating is observed. By the combination of the above observations it is understood that the transient brightening cannot be attributed to only surface charging of heating effects.

In order to determine whether the effects are due to the presence of a strong field, I may truncate the FEL pulse and observe whether emission exhibits a discontinuity due to the disruption of the field (Fig. 7.3). In a highly A shift to lower energies is seen in the band edge features. A similar shift is not observed in the bound exciton spectral features. A reason may be that in the highly doped sample, the majority of electrons are ionized during a long high intensity 1S–$2P^-$ resonant terahertz pulse. The return of any field-induced shift in the oscillator strength cannot be sampled when the ground state donor population is closed zero.

Spectrally resolved ELS of a sample with 10x lower dopant density is also shown for B=5.5 T (Fig. 7.4). In the region between the brightest D^0X line and the band edge all frequencies show brightening during the initial rise of the terahertz pulse. Quenching occurs during the most intense part of the pulse. After truncation there is a jump to higher emission intensity. On the high energy side of the highest energy D^0X transition, i.e. above the free exciton absorption three adjacent traces show three different behaviors: uniform quenching, quenching

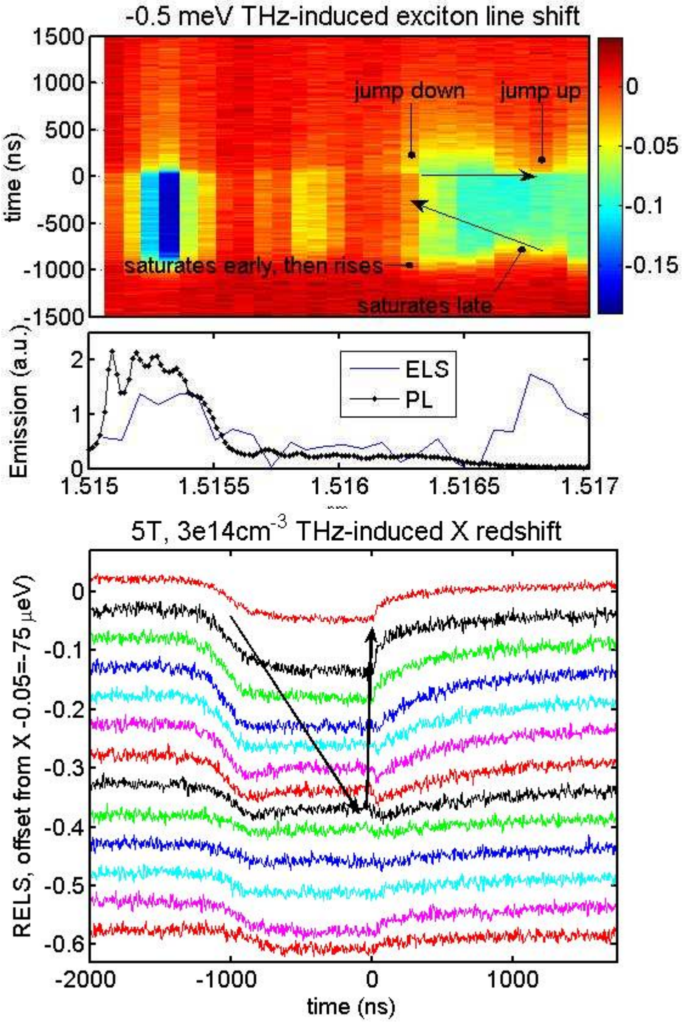

Figure 7.3: (Upper) Frequency resolved response of sample B671 ($n_d - n_a = 3\times10^{14}\mathrm{cm}^{-3}$) at 4.5T (FEL terminal voltage 2.50 MV) to strong terahertz excitation with a right triangle-shaped rising intensity waveform. Below the band edge brightening is observed. Above the band edge, dimming is seen. Within the 10 ns rise time of the YAG laser which activates the terahertz cutoff switch the trend is completely reversed, lower energies dimming and higher energies brightening. (Lower) Same sample at 5T, line cuts of the spectrally resolved data are shown offset by 0.05 arbitrary units for laser step of approximately 75 μeV. The position of peak RELS response in the absence of terahertz is seen to drop to near saturation, but continue to drop in intensity slowly over the next microsecond as the terahertz intensity continues to ramp up. 0.5 meV lower in energy, the line is seen to saturate and then rise slowly with increasing field during the next microsecond. The slow trend is reversed within during the 10 ns falling edge of the terahertz pulse suggesting a terahertz electric field-induced red shift of approximately 0.5 meV.

followed by a rise and a rise followed by quenching. The two traces taken at the highest NIR excitation energy show a fall after the terahertz is truncated, with all lower energies showing a rise. For bound excitons, the rise may be due to rapid relaxation of electrons or a field shift or a combination. For free excitons, the change in the spectrum after the pulse should reflect mostly field shifts.

Additionally, ELS taken in the high purity sample at 1.5159 eV at 5.0T, below the brightest D^0X line, exhibits both a sharp rise and fall after the pulse, which can only be suppressed by blocking the terahertz radiation at the source, so it is not attributable to either an electrical or optical transient associated with the YAG laser that illuminates the cutoff switch (Fig. 7.5). The fast rise is best attributed to a field effect and the fast falling edge to dynamics associated with electronic relaxation. However, the exact mechanism is not clear.

7.3 Discussion

7.3.1 Order of interaction strengths

The cause of the brightening/quenching behavior over the range of investigated terahertz frequencies and terahertz field intensities is not well-understood. Several mechanisms may be present which complicate the analysis, including local field effects and strong field effects. This section introduces the physical origins of several of these and discusses their potential relevance to the presented data.

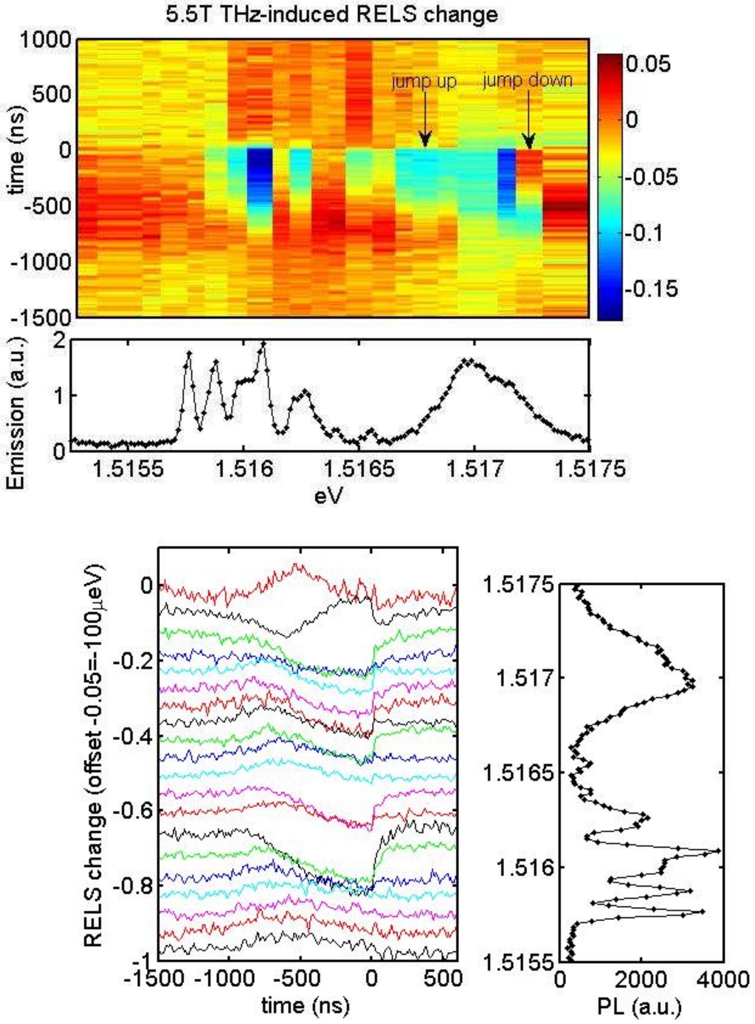

Figure 7.4: Frequency resolved response of sample A421 ($n_d - n_a = 3 \times 10^{13}\mathrm{cm}^{-3}$) at 5.5T (FEL terminal voltage 2.48 MV) to strong terahertz excitation with a right triangle-shaped rising intensity waveform. Below the band edge brightening is observed, followed by quenching. Above the band edge, dimming is seen, followed by a rise. During the 10 ns fall-time of the terahertz excitation emission in the bound exciton region rises sharply, whereas higher energies dim. (Lower) Line cuts of the spectrally resolved data are shown offset by 0.05 arbitrary units for laser step of approximately 100 μeV. No field-induced shift is immediately discernable in the data.

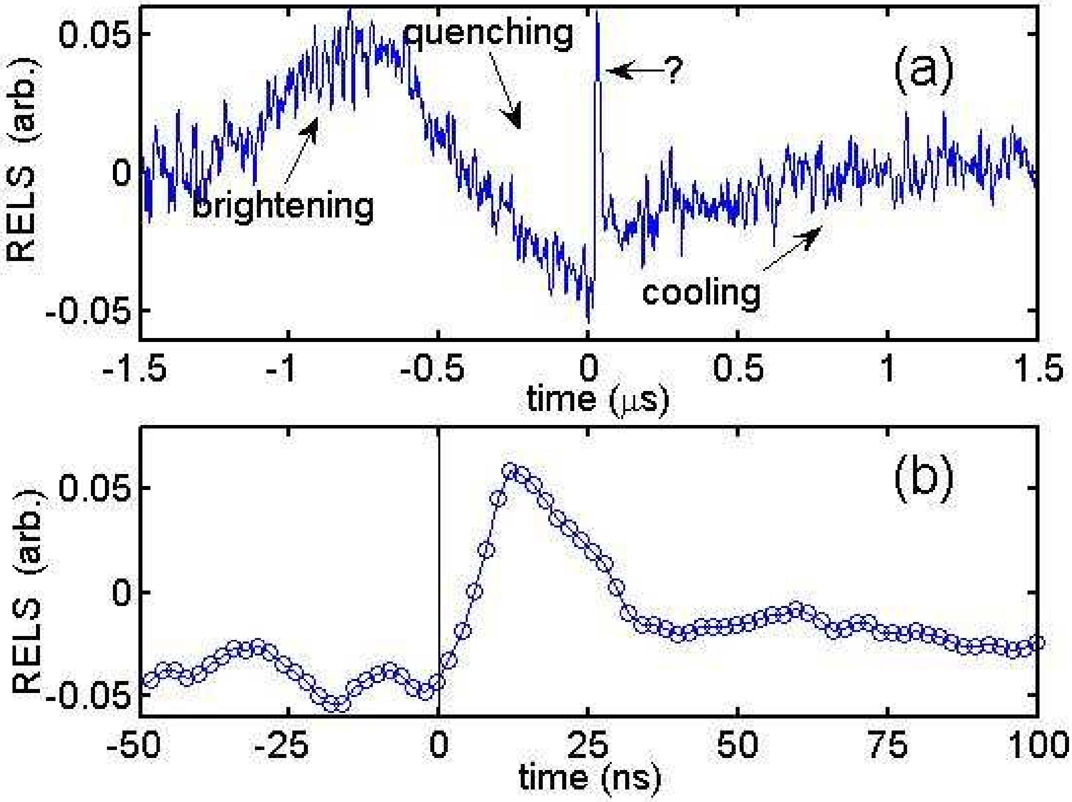

Figure 7.5: (a) ELS response immediately below brightest D^0X resonance. Terahertz response shows competing dynamics of brightening and quenching, as well as transient brightening and quenching after the pulse. (b) Zoom of the indicated region in (a). Detector rise time is 3ns, time resolution is 1 ns, and terahertz fall time is estimated to be less than 10 ns. Transient rise is less than 14 ns. Fall time is less than 20 ns.

Several neighbor interactions change in magnitude when one donor or the other is excited by terahertz radiation and which may effect bound exciton spectra in our samples and are listed below. (As an unfortunate disclaimer, in each of these cases the interaction of two donors is well characterized in the literature as it relates directly to a scaled hydrogen atom problem, but the expected level shift of a donor bound *exciton* to another nearby donor: be it ground state, excited or ionized, is not known. Especially in a strong magnetic field, the several interactions in the three atom problem are nontrivial to solve, given the complexity required to calculated the zero field bound exciton spectrum alone.[35])

7.3.2 Strong field effects

The AC stark shift (see Appendix D), is not a local field effect, but rather the effect of a strong AC field on the effective resonant frequency of an oscillator.

Cole et al.[46] observe a shift of the $2P^+$ state in measurements of coherent $1S$–$2P^+$ population transfer with picosecond terahertz pulses. The shift is to lower transition energy and is attributed to a stark shift. (The comparative energy axis in the published figure is misleading in this sense.) Comparable fields are used in some of the spectral maps taken in which transient brightening is observed. However, transient brightening is observed at magnetic fields both above, below, and on resonance with the $1S$–$2P^-$ transition (3–6.5 T) and is associated with the onset of terahertz radiation rather than the peak terahertz intensity. No consistent shifts are apparent in the spectra consistent with the AC stark effect or Rabi splitting from my analysis of the data.

The AC Stark shift may indeed be present and should be measurable given the sharp spectral lines at high magnetic field, however it may be drown by line broadening.

This leaves local field effects as the most likely explanation for the line shift and broadening. It is puzzling that the off resonant brightening is are not readily observable in the more highly doped samples. A possible explanation may involve the role of acceptor impurities, which is low in the purest samples that also exhibit high mobility and the transient brightening. Admittedly, I don't have a tenable hypothesis involving ionized acceptors. Perhaps the higher free carrier concentrations also play a role.

A second strong field effect is the Franz-Keldysh effect (FKE).[63] In the presence of a DC strong field, optical absorption is allowed below the band gap, and oscillations in absorption appear above the gap. For frequencies and fields for which the ponderomotive force (the average kinetic energy for an electron/hole in an AC field) is less than the energy per photon, the behavior is described by FKE due to the root mean square of the AC field. In the regime where the kinetic energy per particle exceeds the photon energy the behavior is due to the dynamical Franz-Keldysh (DFKE) effect. This is observed for particles with quantized energy levels, such as excitons, with energy spacings similar to the AC frequency, where the AC stark shift competes or adds to the FKE effect.[64] The diversity of behaviors observed are consistent with such competing dynamics however no precise theory is applicable to this case to the knowledge of the author.

In our case, the free exciton internal Rydberg transitions are less than the exciting photon energy, and the binding energy should be reduced by the AC stark effect, resulting in a blue shifting of the interband photon resonance. The bound exciton transitions is sensitive to shifts in both the initial and final state. The final state is a 1S bound electron. Under the AC stark effect, the bound exciton transition should broaden and eventually split with resonant 1S–2P$^-$ excitation due to a normal mode (Rabi) splitting, and either blue shift when the terahertz energy is less than the 1S–2P$^-$ transition or red shift when the terahertz energy exceeds the 1S–2P$^-$ transition. However, the initial state of the bound exciton is sensitive to changes in the band gap. The treatment of the DFKE due to a strong transverse electric field in a strong longitudinal magnetic field is not well known to the authors knowledge. RELS provides an opportunity to investigate such dynamical behavior.

7.3.3 Local field effects

1. *Neutral donor–Ionized donor Coulomb* At typical nearest neighbor distances in these samples, the strongest interaction is expected to be the bare Coulomb interaction of an ionized donor with a neutral impurity,[65]. This results in a more tightly bound electron whose center of charge density is shifted

towards the ionized neighbor. At nonnegligible excitation fractions, an appreciable CB fraction of electrons/ionized donors N_i are generated (though at high magnetic fields the mechanism of excitation is unknown). This is expected to be the main cause of changes to the donor energy spectrum when terahertz is incident at typical dopant densities. It is expected that ionized donor neighbors cause a red shift and broadening of the bound exciton spectrum.[65, 62]

2. *Neutral donor-neutral donor orbital overlap* The orbital overlap of two neutral hydrogen atoms leads to the formation of a molecular bonding orbital. The bond energy depends on the spin and orbital configurations of the two donors but in all cases drops exponentially with distance. The bond strength depends critically on the orbital and spin states of the donors. When considering donor-donor interactions we are no longer able to assume independent sets of energy levels for different spins.[66]

3. *Dipole-dipole interactions (Van der Waals)* Van der Waals (VDW) forces dominate for hydrogenic donor spacings large enough that their orbitals do not significantly overlap ($> 8a_B$). However, VDW attractions and repulsions are typically three to four orders of magnitude down from the scale of the Rydberg in atomic hydrogen and scale strongly with donor separation (r^-3 to r^-7). Dipole interactions between hydrogen molecules (similar to $\mathrm{D}^0\mathrm{X}$) and hydrogen atoms are discussed in e.g. Margenau, pg. 273.[67] Unfortunately,

the asymmetric case relating to a donor and exciton molecule is not directly applicable to the results, which include resonant energy exchange terms allowable only when the atoms are indistinguishable. A further complication comes from the fact that in a magnetic field neutral donor orbits develop a permanent quadrupole moment as they are prolate along the magnetic field axis. Bonding is strongest in the axial direction as orbits are confined in the transverse plan and vice-versa for Van der Waals interactions.

4. *Free electron screening* Screening of the donor charge by free electrons and/or free excitons reduces the attraction of an electron to the donor and is expected to reduce the exciton binding energy.

5. *Collective donor screening* Screening from a collection of donors becomes important at high dopant concentrations near the Mott transitions. Excited donors have a larger radius and screen more effectively. This is similar to saying they are more polarizable at lower energies. At large excitation fractions, enhanced screening is expected result in greater delocalization and lower electron and/or exciton binding for a blue shift of bound exciton energy.[65, 62]

Given the donors spacings typical in our the two strongest terahertz-induced local field effects are likely (1) DC stark shifts from neighbor ionized donors, and (2) screening from incidentally excited free carriers. The two effects are coincident with donor ionization but opposite in the way they effect bound electrons:

free electrons reduce the overall binding energy of neutral donors, while ionized neighbors increase the binding energy of select neighboring donors.

7.3.4 Ionized donors and screening

A blue shift and broadening of bound exciton fluorescence is reported in highly Cl-doped CdS.[65] The theory describing the effect is performed in detail by Hanamura in a concurrent paper.[62] In the experiments performed on CdS, the dopant concentration is varied systematically in a series of samples from well below to above the Mott transition. The peak position and width of the bound exciton spectral peak are noted and the blue shift and broadening are explained in terms of two distinct mechanisms. The blue shift can be thought of as a reduction in binding energy due to increased screening. The widening of the transition and the appearance of the tail to lower energies can be understood to be due to disorder in which the presence of a nearby ionized donor increases the binding energy for the exciton at the donor. The tail is due to the trade off of Stark shift with distance and the Poisson distribution describing the frequency of such spacings. The shift is dominated by the nearest ionized impurity and is strong when that impurity is found to be a short distances from the neutral donor, however such strong shifts have a low occurrence rate due to the large average spacing. Stark shifts are smaller at larger distances, but more probable. Broadening is observed to be a larger effect than the blue shift.

In Hanamura's paper the role of donor excited states is incorporated into the wavevector dependence of the dielectric constant and is shown to reduce the free exciton binding energy. Screening by bound electrons is more efficient in screening the coulomb attraction than free carriers because of the a resonant denominator in the polarizability of the donors at the energies of internal transitions, which are close to the free exciton binding energy. In Fig. 7.1, brightening of the free exciton fluorescence on the high energy side of the free exciton absorption observed to overcome an initial darkening at later times/higher intensities, following an initial reduction at the onset of terahertz excitation. This apparent blue shift of the free exciton energy is observed during the rising edge of the pulse is due to increased screening and polarizability of excited donors at small wavevectors, which more effectively screen excitons.

The effect of screening of by donor bound electrons on the binding energy of the intrinsic or free exciton E_i is given by Hanamura[62] and Kukimoto[65] as:

$$E_i = \frac{E_{i0}}{\left(1 + \frac{\epsilon_1 \omega}{\epsilon_0}(n_d - n_a)\right)^2} \tag{7.55}$$

$$\sim E_{i0}\left(1 - \frac{2\epsilon_1(\omega)}{\epsilon_0}(n_d - n_a)\right) \tag{7.56}$$

ϵ_0 is the relative dielectric constant in the notation of Hanamura and $\epsilon_1(\omega)$ is contribution of the donor polarizability to the dielectric constant at frequency $omega = E_{i0}/\hbar$, which is comprised of a primary contribution from the Lyman-α transition with oscillator strength of 0.416 and smaller contributions from other transitions to excited states including the continuum transition, or else an approximate two level model in which the oscillator strength of bound transitions is accumulated at the ionization energy. The calculations of Hanamura do not take into account matrix elements arising from Balmer transitions involving $n \geq 2$ and higher excited states. With some donors in the 2P state, resonant contributions to the polarizability on either side of the free exciton energy would both contribute to a reducing of the free exciton binding energy, in agreement with the observed reduction in free exciton binding.

Excitable longer range (Van der Waals) interactions

In the range of atomic spacings used in our experiments, the overlap of atomic orbitals between neighboring donors is small, as evidence by the the narrow ensemble linewidth (Fig. 2.3. In this range of separations, the next order of interaction comes from the Van der Waals force.

For similar or dissimilar atoms in a spherically symmetric ground state, there is no permanent dipole and no first order correction to the energy of the system. There is however an attractive force which arises between two such atoms due to mutually induced dipoles arising via nonzero polarizability. This is the Van der Waals attraction and is typified by a $1/r^6$ dependence.[67] In a magnetic field, previously spherical atoms become cigar-shaped due to radial confinement in the plane perpendicular to the magnetic field and obtain permanent quadrupole moments. For such, the Van der Waals energy scales as $1/r^5$.[66]

Notably, for two identical atoms and one is excited and the other is not, the symmetrization of a the wavefunction allows for a condition of “resonance” with a nonzero first order correction of the pair energy, and a longer range $1/r^3$ coupling, which can be either attractive or repulsive depending on the difference in orbital momentum of the two states.[67, 68]

Resonant Van der Waals interactions have been observed in collections of nearly frozen Rb Rydberg gases.[17] In these studies it is important for the thermal energy of the gas to be less than the Van der Waals interaction. The resonant Van der Waals interaction between Rydberg atoms excited to two different levels is manifest as a linewidth broadening. Highly excited states are used to obtain large dipoles. For comparison, in the case of hydrogenic donors the gas is completely frozen in the lattice and highly excited states are certainly cut off above principle quantum number $n = 5$ due to the higher sample density, though large dipoles are a given in neutral donor ensembles even at low Rydberg numbers.

Consider two ground state donors separated such that orbital overlap is small. When one of the donors is excited to the $2P^-$ state, the scaling of the dipole coupling between them changes from r^{-6} to r^{-3}. The coupling constant will vary with the orientation of the vector between them relative to the magnetic field axis as well as the distance, it will however dominate at long distances. At shorter distances, however, the forces may become comparable.

The change in the exciton binding energy is likely nontrivially related to changes in the donor bound electron binding energy due to Van der Waal’s coupling and configuration interaction calculation is probably necessary to determine the proper wavefunctions for the donor bound exciton in the magnetic field. If the bound electron and bound exciton energies are correlated (or anticorrelated), this may explain why at low dopant densities when spacings are large, a large change in the exciton binding energy is observed as donors are excited. At higher densities, a nearest donor may be on average close enough that the change in scaling is not large when a neighbor donor is excited, but the contributions of further donors are screened. This is, admittedly, speculation.

Potential energy curves versus distance for two hydrogen atoms have been studied in various regimes of magnetic field strength applicable to these experiments for both atoms in the ground state as well as for one atom in the lowest excited state including variations of angle between the nuclei relative to the magnetic field.[66, 69] Although the asymmetric combination of one excited and one ground state eventually becomes the overall ground state at fields 10x higher than are used in our experiments, the Van der Waals forces in the most applicable case seem to produce a potential minimum in the binding energy at distances $r \sim 8a_0$ on the order of 10^{-3} Rydbergs.

7.4 Related phenomena and possibilities for future research

In donor ensembles excited state interactions may be observable given the narrow linewidths of the donor bound exciton transition, although I cannot conclude from that data that that photoexcited resonant Van der Waals interactions are responsible for the lineshift/broadening of the exciton transition. The first reason is that the expected shift an observable bound exciton transition due to small perturbations in the neutral donor binding energy from neighbor interactions is not simply estimable and would require at a minimum an intensive configuration interaction calculation. The second is that the effects of donor ionization will dominate and would be difficult to distinguish spectrally.

On the other hand, the apparent availability of excitable neighbor interactions in the weakly coupled limit opens doors for interesting possibilities. Liberman[69] has predicted a superfluid H fluid state indicative of Bose-Einstein condensation at high magnetic fields, such as could be observed in excitons. Bose-Einstein condensation of exciton-polaritons is a active field of research. Although the donor lifetime is longer than exictons, which may be attractive, unfortunately the mass donor mass is *very* large.

The possibility exists, however, for using the state of the bound electron to dynamically modify the Coulomb attraction between free excitons.

Likewise, donor ensembles below the Mott transition may be photoexcited to form an impurity band. Photoexcitation of the impurity band Mott transition has been observed in the insulator $Y_2(SiO_4)0 : Ce^{3+}$.[70] In the case GaAs donors, with a π pulse, the electrons will become locally entangled. If the photoexcited ensemble goes well above the Mott transition massive nonlocal entanglement may be possible, which may be attractive for adiabatic quantum computing applications.

The observation here of photoinduced broadening of the ensemble linewidth is suggestive that observation of the dipole blockade in a collection of neutral donor may be possible. In this experiment, a countable number of donors falls within the focal spot. When one or more is excited to a large Bohr radius it may prevent others from being excited.[71] (The dipole blockade finds application in certain quantum computing schemes with trapped ions.[72])

Additional investigations of familiar strong field effects such as Rabi splitting/AC Stark effect and the dynamical Franz-Keldysh effect may also be illuminating.

Chapter 8

Conclusions

The primary results of this research are as follows.

- Resonant elastic light scattering (RELS) from the donor bound exciton transition D^0X is reduced when the donor is excited. This enables detection of changes in the ground state population of an ensemble of shallow donors. RELS readout at the ionized donor bound exciton transition is also observed.
- RELS readout is a new technique sensitive to the internal orbital dynamics of *bound* charges, and thus compliments photoconductivity spectroscopy, which measures *free* charge.
- RELS detection does not requiring electrical contacts or DC electric fields, which may be disadvantageous, such as when an electric field changes the quantity being measured. We have also demonstrated resonance fluorescence detection of both the bound electron ground state population via the neutral

donor bound exciton resonance (D^0X), and the conduction band population via the ionized donor bound exciton resonance (D^+X).

- Dynamic enhancement in the RELS intensity after the NIR laser is switched on is observed and can be attributed to a surface charging effect where excitons generated in the depletion region separated to screen the surface depletion field. This effect is visible in samples without a doped capping layer to compensate the surface charge density due to surface defects. It is also observed in samples grown on a semi-insulating substrate resulting in a large depletion region at the buried epitaxial interface.

- Reduction of RELS intensity after the NIR readout laser is switch on is not observed. A reduction is expected if shelving of donors into higher states by TES/Auger transitions competes with relaxation out of the donor bound exciton state to the neutral donor ground state. NIR intensity is not observed to limit the efficiency of RELS readout below ~ 10 mW/cm^2 excitation intensity.

- Continuous readout with the NIR readout laser has a detrimental affects on observed donor excited state lifetimes which is attributed to creation of free excitons.

- After resonant excitation of the hydrogenic donor 1S–2P$^-$ bound-to-bound transition, the return of quenched RELS is dominated by a power law type recovery. This result is unexpected under conditions when the photoexcited population of free electrons including high magnetic field, short pulse resonant excitation, small excitation fraction, and low NIR readout intensity, but is observed nonetheless, in all but the weakest levels of excitation, where a power law is indistinguishable from an single exponential. For dopant densities greater than $10^{14}/\text{cm}^3$, nonexponential decay is observed under all conditions.

- The maximum lifetime of the RELS recovery is limited by the $2P^-$ lifetime, which is in turn limited by various experimental factors including dopant density, temperature, and free electron concentration and is measured under the most ideal conditions to be approximately 250 ns. In one sample the average lifetime is measured to be more than 500 ns.
- In very low doped samples transient brightening of the RELS signal when the NIR laser is positioned near, but off resonance with a D^0X transition. This is attributed to a blue shift and broadening of the D0X transition in the presence of excited and ionized neighbor donors indicating that donor-donor interactions are important in samples with dopant densities as low of $3 \times 10^{13}/\text{cm}^3$. Additionally, a blue shift in the free exciton peak indicates efficient screening of the electron-hole Coulomb attraction by a combination of ground, excited and free electrons.
- The observed photo-excitable interactions between distant donors open in-

teresting possibilities for the study of atomic physics in the solid state, but will hinder the use of donors as two-level qubits in the proposed quantum computing architecture.[10]

The following observed phenomena are to my knowledge without satisfactorily explanation and are in need better theoretical perspective.

- It is expected that when the 1S–2P$^-$ transition energy falls below the 2P$^-$–CB transition that ionization of donor-bound electrons by absorption of a second photon should be suppressed. However, in both the experiments reported by Kalkaman, et al. [13] and in our experiments, measurable numbers of free carriers were generated during short pulse (1–3 ns), resonant excitation of the 1S-2P$^-$ transition at fields in the range 4.5–6.5 T, even when excitation is weak enough to only excite a ≤ 0.05 of the neutral donor population. It is the ubiquitous presence of the free carriers which is attribute to the fast recovery of RELS at short times after a truncated resonant THz pulse.

Bibliography

[1] M. Doty. *Coherent Manipulations of Ensemble of Hydrogenic Donors in GaAs.* PhD thesis, University of California, Santa Barbara, 2004.

[2] D. G. Allen, M. S. Sherwin, and C. R. Stanley. Optically detected measurement of the ground-state population of an ensemble of neutral donors in gaas. *Phys. Rev. B*, 72:035302, 2005.

[3]

[4] J. Burghoorn, A. van Klarenbosch, T. O. Klaassen, W. TH. Wenckeach, and C. T. Foxon. A fir photo-hall study of the 1s-2p-1 shallow donor transition in n-gaas.

[5] D. D. Awschalom, D. Loss, and N. Samarth, editors. *Semiconductor spintronics and quantum computation.* Nanoscience and technology. Springer, 2002.

[6] C. H. Bennett and D. P. DiVincenzo. Quantum information and computation. *Nature*, 404(6775):247, 2000.

[7] A.M. Steane. Quantum computing. *Rept.Prog.Phys.*, 61:117, 1998.

[8] C. E. Wieman, D. E. Pritchard, and D. J. Wineland. Atom cooling, trapping, and quantum manipulation. *Rev. Mod. Phys.*, 71.

[9] D. J. Wineland, C. R. Monreo, W. M. Itano, B. E. King, D. Liebfried, D. M. Meekhof, C. J Myatt, and C. S. Wood. Experimental primer on the trapped ion quantum computer. *Fortschritte de Physik*, 46:363–390, 1998.

[10] M.S. Sherwin, A. Imamoglu, and T. Montroy. Quantum computation with quantum dots and terahertz cavity quantum electrodynamics. *Phys. Rev. A*, 60(5):3508–3514, November 1999.

[11] F. Tremblay, M. Pepper, D. Ritchie, D. C. Peacock, J. E. F. Frost, and G. A. C. Jones. Negative magnetoresistance in the variable-hopping-range regime of n-gaas. *Phys. Rev. B*, 39:8059, 1989.

[12] P. C. M. Planken, P. C. van Son, J. V. Hovenier, T. O. Klaassen, W. Th. Wenckebach, B. N. Murdin, and G. M. H. Knippels. Far-infrared picosecond time-resolved measurement of the free-induction decay in gaas:si. *Phs. Rev. B*, 51(15):9643, 1995.

[13] A. J. Kalkman, H. P. M. Pellemans, T. O. Klaassen, and W. Th. Wenckebach. Far-infrared pump-probe measurement of the lifetime of the $2p^-$ shallow donor level in n-gaas. *Int. Journ. of Infrared and Millimeter Waves*, 17(3):569, 1996.

[14] W. Nagourney, J. Sandberg, and H. Dehmelt. Shelved optical electron amplifier: Observation of quantum jumps. *Phys. Rev. Lett.*, 56(26):2797–2799, 1986.

[15] J. C. Bergquist, R. G. Hulet, W. M. Itano, and D. J. Wineland. Observation of quantum jumps in a single atom. *Phys. Rev. Lett.*, 57:1699–1702, 1986.

[16] Th. Sauter, W. Neuhauser, R. Blatt, and P. E. Toschek. Observation of quantum jumps. *Phys. Rev. Lett.*, 57:1696, 1986.

[17] K. Afrousheh, P. Bohlouli-Zanjani, D. Vagale, A. Mugford, M. Fedorov, and J. D. D. Martin. Spectroscopic observation of resonant electric dipole-dipole interactions between cold rydberg atoms. *Phys. Rev. Lett.*, 93:233001, 2004.

[18] G. Kioseoglou, H. D. Cheong, T. Yeo, H. A. Nickel, A. Petrou, B. D. McCombe, A. Yu. Sivachenko, A. B. Dzyubenko, and W. Schaff. Reflectance-based optically detected resonance studies of neutral and negatively charged donors in gaas/alxga1-xas quantum wells. *Phys. Rev. B*, 61:5556, 2000.

[19] R. J. Stone, J. G. Michels, D. Kinder, C. C. Chang, R. J. Nichols, A. M. Fox, and J. S. Roberts. Optical studies of localized excitons in symmetric coupled quantum wells. *Superlattices Microst.*, 21:597, 1997.

[20] J. Cerne, J. Kono, M. Su, and M. S. Sherwin. Photo-thermal transitions of magneto-excitons in quantum wells. *Phys. Rev. B*, 66:205301, 2002.

[21] B. N. Murdin, A. R. Hollingworth, J. A. Barker, D. G. Clarke, P. C. Findlay, C. R. Pidgeon, J.-P. R. Wells, I. V. Bradley, S. Malik, and R. Murray. Double-resonance spectroscopy of inas/gaas self-assembled quantum dots. *Phys. Rev. B*, 62:R7755, 2000.

[22] S. Strauf, P. Michler, M. Klude, D. Hommel, G. Bacher, and A. Forchel. Quantum optical studies on individual acceptor bound excitons in a semiconductor. *Phys. Rev. Lett.*, 89:177403, 2002.

[23] A. Gruber, A. Dräbenstedt, C. Tietz, L. Fleury, J. Wrachtrup, and C. von Borczyskowski. Nitrogen-vacancy center in diamond: Model of the electronic structure and associated dynamics. *Science*, 276:2012, 1997.

[24] F. Jelezko, T. Gaebel, I. Popa, A. Gruber, and J. Wrachtrup. Energy levels and decoherence properties of single electron and nuclear spins in a defect center in diamond. *Phys. Rev. Lett.*, 92:076401, 2004.

[25] R. J. Epstein, F. M. Mendoza, Y. K. Kato, and D. D. Awschalom. Anisotropic interactions of a single spin and dark-spin spectroscopy in diamond. 1:94–98, 2005.

[26] Yanwen Wu, E. D. Kim, Xiaodong Xu, Jun Cheng, D. G. Steel, A. S. Bracker, D. Gammon, Sophia Economou, and L. J. Sham. Selective optical control of electron spin coherence in singly charged quantum dots via oscillating dark and bright states. *Phys. Rev. Lett*, page 097402, 99.

[27] Xiaodong Xu, Yanwen Wu, Bo Sun, Qiong Huang, Jun Cheng, D.G. Steel, A. S. Bracker, D. Gammon, C. Emary, and L. J. Sham. Fast spin state initialization in a singly-charged quantum dot. *Phys. Rev. Lett.*, 99:097401, 2007.

[28] Xiaodong Xu, Bo Sun, Paul R. Berman, Duncan G. Steel, Allan Bracker, Dan Gammon, and Lu J. Sham. Coherent optical spectroscopy of a strongly driven quantum dot. *Science*, 317.

[29] J. Berezovsky, M. H. Mikkelsen, O. Gywat, N. G. Stoltz, L. A. Coldren, and D. D. Awschalom. Nondestructive optical measurements of a single electron spin in a quantum dot. *Science*, 314:1916, 2006.

[30] Walter Kohn. Shallow impurity states in silicon and germanium. *Solid State Physics: Advances in Research and Applications*, 5:257–320, 1957.

[31] G.E. Stillman, C.M. Wolfe, and J.O. Dimmock. Magnetospectroscopy of shallow donors in gaas. *Solid State Communications*, 7:921–925, 1969.

[32] B. J. Skromme, R. Bhat, H. M. Cox, and E. Colas. Identification of donors in gaas by resonantly excited high-field magnetospectroscopy. *IEEE J. Quant. Elec.*, 25:1035–1045, 1989.

[33] R.J. Heron, R.A. Lewis, P.E. Simmonds, R.P. Starrett, A.V. Skougarevsky, R.G. Clark, and C.R. Stanley. Central-cell corrections for si and s in gaas in a strong magnetic field. *Journal of Applied Physics*, 85(2):893, 1999.

[34] H. R. Fetterman, D. M. Larsen, G. E. Stillman, and P. E. Tannenwald. Field-dependent central-cell corrections in gaas by laser spectroscopy. *Phys. Rev. Lett.*, 26(16):975, 1971.

[35] V. A. Karasyuk, D. G. S. Beckett, M. K. Nissen, A. Villemaire, T. W. Steiner, and M. L. W. Thewalt. *Phys. Rev. B*, 49:16381, 1994.

[36] J. Simola and J. Virtarno. Energy levels of hydrogen atoms in a strong magnetic field. *J Phys. B*, 11:3309–3322, 1978.

[37] W. Rösner, G. Wunner, H. Herold, and H. Ruder. Hydrogen atoms in arbitrary magnetic fields: I. energy levels and wavefunctions. *J. Phys. B*, 17:29–52, 1984.

[38] H. Forster, W. Strupat, W Rösner, G. Wunner, H. Ruder, and H. Herold. Hydrogen atoms in arbitrary magnetic fields: Ii. bound-bound transitions. *J. Phys. B*, 17:1301–1319, 1984.

[39] R. H. Garstang. Atoms in high magnetic fields (white dwarfs). *Rep. Prog. Phys.*, 40:105–154, 1977.

[40] P.C. Makado and N.C. McGill. Energy levels of a neutral hydrogen-like system in a constant magnetic field of arbitrary strength. *J. Phys. C: Solid State Phys.*, 19:873–885, 1986.

[41] A. C. Labrujere, T. O. Klassen, W. Th. Wenckebach, and C. T. Foxon. Fir

spectroscopy on shallow donor states in gaas:si. *Int. J. Infr Millimeter Waves*, 9:1057, 1988.

[42] R. O. Mueller and V. W. Hughes. *Proc. Nat. Acad. Sci.*, 71:3287, 1974.

[43] V.G. Golubev, V.I. Ivanov-Omskii, I.G. Minervin, A.V. Osutin, and D.G. Polyakov. *Sov. Phys. JETP*, 61:1214, 1985.

[44] D. M. Larsen. Inhomogeneous broadening of the lyman-series absorbtion of simple hydrogenic donors. *Phys. Rev. B*, 13(4):1681, 1976.

[45] C. R. Stanley and et al. Electrical characterization of molecular beam epitaxial gaas with peak electron mobilities up to approximately 4e5cm$(\mathrm{vs})^{-1}$.

[46] B.E. Cole, J.B. Williams, B.T. King, M.S. Sherwin, and C.R. Stanley. Coherent manipulations of semiconductor quantum bits with terahertz radiation. *Nature*, 410:60, March 2001.

[47] S. G. Carter. *Terahertz electro-optic effects in (In)GaAs quantum wells.* PhD thesis, University of California, Santa Barbara, 2005.

[48] E. Finkman, M. D. Sturge, and R. Bhat. Oscillator strenght, lifetime and degeneracy of resonantly excited bound excitons in gaas. *J. Lumin.*, 35:235, 1986.

[49] S. Charbonneau, T. Steiner, M. L. W. Thewalt, Emil S. Koteles, J. Y. Chi,

and B. Elman. Optical investigation of biexcitons and bound excitons in gaas quantum wells. *Phys. Rev. B Rapid Comms.*, 38:R3583, 1988.

[50] S. Schmidt and R.G. Ulbrich. *23rd Int. Conf. on the Phys. of Semiconductors, Vol. 4*, pages 2741–2744, 1996.

[51] J. Cerne. *Optical studies of quantum-confined carries driven by intense far-infrared radiation.* PhD thesis, University of California, Santa Barbara, 2005.

[52] Frank A. Hegmann and Mark S. Sherwin. Generation of picosecond far-infrared pulses using laser-activated semiconductor reflection switches. In *International conference on millimeter and submillimeter waves and applications III.* SPIE, August 1996.

[53] G. R. Allan, A. Black, C. R. Pidgeon, E. Gornik, W. Seidenbusch, and P. Colter. Impurity and landau-level electron lifetimes in n-type gaas. *Phys. Rev. B*, 31:3560, 1985.

[54] G. Ascarelli and S Rodriquez. Recombination of electrons and donors in n-type germanium. *Phys. Rev.*, 124:1321, 1961.

[55] J. Burghoorn, T. O. Klaassen, and W. T. Wenchebach. The dynamics of shallow donor ionization in n-gaas studied with sub-ns fir-induced photoconductivity. *Semicond. Sci. Tech.*, 9:30–34, 1994.

[56] C. Piermarocchi, Pochung Chen, L. J. Sham, and D. G. Steel. Optical rkky

interaction between charged semiconductor quantum dots. *Phys. Rev. Lett.*, 89:167402, 2002.

[57] C. Piermarocchi and G. F. Quinteiro. Coherent optical control of spin-spin interaction in doped semiconductors. *Phys. Rev. B*, 70:235210, 2004.

[58] G. L. J. A. Rikken, P. Wyder, J. M. Chamberlain, G. A Toombs, and L. L. Taylor. Time-resolved far-infrared magnetospectroscopy of hydrogen-like impurities in semiconductors. *Phys. Rev. B*, 38:2002–2011, 1988.

[59] D. Bimberg, H. Münzel, A. Steckenborm, and J. Christen. Kinetics of relaxation and recombination of nonequilibrium carriers in gaas: carrier capture by impurities. *Phys. Rev. B*, 31:7788, 1985.

[60] O. Z. Alekperov. Capture of carriers by screened charged centres and low-temperature shallow-impurity electric field breakdown in semiconductors. *J. Phys.: Condens. Matter*, 10:8517–8521, 1998.

[61] H. Kobori and T. Ohyama. Bound to unbound state transition of hydrogenic donors in semiconductors with a static screened coulomb potential–a trial on a variational calculation. *J. Phys. Chem. Solids*, 58:2065, 1997.

[62] Eiichi Hanamura. Screening and stark effects due to impurities on excitons in semiconductors. *J. Phys. Soc. Japan*, 28:120, 1970.

[63] L. V. Keldysh. The effect of a strong electric field on the optical properties of insulating crystals. *Sov. Phys. JETP*, 34:788, 1958.

[64] K. B. Nordstrom, K. Johnsen, S. J. Allen, A.-P. Jauho, B. Birnir, J. Kono, T. Noda, H. Akiyama, and H. Sakaki. Excitonic dynamical franz-keldysh effect. *Phys. Rev. Lett.*, 81:457–460, 1998.

[65] H. Kukimoto, S. Shionoya, and S. Toyotomi. Screening and stark effects due to impurities on excitons in cds. *J. Phys. Soc. Japan*, 28:110–119, 1970.

[66] T. Detmer, P. Schmelcher, F. K. Diakonos, and L. S. Cederbaum. Hydrogen molecule in magnetic fields: The ground states of the σ manifold of the parallel configuration. *Phys. Rev. A*, 56:1825, 1997.

[67] H. Margenau. Van der waals forces. *Rev. Mod. Phys.*, 11.

[68] C. Cohen-Tannoudji, B. Diu, and F. Laloë. *Quantum Mechanics.* Wiley and Sons, 1977.

[69] M. A. Liberman and A. V. Petrov. Terms of a hydrogen molecule in a high magnetic field. *Physica Scripta*, 57:573–580, 1998.

[70] J. Choi, S. A. Basun, L. Lu, W. M. Yen, and U. Happek. Excited state impurity band conductivity in $y_2(si0_4)0 : ce^{3+}$. *J. Lumin*, 83-84:461–464, 1999.

[71] T. C. Liebisch, A. Reinhard, P. R Berman, and G. Raithel. Atom counting statistics in ensembles of interacting rydberg atoms. *Phys. Rev. Lett.*, 95:253002–4, 2005.

[72] D. Jaksch, J. I. Cirac, P. Zoller, S. L. Rolston, R. Cote, and M. D. Lukin. Fast quantum gates for nuetral atoms. *Phys. Rev. Lett.*, 85:2208, 2000.

[73] Robert W. Boyd. *Nonlinear Optics.* Academic Press, 1992.

[74] Wojciech Hubert Zurek. Decoherence, einselection, and the origins of the classical. *Rev. Mod. Phys.*, 75:715–775, 2003.

[75] C. R. Pidgeon, A. Vass, G. R. Allan, W. Prettl, and L. Eaves. Nonlinear far-infrared magnetoabsorption and optically detected magnetoimpurity effect in n-gaas. *Phys. Rev. Lett.*, 50:1309–1312, 1983.

[76] V. S. Letokhov and V. P. CHebotayev. *Nonlinear Laser Spectroscopy*, volume 4 of *Springer Series in Optical Sciences.* Springer-Verlag, 1977.

[77] R. Vion, A. Assime, A. Cottet, P. Joyez, H. Pothier, C. Urbina, D. Esteve, and M. H. Devoret. Rabi oscillations, ramsey fringes, and spin echoes in an electrical circuit. *Fortschr. Phys.*, 51:462–468, 2003.

[78] H. Kogelnik and T. Li. Laser beams and resonators. *Appl. Opt.*, 5:1550, 1966.

Appendix A

Samples

Fluorescence recovery was measured in samples provided by Prof. Collin Stanley of the University of Glasgow.

Table A.1 describes properties of the samples as measured by the Glasgow group. Included are the sample name, type of substrate: un-GaAs (undoped GaAs) or SI-GaAs (semi-insulating GaAs), epilayer thickness, thickness of capping layer with doped with Si at $1 \times 10^{18}/\mathrm{cm}^3$, carrier concentration $N_d - N_a$ from Hall measurements $[cm^{-3}]$, and 77 K mobility μ_{77K} $[cmV/s]$.

Samples for photoconductivity measurements were also prepared from samples provided by the Glasgow group according the procedure described in the appendix of ref. [1].

Several of the samples had features which are worth noting. For completeness and reference I list them here.

Sample	Subs	Epilayer [μm]	Cap [nm]	n$_{77K}(N_d - N_a)$	μ_{77K}
A421	SI-GaAs	25	20	$\sim 3.0 \times 10^{13}$	220,000
A422	SI-GaAs	25	20	$\sim 6.0 \times 10^{13}$	228,000
B48	un-GaAs	15	–	7.6×10^{13}	203,000
B763	un-GaAs	16	10	1.3×10^{14}	129,000
B671	un-GaAs	15	20	3×10^{14}	120,000

Table A.1: Table of growth parameters and dopant densities for optical samples measured in a magnetic field.

Sample	Subs	Epilayer [μm]	Cap [nm]	n$_{77K}(N_d - N_a)$	μ_{77K}
B434	un-GaAs	15	20	$\sim 2.8 \times 10^{14}$	138,000
A415	SI-GaAs	25	20	3×10^{13}	220,000
B763	un-GaAs	16	10	1.3×10^{14}	129,000
B671	un-GaAs	15	20	3×10^{14}	120,000

Table A.2: Table of growth parameters and dopant densities for photoconductivity samples measured in a magnetic field.

- Sample B48 on one occasion (August 2005) was observed to have fluorescence recovery times at 4–5 T with long lifetime components in the range 500-1000 ns. This experimental result was not repeated in other samples. The short lifetime component is observed to decrease in magnitude relative to the long lifetime component. No surface charging is observed in sample B48 (April–May 2007) Complete quenching of D^0X RELS was observed in sample B48 at zero magnetic field (April–May 2007), attributed due to an absorbing substrate which reduces background scatter.

- The substrate of sample A422 is transparent at the D^0X transition due to the semi-insulating substrate so that a strong background of scattered light is observed. Sample A422 is observed to transition from nonexponential to single exponential decay at low NIR intensities and very low THz pump powers (February 2008).

- Sample A421 exhibits bright photoluminescence with low acceptor compensation apparent in the spectra. Sample A421 is observed to have a large >100%) increase in RELS when the sample is illuminated, due to a change in the depletion length. (April 2007) Sample A421 exhibits strong changes (positive and negative) in response to terahertz light are various NIR excitation wavelengths. These effects are attributed to either a stark shift, normal mode splitting or local field effect due to excited donors shifting neighboring donors donor bound exciton lines. Other samples exhibit these effects only minimally. (July-September 2007)

- Sample B434 is observed to have excellent photoconductivity, revealing a prevalence of Ge dopants and a minority of Si dopants. (November 2006; April 2007)
- Sample B761, which is the highest doped, exhibits fast nonexponential decay down to the lowest measurable levels of NIR and terahertz intensity (January 2008).
- Photoconductivity sample A415 was approximately short at low temperature (90 ω) and had large leads which were probably uselessly widely spaced (1–2mm).
- Photoconductivity sample B763 showed peaks from what are attributed to be Si and Ge in approximately equal quantities. (January 2008).
- Photoconductivity sample A422 was low resistance 1 kΩ at low temperature, the second time it was used. (Feburary 2008).

Appendix B

Quantifying Quantum Dynamics

This Appendix is an introduction to the benchmark properties of a two-level system aimed at the novice experimentalist.

B.1 Relaxation, dephasing, decoherence, and measurement

In the spin physics community, the terms longitudinal relaxation, transverse relaxation, and dephasing are used to clothe quantum mechanical state evolution in semiclassical language. Standard abbreviations are used for the relevant time scales, respectively: T_1, T_2, and $T2^*$.

B.1.1 $\mathbf{T}_1$

T_1 is the time constant describing the exponential decay of a quantum state from an excited level to a lower one (1/decay rate). This is also called the population relaxation time or longitudinal relaxation, which refers to a spin relaxing or flipping along a longitudinal quantization axis defined by a magnetic field.

In a classical analogy, an ensemble of mechanical oscillators each of slightly different frequency (energy) can be excited by an impulse. The average displacement of the oscillators varies sinusoidally in time, but the amplitude of the average displacement will decay in time as the oscillators lose energy to the environment. The decay time is just the inverse of the energy loss rate of the population and is called T_1.

B.1.2 $\mathbf{T}_2^*$

The time evolution of an eigenstate ψ_n of a time-independent hamiltonian H_0 with eigenenergy E_n (in the Schrödinger picture) is given by:

$$\Psi(\boldsymbol{x}, t) = e^{-iE_n t/\hbar}\psi_n(\boldsymbol{x}) \tag{B.57}$$

The exponential term $\exp(-iE_n t/\hbar)$ multiplies the wavefunction, describing radial rate $\omega = E_n/\hbar$ at which a stationary state acquires phase. The rate of phase evolution is dependent on the energy of the state. Like clock with a hand that varies its speed with altitude, the phase of a quantum mechanical state keeps track of what the energy of a quantum mechanical system has been. Two systems initialized into states of slightly different energy will acquire phase at different rates. The two states will get π out of phase in a time $\pi\hbar/|E_1 - E_2|$, but will eventually come back into phase. For an ensemble with a Gaussian distribution of energies of full width at half maximum (FWHM) ΔE, the average phase following an impulse initialization decays in a time T_2^*.

$$\frac{1}{T_2^*} = \frac{2\Delta E}{\hbar} = \frac{1}{\Delta\omega} \tag{B.58}$$

Here $\Delta\omega$ is the dephasing rate, a half-width at half maximum quantity measured in in radians/sec (ref. [73], pg. 265).

For linear the spectroscopy the following relation is more useful

$$T_2^* = \frac{1}{\pi\Delta f}. \tag{B.59}$$

Δf is the FWHM spectral linewidth in Hz.

In the classical analogy we imagine an array of manufactured mechanical oscillators all set to motion by an impulse. The mean square displacement of the oscillators decays in a time T_1, corresponding to the energy relaxation rate, which depends on the quality factor of the device. But the average displacement decays in a time T_2^*, which depends on how similar the rates of oscillation are from device to device. Thus T_1 is an intrinsic property of an oscillator (or quantum transition), but T_2^* is an ensemble property, a measure of homogeneity between oscillators (or a set of quantum systems).

Quantum mechanical systems may be initialized into a superposition of states, in which a the state Ψ is described as

$$\Psi = a|\psi_0\rangle + b|\psi_1\rangle, \tag{B.60}$$

subject to the constraint $|a|^2 + |b|^2 = 1$.

This property of superposition allows an arbitrary phase to be present between the portion of the wavefunction in either of the eigenstates (with any meaningless overall phase removed).

$$\Psi = a|\psi_0\rangle + \sqrt{1-|a|^2}e^{i\phi}|\psi_1\rangle. \tag{B.61}$$

The two state quantum mechanical system resides in a two dimensional space spanned by the real numbers a and ϕ. We can imagine mapping the state onto a the surface of a sphere, where the projection of the polar angle on the z-axis represents the fraction of the wavefunction in the ground or excited state and the azimuthal angle gives the relative phase difference between those two parts of the wavefunction.

$$\begin{aligned} \Psi &= \sin(\pi a/2)|\psi_0\rangle + \cos(\pi a/2)e^{i\phi}|\psi_1\rangle && \text{(B.62)} \\ &= \sin(\theta)|\psi_0\rangle + \cos(\theta)e^{i\phi}|\psi_1\rangle && \text{(B.63)} \\ & && \text{(B.64)} \end{aligned}$$

Here $0 \leq \theta \leq \pi$ and $0 \leq \phi \leq 2\pi$.

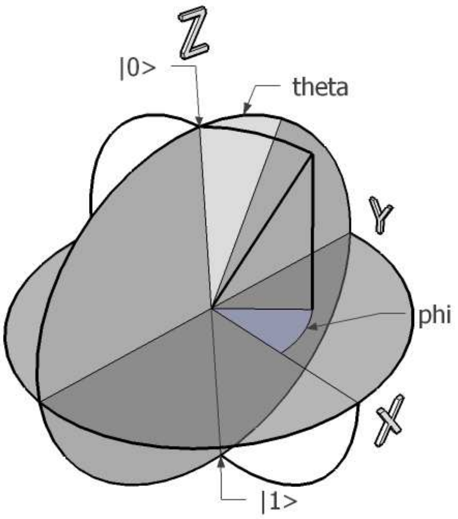

[!hbt]

Figure B.1: schematic of the Bloch sphere representation showing the polar angle θ and azimuthal angle ϕ. Regular coordinate axes are labeled as well as positions of the two eigenstates $|0\rangle$ at the North pole and $|1\rangle$ at the South pole.

This is known as the Bloch sphere representation and is helpful in visualizing the evolution of a two state system (Fig. B.1).

B.1.3 T_2

In quantum mechanical systems there is another quantity with which we must concern ourselves — *decoherence.* Unlike dephasing, which is an ensemble property, decoherence is a strictly quantum mechanical property and can be thought of as the loss of observability of phase certainty, or coherence–same thing–to the environment. This measure is given the name T_2 and can be measured for a single quantum system or for an ensemble in which inhomogeneous broadening is sufficiently small. The cause of decoherence is the expansion of the Hilbert space via entanglements with other degrees of freedom in the environment.[74] Each environmental interaction adds a dimension of entanglement with the environment. The expansion of the Hilbert space via environmental interactions creates an environmentally-induced superstate. In most cases these extraneous degrees of freedom evolve outside the control of the experiment and are not observable, and so the visibility of the quantum coherence or the magnitude of the projection of the state within a given subset of the Hilbert space, goes down. Decoherence gives the appearance of collapse of the wavefunction due to effectively irreversible state evolution outside the observable basis, or the original two-state Hilbert space. Decoherence is a dynamical process, but operates under an assumption similar to the second law of thermodynamics, which is just a statement about probability, however it guides our intuition about dynamical evolution. Macrostates tend to evolve towards greater disorder, because to not do so would be fantastically improbable. Decoherence is similar in this respect. A state free to evolve in a large number of dimensions will not likely remain with its principle magnitude and vector unchanged in a small subset of the dimensions in which interactions may take place.

When the state can no longer be described simply as a superposition of two basis states in a particular subspace, those basis states are no longer eigenstates of the environmentally-induced superstate.[74] Phase differences between states in the superposition become less observable as the superstate evolves/dimensionally expands irreversibly.

All energy conserving interactions (couplings) between a quantum mechanical system and its environment cause decoherence. We can imagine that environmental interference such as a phonon may cause a phase jump in a quantum mechanical system by shifting a transition energy temporarily. The passing perturbation also experiences a change in phase which, in general, is dependent on the state of the system, and in principle measurable. This measuring or entangling of the quantum state by interaction with its environment can be thought of as a loss or radiation of information. When sufficient information has been extracted, it is as if the environment has been fully measured or projected the quantum system into one of its phase-indeterminate eigenstates (North or South pole on the Bloch sphere). However, that measurement information is lost to the observer. Thus apparent wavefunction collapse is the symptom of phase decoherence.

It is apparent that a quantum mechanical system cannot radiate a photon and relax to a lower state with high probability and still maintain excited state character and phase determinacy. Thus, in the absence of environmental interference and inhomogeneous broadening, the energy decay will limit the dephasing time T_2^*. (The homogeneous dephasing time can be at most twice the relaxation time since it is the oscillation of the field amplitude which becomes reduced when phase is randomized, and energy relaxation is proportional to the square of the field, thus the exponent describing the energy decay rate acquires a factor of 2). If present, decoherence will also contribute to dephasing, although the decoherence rate can be much less than an ensemble dephasing rate. This is the same as saying T_2 can be much longer than T_2^*, or that dephasing time T_2^* sets a lower bound on the decoherence time T_2. However, T_2 can also be much shorter than the relaxation time T_1 if coupling to the environment is strong and stochastic. In this case the phase of the excited state becomes immeasurable long before the excited fraction decays.

The following relation is helpful (see e.g ref. [73], chapter 6, pg. 266. Boyd calls decoherence "collisional dephasing".)

$$\frac{1}{T_2} = \frac{1}{2T_1} + \gamma \qquad (\textit{homogeneous} \quad \textit{broadening}) \tag{B.65}$$

γ is the rate of decoherence due to e.g. collisional dephasing in an atomic gas, coulomb or phonon broadening in a solid state system. Note that this relation is for a *homogeneously* broadened (Lorentzian) system only.

The following conclusion is important: *the linewidth of a homogeneously broadened transition is limited first by (1) the lifetime and (2) decoherence from environmental interactions.*

The linewidth of an inhomogeneously broadened ensemble, however, is given not by any microscopic property, but simply by the energy spread in transitions making up the ensemble as in eq. B.1.2. *The linewidth of an inhomogeneously broadened ensemble reveals nothing about the decoherence rate of individual quantum systems, provided it is Gaussian.* If conditions are such that linewidth begins to become Lorentzian we return to the former case. In solid state systems inhomogeneity is the norm and not the exception. For such ensembles, the decoherence time is masked in the linewidths of the individual quantum systems. It can be found discovered by clever means (Sec. B.2).

B.1.4 Measurement

Measurement has been interpreted to mean the collapse of a wavefunction into one of its eigenstates. More specifically, this is a projection measurement. Here I describe two different kinds of measurements.

1. Measurement via a noncommuting variable
2. Quantum nondemolition measurement

Noncommuting variable measurement

In the classic discussion of quantum mechanical uncertainty, a thought experiment is introduced by which the position of an electron is measured via change in the momentum of a photon or other particle. It is emphasized to the quantum mechanics initiate that any information extracted about the position of the electron will induce an uncertainty in the position of the electron, due to the recoil of the electron from the momentum exchange.

This occurs whenever one uses a noncommuting variable (momentum) to measure its conjugate (position).

In this type of measurement, a reported result does not guarantee the current state (position) of the quantum system (electron), it can only say something about what *was* the electrons position.

Another measurement of this type is an absorption measurement. A missing photon indicates the system was in a ground state, and *may* now be in an excited state. (Now we use the arrival of a photon to a specific *position* as our conjugate variable for detecting the quantized *momentum* of a localized state.) Further measurements may yield either result: up or down, as additional photons may cause either stimulated emission or stimulated absorption. Thus repeating the measurement does not necessarily increase confidence in the state of the system.

Quantum nondemolition measurement

Imagine now the electron is in one of two states. From the first state $|1>$ it can only visit the second $|2>$, but from the second state it can visit the third $|3>$, which it can occupy only temporarily. We may attempt to detect the state of the electron by inducing a change in its position from $|2> \rightarrow |3>$. If we excite resonant with the $|2> \rightarrow |3>$ transition and we detect the *emission*, or *scattering* of a photon, we know the electron *is* in state $|2>$. If no photons are ever scattered from the $|2>$–$|3>$ transition the atom is known to be in the first state. (Aside: This measurement scheme requires that nature somehow forbid the $|3> \rightarrow |1>$ transition or else attempts at readout can change the state of the system.)

In this case, the report of the measurement contains information about the present state of the system, not a former state. When a measurement leaves the systems in the state reported by the measurement one has achieved what is known as a quantum nondemolition (QND) measurement.

QND measurement schemes are useful for observing quantum dynamics between two states because they project into one of those states by, e.g., measuring the return of the system to the state in question. Thus, a measurement returns the same result each time it is performed. Even if a single attempt at readout yields a low confidence result, it can be repeated over and over within the lifetime of the state in question (neglecting the Zeno effect), in order to build confidence in the state of the system.

B.2 Measuring relaxation, dephasing and decoherence

The three quantities of interest: T_2^*, T_1, and T_2 are important benchmarks for the robustness of a quantum system for quantum information applications. These can be measured by several experimental techniques which usually increase in difficulty for the quantities as ordered above.

The easiest quantity to measure is often the dephasing time T_2^*, which can be found with *linear absorption spectroscopy.* Linear means working well below the threshold for saturation effects. In this regime the linewidth of a transition yields the ensemble dephasing time according to equation B.1.2. It can also be measured in the nonlinear excitation regime by the the decay of Rabi oscillation amplitude in time.

Lifetime can be measured in several ways. For an inhomogeneously broadened emitting (bright) transition, a simple technique is to pump the transition with a short excitation pulse and time resolve the recovery, for instance with a fast photodiode, photomultiplier tube or streak camera. This is simply *time-resolved fluorescence*. Another way is to use follow the pump pulse with a weak probe pulse which measures the linear absorption at specified delay after the pump pulse. Measuring the absorption at each time delay traces the envelope of the relaxation. This method is called *transient absorption spectroscopy* (TA) or simply *pump-probe spectroscopy* and works also for transitions to states which have efficient nonradiative relaxation pathways. In addition, collection of the probe beam can be very efficient in either transmission or reflection geometries.

In the absence of ensemble pure dephasing, or for a single quantum emitter, the homogenous linewidth (FWHM) yields the relaxation rate in angular frequency.

$$T_1 = \frac{1}{2\pi\Delta f} \qquad (no \quad dephasing) \tag{B.66}$$

If the detector response time is much greater than T_1, a time-gating nonlinear technique called *photoluminescence upconversion* can be used to measure the relaxation. A probe beam is mixed with an ultrafast (typically <100 fs) laser pulse (essentially a delta function in time) in a nonlinear crystal. The emission overlapping in time with the intense ultrafast pulse undergoes sum frequency generation. A spectral filter or monochromator passes the upconverted light to the detector, but spectrally selects against emission at other times which was not upconverted. The timing of the ultrafast pulse is varied in order to trace out the envelope of the decay, averaging with the slow detector at each point to accumulate a good signal.

A second nonlinear technique is *saturation spectroscopy.* For a two level system, the onset of saturation is determined by the excited state lifetime. For more complex systems, models can be derived to fit coupling to reservoirs or other levels.[75]

The last quantity, decoherence time (T_2), can often be the most difficult to measure because in inhomogeneously broadened ensembles the effect of decoherence on dephasing can be overwhelmed by the pure dephasing associated with the spread in transition frequencies. In order to measure decoherence, the *pure dephasing* arising from ensemble inhomogeneity must be removed or otherwise compensated for. The simple approach is to obtain the linewidth of a single quantum system. Provided the lifetime is known or much greater than the decoherence time, this is a viable, but sometimes impractical solution to the problem of removing pure dephasing from the system under study.

A well-established method for measuring a homogenous linewidth is known as *spectral hole burning.*[76] This requires a relatively intense narrow and preferably tunable laser as well as a broadband linear spectroscopic technique. The idea is to use the intense laser to drive a small fraction of the ensemble into saturation while simultaneously measuring the linear absorption spectrum. A dip is observed in the absorption precisely in the region where oscillators are saturated. This dip or spectral hole has a Lorentzian lineshape corresponding to the homogeneous absorption line of oscillators in the ensemble.

A second technique measures the time decay of a *four-wave mixing signal*, which is most common in the study of semiconductor quantum wells in the near infrared spectral region which is rich with tunable and ultrafast lasers.

Pulsed quantum control including *photon echo* or *spin echo* techniques are the last commonly used method. These methods have been developed and perfected especially in the nuclear magnetic resonance (NMR) and electron paramagnetic (or spin) resonance (EPR or ESR) commmunity.

B.3 Pulse quantum control techniques

The important concept in quantum control techniques may not have been immediately obvious in the previous discussion is that pure dephasing–dephasing due to only ensemble inhomogeneity–is *reversible.* Dephasing due to decoherence (finite T_2) on the other hand is irreversible.

A technique known as the Hahn echo can be used to measure the homogeneous dephasing or decoherence of an inhomogeneously broadened ensemble.

First, a pulse, either an AC electric field in resonance with a dipole transition or an AC magnetic field in resonance with a spin flip transition, is applied for a time long enough to create a superposition of up and down. This corresponds to a $\pi/2$ rotation in the Bloch sphere (Fig. B.2) about a horizontal (e.g. X) axis. It is important that this operation is accomplished in a time less than T_2^*. In this superposition state each oscillator will acquire phase at a rate proportional to half the energy difference between the ground and excited state $\exp\left[-i(E_1-E_0)/2\hbar\right]$. Acquiring phase is equivalent to rotation about the equator of the Bloch sphere. Each quantum system precesses at its own rate, which is quite fast, so we imagine moving with the center of the group, in a rotating frame with some getting ahead, others behind. At a time τ later, a second pulse is applied with either twice the pulse duration or four times the intensity (twice the electric field). This π-pulse rotates the component of each state vector (Y) orthogonal to operation axis (X) by 180°, to the opposite side of the Bloch sphere, where they continue to acquire phase. Now, however, the relative positions of all the oscillators have been reversed so that a time τ later they come back into phase. At this point a macroscopic polarization builds up and emission is observed that is proportional to the number of oscillators in phase. This is called a *spin echo* in spin flip experiments or a *photon echo* in optical transition experiments.

Decoherence is stochastic and irreversible and cannot be compensated for. Thus any oscillator which decoheres during the time 2τ following the initial pulse will not contribute to the photon echo. By varying the delay τ between the pulses

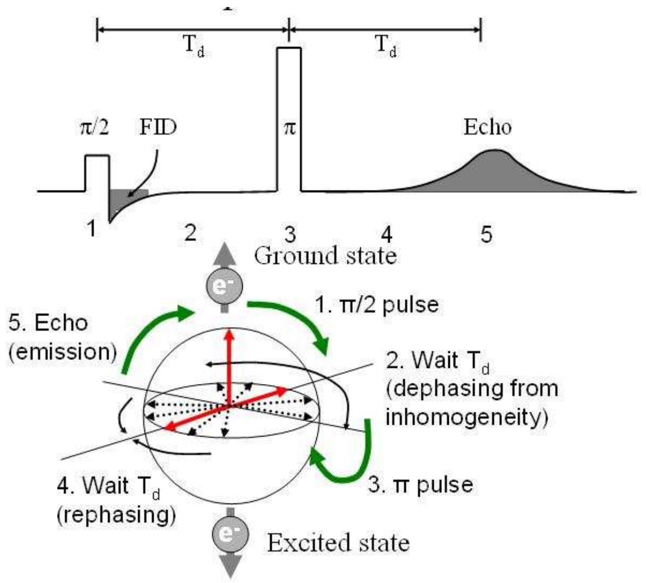

Figure B.2: Two pulse photon/spin echo scheme depicted in the Bloch sphere representation.

a decay is observed in the photon echo amplitude with a time constant which is limited by decoherence, thus revealing the intrinsic decoherence of a single oscillator in an inhomogeneously broadened ensemble.

At the point where a coherent emission of radiation occurs, a projection measurement can be made by another $\pi/2$-pulse. Un-decohered states are observable in the ground state; decohered states are not. As the delay time between pulses is increased the number of states observed in the ground state decays in a time T_2^*.B.3 The three pulse scheme is preferable for systems in which readout of the quantum state is easier than detection of a photon echo.

Provided optical readout of the neutral donor population is possible, a three pulse projected photon echo measurement may be the most attractive method for T_2 measurement. It requires three pulses of duration less than 100 ps with

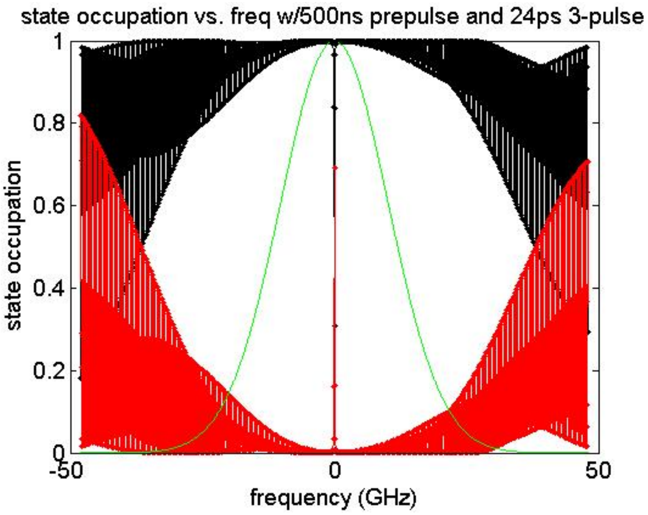

Figure B.3: Two level simulation of ground state (black) and excited state (red) populations within a noninteracting, inhomogeneously broadened ensemble, with excitation from a sliced terahertz pulse on resonance, a series of three 24 ps duration pulses with 10 ns delay $\pi/2$–τ–π–τ–$\pi/2$ pulses contrast ratio of 10^3. Included is 500 ns of "prepulse" at 10^{-3} of the π pulse intensity intended to simulate the effect of leakage from a photoactivated semiconductor switch (see thesis of M. Doty [1] for description of contrast ratio). No relaxation or dephasing is included in this model which demonstrates only the effect of finite pulse length in an inhomogeneous ensemble. See Appendix D for simulation details.

variable delay on the order of 1–10 ns and electric fields of tens to hundreds of volts per centimeter. In Appendix D I present calculations for required field strengths and in Appendix E an apparatus for producing three terahertz pulses of variable amplitude and delay, which will be necessary for such pulsed quantum control measurements.

At this point we return to methods of measuring the ensemble dephasing rate. This rate can go up when the states are excited or when driving radiation is present so it is useful to know the rate at which the ensemble loses phase coherence under strong excitation.

Imagine an experiment in which the resonant excitation pulse length can be varied. The ensemble will begin to become excited due to stimulated absorption. At the point when the entire population is excite the ensemble experiences stimulated emission, returning to the ground state and so on, oscillating back and forth between the ground and excited state as long as the driving field is present. This is Rabi oscillation is equivalent to a continuous rotation about the X or Y axis of the Bloch sphere. However the rate at which the oscillators revolve is slower when they are detuned from the resonant field. Thus, the ensemble will begin to dephase, with the amplitude of the Rabi oscillation decaying in a time T_2^*.

Ramsey fringes are another two-pulse quantum control experiment. One π/-pulse is followed after time t with a second $\pi/2$ pulse, follow by immediate readout of the ensemble state. For $t = 0$, equivalent to a continuous π-pulse, the entire ensemble should be moved to the excited state. However, if during the wait time the ensemble acquires sufficient phase to move to the opposite side of the Bloch sphere, the second pulse will de-excite the ensemble. As a function of t the transition probability oscillates in time, again decaying on the time scale set by the ensemble dephasing rate T_2^*.

For a good experimental paper illustrating the benchmarking of a qubit using pulsed quantum control measurements see ref. [77].

Appendix C

RELS measurements

C.1 Parts needed

- Acton 2750 (750 mm focal length f/9.7 imaging grating spectrometer with #1 1800 g/mm – 500 nm blaze grating and #2 1200 g/mm – 1 μm blaze grating, USB communication, power supply.
- Princeton Instruments CCD (back illuminated, deep depletion, LN2 cooled 1340x400 pixel CCD array, 20x20μm pixels, three gain settings (side switch), shutter included, 2 L volume, controller cable, controller, USB2.0 communication.)
- Powered USB hub (if needed to relay long USB cables)
- The pipe (1mm diameter multimode optical fiber for coupling lots of light easily.)

- The computer named *FEL1380C*
- LabView VI's for Acton
- LabView VI's for CCD
- Roper scientific WinView32 software
- 6.5 T liquid He immersion magnet cryostat and peripherals as described in SOP available in the lab, sample mount and lens, OR
- Cryo Industries sample-in-vacuum liquid He flow cryostat, cold finger sample holder, cartridge heater, and temperature controller.
- New Focus Velocity tunable laser and controller
- Red visible alignment laser
- (optional) Pockels cell-base optical switch. (see Appendix F)
- Hamamatsu C5331 avalanche photodiode in shielded aluminum case with and 15V, RF shielded, ferrited power supply (15 V is down regulated to 5 V inside shielded box), with cage assembly holding focusing optics and 10 nm 820 0.5" diameter spectral band pass filter
- Beam expander and cylindrical lens pair on cage assembly for beam shaping
- 30-70 rectangular beamsplitter in relocatable mount for picking off RELS and sending to spectrometer via fiber

- (optional) Minicircuits FTB-1-6 0.01–125 MHz 1:1 balun transformer (for removing ground loop between detector and scope and reducing low and high frequency noise).

- SR830 DSP lockin amplifier

- SR540 chopper controller, and chopper head with 30 blade wheel

- SR445 4-stage DC-300 MHz voltage preamplifier (daisy chain only 3 gain stages at most in a row, as 4 will oscillate) OR

- Matec 3 stage DC=400 MHz voltage preamplifier with 15 V power supply. (We have three in the lab.)

- LeCroy DDA-120 4-channel oscilloscope

- The YAG or a Regeneratively amplified Ti:Saph laser pulse for slicing the THz.

- Terahertz optics and beam path: beamsplitter and pyro detector, pulse slicer and associated optics and wafers, and *brass* off-axis parabolic mirror to go in front of the magnet bore. Don't use a Melles-Griot electroformed OAP as they are magnetic and could be warped or ripped off in the event of a magnet quench.

C.2 Important information

- DO NOT cool the CCD down unless it is connected to its power supply and the power supply is turned on and the light is on and the fan is on. Static build up during cooling can fry the $40,000 CCD unless the power supply is attached, which continuously reads out the bins when it is not in use.

- Don't let reflected light go back into the NF laser. It will destroy the single mode emission.

- Read the NF laser manual and the CCD manuals completely before attempting to use them. They are very expensive.

- Read the magnet and or cryostat SOP before attempting to either, especially the magnet cryostat.

- Don't be stupid. Set up guards (posts or Al panels) around the magnet in case you walk by with a metal tool. The magnet is close to the corner of the table and very exposed.

- If you are nervous about anything related to the high power lasers or magnets or applying large amounts of force to something or e.g. stretching over optics to reach something or lifting something heavy by yourself–don't. Stop and think of a better way. Your instincts are usually right if you suspect you are doing something stupid.

- Always double check for "bullets" with the room lights on before turning on the magnet.

- Be very careful with the liquid helium level meter probe. The head has broken off several times when it was removed forcefully. Rewiring it again will be impossible so you will have to buy a new one ($350).

- Email me at my permanent email address if you have any questions: laserdad@gmail.com

C.3 Layout and overview

For RELS measurements you will need the FEL and your visible laser to be incident at the same point on a sample. Further, both lasers should be close to a neutral donor/donor bound exciton resonance, respectively. This is a triply resonant experiment–two spectral resonances and a spatial overlap. If you are doing pulsed optical readout you have a time overlap to worry about as well. Additionally, you will need to be careful to avoid stray light, as the signal is the same color as the laser so stray light adds to the background and detector noise and hampers alignment.

Begin by getting the NF laser and red alignment laser co-axial through two variable irises at 5" height above the optical table surface. If you are using the optical switch, you may choose to arrange the lasers and optics as shown in Fig.

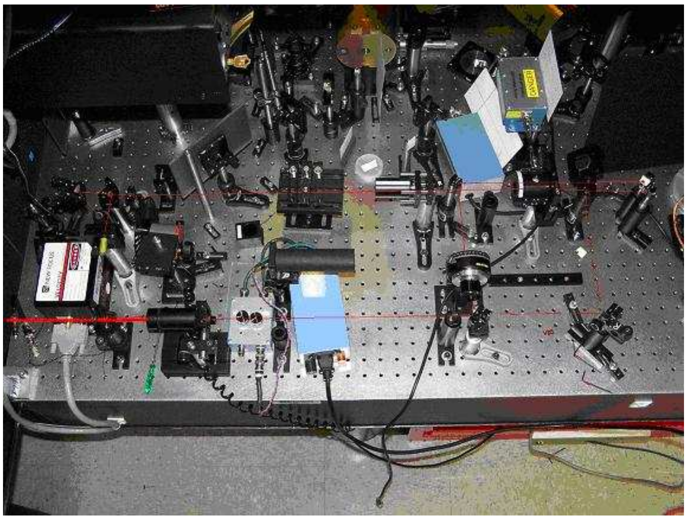

Figure C.1: Layout of laser and optical switch.

C.1.

Following the optical switch use two mirrors to align the lasers again coaxially into a beam expander. The polarization should be horizontal. The beam expander has a variable focus. Be aware the visible laser and NIR laser are different sizes after the beam expander. Use the focus to determine the size of the laser beam near the beam shaping cylindrical lenses at the front of the magnet (Fig. C.2 and Fig. 3.10). The size of the beam determines the numerical aperture—the larger the beam at the lenses, the tighter the focus at the sample. The thing to worry about is clipping of the beam as it enters the magnet or flow cryostat. This will take some trial and error to get a 1.5x1.5 mm or similar size spot

The layout for using a flow cryostat is slightly different (Fig. C.3. You may need to attach a breadboard to the edge of the table to make room for the bulky flow cyrostat, although the cryogen hose is flexible and the cryostat can fit on

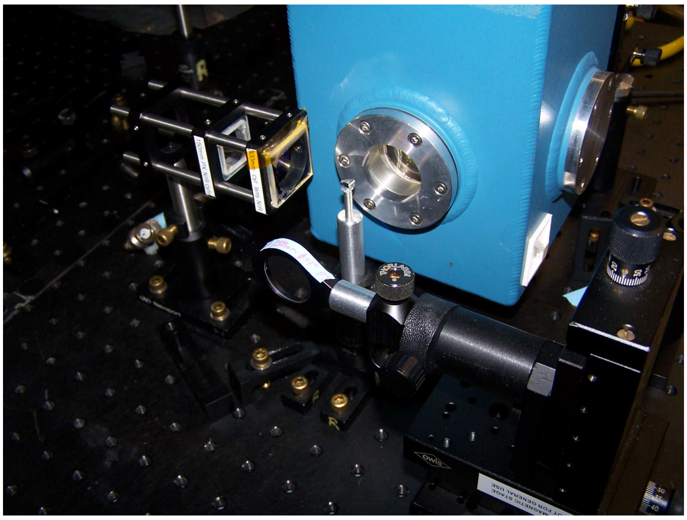

Figure C.2: Beam shaping lenses at input of magnet cryostat. In the most recent experimental setups (not pictured) I replaced the small triangular bending mirror with a long piece of gold-coated Si wafer which I suspended from an optical mount to give the input mirror tip and tilt control, along with one-axis translation in the direction of the incident laser.

the table under the overhead rack. There is no bending mirror inside the crostat. Instead bring the excitation laser through a third window. The terahertz in always incident through the substrate (I haven't measured the transmission), and light collection is normal to the epilayer.

In both measurements you will need a lens to collimate emission. The magnet can fit a "helper lens" inside the bore to pre-collimate the beam. Use another lens outside the magnet as well to direct the beam towards the APD and control divergence. A beamsplitter may be placed after the collimation lens and before the APD to send light to a fiber coupler and then to the spectrometer. The APD uses a 1" diameter lens to prefocus the light to a 0.5" diameter to pass through a band pass filter, then a very short focal length lens to focus on the $\sim$ 1 mm^2

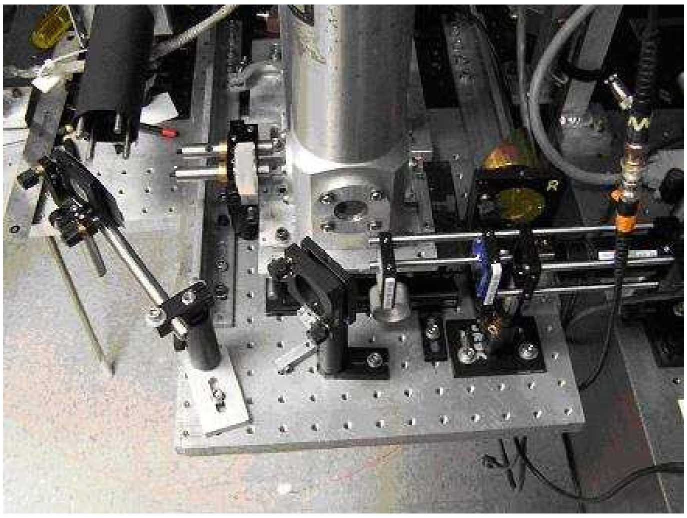

Figure C.3: Optical layout for use of variable temperature flow cryostat for RELS measurements.

detector element.

C.4 Aligning the laser onto the sample

Align the lasers to the sample before cooling the magnet. Shim the magnet insert up with folded 3x5 cards under the collar at the top by about 3–4 mm to compensate for shrinking that occurs when the magnet is cooled. Leave out the helper lens. Direct the laser towards the sample as shown in Fig. 3.10 in Ch. 3. The sample mount I used did not fit snugly in the cryostat, so I had to use layers of kapton tape or thick paper to shim for snugness. You may use the visible laser to prealign, then get out an IR viewer to look at the NF laser spot on the sample (you may have to remove the beamsplitter and APD for this–that's why I use kinematic locators for the bases). Record the spot size for intensity measurements.

Remove the magnet insert and put in the helper lens. Check that the laser is not being clipped by the helper lens.

Now you may cool the magnet and peak up the signal on the APD.

C.5 Collecting fluorescence

The APD is AC coupled with a low frequency rolloff of 4 kHz. To measure signal you have to chop the laser at as high a frequency as your chopper will allow (hence the 30 blade chopper). Once the magnet is cold and pumped to superfluid temperature the liquid will be optically clear and you can align the fluorescence. Tune the NF laser to 816 nm or so. Attenuate the laser slightly to begin so as not to blow up the input of the lockin amplifier. Send the output of the APD to a 3 stage voltage amplifier (the APD inverts, the SR445 doesn't) and then to the lock-in amplifier (frequency externally referenced to the chopper). Adjust the tip and tilt of the input mirror, collimation lens and the slip plate holding the short focal length lens directly in front of the sample to optimize PL. You may have to work hard to make sure you are not looking at laser scatter. This is easily done by tuning to 818.65 nm (the D^0X resonance) and seeing if the signal changes by 50% or more over the piezo tuning range. For samples with semi-insulating substrates you must put something black behind the sample to absorb scattered laser light and make sure you have placed a similar thickens spacer/shim between the two halves of the sample mount to make room for your black absorber (black paper or black PE) or else you will strain the sample (and ruin it) when you screw the two halves of the sample mount box together. (The sample should float freely in the sample box to avoid strain. Strain royally screws up the optical and terahertz spectra. You can do a shake test to see if the sample moves or not when you are putting it in the mount. If not, you have a strained sample and it needs to be looser.) The black absorber should be transparent to terahertz. This you can check with the VDI source and a pryo.

You can also check to see if you are close by switching to the visible alignment laser, which is blocked by the substrate and the bandpass filter and measure the PL. It will be much weaker, but will get you close if stray light is screwing things up.

Eventually tune to 818.65 nm, turn of the motor and use the piezo to peak up the spectral overlap of the laser and D^0X line.

Once the terahertz is incident, you can peak up alignment on the oscilloscope. Terahertz-induced changes in RELS of 1 V or better on the scope are OK at B=0 T tesla with the full NIR power. Very good is 2 V or more. Very poor is a couple hundred millivolts.

C.6 Terahertz alignment

Use the visible alignment laser for the pulse slicer to get the Terahertz on the sample. (Do this after making sure the FEL and pulse slicer alignment lasers are coaxial). This sample mount sits about 1/3 of the way into the magnet bore. It needs <1 cm for the lens mount and $\sim$ 1 cm of space between the sample and the lens. Because the sample is so far from the back window, it can be a little bit tricky to be sure the terahertz is focused on the sample. If you are worried about it, you can put the sample mount in empty and look for transmission. I never had to do this though.

C.7 Noise

The Pockels cells are noisy. To avoid the noise, use ferrites everywhere, including your hair and pockets. Use *thick* Aluminum boxes for amplifiers and APD's. To avoid a ground loop between the grounded APD (with floating power supply) and the grounded scope, I use a 1:1 balun transformer.

C.8 Tips

1. Take CCD spectra each time you run an experiment. This will help you be sure what you are looking at.

2. Save a whole day for mounting new samples so you are not rushed and you

don't ruin the sample.

3. Cold check your photoconductive samples with a liquid helium dunk stick before wiring them up for use in the magnet. The 4 K resistance should be in the MΩ range.

4. Choose samples for the flow cryostat that are long and thin. Mount on one side with cryo-vacuum grease and support the bottom side at the free end with a piece of paper or something, so the sample doesn't tip down. The free end is strain free and should overlap one of the holes in the copper cold finger mount where terahertz can come through. One of the holes is eclipsed by the heat shield (I think it is the top one). This cryostat's leads got rewired and the internal heater leads are missing, so you have to screw on a catridge heater for temperature dependence measurements. The leads usually used for the cartridge heater got rewired to the BNC breakout for a photoconductivity experiment at the inside of the feedthru panel. You will have to switch these back to use a heater for temperature dependent measurements.

5. Use Toluene to remove cryo vacuum grease. Then rinse with isopropanol, acetone, optionally DI water and/or Methanol. That will get the sample clean.

6. When you don't have signal, start at the laser and check the beam to the

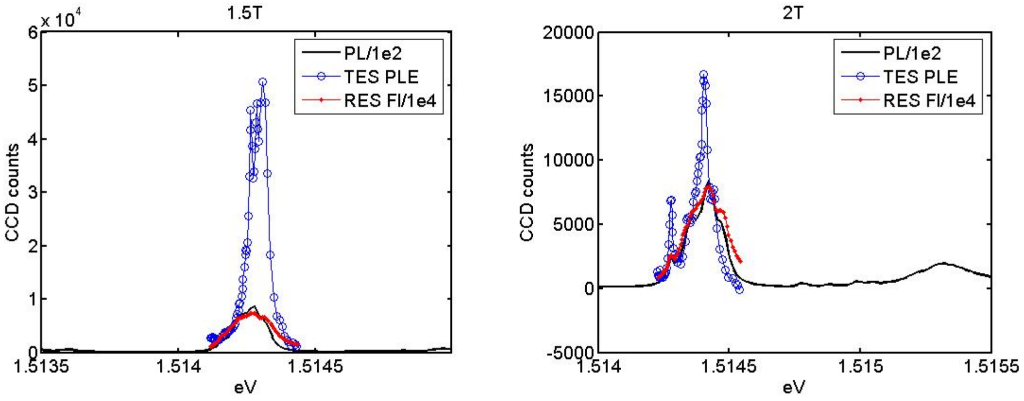

Figure C.4: (Left) B=1.5 T, (Right) B=2 T

sample then to the detector and then follow the detector output to the scope or lockin, then check to make sure the lockin is referenced right and the scope is triggered right. Then do the same for the FEL. Starting by making sure you can get the green alignment laser to your port.

C.9 Extra figures

Here are figures comparing donor bound exciton RELS, PL and TES emission at various magnetic fields as in Fig. 3.12, which gives 1 and 6 T.

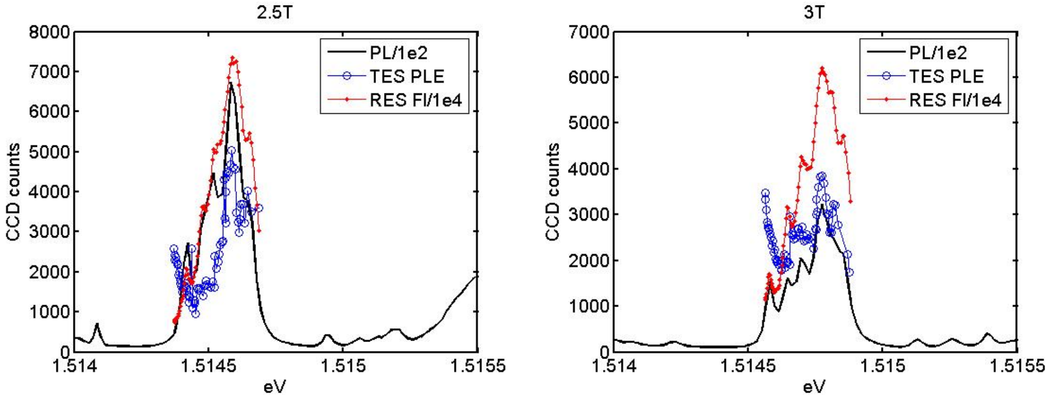

Figure C.5: (Left) B=2.5 T, (Right) B=3 T

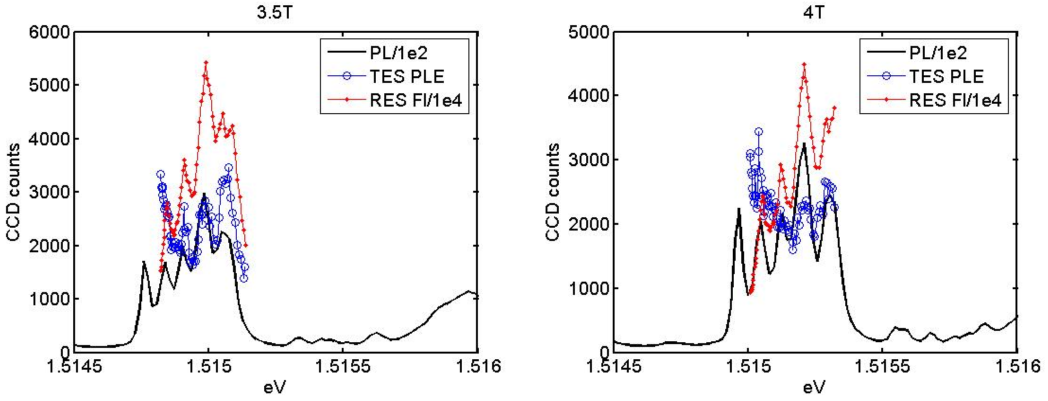

Figure C.6: (Left) B=3.5 T, (Right) B=4 T

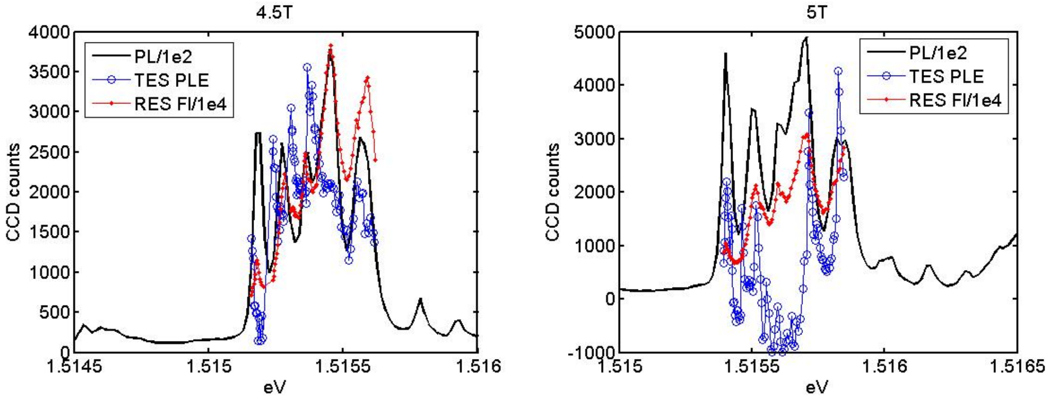

Figure C.7: (Left) B=4.5 T, (Right) B=5 T

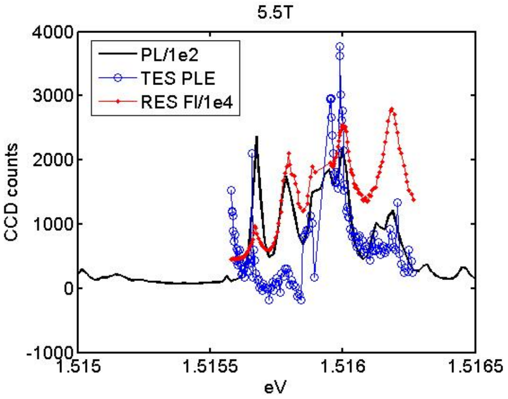

Figure C.8: B=5.5 T

Appendix D

Two level system calculations

D.1 Schrödinger equation in the RWA

In this appendix I calculate the time evolution of a two state system in response to a sinusoidal field within the electric dipole and rotating wave approximation. I include this calculation because most textbooks resort to further simplifying approximations such as setting the drive frequency resonant with the transition frequency, which may or may not have been the case when you took your data, or else showing only the transition probability rather than the coefficients. They also do not show how this calculation can be used to propagate a two-state system as it undergoes successive periods of interaction with an AC field, such as is the case in a Hahn Echo experiment.

The calculation follows Cohen-Tanoudji chapter XIII section B, equations to B-6. Then I move to pg. 1341 Complement $C_X III$ of chapter XIII "Approximation

Methods for Time Dependent Problems", where I depart. Cohen-Tanoudji (C. Cohen-Tanoudji, B. Diu, F. Laloë, Quantum Mechanics, Wiley, France (1997), first printing (a new printing is available, with, hopefully, better typesetting).

Consider a Hamiltonian

$$\hat{H}(t) = \hat{H}_0 + \hat{V}(t), \tag{D.67}$$

with solutions for the time-independent part

$$\hat{H}_0|\phi_n\rangle = E_n|\phi_n\rangle. \tag{D.68}$$

I describe the state of the system at any time t in terms of this orthonormal basis of time-independent solutions.

$$\psi(t) = \sum_n c_n(t)|\phi_n\rangle \tag{D.69}$$

Insert this definition into the Schrödinger equation, distribute the terms of the Hamiltonian and operate on $|\phi_n\rangle$ with $\hat{H}_0$ to obtain the energy eigenvalues of the unperturbed states E_n.

$$\begin{aligned}
i\hbar\frac{d}{dt}|\psi(t)\rangle &= \hat{H}(t)|\psi(t)\rangle && \text{(D.70)}\\
i\hbar\frac{d}{dt}\sum_n c_n(t)|\phi_n\rangle &= \hat{H}(t)\sum_n c_n(t)|\phi_n\rangle && \text{(D.71)}\\
&= \left[\hat{H}_0 + \hat{V}(t)\right]\sum_n c_n(t)|\phi_n\rangle && \text{(D.72)}\\
&= \sum_n c_n(t)\left[E_n + \hat{V}(t)\right]|\phi_n\rangle && \text{(D.73)}\\
& && \text{(D.74)}
\end{aligned}$$

When $|\phi_n\rangle$ consists of discrete states as I have assumed here, then the Schrödinger equation reduces to a set of coupled time-dependent differential equations whose solution depends only on $\hat{V}(t)$ and $c_n(0)$.

We may obtain these n equations by multiplying by $\langle\phi_m|$ on the left, and using the definition D.67 with the orthonormality condition $\langle\phi_m|\phi_n\rangle = \delta_{mn}$.

$$\begin{aligned} i\hbar\frac{d}{dt}\sum_n c_n(t)\langle\phi_m|\phi_n\rangle &= \sum_n E_n c_n(t)\langle\phi_m|\phi_n\rangle + \sum_n \langle\phi_m|\hat{V}(t)|\phi_n\rangle && \text{(D.75)} \\ i\hbar\frac{d}{dt}\sum_n c_n(t)\delta_{mn} &= \sum_n E_n c_n(t)\delta_{mn} + \sum_n c_n(t)V_{mn}(t) && \text{(D.76)} \\ i\hbar\frac{d}{dt}c_m(t) &= E_m c_m(t) + \sum_n c_n(t)V_{mn}(t) && \text{(D.77)} \end{aligned}$$

Now I explicitly include in the time dependence of $c_n(t)$ which is due to the time evolution of the unperturbed states, $\exp(-iE_nt/\hbar)$. This takes us to the interaction picture where the solutions to $\hat{H}_0$ are stationary and time evolution of solutions is only due to the interaction Hamiltonian $\hat{V}(t)$.

$$c_n(t) = b_n(t)e^{-iE_nt/\hbar} \tag{D.78}$$

Making this substitution into D.77 gives me two coupled equations for $b_n(t)$

$$\begin{aligned} i\hbar\frac{d}{dt}\left[b_1(t)e^{-iE_1t/\hbar}\right] &= E_1b_1(t)e^{-iE_1t/\hbar} + b_2(t)e^{-iE_2t/\hbar}V_{12}(t) && \text{(D.79)} \\ i\hbar\frac{d}{dt}\left[b_2(t)e^{-iE_2t/\hbar}\right] &= E_2b_2(t)e^{-iE_2t/\hbar} + b_1(t)e^{-iE_1t/\hbar}V_{21}(t), && \text{(D.80)} \end{aligned}$$

Carrying through the differentiation cancels the first terms on the right. I can move the exponential time dependence and constants to the right.

$$b_1(t)' = b_2(t)e^{-i\omega_{21}t}\frac{V_{12}(t)}{i\hbar} \tag{D.81}$$

$$b_2(t)' = b_1(t)e^{i\omega_{21}t}\frac{V_{21}(t)}{i\hbar} \tag{D.82}$$

Let us assume $\hat{V}(t)$ is an oscillating electric field $E(t) = E_0 \sin(\omega t)$ in the presence of two states of definite parity, the initial sate $|1\rangle$ and final state $|2\rangle$ with a resonant frequency $\omega_{21} \equiv (E_2 - E_1)\hbar$, and nonzero dipole matrix element $z_{21} = z_{12}$.

With n as the final state and m as the initial state we have

$$V_{nm}(t) \equiv \langle\phi_n|\hat{V}(t)|\phi_m\rangle = iq|E|z_{nm}\frac{\omega_{nm}}{\omega} = V_{mn}^*(t). \tag{D.83}$$

(The last statement is justified by $\omega_{nm} = -\omega_{mn}$, which ensures the perturbation is Hermitian.)

Now I substitute $\sin(\omega t) = [\exp(i\omega t) - \exp(-i\omega t)]/2i$, distribute, and keep only slowly varying exponents (the ones with minus signs) I obtain the following. This "rotating wave approximation" is valid when the Rabi frequency is much less than the drive frequency (i.e. $qEz/\hbar \ll \omega$.)

$$b_1(t)' = -b_2(t)\frac{iq|E|z}{2\hbar}\frac{\omega_{12}}{\omega}e^{i(\omega-\omega_{21})t} \tag{D.84}$$

$$b_2(t)' = -b_1(t)\frac{iq|E|z}{2\hbar}\frac{\omega_{21}}{\omega}e^{-i(\omega-\omega_{21})t} \tag{D.85}$$

Here I can use the magnitudes of the perturbation

$$v = iq|E|z\frac{\omega_{12}}{\omega}, v^* = iq|E|z\frac{\omega_{21}}{\omega} \tag{D.86}$$

to simplify notation. Notice they are complex conjugates as required, since $\omega_{21} = -\omega_{12}$.

I will further simplify by defining

$$\Delta\omega \equiv \omega - \omega_{21}, \tag{D.87}$$

to obtain

$$b_1(t)' = -b_2(t)\frac{v}{2\hbar}e^{i\Delta\omega t} \tag{D.88}$$

$$b_2(t)' = b_1(t)\frac{v^*}{2\hbar}e^{-i\Delta\omega t}. \tag{D.89}$$

These are equivalent to Cohen-Tanoudji eq. 4-a and 4-b, pg 1341.

In order to decouple them I differentiate the first.

$$b_1''(t) = \frac{-iv\Delta\omega}{2\hbar}e^{i\Delta\omega t}b_2(t) - \frac{v}{2\hbar}e^{i\Delta\omega t}b_2'(t) \tag{D.90}$$

Now I eliminate $b_2(t)$ by solving equations D.88 and D.89 for $b_2(t)$ and $b_2'(t)$, respectively and substituting into equation D.90.

$$0 = b_1''(t) - i\Delta\omega b_1'(t) + \frac{|v|^2}{4\hbar^2}b_1 \tag{D.91}$$

This differential equation can be solved by various means. I assume $b_1(0) = 1$ and used the Laplace transform method to obtain the following for $b_1(t)$.

$$b_1(t) = e^{\frac{i\Delta\omega t}{2}}\left(cos(Xt) - \frac{i\Delta\omega}{2}\frac{\sin(Xt)}{X}\right) \tag{D.92}$$

Here I have written the result succinctly by defining X.

$$X \equiv \sqrt{\frac{\Delta\omega^2}{4} + \frac{|v|^2}{4\hbar^2}} \tag{D.93}$$

By differentiating $b_1(t)$ and inserting into equation D.88 I obtain the time dependence for the $|2\rangle$ state.

$$b_2(t) = -e^{-\frac{i\Delta\omega t}{2}} \sin(Xt)\frac{|v|}{2\hbar X} \tag{D.94}$$

The time dependent coefficients $c_n(t)$ are obtained from definition D.78.

$$c_1(t) = b_1(t)e^{-iE_1t/\hbar} = b_2(t)e^{i\omega_{21}t/2} \tag{D.95}$$

$$c_2(t) = b_1(t)e^{-iE_2t/\hbar} = b_2(t)e^{-i\omega_{21}t/2} \tag{D.96}$$

The validity of the solution can be seen by taking various limits. As $\omega \longrightarrow \omega_{21}$ we obtain the familiar result.

$$c_1(t) = e^{i\omega_{21}t/2}\cos\left(\frac{|v|t}{2\hbar}\right) \tag{D.97}$$

$$c_2(t) = e^{-i\omega_{21}t/2}\sin\left(\frac{|v|t}{2\hbar}\right) \tag{D.98}$$

The free evolution operator is due to the time-independent Hamiltonian $\hat{H}_0$, where each state acquires a phase $\exp(-iE_nt/\hbar)$.

$$\hat{H}_0(t) = \begin{pmatrix} e^{i\omega_{21}t/2} & 0 \\ 0 & e^{-i\omega_{21}t/2} \end{pmatrix} \tag{D.99}$$

Or equivalently

$$\hat{H}_0(t) = \begin{pmatrix} 1 & 0 \\ 0 & e^{-i\omega_{21}t} \end{pmatrix} \tag{D.100}$$

If we solve for the opposite initial condition $b_2(0) = 1$, we will have all the matrix elements of the time dependent matrix elements of the perturbation operator. Then we may propagate any state by constructing the operator corresponding to the perturbation and then operate on the state. I can repeat the Laplace transform with the opposite initial condition to obtain solutions for time evolution of the population which starts in the excited state, or else I can just let $\Delta\omega \rightarrow -\Delta\omega$ and swap solutions, since I know the operator is Hermitian.

The Hamiltonian due to an AC field can be written.

$$\hat{V}(t)' = \begin{pmatrix} c_1(t) & c_2(t)[\Delta\omega \rightarrow -\Delta\omega] \\ c_2(t) & c_1(t)[\Delta\omega \rightarrow -\Delta\omega] \end{pmatrix} \tag{D.101}$$

An overall phase can be removed to obtain the operator describing the time evolution when the AC field is present.

$$\hat{H}(t) = \begin{pmatrix} \cos(Xt) - \frac{-i\Delta\omega}{2}\sin(Xt)/X & -\frac{|v|}{2\hbar}\sin(Xt)/X \\ -e^{-i\Delta\omega t}\frac{|v|}{2\hbar}\sin(Xt)/X & e^{-i\Delta\omega}\left[\cos(Xt) + \frac{i\Delta\omega}{2}\sin(Xt)/X\right] \end{pmatrix} \tag{D.102}$$

To follow a two state system as it undergoes successive operations in an AC field and periods of free evolution, I only need to multiply the state vector by the appropriate sequence of matrices and then square the resulting state amplitudes to get the probability distribution.

I wrote Matlab scipts for doing this. The files can be found in the simulation directory of the computer *FEL130C*, in the file *coherent THz dynamics*. See. e.g. the file *threepulse.m*. In this software the perturbation Hamiltonian $\hat{H}(t)$ is called V, and the bare Hamiltonian is called H.

A two-pulse (Hahn echo) sequence is used for measuring spin or photon echo decay in a two state system. The first pulse provides an integrated electric field sufficient to make $c_1^2 = c_2^2 = 1/2$, an even superposition corresponding to a rotation of $\pi/2$ of the state vector in the Bloch sphere representation. The second pulse implements a complete transfer of population or rotation by π about the same Bloch sphere axis (phase) as the previous pulse.

On resonance, the $\pi/2$ condition is

$$\frac{\alpha t}{\hbar} = \frac{q|E|zt}{\hbar} = \pi/2, \tag{D.103}$$

where t is the duration of the pulse and $|E|$ is the magnitude of the electric field. The π pulse can be implemented by either twice the field (four times the intensity) or twice the duration.

The calculations of give magnetic field dependence of the dipole moments z for bound electron 1S–2P transitions.

In order to calculate the required intensity required to acheive the necessary electric field for a π pulse from a THz pulse of fixed or known pulse length or vice-versa, the following relation is useful.

$$I = \frac{n\epsilon_0 c|E|^2}{2} \tag{D.104}$$

Although, the familiar and easy to remember circuit definition $P = V^2/(2Z)$ can be more practical since the constants involved are simpler. I may scale the circuit definition by the beam area, in order to use the experimentally relevant parameter: intensity, and electric field.

$$I = \frac{|E|^2}{2Z_{GaAs}} \tag{D.105}$$

Here the impedance of GaAs is given by $Z_{GaAs} = 377\Omega/n_{GaAs} = 105\Omega$.

The foregoing should suffice for calculations of two state dynamics. Since the donors are modelled as independent quantum systems, inhomogeneous broadening can be treated by performing the calculations over a range of energies and then averaging the result with a spectral weighting function such as a Gaussian.

The spectral breadth of the FEL is approximately 1 GHz. In long pulses this may become a source of unmodeled dephasing.

Energy relaxation and excitation to other states or the conduction band are also not modelled. Relaxation is easiest to treat within the density matrix formalism.

Energy level shifts due to AC perturbations are best modelled in the Floquet theory, section D.2, for which exact numerical results can be obtained.

In the following script, a factor of 2 has been factored from the denominator so that it represents a generalized Rabi frequency X, i.e. $X \to 2 * X = \sqrt(\Delta\omega^2 + |v|^2/\hbar^2)$.

D.1.1 Matlab code

V.m

```
function p2=V(p1,omega21,omega,t,E,Z)
    beta=E*1.602e-19*omega21/omega*Z/1.05e-34;
    x=sqrt((omega-omega21).^2+beta.^2);
    delta=omega-omega21;
    v11=cos(x.*t/2)-i*(delta)./x.*sin(x.*t/2);
    v12=-beta./x*sin(x.*t/2);
    v21=-exp(-i*(delta).*t)*beta./x.*sin(x.*t/2);
    v22=-exp(-i*(delta).*t).*(cos(x.*t/2)+i*(delta)./x.*sin(x.*t/2));
    v=[v11,v12;v21,v22];
    p2=v*p1;
 return
 %propagates the quantum state with amplitudes (p1(1) p1(2)) through time
 %t, during which a sinusoidal perturbation of E*sin(omega*t) is
 %acting. beta=q*E*omega21/omega*<Z>/hbar, where <Z> is the dipole moment
 %between the initial and final states. This is in the rotating wave
 %approximation.
```

H.m

```
function p2=H(p1,omega21,omega,t)
    h11=1;
    h12=0;
    h21=0;
    h22=exp(-i*(omega-omega21).*t);
    h=[h11,h12;h21,h22];
    p2=h*p1;
 return
 %propogates the quantum state with amplitudes (p1(1) p1(2)) through time
 %t, during which no pertubation is acting on the system.
```

Threepulse.m

```
close all clear
%experimental conditions
wn=35;%FEL operating wavenumber
omega=2*pi*2.9979e10*wn; %FEL frequency in radians/sec
wid=*0.4 %transition width in wavenumbers
fwhm=2*pi*2.9979e10*wid; %peak full width half max in radians
%omega21=omega; %on resonance, vary other parameters
oif=(omega-2*fwhm):fwhm/100:omega+2*fwhm; %range of frequencies to compute
```

```
os=0; %wavenumbers off resonance
oif=oif-2*pi*2.9979e10*os;
fp=10 %watts of FEL power delivered to the sample
bd=0.04 %beam diameter incident at the last off axis parabolic mirror (meters)
fl=5*0.0254; %mirror focal length (meters);
sr=1e-2/wn*fl/bd; %spot radius
intensity=fp/(pi*sr^2);
n=3.5; %index of refraction of GaAs
E=sqrt(2*intensity/n/8.85e-12/2.9979e8); %compute electric field
Z=5e-9; %dipole moment (meters)
td=1d-9; %delay time

%intial state
p(1,1)=1; p(2,1)=0;

%calculate quantum state coeficients for each frequency
for n=1:length(oif)
    x(n)=oif(n);
    p=V(p1,oif(n),omega,t,E,Z,);   %pi/2 pulse
    p=H(p,oif(n),td);               %delay
    p=V(p1,oif(n),omega,t,2*E,Z);    %pi pulse
    p=H(p,oif(n),td);               %delay
    p=V(p1,oif(n),omega,t,E,Z);     %pi/2 pulse
    P0(n)=abs(p(1))^2;
    P1(n)=abs(p(2))^2;
end
```

D.1.2 Including relaxation, decoherence, and dephasing

For a more general treatment of the two-level system refer to Ref. [76], ch. 2. The two level system is treated analytically in the rotating wave approximation, with relaxation and homogeneous dephasing added in phenomenologically. The two level system is also treated within the density matrix formalism. Inhomogeneous effects are included in the general result as a dependence on wavevector times velocity of a particle in a doppler broadened ensemble. This $k \cdot v$ dependence

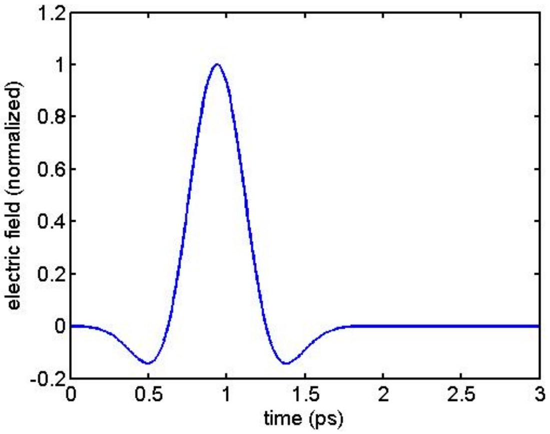

Figure D.1: Electric field generated by time domain spectrometer. Far field broadband emission results when a femtosecond laser pulse excites carriers in a normally insulating gap between two biased electrodes.

can be simply exchanged for a direct dependence on energy offset.

D.1.3 Beyond the rotating wave approximation

When a short, intense broadband source (Fig. D.1) such as a pulse from a terahertz time domain spectrometer is used to excite a system, there is usually no recourse but to resort to numerical methods.

Numerically solving the time dependent schrodinger equation as a system of coupled equations for the time evolution of the constants multiplying the energy eigenstates is not difficult.

Here is an example in Maple code.

```
#define constants V=eEZ/(2hbar)/1e12, where e is charge and Z is
dipole, and E is electric field

>restart:
>omega:=2*evalf(Pi);#resonant frequency in units of THz
>V:=6e-3;#units of THz pi:=evalf(Pi):
```

```
>x:=0.8; #scales frequency of
time domain single cycle pulse

#plot electric field in units of ps
>plot(sin(x*omega*t)*exp(-((t-0.75*2*Pi/(x*omega))
/(1.85/(x*omega)))^2),t=0..3);

#define coupled equations as is ref. \cite{letokhov}, eq, 2.11,
for ground and excited state wavefunction coefficients a1 and a2.

>Eqa1:=I*diff(a1(t),t)=V*sin(x*omega*t)*exp(-((t-0.75*2*Pi/(x*omega))
/(1.85/(x*omega)))^2)*a2(t)*exp(-I*omega*t);
>Eqa2:=I*diff(a2(t),t)=V*sin(x*omega*t)*exp(-((t-0.75*2*Pi/(x*omega))
/(1.85/(x*omega)))^2)*a1(t)*exp(I*omega*t);

>IC:=a1(0)=1.,a2(0)=0.; #initial conditions (ground state)
#define system to solve, including absolute error
>XV:=dsolve({Eqx,Eqv,IC},{a1(t),a2(t)},type=numeric,abserr=1e-5);
>XV(10.); #obtain coefficients at time t=10ps
#plot excited population
>with(plots):odeplot(XV,[t,abs(a2(t))^2],0..5,numpoints=20,color=navy);
#plot both
>odeplot(XV,[[t,abs(a1(t))^2],[t,abs(a2(t))^2]],0..10,numpoints=20);
#my wife Amanda is the bast
```

Broadband excitation results in a very weak excitation of a sharp resonance. For a peak electric field of 16 V/cm, and a dipole moment of 5 nm, the excited state population is about 5×10^{-6}. (Three times that if you are at zero field and include 2P state degeneracy.) The two state approximation is iffy here, but most of the oscillator strength is in the 1S-2P transition, anyway, and provided the power at high frequencies is dropping off fast, it may be at least order of magnitude accurate.

If the time between pulses is 12 ns and the lifetime is 120 ns, then the average

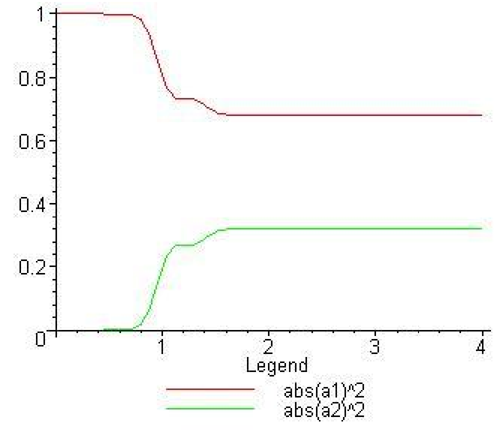

Figure D.2: Numerical simulation of population evolution of a two state system with 1S-2P neutral donor transition properties under excitation from a time domain pulse with peak amplitude of 750 V/cm (Fig. D.1) No degeneracy of the excited state is assumed.

continuous excitation fraction (including 2P degeneracy) is $10 \cdot \cdot 5e-6 = 1.5 \times 10^{-4}$. This assumes no depletion of the ground state via e.g. transitions to higher excited states and the continuum which decay to other bottleneck states.

With 50 times higher electric field the single pulse excitation fraction is on the order of 0.1 (Fig. D.2.

D.2 Floquet Theory of the two level system

Here I present useful results for calculating expected donor level shifts based on numerically exact (and analytical in the RWA) solutions from Floquet theory. I follow the notation and method presented by M. Holdhaus in an unpublished manuscript.

Floquet theory finds exact, numerically solvable time periodic solutions $\psi_n(t) =$

$u_n(t)exp(-iE_nt/\hbar)$ to differential equations with time periodic driving terms, such as the Schrödinger equation for an atom in an AC electric field. The eigenvalues E_n of the time periodic solutions are termed *quasienergies.*

The advantage of Floquet theory is that the shift of the quasienergy levels due to either resonant or off resonant excitation can be calculated nonperturbatively, and in the case of the rotating wave approximation, analytically.

In the rotating wave approximation I may write

$$\psi_n(t) = u_n(t)e^{-iE_nt/\hbar} \tag{D.106}$$

Here $u_n(t)$ is periodic on the time interval T, in the same way that Bloch solutions are periodic in space.

$$u_n(t+T) = u_n(t). \tag{D.107}$$

Now consider a two state system with unperturbed solutions $E_1 = -\hbar\omega/2$, and $E_2 = \hbar\omega/2$.

I define the following:

$$\omega_0 = \frac{E2 - E1}{\hbar} \quad \text{(transition resonance freq.)} \tag{D.108}$$

$$\omega = \text{AC driving frequency} \tag{D.109}$$

$$\omega_1 = \frac{|v|}{\hbar} = \frac{q|E|z}{\hbar} \quad \text{(Rabi freq.)} \tag{D.110}$$

$$\Omega = \sqrt{(\omega_0 - \omega)^2 + \omega_1^2} \quad \text{(generalized Rabi freq.)} \tag{D.111}$$

$$\tag{D.112}$$

The quasienergies $E_{(x,y)}$ are labelled with subscripts to distinguish the solutions. Solutions are periodic in frequency (energy) space, much like solutions to the Bloch equation are periodic in momentum space and can be divided into zones. The first index indicates which state is represented. Many states can be represented, just as many bands solutions are present in a band diagram and may be numbered. However, in our case the two states can be distinguished by a + (up) and - (down). The second index indicates in which zone (0=first zone) the solution originates.

For a drive frequency greater than the resonance frequency ($\omega > \omega_0$), the Floquet theory yields time periodic quasienergies solutions in the 0th zone which scale linearly with the generalized Rabi frequency Ω.

$$E_{(+,0)} = \frac{\omega}{2} - \frac{\Omega}{2} \tag{D.113}$$

$$E_{(-,0)} = -\frac{\omega}{2} + \frac{\Omega}{2} \tag{D.114}$$

$$\tag{D.115}$$

In this case the transition energy is reduced or squeezed by the off-resonant perturbation, which a manifestation of the AC Stark effect.

For a drive frequency less than the resonance frequency ($\omega < \omega_0$) the quasienergies are repelled.

$$E_{(+,0)} = \frac{\omega}{2} + \frac{\Omega}{2} \tag{D.116}$$

$$E_{(-,0)} = -\frac{\omega}{2} - \frac{\Omega}{2} \tag{D.117}$$

$$\tag{D.118}$$

On resonance ($\omega = \omega_1$), when the energy of the photons in the drive field equals the energy of the transition, real transitions occur. Both AC stark effects are present in this case, resulting in normal mode splitting.

$$E_{(+,0)} = \frac{\omega}{2} \pm \frac{\Omega}{2} \tag{D.119}$$

$$E_{(-,0)} = -\frac{\omega}{2} \pm \frac{\Omega}{2} \tag{D.120}$$

$$\tag{D.121}$$

For the purposes of detecting neutral donor level shifts, I assume the D^0X energy is not sensitive to the presence of THz excitation. This presumes there are no transitions originating from a D^0X state in the region of 1 THz. A transition from a bound exciton to a free 2P exciton state may be in this range. I choose to neglect this transition because I have not found it referenced in the literature, so that it may have a much smaller dipole than the neutral donor transition.

If this is the case, a change in the $D^0X \rightarrow D^01S$ transition energy is sensitive to the energy shifts in the D^01S ground state induced by the THz AC stark effect. When a narrow linewidth laser is near a D^0X transition, the elastic light scattering (ELS) may increase or decrease with a shift in the D^0X transition energy, depending on the direction of the shift relative to the position of the laser line. If the shift is in the direction of the laser line brightening occurs. If the shift is away from the laser line, the ELS cross section is reduced. The sign of the shift may change if the THz intensity causes a D^0X transition to shift towards and then past the laser line so that past the laser line so that a further increase in intensity results in weaker ELS. Additionally, shifts of other nearby D^0X transitions may affect the ELS. For this reason a spectral map of the THz-induced ELS is desirable, with data for THz excitation both above, on, and below resonance.

Appendix E

Delay line procedures

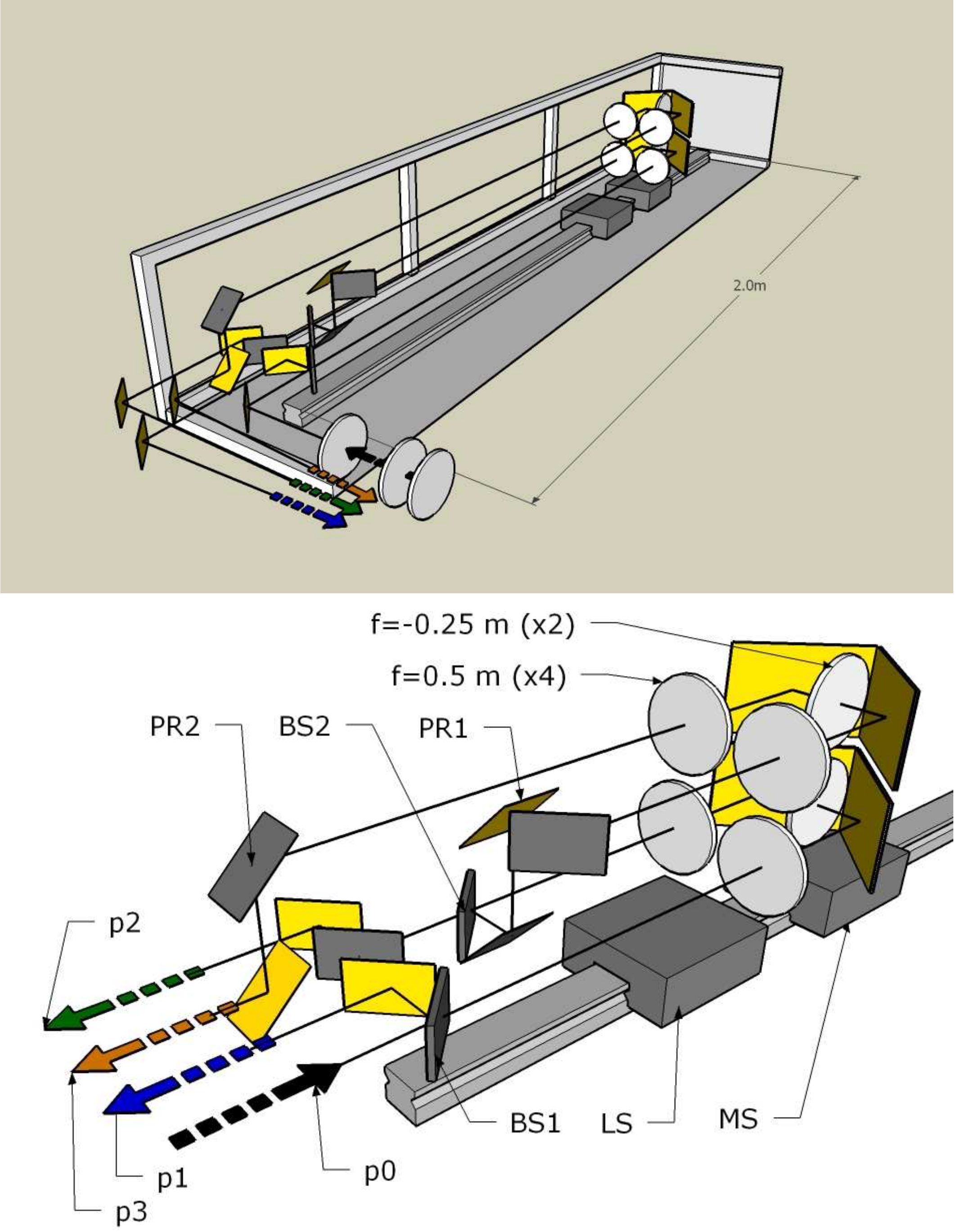

Figure E.1: 3D schematic diagram of delay line.

Contents

E.1 Important information

- Reference publication D. G. Allen, M. S. Sherwin, S. Takahashi, G. Ramian, and L. Persechini Rev. Sci. Instrum. 78, 113103 (2007).

E.2 Description

E.2.1 Pulse amplitude and delay

The optical delay line is designed to deliver two or three THz pulses of variable amplitude and variable time delay spacing of ∼0–25 ns for pulsed ESR, THz photon echo, and coherent quantum control measurements. Variable pulsed excitation of an ensemble of quantum states is achieved by adjusting pulse amplitude, rather than pulse length, since the pulse slicer or a difference frequency source delivers only one pulse of a fixed duration per FEL or NIR pulse, respectively. Alternatively, a short exciton lifetime material such as GaAs may be used as a

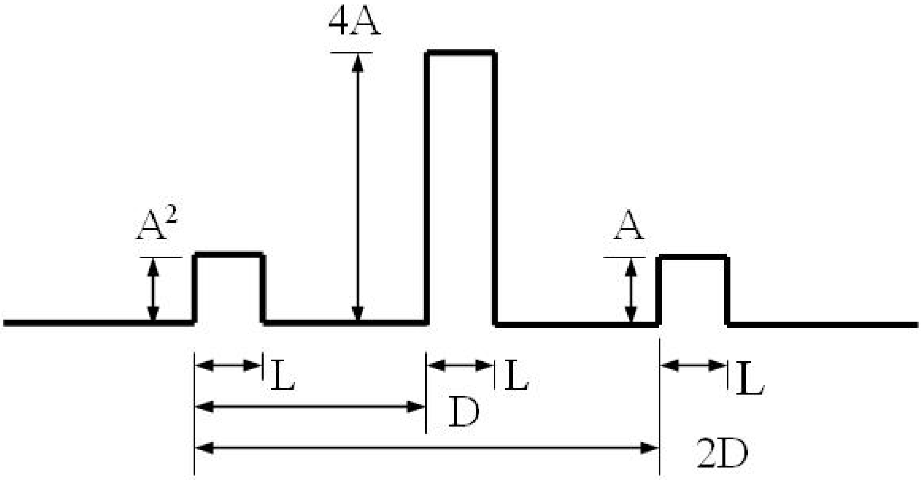

Figure E.2: Diagram showing three pulse sequence for narrowband radiation of electric field amplitude A, suitable for projected Hahn echo measurements of decoherence times in ensembles. Electric field amplitude A is chosen so that A times pulse length L gives p/2 rotation of quantum state, 2A*L gives a p pulse, and so on. The pulse length L is determined by pulse slicer and the delay time D is controlled by the total delay path length divided by the speed of light. Decoherence is mapped onto a popluation difference which can be measured via e.g. an optical quantum nondemolition technique.

switch and a visible delay line implemented to excite reflection of multiple pulses during a single FEL pulse.

In the delay line, pulse amplitude is controlled with variable etalon beamsplitters made from silicon wafers capable of 0–90% reflectivity varied by changing the etalon spacing with a lockable dovetail translation stage (manual control via vacuum rotational feedthrough).

The pulse separation, or delay, is controlled by varying the length of a detour path, i.e. mirror pair mounted on a sliding stage. Utilizing a folded path with a second circuit parallel and superior to the first, the 72” rail provides more than

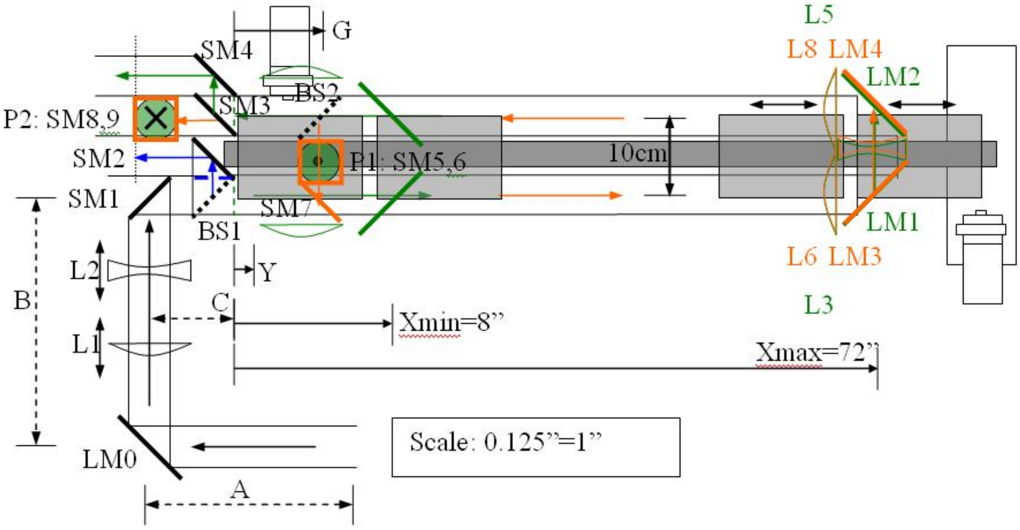

Figure E.3: Beam path length definitions for distance measurements listed in the text body.

24ns of delay, or equivalently three pulses with more than 12ns of respective delay. See the diagram below for details.

The path distances and relevant calculations of delay and focus are described below. Alphabetic labels refer to paths shown figure E.3.

1. Entrance path: A+B+C

   collimation mirror of pulse slicer transmission switch to LM0: A

   LM0 to SM1: 50.5

   SM1 to BS1: $C = 3.5$

2. Beam 1 (blue): $7 - 2Y$

   Beam waist to BS1: $-Y$

   BS1 to SM1: 2

SM1 out: $5 - Y$ (focal difference is $7 - 2Y$, as shown $f = +5$)

3. Beam 2 (green): $2X + 11.75$

   Beam waist to LM1: X

   LM1 to LM2: 4.75

   LM2 to beam waist: X

   Beam waist to SM3: Y

   SM3 to out: $2 + 5 - Y$ (focal differential is +7, as shown)

4. Beam 3 (orange): $4X + 2G + 9.75$ ($4X + 19$ for $G = 4.625$)

   Beam waist to BS2: $X + 4.75 + (X - G) = 2X + 4.75 - G$

   BS2 to SM7: $4.75 + 4.5 = 9.25$ (Beam waist again at $BS2 + G$)

   SM7 to LM3: $X - (9.25 - G) = X - 9.25 + G$ (LM3 distance X from beam waist)

   LM3 to LM4: 4.75

   LM4 to beam waist: $(X - 9.25 + G) + G = X - 9.25 + 2G$

   Beam waist thru SM8 and SM9 and out: $Y + (4 - Y) + 4.5 + 1 = 9.5$ (focal differential is +9.5)

Path 2 minus Path 1 is $2X + 4.75 - 2Y$. Path 3 minus Path 2 is 2X+2G-2. Equate and solve for Y: $3.375 - G$. For mirrors at same vertical location $G = 4.625$, $Y = -1.25$, Delay $= 2X + 7.25$, Mirror min limit at $x = 14.75$ ($D_{01} = 0.946$ m, 3.11 ns), max at $x = 71.75$ ($D_{01} = 3.829$ m, 12.77 ns) Minimum delay in focus depends on minimum mirror/lens separation (∼0.06 m for ∼3.5 ns).

E.2.2 Diffraction compensation

Since free space THz beams suffer from diffraction much more than optical beams, a delay line must compensate for diffraction so that the beam properties (diameter and radius of curvature), of the delayed pulse(s) are the same as the input beam and invariant with changes in the delay. In our system we utilize three lenses (one with focal length -0.25 m sandwiched between two of focal length 0.5 m) to compensate for diffraction. The negative lens is fixed between two 45 degree end mirrors on a sliding stage. The two positive focal length lenses are mounted on a separate sliding stage, equidistant from the negative lens. The spacing between the lens and mirror stages controls the beam properties of the delayed pulse. In our setup, with the second delay path directly above first, there are also two sets of lenses and mirrors (one above the other). We ensure the input beam has a beam waist of a given diameter (∼12 cm for an THz beam or ∼4 cm for an 250 GHz beam) located 1.25" after the first beamsplitter. We then use the q parameter transfer method to calculate the location of the lenses that will place an identical beam waist at the output. The files are on computer *FEL1380C*, located in 1380D in (User name *Exciton*, password *niobium*) My documents\Simulations\Gaussian Beams.

E.2.3 Input Match

In order to get the right size beam waist at the input of the delay line we use a combination of three lenses (as simulated with Matlab). The last optic the incoming pulse sees before being diverted into the purged delay line box is a -0.25 m focal length lens. Tracing the beam backwards from the input, this lens “expands” the beam. The location of this lens roughly determines where the beam waist will be. A second lens of positive focal length 0.25 m serves recollimate the beam when it has reached the large diameter approximately that of the THz beam coming out of the pulse slicer. Varying spacing between this lens and the last has the strongest effect on the beam reduction ratio. However, since the beam is larger at the second lens, it actually over-collimates, so that the (imaginary backwards moving) beam is now refocusing. A third -0.5 m lens is placed to straighten the beam out to match the radius of curvature coming out of the pulse slicer. These lenses must be repositioned if switching from 1 THz to 250G Hz. Kinematic locators placed on the optical rails allow the lenses to be replaced repeatably. Two lenses, rather than three are sufficient in certain restricted arrangements.

E.2.4 Optical materials

In order to minimize reflection and absorption losses we originally chose a lens material with a low index of refraction and low loss tangent: high density polyethylene (HDPE). This is transparent at THz frequencies and below. In a paper published recently (Journal of the Korean Physical Society, Vol. 49, No. 2, August 2006, pp. 513–517) we learned out polypropylene (PPE) is better at longer wavelengths and remade the lenses with better surface quality. The lenses are 4" in diameter and were custom-made by the physics machine shop on the CNC lathe. Additional lenses of ±0.5, ±0.25 m focal lengths will be easy for them to fabricate since the forms and cutting paths are already made and figured. (Tip: To get -0.5 m from a -0.25 m lens just face off one of the convex surfaces in a lathe. To align the mirrors with an optical beam we incorporated flip mounts and kinematic positioners so that the translucent lenses could be easily removed and replaced. Mirrors consist of ∼600 nm of Au evaporated onto 650 μm 6" Si substrates with a 10–20 nm Ti or Ni bonding layer, which have been cleaved to necessary sizes. Input/exit mirrors are ∼2x3", end mirrors are ∼4x6". Evaporations were done using E-beam #4 at the UCSB nanofabrication facility with custom octagon-shaped 6" wafer mounts, which can be found in the Sherwin group processing boxes at the Nanofab. Wafers were purchased from University Wafer in a box of 25. Leftover wafers are stored in the cabinet next to the clean bench in Broida 1217. The two beamsplitters consist of two 500 μm thickness, 4" diameter high resistivity wafers each. The primary wafers are permanently mounted to the removable front plate of a kinematic mirror mount (custom, Physics Shop). When out, the wafers should be stored in a custom clear plastic mounting box. The secondary wafers are removable, and can be stored in 4” stackable wafer carriers. These ”free” wafers have mall Nd magnets glued to them with Loctite instant bond glue (Thorlabs). The magnets locate against three steel balls in the translating beamsplitter mount. There is also a Au-coated wafer for improved visible alignment, if desired. Note: the three steel balls do not provide a perfectly vertical surface. Beamsplitter alignment may be checked by profiling the beam while adjusting the alignment screws.

E.2.5 Movement

The movement of the stages is controlled by two stepper motors that drive separate timing belts which are attached to the lens and mirror sliding stages, respectively. The location of the stages is controlled by LabView software. The software keeps track of the position of the positive focal length lenses and the mirror centers relative to the beam waist position, with forward (positive meters) understood to be the direction an incoming beam travels (North). When moving, the program converts meters to steps using a calibrated conversion factor which is different for each stepper. For calibration, we positioned limit switches at the ends of travel and on the mirror stage. Hard stops are located immediately beyond the limit switches. We also located an optosensor (200 μm accuracy and repeatability) in the path to act as a home switch. The stepper driver/controllers are Jova Solutions TIMS 0201 devices and are computer controlled via LabView vi’s on *FEL1380C* in the C:\TIMS stepper files directory. The driver/controller requires a 1Amp power supply at >10 V and can be configured to stop at both software and hardware limits. Separate power supplies power the two motors to eliminate cross talk and provide sufficient current while stepping both motors at the same time. *Note: the lens slider cannot reach its programmed minimum delay if the lower level HDPE positive focal length lenses are flipped out. So be careful when you flip the lenses out.*

E.2.6 Atmospheric absorption

In order to reduce the considerable absorption of THz due to atmospheric water vapor, we enclosed the entire delay line in a sealed box with removable lids. The THz beam input and outputs have a switchable 1 mil and 4 mil polyethylene window. The 1mil window affords <2% reflection per surface at 250 GHz; the 4 mil window is optimal for 1 THz with similarly low reflectivity. The removal of water vapor is accomplished by using a diaphragm pump to circulate the air through a desiccator with a replaceable desiccant; positive pressure is maintained by a continuous flow of house dry nitrogen gas (<3 l/m). Air is withdrawn from the front (input/exit) and injected at the rear. Relative humidity is monitored by a NIST traceable hygrometer located near the exit ports. <0.05% relative humidity can be achieved in less than two hours.

E.2.7 Delay compensation

The minimum delay achievable between the first and second pulse is $\sim$3.5 ns, depending on wavelength. This is limited either by the minimum spacing between the lens and mirror stage or the lens lower limit. If this is not low enough, an additional delay can be added to the first pulse to decrease its delay relative to the second pulse (to zero, or even negative delays). This additional delay path is diffraction compensated for 1 THz, but the absolute time difference not yet been calibrated. It may also be possible to diffraction compensate for 250 GHz, but the lens mounting situation may prove problematic.

E.3 Standard operating procedures

E.3.1 Powering up

Before attempting to move the stages, check the power supply and USB connections. Turn on both power supplies and check the external USB hub that powers the USB stepper firmware to ensure that two green lights are lit where the USB cables from the stepper controllers are plugged in. Check the rail path and remove any obstacles.

E.3.2 Software

The current VI to use for controlling the steppers is on *FEL1380C* in C:\TIMS stepper files and is called *delay control.vi.* Open *delay control.vi* using LabView 7.1

E.3.3 Configuration

Select the current optical configuration for the delay line and the wavenumber. (If you change the configuration or wavelength you must click *DONE* and then restart the vi with the correct settings, as these are not updated after the vi starts initially.

E.3.4 Software

Click the LabView vi run button on the menu bar. See figure E.4

E.3.5 Startup

At the beginning of the day, before trying to position the stages precisely, click the large *HOME* button. This is necessary each day to regrease the internal bearings of the stages. Otherwise, too much friction may cause steps to be skipped. While homing the stages return to their respective ends, and then step forward to their respective optosensors. The backlash on these stages is about one step, which is too small to worry about. If the backlash becomes noticeable, see the

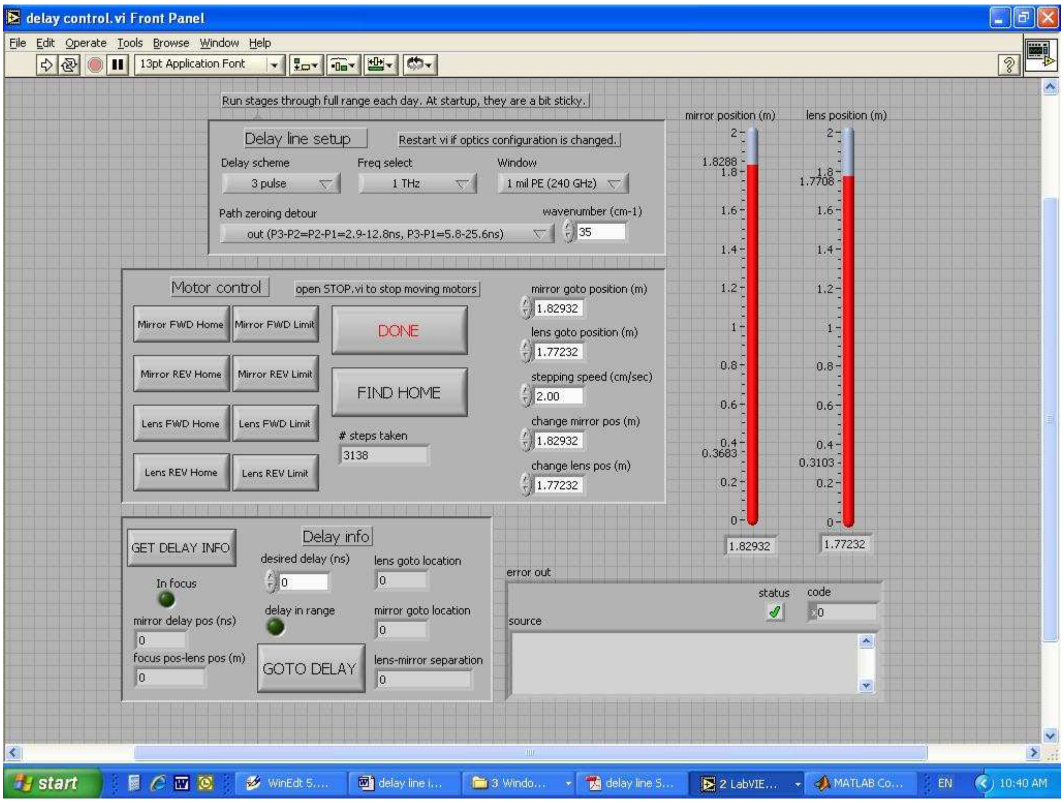

delay control.vi Front Panel

Run stages through full range each day. At startup, they are a bit sticky.

Delay line setup

Restart vi if optics configuration is changed.

Delay scheme
3 pulse

Freq select
1 THz

Window
1 mil PE (240 GHz)

Path zeroing detour
out (P3-P2=P2-P1=2.9-12.8ns, P3-P1=5.8-25.6ns)

wavenumber (cm-1)
35

Motor control

open STOP.vi to stop moving motors

steps taken
3138

mirror goto position (m)
1.82932

lens goto position (m)
1.77232

stepping speed (cm/sec)
2.00

change mirror pos (m)
1.82932

change lens pos (m)
1.77232

mirror position (m)
1.8288
1.82932

lens position (m)
1.7708
1.77232

Delay info

desired delay (ns)
0

lens goto location
0

mirror delay pos (ns)
0

mirror goto location
0

focus pos-lens pos (m)
0

lens-mirror separation
0

error out

status
✓

code
0

source

Figure E.4: Screen capture of LabView vi *stepper control.vi.*

section on retensioning the belts. You will not be able to do any other front panel operations while stage motions are in progress. Note: the optosensors have a TTL inverting circuit on their output which is necessary for correct operation. This must provided ∼5 V when high in order to work. The limit switches connect and digital input to ground when closed.

E.3.6 Motor Control

If it is evident that the positions of one or more of the stages do not match the value shown on the vi front panel (sliding indicators on the right side), then send the errant stage to its home or limit using one of the various home and limit buttons (left side). In the middle are controls for deliberately altering the recorded position of the stage or sending either the mirror or lens stage to a specified position. This may be done by simply entering a new value.

E.3.7 Changing the delay

The lower left set of controls is for sending the lens and mirrors to a specific delay. Clicking *Get Delay Info* will return information about where the mirror and lens stage are. The current delay indicator tells where the mirror stage is, and the other numeric indicator tells how far out of focus the lens stage is, for the current wavelength. If the focus is satisfactory (<1 mm off), the *In Focus* indicator will be lit. To move to a new delay enter a value in the Goto Delay numeric control. If the delay is attainable an indicator will be lit. Click the "Goto Delay" button to actually move the mirrors and lenses to the desired delay. The firmware prevents either the lens or mirror stage from moving in the forward (reverse) direction when its forward (reverse) limit switch is closed. If you send the stages to a new delay and find that only one stage is moving, the stages were probably in contact when you sent the command. Simply wait until the other stage is done moving and then click the "Goto Delay" button again.

E.3.8 Retensioning the timing belts and recalibrating the steppers

If backlash becomes a problem or steps are being skipped, it may be due to loose timing belts. If this appears to be the problem you must retension the belts. The stepper motor and gear at the east end of the box can be loosened and pulled back to tension the belts. Afterwards the stepping parameters must be recalibrated. Run each stage to its respective limit and see how many steps it takes to get from one side to the other. Check what maximum speed allows you to do this repeatably. (The fewest number of steps is correct. More steps means steps were skipped trying to accelerate or trying to move too quickly. Next, use calibrate.vi to calculate the correct stepper settings if the timing belts are retensioned. Enter these new settings along with the maximum stepping speed into the global vi called *stepper settings.vi.* This vi stores the ranges of travel of the respective stages, the meters to steps conversion factors, home and limit switch locations and other important default settings. For instance, we must always use *half-stepping* mode, because the motors do not have enough torque to drive the stages with full steps.

E.3.9 Debugging

If an error pops up or only one of the stages is moving or something goofy. Close the program by hitting the *DONE* button. If that doesn't work hit the stop button. If nothing is wrong and you hit the *STOP* button, something WILL be wrong. You close the program before it had a chance to close down the connections with the firmware. Now you will have to close the connections manually using *close.vi*. Open one of the subvi's to see what the last mirror and stepper TIMS session numbers were. Use these numbers to close each TIMS controller manually. Other tactics include unplugging the USB connections (after shutting of the 10 V power to the stepper motor) and plugging them back in. Lastly, there is a TIMS LabView-based control panel provided by the company that you can access from the start menu. When you open it you will find a souped-up version of my delay control program. You can open and close the respective controllers via their serial numbers (see stepper settings.vi). You can also move them. But, please, if you do, be sure you have set the controllers to half step, and set the current limit to something reasonable and don't be an idiot by changing this you don't know about.

E.3.10 Triggered operation

The stages can be setup to move on an external trigger (FEL trigger, signal for instance). If the clear I/O pin is enabled using a TIMS vi, a rising transition on the trigger will be held by a flip-flop chip and the value can be readout by GPIO pin 5, which is an analog digital converter (ADC). The flip-flop does not provide enough voltage (only 3.5 V) to register as high on a TTL digital input (∼5 V), so the ADC must be used and the voltage compared (in a vi) to a threshold (below 3 V) in order to see whether a pulse has arrived. If a pulse has arrived, a vi can tell the motors to go to a new delay. During that time, the clear I/O pin is low, so that no pulses coming in the mean time are counted. Once the stepping is complete, enable the clear pin using a TIMS vi and the process can repeat. I might be backwards on the clear pin, but it's one way or the other, so it shouldn't be hard to figure out.

E.3.11 Purging

When using THz radiation, it is imperative that the box is purged of as much atmospheric moisture as possible. Sub-mm wave radiation is probably fine without purging. This won't happen if the desiccant in the desiccators has gone bad. That will happen if you leave the system open for a long time. The purge line has two valves that isolate the pump, desecrator, and in-line filter, which you must shut when the purge system is not in use, or your desiccant will die. To purge, screw the plastic frame with the appropriate PPE film window to the inside edge of the input frame. The plastic window should be in a padded yellow document mailer on top of the optical table rack. Replace the acrylic lids with Al angle bracket stiffeners. They only go on one way and should be labelled. Secure the latches. Be sure there are no leaks. Use small clamps to hold the two lids together at the seam between the lids. Turn on a few liters/min of nitrogen flow. Open the valves and plug in the pump. The pump draws air out of the east end and replaces it at the west end. If you can hear sound coming out of the seam between the lids, air is escaping—fix it. The hygrometer can be used to monitor the purge process. <1% relative humidity should be achieved in less than two hours. If the plastic front window and lids are not in place, desiccation will not be unsuccessful.

Appendix F

Optical switch procedures

F.1 Important information

F.1.1 Notes

- Read the New Focus Velocity tunable laser instruction manual before using it. The output is 814.5–825 nm, ~5 mW, and vertically polarized.

- Note that the beam size, profile and astigmatism are different for the tunable laser and alignment laser.

- Do not attempt to trigger the Pockels cell faster than 50 Hz.

- The LabView files for operating the laser are located on computer *FEL1380C* (that's the computer's name, not the room name anymore), user: exciton, password: niobium. The most current vi for computer controlling the laser is Dan Allen's documents\Instruments specs and vi's\New Focus Tunable Laser\750 CCD2version7p1.vi. This vi also controls the Acton monochromator, the Princeton Instruments CCD, and LeCroy scope.

- Use care with electrical signals and NIR laser beams.
- The Pockels cell uses voltages as high as -2.5 kV, and will contribute a huge amount of electrical noise to the environment when it fires.
- You must use a double pass setup in order to get a half wave of rotation from this Pockels cell. The setup described here is not the most efficient use of optics or laser power, but it is the most effective I have found in getting a high contrast ratio. You may be tempted to use a retroreflector in the place of the roof mirror assembly. I have tried a corner cube prism and also a hollow retroreflector, with poor results (contrast ratio <100). It seems the beam experienced depolarization or polarization rotation upon reflection. I eventually went with two gold mirrors in a roof arrangement and that worked better.

F.1.2 Overview

This setup is designed to deliver either microsecond duration optical pulses or continuous wave laser illumination with horizontal output polarization for optical light scattering measurements of donor bound exciton bound state dynamics with terahertz excitation.

Table F.1: List of parts and abbreviations.

Part name (m)	Symbol
Tunable laser	TL
Alignment laser	AL
Periscope mirror1	$PER1$
Periscope mirror 2	$PER2$
Flip mount 1	$FM1$
Iris 1	$IR1$
Filter block	FB
Polarizer 1	$POL1$
Half waveplate 1	$WP1$
Pockels cell	PC
Flip mount 2	$FM2$
Iris 2	$IR2$
Roof mirror assembly	RMA
Pick off mirror	PM
Cross polarizer	$POL2$
Half waveplate 2	$WP2$
Flip mirror 3	$FM3$
Bending mirror	BM
Iris 3	$IR3$
Si photodiode	DET
Beam expander	BX

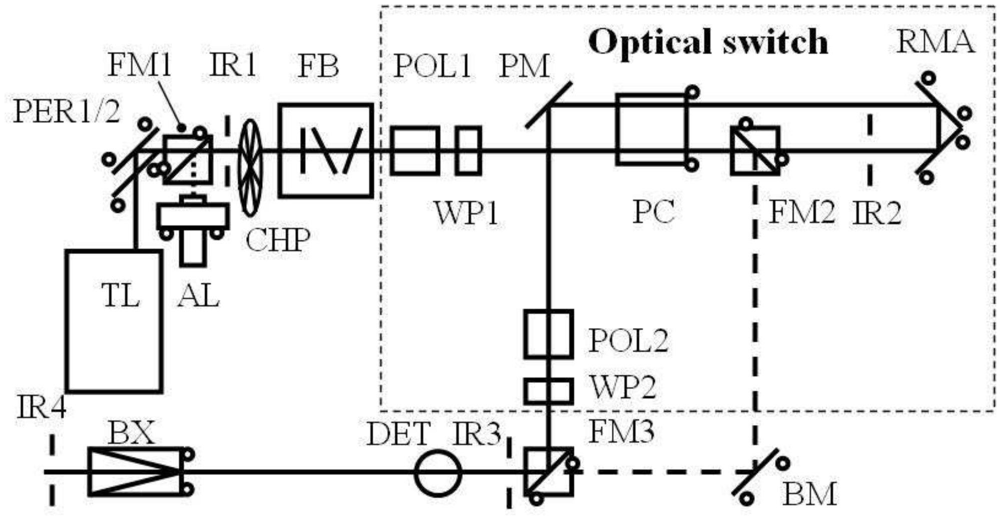

Figure F.1: Layout of optical switch beam paths and optical elements.

F.2 Optical path alignment

1. Insert variable apertures (irises) IR1 and IR2 at 5–5.1” beam height.

2. Insert in the polarizer (POL1) and waveplate (WP1). Align POL1 to maximize transmission (near horizontal). Put WP1 near 0 or 90 degrees. Later you will adjust WP1 to get the polarization horizontal.

3. Power on the controller and turn on the New Focus velocity tunable laser.

4. Align tunable laser (TL) output through irises IR1 and IR2 using periscope mirrors (PER1, PER2) and a fluorescent IR alignment card. *Do not use a sensitized card, which although it may make the beam easier to see, will blur the spot and hamper fine alignment.* Alternatively you can use the IR viewer with an iris for reducing the input aperture to preventing saturation

at the laser spot.

5. Align the 673 nm alignment laser (AL) through IR1 and IR2 using tip/tilt laser mount and the bending mirror on the first flip mount (FM1). Switch this mirror gently, as it has a tendency to twist if pushed hard. If the AL and TL ever become misaligned, check this first. For the following steps you may use either the red alignment laser or the New Focus laser. The red alignment laser will be helpful for aligning to a sample in a cryostat.

6. Insert the Pockels cell (PC) parallel to the beam and centered vertically. The crystal axis is in the direction of the high voltage cable and should be horizontal. Insert roof mirror assembly (RMA). Align RMA so that the return beam is separated by 4–6 mm from incident over the entire length of the IR1–IR2 path. Keep the spacing small enough to fit both beams through the Pockels cell but large enough so that the beam may be picked off without clipping either the incident or return beam. *The contrast ratio of the optical switch depends critically on the collinearity of the incident and return beam.*

7. Insert FM2 and remove the third flip mount (FM3). Use FM2 and the bending mirror (BM) to align the beam through IR3 and IR4. Check that AL and TL are collinear. If not, redo the alignment of the TL and AL to IR1 and IR2, then continue to align to IR3 and IR4 until they are perfectly collinear. Remove FM2.

8. Insert the pick off mirror (PM), cross polarizer (POL2) , waveplate (WP2), FM3, and second set of irises (IR3, IR4). Put the cross polarizer to horizontal, initially, to transmit. WP2 can stay at 45 degrees. You may later adjust it to achieve horizontal polarization for Brewster's angle incidence on samples in the cryostat. Do not insert the beam expander yet.
9. Align the picked off return beam through IR3 and IR4 by adjusting PM and FM3.
10. Insert the 5x beam expander (BX) and center the emerging beam in IR4. Use bending mirrors and the BX tip and tilt to direct the beam. Use the threaded focusing tube and lock ring to adjust the size of the beam near the cryostat where you will shaping the beam with cylindrical lenses and focusing to the sample.

F.3 Aligning the Pockels cell and optimizing the contrast ratio

1. Check that TL is on and FM1 is out. Switch out FM3 and insert FM2.
2. Insert a DC coupled Si photodiode (DET) with variable gain at the output of the optical switch, or attach an amplifier with a variable number of gain stages to the detector and view the output on the scope. Set gain to minimum. Insert the chopper (CHP) and view the signal on the scope and then

on a lockin amplifier. Write down the signal amplitudes or measure with a power meter for later diagnostics.

3. Orient POL2 to vertical to cross polarize the optical switch. Rotate WP1 and note maximum signal amplitudes on scope and then on the lockin. Now rotate WP1 to achieve minimum transmission (adjust gain as necessary). Note minimum signal amplitudes. Remove the chopper.

4. Prepare a signal generator with TTL pulses at a rep rate of less than 50 Hz; 10 Hz is normal. Trigger the scope with the synch signal from the generator. Plug in the Pockels cell DC power supply. Send the TTL pulses to the Pockels cell. Adjust the detector gain until you can most easily view the switched signal.

5. Fine adjust WP1 and the Pockels cell tip and tilt to maximize the switched amplitude while minimizing leak-through, by viewing the optical switching on the scope. You may have to adjust POL2 slightly to optimize this, as the Pockels cell axis is fixed. You may try using the method of making a small adjustment one way with POL2, then optimizing WP1 for minimum leak-through and Pockels cell tip and tilt for maximum switching amplitude. Continue rotating POL2 in that direction if contrast ratio got better, or go other way if worse. The Pockels cell tip and tilt are very sensitive. You may want to purchase a more sensitive and more stable tip/tilt mount, such as a New Focus opticlaw mount or tip/tilt stage. Cable strain can alter the

contrast ratio. I have good luck when the power supply is loosely anchored, rather than clamped tightly, since that hampers fine adjustment.

6. When the switching amplitude gets large enough you will see that at short times the signal may be larger than at long times. This is due to the difference between the AC and DC polarizability of the PC crystal. You may need to adjust the voltage to the Pockels cell to optimize the flatness of the time response and full switching amplitude. Ringing may be present in the optical power due to electrical ringdown in the circuit. You care most about short time (<100 ns) response. Optimize this rather than the long >1 μs response. Remove the cover to the Pockels cell drive. Use a narrow, long screw driver to adjust the voltage while watching the output on the scope. The ten turn potentiometer will click when it reaches its end of travel. Further turns will produce more clicks, but no more voltage. 80% of maximum voltage should be sufficient if the incident polarization is correct and the return beam is collinear. When optimized, turn off the function generator pulses and replace the chopper to quantitatively measure the leak-through. I have gotten on/off contrast ratios of ∼500–1000.

When finished, the beam emerging from either BM or FM3 should be nearly horizontally polarized and the switched beam coming from the switch should be ∼80% of the continuous wave signal available from the FM2–BM beam path. Recheck collinearity of AL and TL before aligning to the sample from the FM2–

BM beam path. Adjust AL tip/tilt and FM1 tip/tilt if necessary to achieve this.

Do not touch the TL beam path anymore.

Appendix G

CCD spectroscopy procedures

G.1 Parts needed

- Acton 2750 (750 mm focal length f/9.7 imaging grating spectrometer with #1 1800 g/mm – 500 nm blaze grating and #2 1200 g/mm – 1 μm blaze grating, USB communication, power supply.

- Princeton Instruments CCD (back illuminated, deep depletion, LN2 cooled 1340x400 pixel CCD array, 20x20μm pixels, three gain settings (side switch), shutter included, 2 L volume, controller cable, controller, USB2.0 communication.)

- Neon lamp mounted to optical pose wired to 120 V plug (available at e.g. Radio Shack).

- Powered USB hub (if needed to relay long USB cables)

- Lens tissue (for diffusing neon lamp of femtosecond laser, etc.)
- The pipe (1mm diameter multimode optical fiber for coupling lots of light easily.)
- The computer named *FEL1380C*
- LabView VI's for Acton
- LabView VI's for CCD
- Roper scientific WinView32 software

G.2 Important information

- Gratings prefer vertical polarization
- Do not cool down the CCD unless it is plugged in to the controller and the controller is plugged in and powered on (indicator glows). Static may build up on chip and blow up the CCD as it cools.
- Multimode fibers impose a frequency modulation on light transmitted through which is evident in the spectrum. A white light source such as an incandescent bulb (e.g. flashlight) can serve as a background to remove this modulation.
- The CCD case needs to be pumped out every 6 months. You will be able to tell when it needs to be pumped out because it only holds LN2 for a few

hours instead of more than a day. Borrow an adapter from the Awschalom lab.

- VI's are located in the computer FEL1380C (now found in room D), user: exciton, password: niobium. In My Documents\ Instruments Specs and VI's.

G.3 Getting started

1. Get all the parts.

2. Get the spectrometer ready: Open the Acton software or the vi monocontrol.vi or most current version in the ACTON SP2750\ARC_instrument_dll_SDK folder. Do not use `monocontrol2.vi` which is a sub-vi for other vi's to call. Run the vi, select the grating, set the output flipper mirror in or out for single channel or array, and set the wavelength. For safety and grating cleanliness, manually close the slits to 0.0 mm when not in use. The maximum width is 3mm. Do not open further than 3 mm.

3. Get the CCD ready. Mount the CCD if it is not mounted. Try to make it as vertical as possible. The screw stop is set at the focus position and should never need to be adjusted. Plug in CCD, CCD controller, Acton spectrometer and neon lamp.

4. Power on the CCD controller.

5. Use a funnel to add liquid nitrogen to the CCD. Add 300–500 ml or so, wait five or ten minutes, then fill the rest of the way. Replace the cap but do not screw down cap immediately. Wait a half hour or so until it stops boiling vigorously. Top-off later in the day. When the pressures gets high enough a pressure release valve will blow. Do not be startled.

6. Wait 1–2 hrs for the CCD to cool.

7. Set the neon lamp near the entrance slits and plug it in. Place a few sheets of tissue paper between the lamp and the spectrometer entrance.

8. Open the slits 10μm.

9. Open the software `operateCCD_7p1.vi` or most recent version in the Instruments specs and VI's\PrincetonInstruments folder. Set the region of interest before you run the vi. I use the full CCD 1–1340, and 1–400, pixel binning of 1. Make sure background subtraction is *on*. Run the vi. Move the background window over so you can see both the exposure and background. Check the temperature. Set exposure to 1 s. Take background. Save the background. Choose the background spectrum you just saved. Now the directory path is set. Get exposure. Get spectrum or Save spectrum. Now you have a background file and test file you can use with WinView32. You can modify the VI to save the full CCD image, a text file of the spectrum

(columns are pre-binned), or both.

10. If the shutter doesn't open during an exposure (it shouldn't open for a background) toggle the shutter condition and keep trying backgrounds and exposures until it works right. Sometimes it gets messed up, even with WinView32.

11. Stop the VI by pressing the *End/Stop* button. Never stop the VI with the stop sign button or risk having communication problems when you try to start the VI again.

12. Open WinView32 (you can't run this at the same time as LabView without generating a create camera error that will cause you grief and turning of and turning on again of instruments and/or computers.)

13. Go to experiment, choose the tab data corrections. Choose your background file that you saved. Choose cosmic ray subtraction. Select the whole CCD for the region of interest usually. FYI, coming in straight, the entrance slits illuminate the vertical pixels 100–300. Choose your desired exposure time. Choose the name and directory of your data file (the one you just saved). FYI, you can't create a new blank background file in this program, which is why you use the VI first, to create files in the first place. Otherwise you have to take a spectrum called "test1.spe" without a background, then save that file as a background, toggling the shutter state, then taking a new

spectrum, renaming files as you go. The file format is `.spe`, which is useless for all intents and purposes. To change to .txt use the WinView32 convert to txt function, which is pretty self explanatory. You can get the active window (the last picture you selected) or click choose multiple images via a file folder browser pop up. You choose the export directory and format and the program converts all the `.spe}` files to `.txt` (saves a new file with the addendum `_1.txt`.

14. The most useful thing about WinView32 is the *Focus* function which takes repeated exposures and displays them on the screen in a large window. This is most useful for alignment of a source into the spectrometer or peaking up a signal. The worst part is that you can't get a spectrum without hardware binning all the pixels, which, of course reduces the SNR since you aren't subtracting the background counts for each pixel. Background count rates vary from pixel to pixel, but the rate is fairly constant at a constant temperature. If you need to do long stable exposures, be sure the CCD is pumped out so that it can reach its minimum temperature and lock the temperature stably.

15. Use the focus capability to align the CCD so that the spectral lines are vertical. Right click in the data window and adjust the window settings so that you have a vertical line cursor. Adjust the data range for contrast so that you can see the lines of interest clearly. This is very important for high

resolution spectroscopy. The set screw clamp on the acton spectrometer is not so strong, so you can bump the CCD if you are not careful. As mounted at the time of writing, the CCD is on an upper support table above the millennia and Tsunami. As mounted, the CCD is nearly vertical when the cap can be pulled out via a thru hole in the overhead dust cover/table/rack thing.

16. Close Winview32.

17. FYI, A more powerful program WinSpec, has been installed on the laptop Sam by a visitor to the university. This can control both the spectrometer and CCD. It will also provide a nanometer or wavenumber scale for the spectrum.

G.4 Calibration

You can try to follow any logical procedure you can think of for calibrating this instrument using the Acton spectra pro software , but you will fail because there are only two fit parameters: grating groove density and relative, but the grating dispersion is nonlinear, so you need a higher order term. This is a very disappointing aspect of this spectrometer, in addition to the abundance of stray rediffracted light due to the symmettric design, the lack of a repeatable angular stop for mounting the CCD, etc. The best way to calibrate is to use the Neon lamp to find spectral lines within a CCD spectrum at a grating setting you can use for your experiment. Then fit those lines to a second order polynomial since the dispersion across the face of the grating is nonlinear, especially at longer wavelengths with the 1800 g/mm grating.

The following VI's can be used in coordination to plot a calibrated spectrum using Matlab.

`dispersion.m`: An executable function that calculates CCD dispersion at input center wavelength (near 818 nm) based on interpolating Ne lines from either side of 818 nm.

```
function disp=dispersion(wl)
disp=0.00884+(0.00831-0.00884)/(837.481-807.648)*(wl-807.648);
return
```

nmaxis4.m: An executable function that delivers a nm scale axis based on the center wavelength (spectrometer goto wavelength), the grating number (1 or 2) and the number of horizontal pixel data points in the spectrum.)

```
function x=nmaxis4(cw,gr,num)
m=1:num;
if gr==2
    dx0=0.018066; %nm/pixel
    ddx=0.01145; % percent change over region near 820
    cp=688.134;
    x=cw+dx0*(1-ddx*(m/1340)).*(m-cp);
else
    dx0=dispersion(cw); %defaults to grating one
    cp=685.9037+(692.74-690.2)/(825.938-813.641)*(cw-813.641);
    x=cw+dx0*(1-(m-cp).*0.024/1340).*(m-cp);
end return
```

nmaxis4.m calls dispersion.m. Also, this is the via which you must adjust after removing the CCD and replacing it, because the center pixel position is moved by several pixels each time you do this. To do this, choose a neon line near your spectral region of interest. You can download these lines from the NIST spectral database or look them up in a file Storage Hard Drive\Dan's Stored Documents\Data\Calibrations\NIST neon lines.doc. or look them up in the Matlab script `dispfit3.m}`.

```
dispfit3.m
clear
close all
cw=813;
roi=[100,300];
nf=5000;
dx0=0.0086;
ddx=0.0002;
f=[dx0,ddx];
file='813nm_25umslits_1sec_1.txt';
data=sumup(roi,file);
peak=peakfind(data,nf);
peak=peak+1;
peaks=pixmaxfit(peak,data); p=length(peaks);
fprintf('%g peaks found \n',p);
wl813=[808.24580,811.85492,812.89108,813.64057];
wl828=[824.86823,825.9379,826.60772,826.71165,830.03263,830.15597];
wl832=[826.60772,826.71165,830.03263,830.15597,836.57485];
wl817=[811.85492,812.89108,813.64057]; wl=wl813 difwl=diff(wl);
option=optimset('TolX',1e-7);
f2=fminsearch('leastsq4',f,option,peaks,difwl,cw);
dx0f=f2(1)
ddxf=f2(2)
x=nmdispfit2(cw,f2,peaks)
```

This calls several Matlab scripts, all of which can be found in nearly any recent directory of the Storage Hard Drive\Dan's Stored Documents\Data folders. I think this is the VI that calculates the dispersion I have hardwired into `dispersion.m`.

As I was saying, choose a Ne line; I use 813.64nm. Send the spectrometer to this wavelength, estimate where the peak is, then use the program pixmaxfit.m to fit the peak to a Gaussian, with the peak maximum as the *startpix* input. The fit is accurate to much less than one pixel width.

```
pixmaxfit.m

function pixmax=pixmaxfit(startpix,spec) s=length(spec);
ps=length(startpix); x=1:s; for l=1:ps
    sp=spec;
    sp=(abs(sp)+sp); %get rid of any negatives
    n=1;
    %get region near peak
    for n=1:21
        if startpix-n>0
        d(n)=sp(startpix(l)-(11-n));
        x2(n)=x(startpix(l))-(11-n);
        end
    end
    %initial fit parameter guesses
    fp(1)=sp(startpix(l)); %guassian height
    fp(2)=1; %guassian width
    fp(3)=x2(11); %guassian center
    %set options, get the fit parameters
    option=optimset('TolX',1e-5);
    fp2=fminsearch('leastsq',fp,option,x2,d);
    pixmax(l)=fp2(3);
    fprintf('peak at pixel %g\n',pixmax);
    specmax(l)=spec(round(fp2(3)));
end
figure
plot(x,spec,'k.-',pixmax,specmax,'r.')
return
```

Now enter the value for the calculated center pixel into nmaxis4.m, as the first term in the cp definition. E.g. If I get 685.9037 from pixmaxfit.m, then the cp definition line in nmaxis4.m should be the following. The extra terms are necessary to reference the grating value to the known center pixel position.

```
cp=685.9037+(692.74-690.2)/(825.938-813.641)*(cw-813.641);
```

Now your CCD is calibrated.

G.5 Taking and plotting data

Remove the Ne lamp. Take spectra as desired. The minimum linewidth is for a slit width of 10–15 μm. 20 μm slits only slightly reduce the linewidth, which can be fit to something of cross between a Gaussian and a sinc lineshape.

You may use `operateCCD_7p1.vi` to take data, since it bins and saves your spectra in a text file labelled `.spe.txt`. To plot the data on your calibrated nm or eV axis, use the Matlab script `nmplotCCDspec.m`, or `evplotCCDspec.m`.

If you use WinView32 and convert your data to txt files, then you must first bin the data using the `sumup.m}` file, before plotting. To do this use `eVplot4.m}` or `nmplot4.m`. Use these scripts for any spectrum ending with `1.txt`.

Example scripts are shown below, encoding for the option to make a logarithmic plot.

```
nmplotCCDspec.m
clear
close all

file='pl3p82T_15s.spe.txt';
%file='pl815_20s_5T_d2.spe.txt';
```

```
spec=load(file);
cw=818.00; %monochomator center wavelength
gr=1;
%x=eVaxis4(cw,gr,length(spec));
x=nmaxis4(cw,gr,length(spec)); lg=0; figure hold on if lg==1
    %getting data ready to take log
    spec=spec.*(1+sign(spec)); %zero if negative
    spec=1+spec; %get rid of zeros
    plot(x,log10(spec));
    aa=gca;
%     set(aa,'XLimMode','manual','YLimMode','manual',...
%     'XLim',[1.508,1.518],'YLim',[2,7],...
%     'FontSize',12,'LineWidth',2)
else
    plot(x,spec/0.9e5,'k.-')
end
%
xlabel('nm') ylabel('CCD counts') title(file)

eVplot4.m
clear
file='pl816p5_od0p9_30s_1.txt';
y=[100,300];
gr=1;
cw=818.;
spec=sumup(y,file);
eV=eVaxis4(cw,gr,length(spec));
figure

lg=1;
if lg==1
    %getting data ready to take log
    spec=spec.*(1+sign(spec)); %zero if negative
    spec=1+spec; %get rid of zeros
    plot(eV,log10(spec));
    aa=gca;
    set(aa,'XLimMode','manual','YLimMode','manual',...
    'XLim',[1.508,1.519],'YLim',[0,7],...
    'FontSize',12,'LineWidth',2)
else
    plot(eV,spec,'k.-')
end
%
```

```
xlabel('eV') ylabel('CCD counts') title(file)
```

Appendix H

Gaussian beam calculations

H.1 Important information

This appendix details matlab files developed for simulating Gaussian beams in the paraxial approximation for help in predicting terahertz beam divergence and focusing properties.

For useful detail on the theory of the q-parameter and transfer matrix methods used in this simulation see the classic paper by Kogelnik[78].

This theory applies to beams with a cross section intensity profile which is Gaussian in shape. Such beam profiles are typically obtained from laser gain media, spatial filters, and corrugated feedhorns. The formalism operates is in the paraxial approximation ($sin(\theta) = \theta$), and is suitable for weakly focused beams. The q-parameter method is third place out of four in the successive levels of electromagnetic approximations which includes unapproximated full wave (e.g.

FDTD), Fresnel Kirchhoff integral method (spherical wavefront approximation) , paraxial approximation (parabolic wavefront), and ray optics approximation (flat wavefront). To perform more accurate calculations you may try getting help from Gerry Ramian who has developed his own 3D Fresnel-Kirchoff simulation software. The present method is a 1D simulation which does not take into account any mirror or lens nonidealities, including but not limited to manufacturing errors in sphericity, decentering, spherical aberration, astigmatism, absorption, etc. Far field diffraction and refraction at interfaces are the salient features of a q-parameter simulation.

The q parameter is a complex number defined in the following way.

$$\frac{1}{q} = \frac{1}{R} - \frac{i\lambda}{\pi/w^2}, \tag{H.122}$$

where R is the radius of curvature and w is the $1/e$ beam waist radius of the Gaussian beam. This parameter is transformed by free space propagation and refraction or reflection at interfaces according to the simple rule

$$q_2 = \frac{(Aq_1 + B)}{(Cq_1 + D)}. \tag{H.123}$$

A, B, C and D are parameters which can be calculated for free space propagation, refraction and transmission at interfaces and used to calculate beam transformations through complicated sequences of optical elements by iterating the transformation, much like the ABCD transfer matrix method used in ray optics.

H.2 Annotation of Matlab scripts

The lowest level Matlab scripts used for Gaussian beam simulations encode these transformations.

H.2.1 User-set variables

- *lambda* or *wn* (wavelength [m] or wavenumber [cm-1], varies depending on script)
- $n1$, $n2$ (two possible different indices of refraction)
- N (current index of refraction, global variable, assign N=n1 to start)
- W (initial beam waist radius)
- *cr* (curvature=1/initial radius of curvature in meters)

H.2.2 Dependent variables

- $z1$ Rayleigh range
- q (Array storing all previous values of q parameters and positions q parameter was evaluated at)
- *wa* (initialized beam waist radius array variable-stores position and beam waist)

H.2.3 Global variables

- N (assign current index of refraction to this global variable which is needed by subroutines to calculate the beam waist at each position)

- w (This array variable serves as log of previous beam waist values and specific positions. Beam waist radii must be kept track of separately from q parameter since beam waist size depends on current index of refraction.)

H.2.4 Lowest level subroutines for q parameter transformation

- thinlens.m (thin lens)

- sphmirror.m (spherical mirror)

- dielsph.m (dielectric spherical interface transformation)

- dist.m (travel a given distance)

- newmat.m (flat interface at a new material with a different index of refraction)

H.2.5 Subroutines for calling lowest level routines, and e.g. updating position, and extracting beam waist parameters

- sphint.m (calls sphmirror.m)
- thicklens.m (calls dielsph.m and dist.m for transmission through a thick lens with defined front and back surface radii and a given thickness)
- thicklenssb.m (backward progagation through a thick lens)
- freeprop.m (calls dist.m, evaluates it over 100 equally spaced points and extracts beam waists at those points) freepropL.m (calls dist.m and evaluates it over 1000 when finer steps are desired)
- backprop.m (negative distance)
- backpropL.m (negative distance, fine spacing)
- lens.m (calls thinlens.m)
- lensprop.m (calls lens.m and increments the position a small amount which helps when plotting beam waist vs. position)
- flatint.m (calls newmat.m)

H.2.6 Utilities

- rad.m (calculates the beam waist radius of curvature for the input q parameter
- getradius
- waist.m (called by subroutines to calculate beam waist from q parameter, updates global)

H.2.7 Example code

Here is example code for how to run the simulation from the file "inputmatch1THz.m".

```
close %close plot window 2
close %close plot window 1
clear %clear all variables in memory (for stability)
%enter intial beam parameters
W=0.01; %1/2 of beam diameter (meters) coming out of port from FIR FEL
%W=650e-6/2; %beam 1/e^2 intensity RADIUS (meters) 1300um pinhole
cr=0; %inverse radius, 1/beam radius of curvature, positive if expanding
wn=35; %wavenumber
n1=1; %index of refraction
n2=3.4; % other index of refraction

%compute starting q values
global N wa lambda
lambda=1/wn*1e-2;%lambda in meters
N=n1; wa=0;
z1=N*pi*W^2/lambda; %rayleigh range
q(1,1)=1/(cr-i/z1); q(2,1)=0; wa(1)=waist(q(1,1));

%in to meters conversion
con=0.0254;
```

```
%mirror focal lengths and distances in inches
f1=2.2; %in
f2=4.8; %in
f3=5;   %in
f4=1.5  %in
d1=2.2; %in
d2=4.8; %in
d3=5;   %in
dx1=0.1;  %in
spac=8 %in
dx2=10  %in

% % begin propagation
q=freeprop(q,7*con);    %to table and 45deg mirror
q=freeprop(q,12*con);        %to last lens
q=lens(q,-0.25);        %pass through lens
q=freeprop(q,9.15*con); %propagate distance
q=lens(q,0.25); %pass through another lens
q=freeprop(q,2*con); q=lens(q,-0.5);

q=freeprop(q,10*con);


%end propagation

%plot beam waist
z=q(2,:); %pick of second row: position

figure
plot(z,2*wa,'k') %plot 1/e^2 beam diameter versus position
xlabel('position') ylabel('beam diameter (m)') title('Input to
delay line at 35cm-1')

% figure
% plot(z,real(1./q(1,:)))
% ylabel('beam curvature (m) 1/radius of curvature')
gf=real(1./q(1,:)); gf(length(gf))
```

Appendix I

Difference frequency generation procedures

I.1 Important information

I.1.1 Notes

- An SOP document exists for Tsunami/Regen, use it.
- LabView files located on computer *FEL1380C* (that's the computer's name, not the room name anymore), user: exciton, password: niobium, my documents\Instrument specs and vi's\newport stepper and dfg.
- Pulse compressor schematics are located in Instruments specs and vi's\pulse compressor or in the equivalent folder in Dan's documents on the laptop *Sam*.

- When reporting work done with this instrument please reference the initial experimental report of DFG by this method: Yun Shik Lee, CLEO 2007, who explained the design to us. We did not invent this. There was theory before this as well which you can look up.

- Remove all watches and rings and use proper laser safety for any of these procedures (proper signage, laser goggles, IR viewer, beam blocks etc.).

- Chirped pulse difference frequency generation relies on a smooth spectrum coming from the Ti:Saph laser amplifier. Do everything possible to ensure the spectrum of the regenerative amplifier (Regen) is as smooth as possible. This entails cavity end mirror and Pockels cell adjustments of the unseeded spectrum. The input Pockels cell (PC1) of the Regen has a strong effect on slow modulation of the spectrum. Small adjustments can be made, frequently optimizing the front cavity mirror, since the Pockels cell is wedged. This also shifts the emission peak by changing the the frequencies centered on Brewster's angle at the face of the gain crystal. The pump beam may need small adjustments if the cavity is changed. If the cavity axis changes, the second stage amplifier and input to the Regen compressor will also have to be adjusted, per instructions in the Regen SOP. The output Pockels cell (PC2) also has an effect on the spectrum, but primarily effects contrast ratio. Spectral quality seems to come with contrast ratio. I have no solution for observed fast modulation of the Regen spectrum. The spectrum does not appear to be long term or even day to day stable and may fluctuate on minutes time scales. The spectrum can be monitored during experiments by viewing scattered Regen light with a compact spectrometer.

I.1.2 Overview

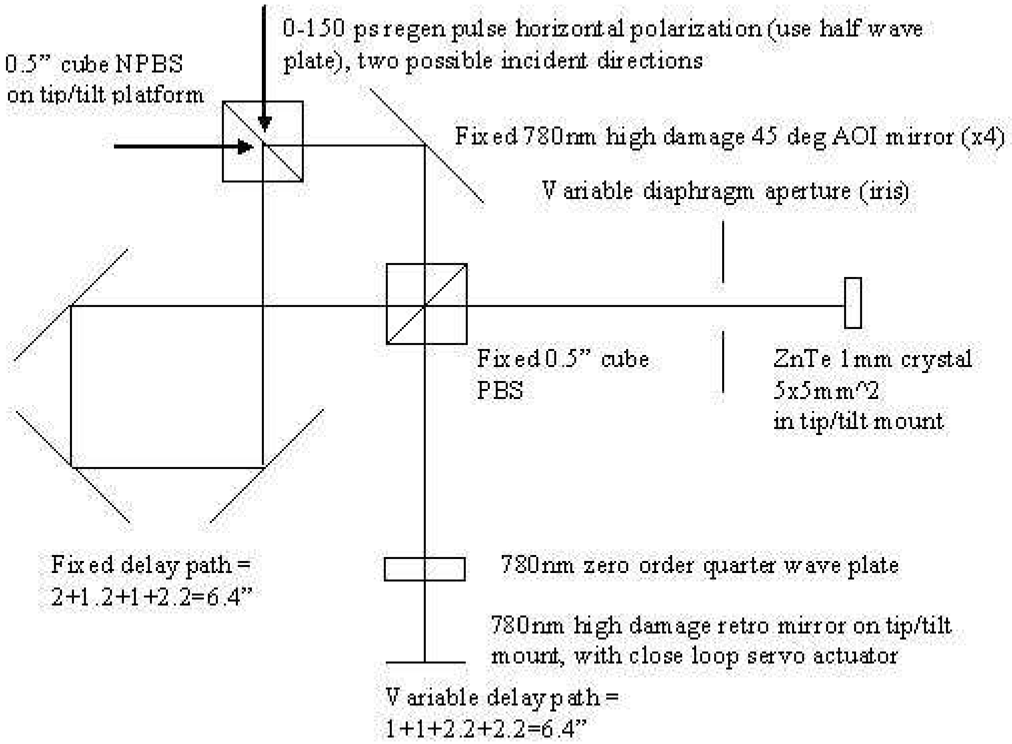

Figure I.1: Diagram of difference frequency generation (DFG) polarizing interferometer. The linearly chirped 10–100 ps, 780–800 nm pulse is incident from either the left or top, two beam of orthogonal polarization emerge at the right and mix in a nonlinear crystal via Type II (collinear, non-birefringent geometry).

In this experiment a 200 ps linearly chirped (red first) pulse from a regenerative amplified Ti:Saph femtosecond laser (10 Hz,10 mJ) is compressed by a variable amount to approximately 20–50 ps. The chirped pulse is then sent into a polarizing interferometer shown if figure I.1.

The interferometer creates two collinear orthogonally polarized beams of variable delay. In each pulse the frequency ramps in time. During the temporal overlap of the two pulses there is a constant difference frequency. Thus, phase-matched difference frequency generation (DFG), or narrow band optical rectification, occurs in a suitably oriented crystal with second order dielectric susceptibility ($\chi^2 \neq 0$). For ZnTe, narrowband radiation of tens of ps duration at frequencies between 1–3 THz can be generated under phase matched conditions with crystals 1.5 mm or less in length. 2 THz is the optimal frequency for phase matching. DFG is less efficient at higher frequencies due to weaker overlap of the two pulses and less efficient at lower frequencies because longer crystals are required to obtain the same number of cycles. GaSe is an alternative birefringent crystal which can be used for DFG, although we don't have any.

I.2 Pulse compressor alignment

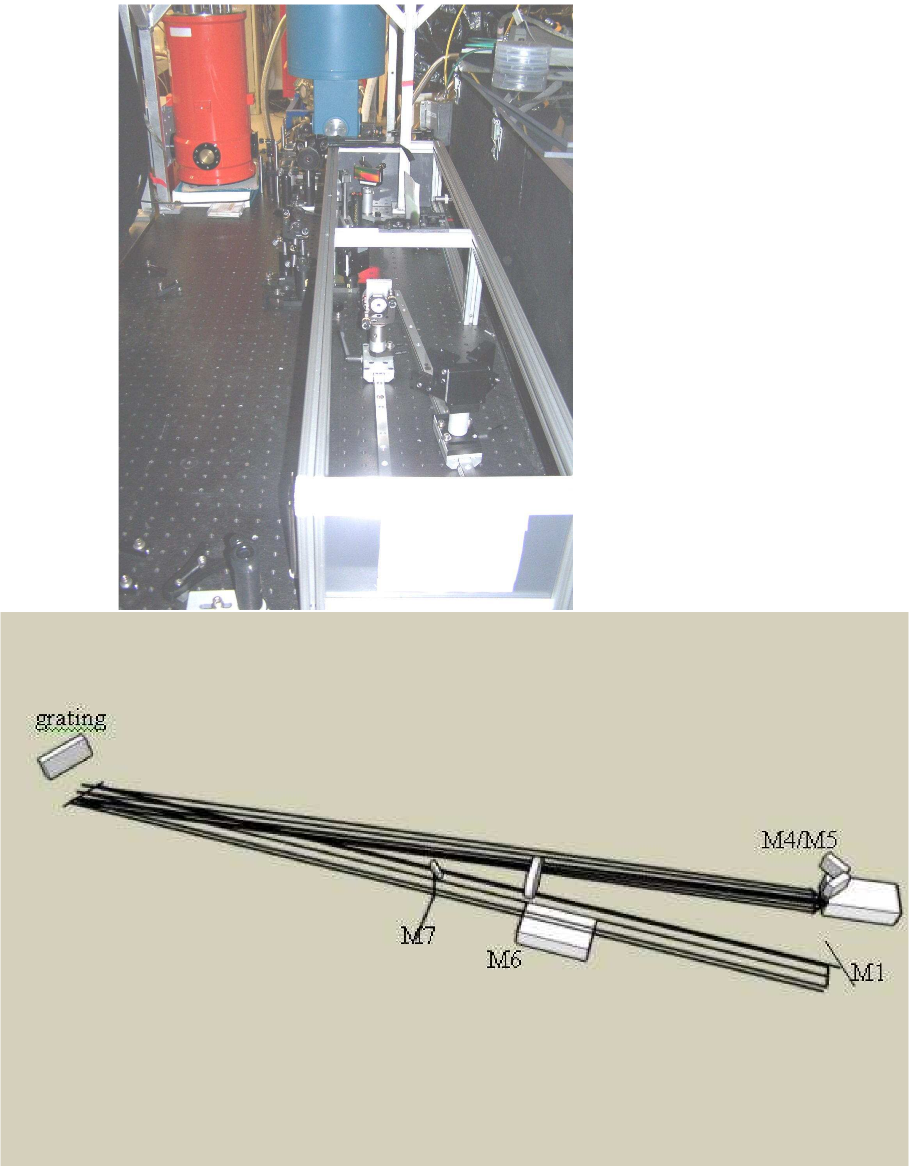

Figure I.2: (Top) Experimental layout. (Below) Pulse compressor beam path schematic layout. The beam path sequence is: M1 (collimated, all wavlengths collinear, slightly down),GR (wavelengths spreading), M4,M5,GR (collimated, wavelengths, parallel), M6, GR (wavelengths converging), M5, M4, GR (wavelengths collinear), M7 out.

Pulse compressor theory

Red gets slowed down relative to the blue in this arrangement. See diffraction calcs.xls in Dan's documents on computer "Sam". These are example calculations for a center wavelength of 790nm and a full bandwidth of 10nm. The delay is calculated as the time the 800 is delayed relative to the 790 for an incident fs pulse. Of course, you can get more than 10 nm bandwidth, but it will just miss M4 and M5. If you buy bigger mirrors you can have more bandwidth.

Table I.1: Delay time versus distance from grating to center of roof mirror (M 4 M 5) assembly.

Half length (m)	Spread (m)	delay (m)	delay (ps)
0.1	0.002833	0.006197	20.65507
0.2	0.005666	0.012393	41.31014
0.3	0.008499	0.01859	61.9652
0.4	0.011333	0.024786	82.62027
0.5	0.014166	0.030983	103.2753
0.6	0.016999	0.037179	123.9304
0.7	0.019832	0.043376	144.5855
0.8	0.022665	0.049572	165.2405
.9	0.025498	0.055769	185.8956
1	0.028331	0.061965	206.5507

I.2.1 Routine or fine alignment

For easy, routine adjustments, perform the M1 adjustment and the M6 adjustment only. Then proceed to interferometer alignment, section I.3.

I.2.2 Coarse alignment

You shouldn't have to do this unless somebody screwed up. (Could have been me.)

Light source

1. Choose a light source. A 780–810 nm laser diode (we have an 808 nm in a thorlabs TC mount.) will do, or if you like, use the Tsunami in CW mode. Grating adjustments will be smaller the closer you are to 790 nm. The incident polarization must be vertical for the grating. As an alternative to using a separate source to align the interferometer, you can send the CW tsunami beam into the regen without the YAG pump beam. Take the leak through from unpumped cavity emerging from the regen and align the pulse slice and interferometer to it.*Do not turn on the YAG under any circustances while this alignment is going on and an narrowband beam is in the cavity.* You will have to peak up the alignment when you turn the Regen on, since the seeded beam is different than the unseeded beam due to incomplete overlap of the YAG and Tsunami. Anyway, it is the easiest option in terms

of setup

2. Turn it up your source as low as possible to keep the bandwidth small. But if you can't see it with an IR viewer then turn it up all the way. If you can see it with your eye quite well, put on goggles you fool-it's so bright you would be crazy to look at if it were green and visible.
3. Make sure it is well collimated.
4. Align it through the iris along the path from the Regen to the input of the pulse compressor. The path is not level, but slightly down due to the height at which the uncompressed beam emerges from the Regen.

M1 adjustment

1. Temporarily insert the iris into the post directly in front of the grating.
2. Use M1 to get the beam through the iris. Remove the iris.

Grating adjustment

1. Adjust the grating rotation (horizontal axis adjust) until the center of the laser spot hits M4 in the center over the entire range of travel. This will should be possible for a small range of wavelengths near the design wavelength of 780-800nm.

2. Adjust the grating vertical axis so the beam is roughly level. A slight down or upward tilt is tolerable, and perhaps helpful for the next stage.

3. Put a beam block in to block the zero order reflection, if desired (hint, always desired when you use the regen).

M4/M5 adjustments

1. For the beam to return to the same size spot at the exit, M4 and M5 must be exactly perpendicular.

2. Check perpendicularity by moving the M4/M5 slider back and forth and making adjustments until the wide beam hitting the grating for the second time doesn't drift horizontally when you move the slider. (It will wobble vertically, the stage sucks). This may be easiest to check with a narrow

Figure I.3: Image of laser spots incident on the grating. The lateral separation between incidence 1 and 2 is due to the offset which occurs upon reflection from the roof mirror assembly (M4/M5). The downward trend is due to a slight downward tilt of the M4/M5 assembly and/or M6.

band light source.

3. Adjust the grating or M4/M5 vertically to get the beam onto M6 (no touching the horizontal axis!).

4. If the spread beam is not centered horizontally on M6, you are not a happy camper. The reason is that you will have to adjust the position of the grating along the incident beam axis to make it so. This will require iteration of steps above. Enjoy. I really doubt this will be necessary. Check the alignment through all the irises before you decide to move the grating.

M6 adjustments

1. If the beam is vertically misaligned, this is good so that you can see multiple reflections on the grating while you do horizontal alignment.

2. Adjust M6 horizontally to retro reflect the beam so that the third incidence on the grating is directly above or below the second incidence.

3. Now go back and make the beam approximately level, with a slight downward tilt so that the fourth incidence on the grating appears directly below the spot from the first incidence. You may have to cheat and use the horizontal adjust on M6 to get the spots to line up. Such is life.

4. Adjust the vertical M6 adjuster so that the collimated beam emerging from the fourth incidence is picked off by M7.

M7 adjustments

1. The outgoing beam should hit M7. Move it forward or backward to capture as much of the beam as possible.
2. Adjust tip and tilt to get the beam onto the first periscope mirror PR1.

I.3 Polarizing delay interferometer alignment

Here we discuss the alignment of the mirrors in the interferometer. One path is fixed and largely unadjustable, except coarse rotation by loosening screws on the bottom and twisting manually. The other path is variable length and has one tip/tilt prism mount for initial vertical angle adjustment, one fixed mirror which allows coarse rotation for horizontal angle, and one tip/tilt 0 degree mirror which allows for height and horizontal adjustment of the output beam angle. Both emerging beam should pass between two irises at the output. Use the following procedure to ensure the beam is incident along the correct path and that the pulses emerging from the two separate paths are collinear.

I.3.1 Input beam alignment

This part is unfortunately necessary whenever alignment in the pulse compressor changes. Care in this alignment is important and helpful later on as you may be able to skip interferometer alignment if you get it right. The following instructions are for the Tsunami, which is less dangerous option to get familiar with alignment than the Regen and most of the basics hold. Alignment with the Regen is discussed in section I.5.

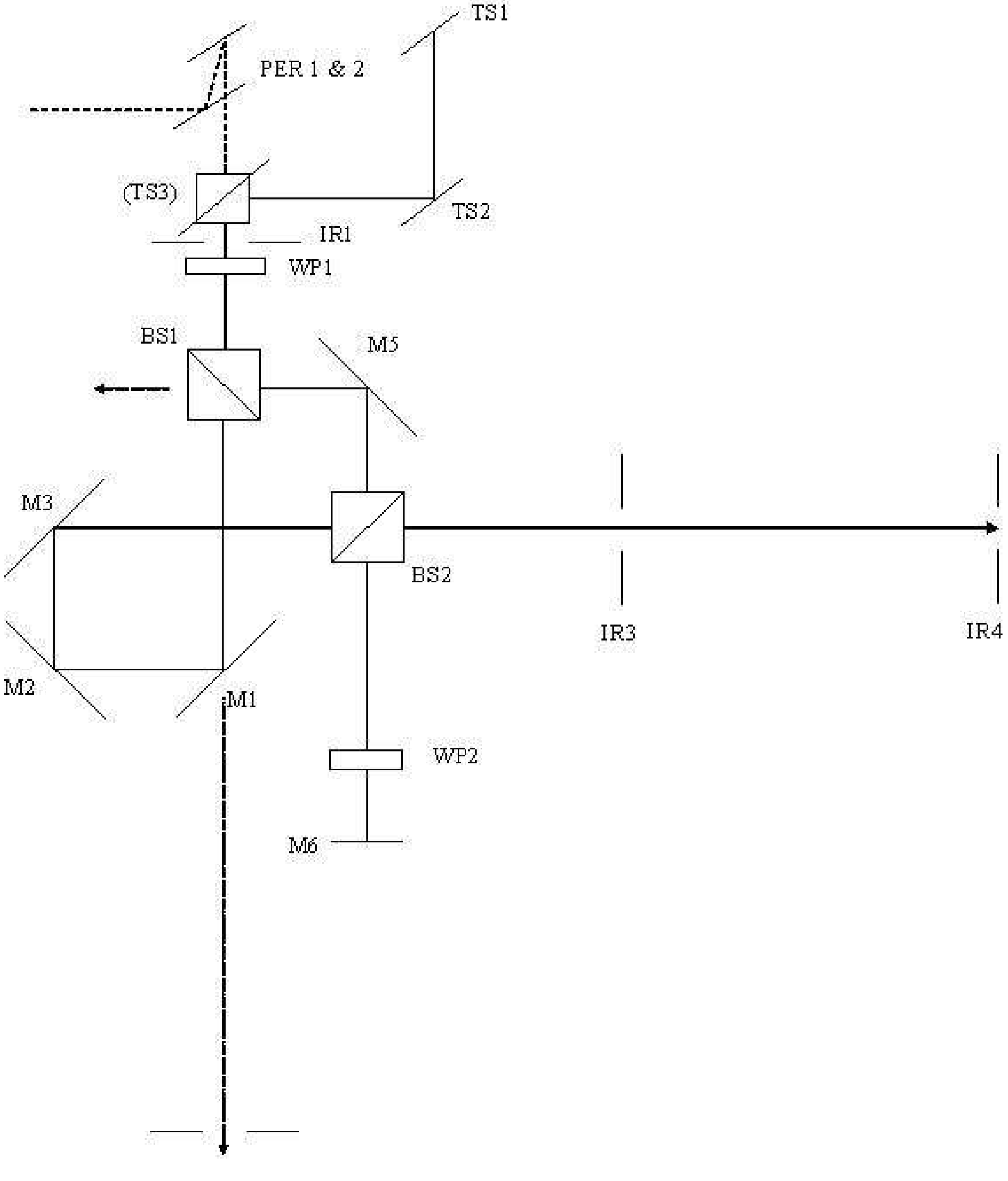

Figure I.4: Interferometer alignment

Tsunami Ti:Saph oscillator

1. Warm up Ti:Saph oscillator according to SOP. Use only as much power as is necessary. *Do not modelock the beam for this alignment procedure.*
2. Remove the interferometer and reclamp to the table in a safe place.
3. Insert TS1 and TS3 (flip mount)
4. Direct a minimum about of power along the now open path between IR1 and IR2. Use reflective attenuator not absorptive to reduce beam power for best safety.
5. Use TS1 an TS2 to center beam in IR1 and IR2.
6. Replace interferometer.

I.3.2 Polarization adjustment

Perform this before interferometer adjustments and afterwards if necessary.

1. Insert WP1. Make sure not to clip beam.
2. Insert a card between WP2 and M6 to block the variable beam path
3. Rotate WP1 to minimize reflection from BS2 emerging from BS1 (horizontal dotted line in figure I.4).
4. Remove card and place between M1 and M2 to block fixed beam path

5. Coarse adjust the rotation of WP2 to minimize reverse transmission through BS2 emerging from BS1 (horizontal dashed line in figure I.4).

I.3.3 Preparation for interferometer adjustments

1. Always perform beam alignment (section I.3.1) before this procedure. Since this is the worst part, make sure the beam alignment is dead on before you begin.
2. You will need the tsunami in CW mode for this procedure. If Tsunami is already passive modelocked, lower the power 10% or until mode locking becomes unstable, then shut the shutter and reopen it. Repeat until the laser stops passive modelocking.
3. Move the mirror close to zero path difference using the vi *stepper scan 4.vi.* The mirror surface should be ~56 mm from center of BS2.) If you want to align with a fs pulse because the CW mode is giving you trouble (I don't know why it would), you can use a card in the compressor to limit the bandwidth.

I.3.4 Fixed path alignment

1. Insert a card somewhere between BS2 and M6 to block the variable path.
2. Coarse adjust M1 and M3 rotation (9/64 hex screw accessible from bottom side) to center beam horizontally through post-mounted irises IR3 and IR4.

Note that the beam height is not adjustable, so adjust the height of IR3 and IR4 to center the beam.

3. Remove card.

I.3.5 Variable path alignment

1. Insert a card between M1 and M2 to block the fixed beam path.
2. Coarse adjust M5 rotation and M6 tilt to center the beam through IR3 and IR4. You may want to check that BS1 is at the right rotational angle since it is not in a kinematic mount.
3. Use either of the tip/tilt screws on BS1 together with the tip screw on M6 to center the beam vertically through IR3 and IR4.

I.3.6 Optimize fringe visibility

1. Insert a polarizer at 45 degrees to horizontal between IR3 and IR4. This makes the two polarizations indistinguishable. Otherwise, interference fringes would not be visible.
2. Insert a 30mm lens after the polarizer to focus the tsunami so that the fringe pattern is blown up and easily visible past the focus.
3. Use a card and IR viewer to view the beam after it has expanded. Block either beam in turn with another card to see whether fringes you see are

due to interference of the two beams or self interference within an optical element such as a beamsplitter or the polarizer itself. These lines should be closely spaced, if present, and you will just have to ignore them, or perhaps adjust the angle of the face of the polarizer to the incident light by rotating it slightly in its post.

4. If interference fringes are horizontal, adjust M6 horizontally to make the fringes spaced as far as possible. Repeat for the vertical direction until a single fringe occupies the whole beam area. You should see the beam spot "blink" if you bump something. *Hint: the closer you are to zero path delay the easier this is. You must be within the coherence length of your laser source from ZPD to clearly resolve fringes. Also, aperture down the beam to see effects more clearly. The maximum aperture over which you can maintain a single fringe gives you an idea of the spatial coherence in the beam.*

I.4 Find zero path difference (ZPD)

I.4.1 Procedure

1. Make sure the Tsunami is passive modelocking stably and beam, polarizer, and interferometer adjustments are complete. Use a chopper and lockin amplifier as described in the previous section.

2. Remove the ZnTe crystal.

3. Insert a polarizer at 45 degrees, followed by a 30mm lens.

4. Insert a chopper in the Tsunami beam. Make sure scattered light is shielded. Use a speed greater than 1kHz for best results. Be your chopping frequency is lower than the RC time constant from the lockin input impedance and the diode capacitance. If that is a problem use a transimpedance amplifier. I didn't, but I imagine it would make things easier.

5. Insert a GaP photodiode near the focus of the lens. Adjust the distance from the lens until blue light appears at the surface of the photodiode.

6. Plug the output of the diode into the lock-in amplifier. The two photon absorption background photovoltage signal should be in the range 30-120 mV. Set the lockin time constant to 30 ms.

7. Scan the variable beam path mirror over a range of 1–2 mm at speeds less than 0.05 mm/s. Use Newport ESP300 motion controller and closed loop

servo actuator and *stepper scan 4.vi* in the folder on computer *FEL1380C* referenced at the beginning of this document. Observe the previous ZPD recorded in the vi. Look for a peak in the photovoltage that is repeatable near that position. If you can't find it, you may have to move to a new region and re-optimize fringe visibility (section I.3.6). The two photon interferogram for a 150 fs pulse should resolvable at slow scan speeds (~ 500 nm/s), see below, where path delay PD is mapped to delay time T according to $T[fs] = PD[mm] * 2/(1000mm/m)/(3e8m/s) * 1e15(fs/s)$. Note that the 4 cm glass includes to 0.5" beamsplitters and a calcite polarizer.

8. Record the ZPD in the vi and at the end of this document in a log note. If you are ambitious you could find out the dispersion coefficients of calcite and the glass in the beamsplitters and then try to optimize the prism setting in the Tsunami to minimize the pulse length. If a FROG or GRENOUILLE setup is not available, this autocorrelator may be used to check the tsunami pulse width. The preferred way to adjust the prism and tuning slit is to adjust simultaneously in the same direction by sandwiching both micrometers between the sides of your hands and making *small* changes. Although the scanning interferometer will take quite a while to get the spectrum. Using a borrowed GRENOUILLE spectrometer and a small portion of the Tsunami beam, with the Tsunami operating at 795 nm center wavelength with 11 nm bandwidth and 570 mW power a transform limited pulse width of 80 fs

was observed, when a 3X beam expander with a thick negative lens and a achromat was inserted into the beam a 100 fs pulse was seen. The pulsed measured through the interferometer should be chirped significantly by the thick optics, especially if a calcite polarizer is used. Use the free program Topticalc (available from Toptica Photonics) to estimate the chirp from each element. Divide the autocorrelation FWHM by $\sqrt{2}$ and correct for chirp to obtain the actual pulse length.

I.4.2 Troubleshooting mirror motion

1. If you can't move to a certain position, check that the global soft limits in the vi are correct.

2. If you can't move at all, you have likely hit a hard stop. If this is the problem, the motor will not turn on (no green light on the ESP300). You can manually turn the screw away from the hard stop until the motor will respond to a turn on command. If you cannot grab the screw then you will have to remove the actuator and carefully take out the screws on the bottom side, unscrew the circuit board that holds the limit switches, so that the spring loaded limit switches can "un-limit" and restore the drive current to the motor. Now you can move the motor away from the limit using the software, and then put everything back together.

I.5 Prepare Regen pulse for THz generation

Disclaimer: I have not yet been able to see an autocorrelation from a stretched Regen pulse. I imagine it is a matter of finding the right intensity, pulse length, and scan range. In any event you can follow these instructions to get the Regen pulse ready to generate THz. If you are going through this procedure to rough align, it will be sufficient to block the YAG pump beam going to the second amplifier crystal and use the 1–2 mJ, 200 ps pulses dumped from the Regen cavity without further amplification. The mode pattern will change (widen, i.e. lengthen when periscoped out) when you use the second crystal, so you will have to realign the beam pointing at the regen output mirror and pulse compressor m1 to alignment pinhole and pulse compressor m6.

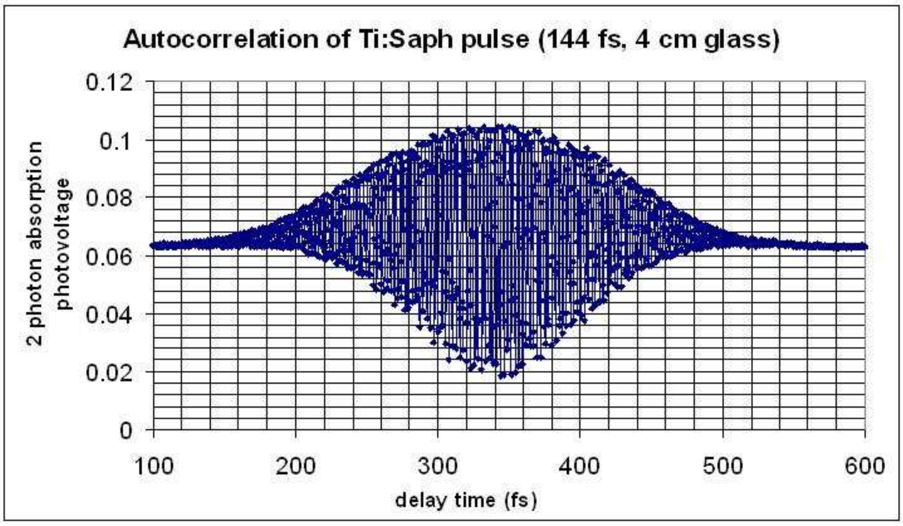

Figure I.5: Autocorrelation of Ti:Saph pulse taken with GaP photodiode and DFG setup. Note a 45 degree polarizer is required to obtain either a linear (Si photodiode—good luck not saturating.) or two-photon (GaP photodiode) interferogram.

I.5.1 Setup

Don't blow up the waveplates and polarizers

1. Note polarizer and waveplate damage thresholds. Do not exceed them. Transmission through the pulse compressor is at best 0.5. The beam diameter is on the order or 0.25 cm^2, with pulse energies of at most 5 mJ/pulse emerging from pulse compressor total beam intensity is 20 mJ/cm^2 on the waveplate and beamsplitter cubes. A Glan Taylor polarizer from Melles Griot will withstand only 5 mJ/cm^2.

2. Adjust the Regen pulse picker timing to select a pulse after the maximum, so that power will decrease as cavity build up time shortens over the coarse of the several hour full warm up. Reduce power to below the damage threshold. Measure beam power with power meter to be sure.

Don't blow up any mirrors/lenses

1. Do not use glued achromat lenses, use air-spaced lenses if achromats are necessary. Use NIR antireflection coated lenses, if lenses are necessary. Use only dielectric mirrors coated for 780 or 800nm. High damage threshold is not strictly necessary, but nice since they are easy to clean.

2. Check mirrors for dust, especially PER1.

3. Do NOT attempt to clean the grating. Blowing softly with nitrogen is the

only way to hope to dislodge a very large piece of dust. Just keep the lid on the pulse compressor whenever possible.

Don't blow up your eye

1. Make sure laser safety signs are up.
2. Wear goggles don't be a fool. People at UCSB have blinded an eye before. Use the brown goggles that block both green and red lasers.
3. Make everybody in the room wear goggles.
4. Make sure beam blocks and beam dumps are in place when the beam is not being used.
5. View the beam with goggles in place using the fluorescent ceramic (Kentek) sticks on metal posts. You may discover that the Regen beam is chromatically asymmetric. The most intense part of the beam visible on the fluorescent sticks is infrared while the more visible part of the beam occurs at a different position from the center of peak intensity. Minimizing spatial chirp is essential for DFG.

Ready the Regen

1. Insert a 0 degree mirror to pick off the stretched pulse before it enters the Regen compressor so as to reflect it out the exit. The screw that clamps the base will use the threaded hole which usually holds an iris. Put the mirror

as far back from the entrance as you can. It will have to be tilted slightly upwards and part of the beam may be eclipsed.

2. Check beam alignment through two irises prior to the input aperture of the variable pulse compressor at the other end of the table.

I.5.2 Set initial pulse compression value

1. Find the location of the minimum compressed pulse length by using the following simple technique. Insert a mirror at the output of the variable pulse compressor and direct it at a beam dump about 20 cm away. Insert e.g. a f=100 mm achromat lens into the emerging beam path so that the beam reaches a focus in air and then begins to diverge somewhat before hitting the beam dump. (Actually an achromat lens is not strictly necessary, but a NIR antireflection coated lens is good idea.) It is important that the beam has diverged enough when it hits the beam dump that a snapping sound is not heard when the beam impacts, because you will be listening for snapping from the beam at the focus.

2. Vary the position of the M4/M5 slider and listen carefully for the snapping or popping sound that happens at the focus when the compressed pulsed generates white light and ionizes the air. If you don't hear any snapping, use a slightly shorter focal length lens. Find the slider position of maximum popping sound.

3. Mark the position on the rail with, e.g., a sharpie marker with an arrow pointing to which side or the line the slider should be. I found a minimum pulse length near 36.5” or 0.93 m from the grating. This position depends on the chirp in the pulse is coming out of the Regen (nominally 200 ps, although no bandwidth is specified so the actually nm/ps of chirp is not known), and the (fixed) grating angle in the variable compressor. I know the compressor angle since I built it, so you can back out the Regen pulse length and chirp based on the calculations in table I.2 and a spectrum of the regen prior to the compressor from which you can obtain the pulse bandwidth. The dispersion (nm/ps) is the same, but the total delay is reduced to 0.9 of the value in the table.

4. Measure from the zero point the delay path length required to get from the nominal ¡1 ps fully compressed pulse out to whatever pulse length you want to operate at based on the dispersion described in table I.2. Note that the calculations for the compressor chirp are for a 10 nm bandwidth, but the compressor grating and mirrors only allow 9 nm at best.

5. Set the M4/M5 roof mirror slider to the distance from the grating required to achieve you desired delay. Use table I.2

6. Set the retro mirror close if M4/M5 slider is far or far if M4/M5 slider is close so as to not interfere and also to preserve total path length and emerging angle.

7.

I.5.3 Align interferometer with Regen pulses

Send Regen into the variable pulse compressor through two irises, perform fine alignment of the variable pulse compressor as described in section I.2, align the interferometer as described in section I.3.

I.5.4 Optimize fringe visibility

When you have sufficient beam parallelism and overlap (be as anal as you can) to begin optimizing the fringe visibility use the following procedure. Refer to figure I.6

1. Move 0 degree retro mirror to the ZPD position.
2. Prepare a vertical slit (e.g. cut one out of 3x5 cards) with a width of a few mm. Attach it to a base that is heavy enough to support it without tipping. Insert the slit into the variable compressor in front of the grating so that it passes the first incident and reflected beam but eclipses most of the returning stripe, thereby limiting the bandwidth. A narrow bandwidth permits a long coherence length, which will make it easier to resolve fringes.
3. Use the iris at the exit of the interferometer (IR3) to aperture the beam down to about 2mm in diameter.

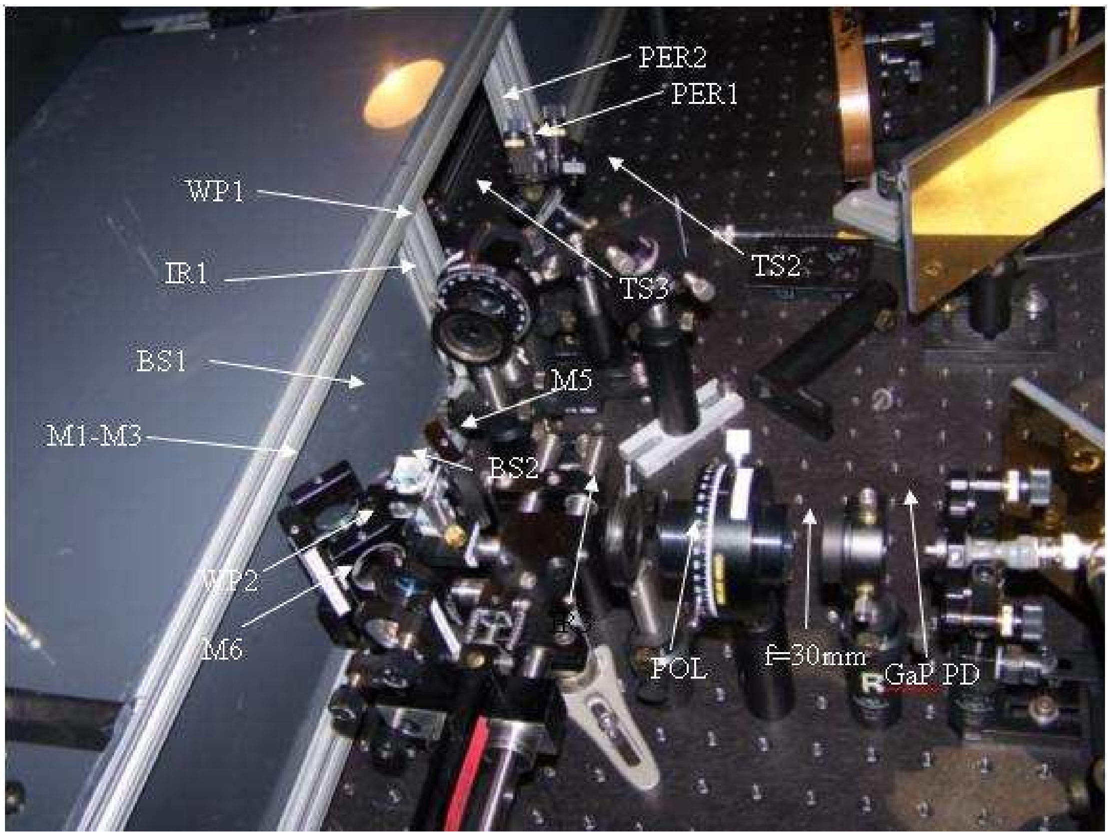

Figure I.6: Interferometer alignment setup.

4. Make sure the Regen power is low enough that you can focus the beam and not have problems with self-focusing. If your bandwidth is narrow enough this shouldn't be a problem.

5. Insert the 45 degree polarizer to resolve the fringe pattern.

6. Insert a short focal length lens after the polarizer (e.g. 30 mm) to expand the size of the fringe pattern.

7. Place a card ∼1 m from the lens, or far enough away that the beam is large enough to view easily with the IR viewer and large enough not to saturate the IR viewer. This is the key.

8. Twist the the polarizer in its post holder to make the interference fringes from the polarizer itself become narrow enough that they are not a problem.

9. Tweak the horizontal and vertical adjust of interferometer retro mirror (M6) to get the fringes as wide as possible. Open the aperture if necessary to continue optimizing the angle. This gives a good estimate of your spatial coherence.

I.6 Realigning after pulse length adjustments

If you have already aligned the spectrometer, the full alignment procedure does not need to be followed. Go to zero path delay. View the beam at the exit of the DFG interferometer. Adjust compressor M6 to get the beam centered on IR1. (Check the transmission through IR1 with the fluorescent stick.) Close down IR1 and view the spot at IR3. Adjust PER2 horizontal adjust to overlap the spots from two arms of the interferometer. Adjust PER2 vertical to transmit through IR3. View the spots a meter away from the output with a fluorescent stick. Adjust interferometer retro mirror M6 to make the spots coincide. Repeat PER2 and interferometer M6 adjustments once or twice.

I.7 Aligning the crystal

Insert the ZnTe crystal at the exit of the interferometer. See the appendix on difference frequency generation and optical rectification to determine the preferred crystal orientation. Use an IR viewer to center the surface reflection from crystal back onto IR1. This is critical for phase matching.

I.8 Optimizing the DFG signal

To optimize the DFG signal, use the shortest possible pulse length and place the bolometer right at the exit of the crystal. Iteratively scan the interferometer to observe the DFG spectrum, then make adjustments to the crystal and/or the interferometer retro mirror at delay positions where the DFG signal is strong and SNR is highest (Fig. I.7).

I.9 How to get THz pulse length without an autocorrelator

Measure bandwidth

Measure the spectrum of the Regen pulse emerging from the pulse compressor using the Acton 2750 monochromator and Princeton instruments CCD. The CCD takes two hours to cool down. *Do not cool it down unless it is powered on. Static could build up and blow up the amplifier circuit.* Relevant LabView vi's are *FEL1380C\Dan Allen's documents\instruments specs and vi's\acton 2750\ARC_Instrument_dll_SDK\monocontrol.vi and FEL1380C\Dan Allen's documents\instrum*

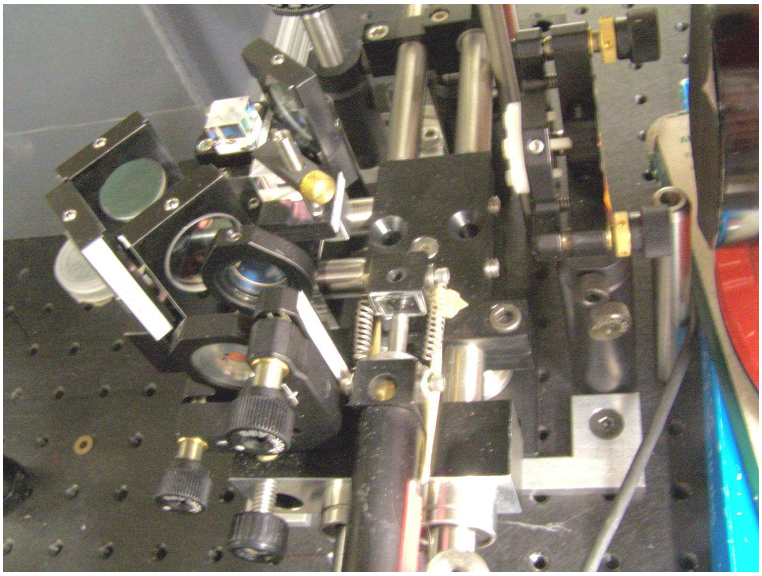

Figure I.7: A close up of DFG measurement. Note proximity of bolometer to crystal (concealed within white delrin mount) and thick black paper and black polyethylene for blocking the Regen beam from hitting the Si:composite bolometer. Some bolometers have visible filters. The Si bolometer does not; the InSb does.

specs and *Instruments specs and vi's\Princeton Instruments CCD\operateCCD.vi.* I have used a fiber to couple the light to the input, but this technique is not ideal. It is better to get a compact spectrometer and detector such as the Photon Control fiber spectrometer which uses the specsoft software. (Don't use a fiber with the photon control spectrometer. Just let diffuse light couple in directly through its entrance slit. The fiber adds modulation to the spectrum.)

Measure chirp

Take out the polarizer and lens. Put the ZnTe crystal in front of the Regen beam in the proper orientation for Type II DFG. Relay the emerging THz to a bolometer and measure the spectrum with a Michelson interferemeter. Measure the spectrum as at several of delay points to estimate the chirp. Alternatively you may cool a sample of low doped GaAs, tune the New Focus laser into resonance with the D0X line, and scan the delay near ZPD. Look for the lowest frequency peaks (nearest ZPD) which are symmetric about the ZPD point. This is 1 THz. Estimate the chirp based on the round trip distance from ZPD (which is the same as micrometer distance between the 1 THz peaks).

Calculate pulse length

Given the round trip distance required to get 1THz of frequency delay. Given the bandwidth you can back out the pulse length and given the spectral density you know the pulse shape, provide the chirp is indeed linear, as it should be.

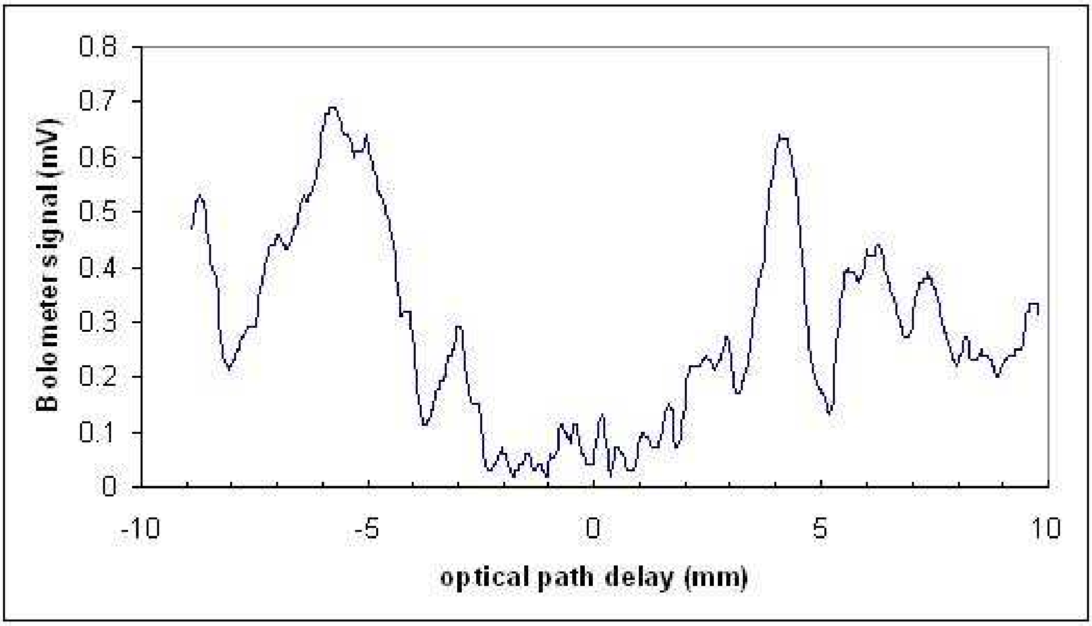

Figure I.8: A difference frequency generation spectrum taken with a Si:composite bolometer and >2 mJ optical energy at approximately 10-20 ps Regen pulse length. Lockin detection is used at 10 Hz (with 4-pole low pass filter, 60 and 120 Hz notch filters, synch filter and room lights off). Note some symmetry about the zero path delay point and lack of signal at zero path delay.

Estimate THz pulse length

Multiply the time spectrum of pulse with one delayed by however much you need to get THz frequency you desired. This is your THz pulse length.

Appendix J

Polarization effects in DFG and optical rectification

J.1 Nonlinear polarizability

The polarization of a crystal in response to an electric field can be represented by a sum of products, increasing in order of electric field, in the form of a power series expansion. (reference Boyd Nonlinear optics)

$$\begin{aligned} \boldsymbol{P}(t) &= \epsilon_0(\chi^{(1)}\boldsymbol{E}(t) + \chi^{(2)}\boldsymbol{E}(t)^2 + \chi^{(3)}\boldsymbol{E}(t)^3 + \ldots) && \text{(J.124)} \\ &= \boldsymbol{P}^{(1)}(t) + \boldsymbol{P}^{(2)}(t) + \boldsymbol{P}^{(3)}(t) + \ldots && \text{(J.125)} \\ & && \text{(J.126)} \end{aligned}$$

Each of the terms in the expansion is a tensor product, and each product yields a three component vector $\boldsymbol{P}^{(i)}$ which contributes to the total polarization. I consider materials for which the first and second order response contribute significantly to the total polarization vector $\boldsymbol{P}(t)$.

In the absence of externally applied fields, ionic positions in a lattice reside at potential minima. At each minimum, the spatial potential is approximately parabolic and a linear restoring force is expected in response to an infinitesimal applied electric potential. This is the reason for the ubiquitous linear polarizability of solids, where $P^{(1)}(t) \propto E(t)$.

At higher fields, ionic displacements become large enough to sample the anharmonic character of their potential wells. The spring constant of the restoring force becomes dependent on the displacement, resulting in a nonlinear response. If ionic positions are arranged around a center of inversion symmetry in a lattice, the lowest (2nd) order nonlinear polarizability will be cancelled by opposed dipoles. However, if no such center of inversion symmetry exists, meaning we are dealing with a noncentrosymmetric crystal, an asymmetrical polarization response is expected for large enough applied fields. Asymmetrical polarization is conceptually similar in behavior to a diode, which responds differently to electric fields in different directions. This nonlinear response enables rectification or mixing of frequencies for sum and difference frequency generation.

Consider a crystal with second order polarizability in the presences of a strong time-dependent electric field. To be general, I consider interactions of the crystal with components of the electric field along different directions, as well as different frequencies, so that the for instance:

$$\boldsymbol{E}(t) = \boldsymbol{E}_1 \sin(\omega_1 t) + \boldsymbol{E}_2 \sin(\omega_2 t). \tag{J.127}$$

The first order susceptibility $\chi^{(1)}$ is a first rank tensor, or square 3x3 matrix made up of elements χ_{ij}, which give the polarizability in direction i due to a field along the j axis. Diagonal terms differ a crystal exhibits different polarizability in different directions. Off-diagonal terms are present when the crystal axes are not orthogonal and not of equal length. However, no mixing of frequencies is obtained from this term, no matter the crystal symmetry, as expected for a linear system.

$$\boldsymbol{P}^{(1)}(t) = \epsilon_0 \begin{pmatrix} \chi_{xx} & \chi_{xy} & \chi_{xz} \\ \chi_{yx} & \chi_{yy} & \chi_{yz} \\ \chi_{zx} & \chi_{zy} & \chi_{zz} \end{pmatrix} \begin{pmatrix} E_{1x}(t) + E_{2x}(t) \\ E_{1y}(t) + E_{2y}(t) \\ E_{1z}(t) + E_{2z}(t) \end{pmatrix} \tag{J.128}$$

The second order susceptibility $\chi^{(2)}$ is a second rank tensor, a rectangular 3x9 matrix. Elements are $\chi^{(2)}_{ijk}$, which give the polarization along the i direction, due to the product of electric fields in the j and k directions. The electric field can be written as a 9 component vector (9x1 matrix) including all possible combinations of $E_{1j}E_{2k}$. The resulting second order polarization is a three component vector $\boldsymbol{P}^{(2)}$. Materials may be cubic and isotropic, but still possess a nonzero $\chi^{(2)}$, by virtue of a noncentrosymmetric arrangement of various atoms within the unit cell, as is the case for Zinc-blende crystals such as GaAs and ZnTe which have tetragonal bonding with positions similar to those of carbon in diamond, but with ionic bond character. Zinc-blende crystals are of the symmetry class $\bar{4}3m$

For this symmetry all terms in $\chi^{(2)}$ where indices are repeated are zero. The remaining terms are identical. In the following I suppress the time dependence by assuming the $\boldsymbol{E}_1$ and $\boldsymbol{E}_2$ are harmonic so that the result can be applied to any two Fourier components of a time-dependent electric field.

$$\boldsymbol{P}^{(2)}(t) = \epsilon_0 \begin{pmatrix} 0 & 0 & 0 & 0 & 0 & \chi^{(2)} & 0 & \chi^{(2)} & 0 \\ 0 & 0 & \chi^{(2)} & 0 & 0 & 0 & \chi^{(2)} & 0 & 0 \\ 0 & \chi^{(2)} & 0 & \chi^{(2)} & 0 & 0 & 0 & 0 & 0 \end{pmatrix} \begin{pmatrix} E_{1x}E_{2x} \\ E_{1x}E_{2y} \\ E_{1x}E_{2z} \\ E_{1y}E_{2x} \\ E_{1y}E_{2y} \\ E_{1y}E_{2z} \\ E_{1z}E_{2x} \\ E_{1z}E_{2y} \\ E_{1z}E_{2z} \end{pmatrix} \tag{J.129}$$

$$= \epsilon_0 \chi^{(2)} \begin{bmatrix} E_{1y}E_{2z} + E_{1z}E_{2y} \\ E_{1x}E_{2z} + E_{1z}E_{2x} \\ E_{1x}E_{2y} + E_{1y}E_{2x} \end{bmatrix} \tag{J.130}$$

J.1.1 Crystal orientation

In order for a nonlinear polarization to contribute to a transverse electromagnetic wave, the generated polarization must be perpendicular to the k vector along which the pump laser difference momentum is minimum (i.e. $\Delta\vec{k} = 0$). In the case of $\bar{4}3m$ crystal symmetry, which has a cubic structure, incident electric fields must have components along at least two crystal axes, since elements of $\chi^{(2)}$ are only nonzero when indices are distinct. This means a second order polarization develops in the direction given by the cross product of two incident polarization vectors. The simple choice of cross polarized lasers copropagating along a simple crystal axis (e.g. [001]) produces no radiation, because the second order polarization is along the direction of the propagation, and the polarization vector cannot be parallel to the pointing vector for a transverse wave.

Fortunately other orientations allow for difference frequency generation. For cross-polarized, copropagating pump lasers of slightly different frequency, the direction of lowest wavevector mismatch is in the direction of propagation. Incidence on a facet of the [110] plane allows for maximal THz generation when one the laser polarizations is along the [1$\bar{1}$0] direction. This will be shown later on. For co-polarized, copropagating pump lasers, or a single broadband laser pulse, THz generation occurs in the direction of propagation

J.2 Phase matching

The square of an electric field made up of two or more time periodic electric fields, produces sum and difference frequencies. In the case of two closely spaced optical frequencies ω_1,$omega_2$, a second order polarization may be generated at a far infrared frequency ω_{THz}, according to the relation.

$$\omega_{THz} = \omega_1 - \omega_2. \tag{J.131}$$

In the absence of dispersion at the incident frequencies ($n_1 = n_2$), the condition for optimal difference frequency generation is

$$\vec{\boldsymbol{k}}_{THz} = \vec{\boldsymbol{k}}_1 - \vec{\boldsymbol{k}}_2. \tag{J.132}$$

The two constraints (eqs. J.131 and J.132) necessitate the far infrared and optical indices of refraction be identical.

$$n_{THz} = n_{NIR} \tag{J.133}$$

This can be achieved in crystals with birefringence (GaSe), or in materials which exhibit anomalous dispersion (ZnTe, GaP), since in normal material the NIR index of refraction is less than the THz index. (Oscillators do not contribute to dielectric response above their resonant frequency.)

When perfect phase matching is not achieved the amplitude of the generated radiation will oscillate along the length of the crystal x according to the exponential $exp(-i\Delta\vec{k} \cdot \vec{x})$, where $\Delta\vec{k} = \vec{k}_1 - \vec{k}_2$.

The resulting coherence length l_c for difference frequency generation is

$$l_c \equiv \frac{\pi}{|\Delta k|} = \frac{\pi c}{\omega_{THz}|n_{NIR} - n_{THz}|} \tag{J.134}$$

In the presence of dispersion at optical frequencies, the phase matching condition on the indices of refraction is modified (reference A Nahata, A S Weling, T

F Heinz, Appl. Phys. Lett. 69, 2321 (1996)). In order for phase of the generated radiation to add coherently to the radiation generated at previous locations in the crystal, the group velocity of the incident (NIR) fields must propagate near the phase velocity of the difference frequency (THz).

$$\frac{\partial \omega_{NIR}}{\partial k_{NIR}} = \frac{\omega_{THz}}{k_{THz}} \tag{J.135}$$

The effective index for the pump lasers is altered by dispersion, yielding a dispersion-dependent effective index of refraction.

$$n_{eff} = n_{NIR} - \lambda_{NIR} \frac{dn_{NIR}}{d\lambda} |_{\lambda_{NIR}} \tag{J.136}$$

Where n_{NIR} is the median index of refraction in the region of the two NIR pump frequencies.

The effective coherence length now becomes

$$l_c = \frac{\pi c}{\omega_{THz} |n_{NIR} - \lambda_{NIR} \frac{dn_{NIR}}{d\lambda} |_{\lambda_{NIR}} - n_{THz}|} \tag{J.137}$$

J.3 THz generation

I now consider a crystal in which phase matching is achieved in one of two ways:

1. copolarized, collinear pump frequencies (Type I–optical pulse rectification)
2. cross polarized, collinear pump frequencies (Type II–difference frequency generation)

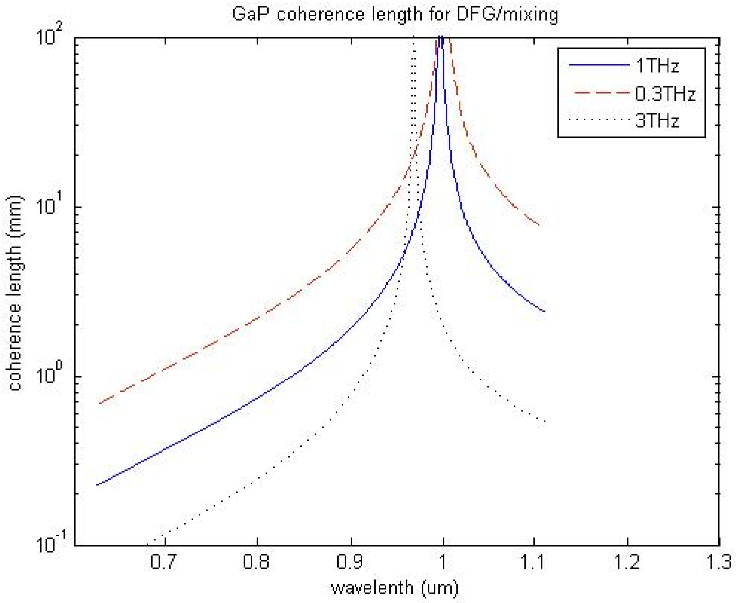

Figure J.1: Plot of coherence length in [110] GaP versus NIR excitation wavelength for GaP for three values of the difference frequency, including the effects of NIR dispersion. Values for ZnTe are available in reference (A Nahata et al., Appl Phys. Lett 1996)

J.3.1 Type-I difference frequency generation: optical rectification

Optical rectification usually refers to difference frequency generation between fourier components of a broadband, ultrashort laser pulse. A single cycle Terahertz pulse transient can be generated. The high frequency rolloff begins at the 3dB frequency bandwidth of the optical pulse. The lowest frequency generated is typically limited by the crystal length.

Consider a broadband laser pulse with frequency components $E_1 \exp(-i\omega_1 t)$ and $E_2 \exp(-i\omega_2 t)$ (with complex conjugates). The components are copolarized and collinear at normal incidence to the [110] facet of a $\bar{4}3m$ crystal, such as

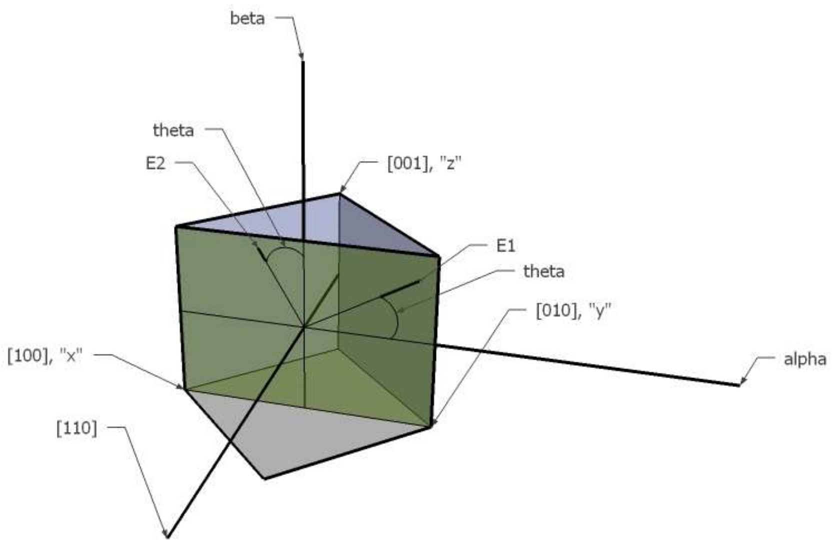

Figure J.2: Laser incident on [110] crystal. For optical rectification a single laser is incident, with mixing occurring between co-polarized frequency components arriving simultaneously on the crystal. For difference frequency generation, two beams with orthogonal polarization are incident (E_1 and E_2) on the crystal.

ZnTe. The polarization lies an angle θ from the $[\bar{1}10]$ direction. With $\hat{x}$, $\hat{y}$, and $\hat{z}$ representing the crystal axes, I express the incident electric fields E_1 or E_2 in terms of the angle θ.

$$\vec{E}_{1,2} = E_{1,2}\left[\frac{1}{\sqrt{2}}\cos\theta(-\hat{x}+\hat{y}) + \sin\theta\hat{z}\right] \tag{J.138}$$

The resulting second order polarization is given by equation J.129.

$$\boldsymbol{P}^{(2)} = \epsilon_0 \chi^{(2)} \begin{bmatrix} E_{1y}E_{2z} + E_{1z}E_{2y} \\ E_{1x}E_{2z} + E_{1z}E_{2x} \\ E_{1x}E_{2y} + E_{1y}E_{2x} \end{bmatrix} \tag{J.139}$$

$$= \epsilon_0 \chi^{(2)} 2E_1E_2 \cos\theta \begin{bmatrix} \sqrt{2}\sin\theta \\ -\sqrt{2}\sin\theta \\ -\cos\theta \end{bmatrix} \tag{J.140}$$

$$\tag{J.141}$$

Immediately an overall cosine dependence with respect to the $[\bar{1}10]$ direction can be seen as well as the tendency of the emission to be cross polarized to the pump beam. (The sine term in the first two components gives a null in emission along the $[\bar{1}10]$ direction at $\theta = 0$, while the cosine in the third component is maximized.)

Because second order polarization only occurs when electric field components are present along orthogonal crystal axes, optical rectification does not occur when the pump laser polarization is parallel to a crystal axis. This makes it easy to determine which facet of a [110] cut crystal is the surface normal to the [001] direction. It is the direction which produces no optical rectification when it is aligned parallel to the pump polarization.

As the crystal is rotated a component develops along another crystal direction, which leads to an increase in total second order polarization. A maximum is reached near $\theta = 35°$, where signal begins to decrease as the crystal is rotated away from the preferred $[\bar{1}10]$ mixing axis.

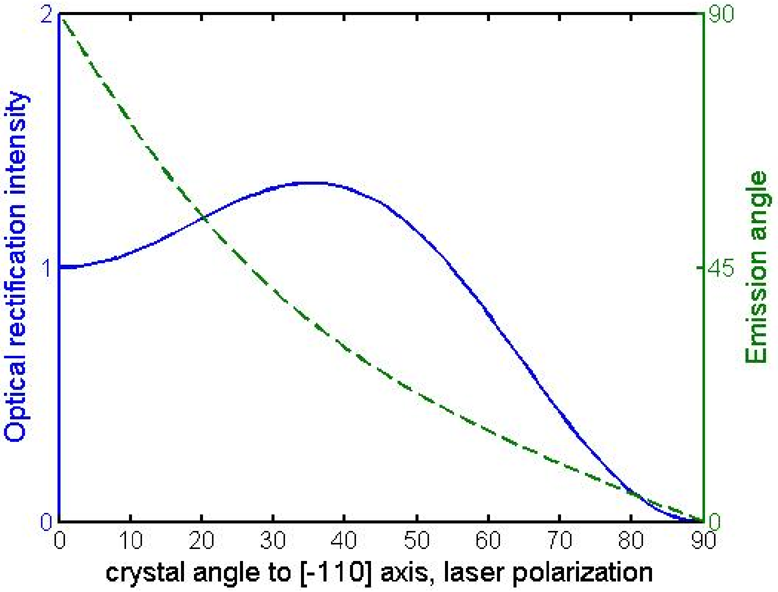

Figure J.3: Intensity and second order polarization generated by optical rectification. The broadband pump laser pulse is incident on the [110] face of a $\bar{4}3m$ symmetry crystal. The horizontal axis is the angle of laser polarization vector to crystal $[\bar{1}10]$. The second order polarization angle is also plotted relative to the $[\bar{1}10]$ axis, imagining the case where the laser polarization is rotated relative to the crystal.

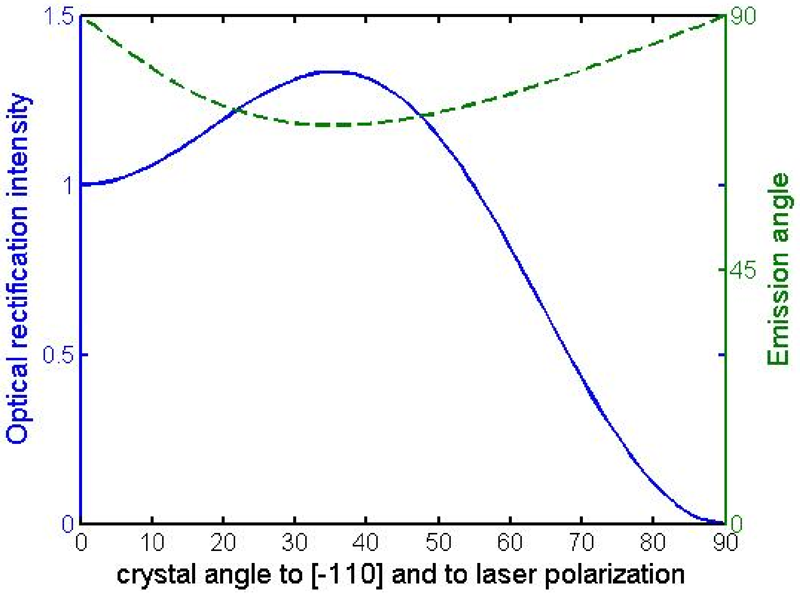

Figure J.4: Similar to above, except the second order polarization angle is measured in real space angle relative to the incident laser polarization vector, as when the crystal is rotated relative to the laser pulse.

In a difference frequency generation experiment where very short pulses are used, optical rectification of individual pulses is possible. Optical rectification is distinguished by its independence with respect to the relative delay between the pulses (aside from a small factor having to do with loss that makes the optical rectification more efficient when the pulses are well separated). With two orthogonally polarized lasers incident on the crystal a maximum is observed when the preferred mixing axis is 45° to either laser polarization.

J.3.2 Type-II difference frequency generation

Type-II difference frequency generation occurs when the beams mixing in the crystal are coaxial and have orthogonal polarization vectors.

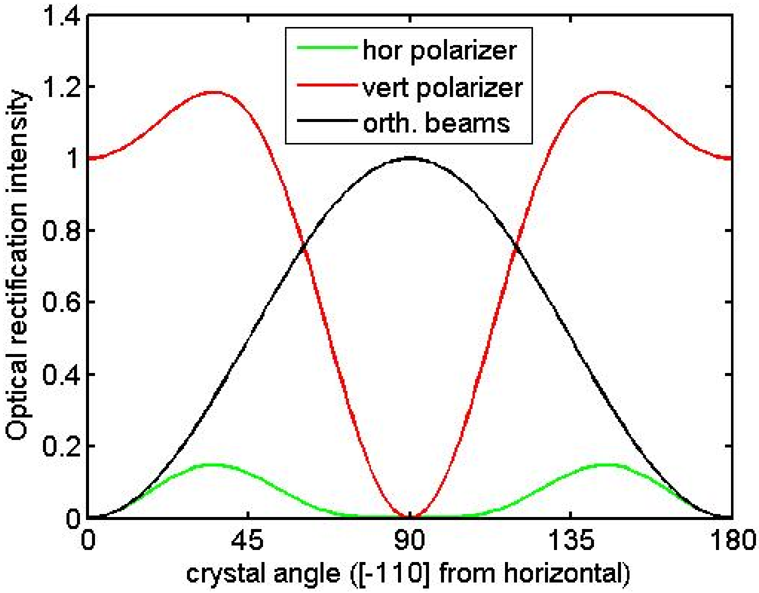

Figure J.5: Second order polarization detected after a polarizer oriented either parallel (green) or perpendicular (red) to the incident laser polarization vector. The black trace shows what is expected if two identical, orthogonal ultrafast pulses are incident on the crystal at different times so that they do not undergo difference frequency generation, but rather self-mix. If the polarizer is removed, a maximum emission in the absence of a polarizer occurs when the angle from the $[\bar{1}10]$ axis from either polarization vector is 45°, and no null is observed as the crystal is rotated.

$$\vec{E}_1 = E_1\big[\frac{1}{\sqrt{2}}\cos\theta(-\hat{x}+\hat{y})+\sin\theta\hat{z}\big] \tag{J.142}$$

$$\vec{E}_2 = E_2\big[\frac{1}{\sqrt{2}}\sin\theta(\hat{x}+\hat{y})+\cos\theta\hat{z}\big] \tag{J.143}$$

$$\tag{J.144}$$

The resulting second order polarization is given by equation J.129.

$$\boldsymbol{P}^{(2)} = \epsilon_0\chi^{(2)}E_1E_2\begin{bmatrix} \frac{1}{\sqrt{2}}\big[\cos^2\theta-\sin^2\theta\big] \\ \frac{1}{\sqrt{2}}\big[\sin^2\theta-\cos^2\theta\big] \\ \cos\theta\sin\theta \end{bmatrix} \tag{J.145}$$

The second order polarization remains in the plane of incidence, and is almost stationary with the mixing axis ($[\bar{1}10]$). A minimum occurs when the mixing axis is 45° to either polarization vector. A four-fold symmetry in emission strength vs. crystal angle is expected. This technique requires the pump beams be aligned coaxially to maximize spatial overlap and minimize wavevector mismatch.

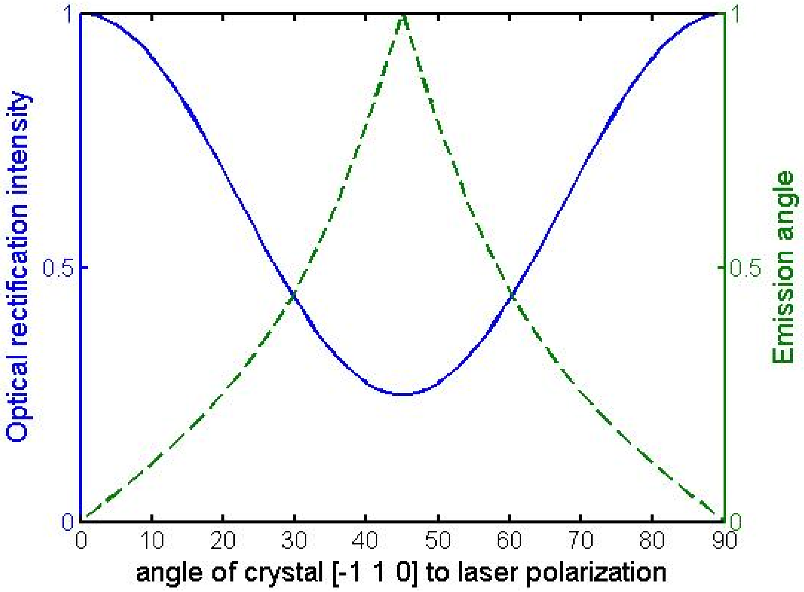

Figure J.6: Intensity and second order polarization generated by type-II DFG. Two frequencies are incident on the [110] face of a $\bar{4}3m$ symmetry crystal with orthogonal polarization. The horizontal axis is the angle of laser polarization vector to crystal $[\bar{1}10]$. The second order polarization angle is also plotted relative to the $[\bar{1}10]$ axis, imagining the case where the laser polarizations are rotated relative to the crystal.

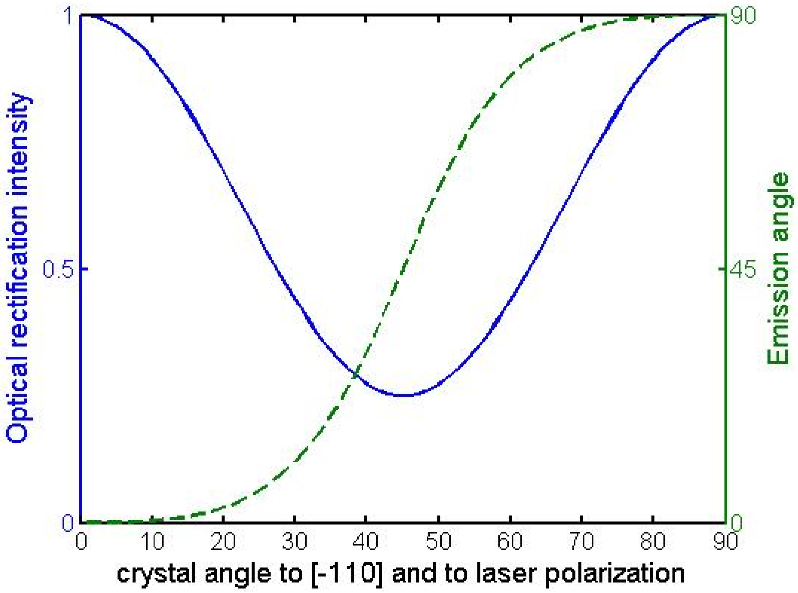

Figure J.7: Similar to above, except the second order polarization angle is measured in real space angle relative to the incident laser polarization vectors, as when the crystal is rotated relative to the laser pulse.

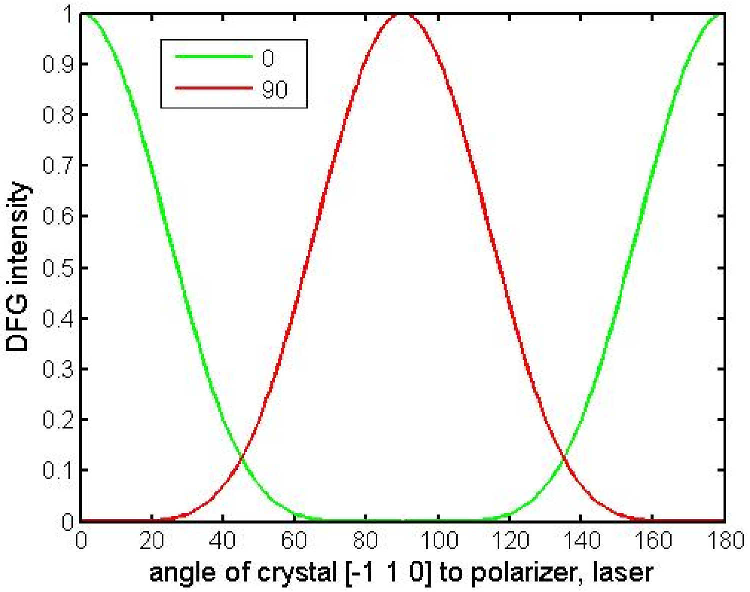

Figure J.8: Second order polarization detected after a polarizer oriented either parallel (green) or perpendicular (red) to the incident laser polarization vector.